

AD-A275 598



1

ANNUAL REPORT

NOVEMBER 1993

**Innovative Processing**  
**of**  
**Composites for Ultra-High**  
**Temperature Applications**

by

**Reza Abbaschian**  
**Department of Materials Science and Engineering**  
**University of Florida**  
**Gainesville, Florida**

**Sponsored by: The Advanced Research Projects Agency**

**Monitored by: The Office of Naval Research**

**ARPA Grant No. N00014-91-J-4075**

**DTIC**  
**SELECTE**  
**FEB 03 1994**  
**S E D**

154px

**94-03986**

**BOOK II OF III**

**Approved for public release**  
**Distribution unlimited**

**94 2 03 200**

## Executive Summary

The overall objective of this program was to provide a fundamental understanding of the processing science and technology necessary to fabricate ceramic-matrix, intermetallic-matrix, and metal-matrix composites with superior mechanical properties in high temperature and oxidizing environments. The composites are intended for use as structural materials for advanced aerospace applications at temperatures exceeding 1200°C (2200°F).

In order to accomplish the program objective, interactive research groups were established in three key areas of (a) Fiber Fabrication, (b) Coatings and Infiltration, and (c) Composite Fabrication. The objective of the fiber fabrication group was to develop new fibers which have superior strength and toughness at high temperatures and in oxidizing environments. The research effort focused on the development of two types of fibers: (1) glass-free mullite-based fibers, and (2) oxygen-free silicon carbide fibers. The coatings program had two primary objectives: (1) to control the characteristics of matrix/reinforcing phase interfaces (e.g., to control chemical reactions and bonding at a matrix/fiber interface) and (2) to develop coatings that will improve the oxidation resistance of metal-matrix and intermetallic-matrix composites. Coatings methods utilized included chemical vapor deposition, sol-gel processing, and solution coating with polymeric precursors to ceramics.

The composite fabrication group investigated various methods to incorporate reinforcing phases (i.e., fibers, whiskers, and particulates) into ceramic-, metal-, and intermetallic-matrices. Processing methods investigated included colloidal processing, chemical vapor infiltration, reactive hot-compaction and *in situ* coating, and microwave sintering. The objectives were not only to utilize innovative processing techniques, but also to develop an improved scientific understanding of processing-microstructure relationships in composites fabrication.

This annual report consists of seven sections compiled in three books as described below:

### Book I

- |           |  |
|-----------|--|
| Section 1 | Processing and Properties of Silicon Carbide Fibers<br>Principal Investigators: C.D. Batich<br>M.D. Sacks    |
| Section 2 | Processing of Mullite Composite Fibers<br>Principal Investigators: A.B. Brennan<br>J.H. Simmons              |
| Section 3 | Chemical Vapor Deposition (CVD) and Chemical Vapor Infiltration (CVI)<br>Principal Investigator: T. Anderson |

Book II

Section 1 Processing and Properties of Intermetallic Matrix Composites  
Principal Investigator: R. Abbaschian

Section 2 Mechanical Alloying of MoSi<sub>2</sub>  
Principal Investigator: M.J. Kaufman

Book III

Section 1 Processing of Ceramic Matrix Composites  
Principal Investigator: M.D. Sacks

Section 2 Processing of BaO-Al<sub>2</sub>O<sub>3</sub>-2SiO<sub>2</sub> Fibers.  
Principal Investigator: D.E. Clark

|                    |                                     |
|--------------------|-------------------------------------|
| Accession For      |                                     |
| NTIS CRA&I         | <input checked="" type="checkbox"/> |
| DTIC TAB           | <input type="checkbox"/>            |
| Unannounced        | <input type="checkbox"/>            |
| Justification      | <i>per ltr</i>                      |
| By .....           |                                     |
| Distribution/      |                                     |
| Availability Codes |                                     |
| Dist               | Avail and/or Special                |
| <i>A-1</i>         |                                     |

DTIC QUALITY INSPECTED 8

**BOOK II**

**Section 1**

**Processing and Properties**

**of**

**Intermetallic Matrix Composites**

**Principal Investigator: R. Abbaschian**

# Processing and Properties of Intermetallic Matrix Composites

**Principal Investigator: R. Abbaschian**

## **Objectives**

The overall objective of this program is to develop intermetallic-matrix composites for structural application above 1200°C. The development of intermetallic-matrix composites is motivated by their inherent useful properties such as excellent oxidation resistance, high melting points and relatively low densities. The main disadvantages of intermetallics are poor fracture toughness at ambient temperature and low creep resistance and strength at high temperatures. It is expected that their inherent advantages can be effectively utilized via artificial compositing. The approaches used are to improve fracture toughness via ductile phase toughening, and to increase the creep resistance and strength via high strength ceramic reinforcements such as SiC whiskers. Two classes of alloys have been selected for investigation: (1) molybdenum disilicide ( $\text{MoSi}_2$ ), and (2) Nb-based aluminides with the major focus on  $\text{NbAl}_3$ .

## **Research Summary**

To achieve the goal of this program, the present investigation has been carried out in three stages: (1) Developing a coating technique to prevent the deleterious interactions between ductile reinforcements and the brittle matrices; (2) Evaluating the effects of size, morphology and orientation of ductile phases, and the matrix/ductile reinforcement interface on the toughness of brittle matrix composites, modeling these effects, and providing guidelines for the design of ductile-phase-reinforced composites. The evaluation of ductile-phase-toughening is only carried out in  $\text{MoSi}_2$  matrix composites because it is believed that the general rules disclosed would also be suitable for other ductile-phase-toughened brittle matrix composites; (3) Incorporating SiC whiskers into the brittle matrices to improve high temperature strength and creep resistance, and at the same time to tailor the thermal expansion coefficient of the matrices to enhance ductile phase toughening. The specific results are summarized below and further information is provided in the attached publications.

## **MoSi<sub>2</sub> Matrix Composites**

Niobium filaments and plates have been chosen as a ductile reinforcement in the present study because its thermal expansion coefficient is closest to that of  $\text{MoSi}_2$ , and it also has a high melting temperature. For controlling the matrix/reinforcement

interaction, chemical compatibilities of various potential coating materials (mullite,  $\text{Al}_2\text{O}_3$ , and  $\text{ZrO}_2$ ) with  $\text{MoSi}_2$  and Nb were studied via microstructural and compositional analyses [1,2]. Based on these analyses,  $\text{Al}_2\text{O}_3$  was chosen as the final diffusion barrier coating because it is chemically compatible with both  $\text{MoSi}_2$  and Nb, and it also has a thermal expansion coefficient close to those of both the matrix and reinforcement.

The techniques investigated in the present study to produce  $\text{Al}_2\text{O}_3$  coating on Nb surface included (1) sol-gel processing; (2) physical vapor deposition; (3) hot dipping the reinforcement in molten aluminum, followed by anodizing Al to form  $\text{Al}_2\text{O}_3$ . The process control parameters for the techniques and the effectiveness of the coatings as a diffusion barrier were evaluated [3]. The results indicated that a thick and dense  $\text{Al}_2\text{O}_3$  coating is necessary and effective in eliminating the interactions between Nb and the matrix of commercially pure  $\text{MoSi}_2$ . The results also showed that the best coating is provided with physical vapor deposition, followed by sol-gel technique.

Effects of the matrix/reinforcement interface, the mechanical properties and size of the ductile phase on the flow behavior of constrained ductile phase were evaluated [4-7]. Based on the observations from the tensile tests on a single Nb lamina imbedded in  $\text{MoSi}_2$  matrix, an approximate model was proposed which gave insight into the influence of yield strength, work hardening, matrix/reinforcement interfacial bonding strength and size of the ductile reinforcement on the flow behavior. The flow behavior of the constrained ductile phases was related to the fracture toughness of composites via small-scale-bridging model, and the major conclusions are: toughness of composites is enhanced by a relatively weak bond at the matrix/reinforcement interface, by large size of ductile reinforcements, and by a ductile phase with a high yield strength and high work hardening rate [5,7]. The developed stress-displacement function has also been used to calculate the bridging stress across the crack surface in a large-scale-bridging model proposed in the present study [8].

The role of the matrix/reinforcement interface in the fracture toughness of  $\text{MoSi}_2/\text{Nb}$  composites has been assessed via four-point bend tests on chevron notched specimens [9]. Variation of the interfacial bonding was obtained by depositing different oxide coatings ( $\text{Al}_2\text{O}_3$  and  $\text{ZrO}_2$ ) or by the development of a reaction product layer between the matrix and reinforcement. Measurement of fracture energy (bond toughness) of the interfaces was carried out on chevron notched short bar [9,10]. It has been established that whether or not a strong interfacial bonding is conducive to toughness depended on the criterion used to describe the toughness of the composites [9], or result in consistency with the prediction of the large-scale-bridging model developed in the present study [8].

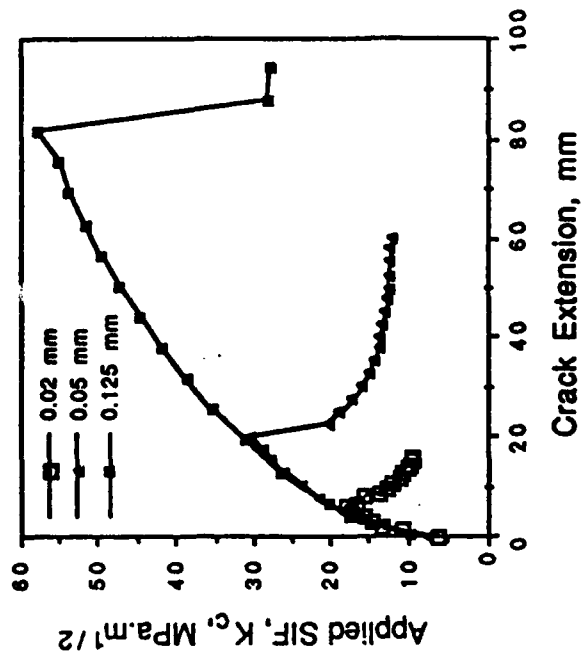
Four-point bend test has also been used to evaluate the effects of the size and orientation of ductile laminae on the toughness of the composites. The results

exhibited that toughness of the composites increased with increasing size of Nb laminae, and ductile laminae offered two dimensional toughening, i.e., fracture toughness in two orientations has been increased to about 11 - 14 MPa.m<sup>1/2</sup> from 3 MPa.m<sup>1/2</sup> for unreinforced matrix [11].

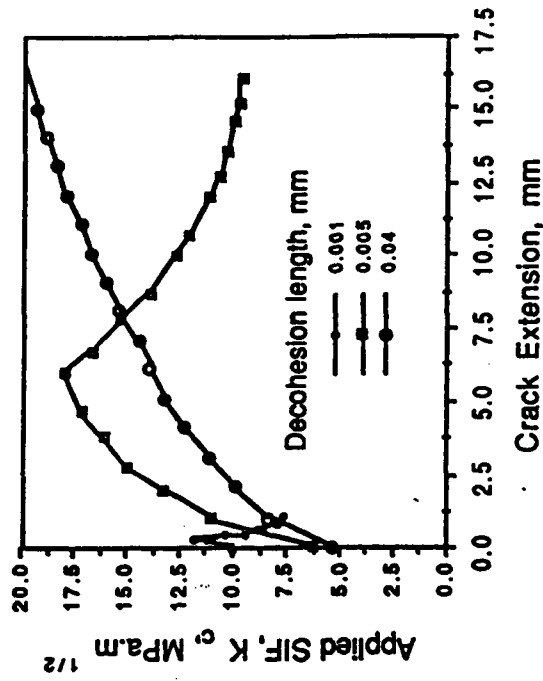
Effects of ductile reinforcements on the stiffness and strength of the composites have been evaluated using MoSi<sub>2</sub>/Nb laminates [12]. The results suggested that residual thermal stresses had an influence on the stiffness of the composites and toughening by a ductile phase with a lower elastic modulus than that of the matrix would cause a decrease in the strength of the composites [12].

All the toughness evaluations and examination of the interaction of cracks with ductile reinforcements indicated that (1) ductile phase toughening involved large-scale bridging, i.e., the bridging-length was at the same magnitude as the crack length, the specimen size or the distance from the crack to the specimen boundaries [2,13]; and (2) the toughening of brittle matrix with ductile phase could be described by the equilibrium stress distribution across the crack surface [11]. According to these observations, a general approach has been proposed to compute the ductile phase toughening in the case of large-scale-bridging [8]. The approach, which allowed for the prediction of the typical R-curve behaviors of ductile-phase-toughened composites, encompassed the effects of the bonding strength of the matrix/reinforcement interface, the size of ductile phases, and the intrinsic mechanical properties of the ductile phases and matrix. Some important results from the model are presented in Figure 1. Note that the maximum crack-growth resistance increases with increasing size of the ductile phase (Figure 1(a)) and the decohesion length at the matrix/reinforcement interface (Figure 1(b)). However, the interface with a small decohesion length gives rise to a steep initial slope of R-curve, indicating that a high crack-growth resistance is associated with a strong interface when the crack is small. The duality of the interface suggests that a weak interface would be beneficial if the cracks to be dealt with are short. (Detailed results are provided in Publication 8.)

Incorporation of SiC whiskers into MoSi<sub>2</sub> matrix has been initiated via tape casting technique. The motivation of using this technique was that the orientation of SiC whiskers could be controlled by adjusting the thickness of the tape and the tapes with different compositions and different whisker orientations could be stacked and laminated together in nearly any combination. Thus, laminates could be custom designed to yield desired properties. A slip formulation (organic solvent, dispersants and binders) for tape casting MoSi<sub>2</sub>/SiC suspension has been developed. The formulation not only enhanced the uniform distribution of SiC-whiskers in MoSi<sub>2</sub> matrix, but also had a very low binder burnout temperature (<300°C) which was greatly beneficial for the non-oxide materials. Typical microstructures of SiC-whisker-reinforced MoSi<sub>2</sub> composites produced via hot pressing of the tape cast laminae have been shown in Figure 2. Note that to some extent, alignment and



(a)



(b)

Fig. 1 Calculated R-curve behaviors of composites (a) with different sizes of Nb laminae, and (b) with different decohesion lengths at the interface. Volume fraction of Nb is 20%.

# Microstructure of the Consolidated $\text{MoSi}_2$ - 30 vol.% $\text{SiC}_w$ Composites

(Sections parallel to the tape travel direction and the hot press plane)



Figure 2

uniform distribution of SiC whiskers has been achieved. On-going work will be directed to characterize the mechanical properties of the tape cast composites and finally combine tape casting technique and ductile phase toughening to produce hybrid composites.

### Niobium aluminid Matrix Composites

Reactive hot compaction (RHC) has been successfully utilized to produce NbAl<sub>3</sub> matrix with close to 100% theoretical density at relatively low processing temperatures of around 1300°C. The effects of process control parameters such as ratio of the elemental Nb and Al powder, particle size, and heating rate, on the microstructure of NbAl<sub>3</sub> matrix have been evaluated [14,15]. By controlling the initial stoichiometry, NbAl<sub>3</sub> matrix composites containing a dispersion of Nb<sub>2</sub>Al or Nb<sub>3</sub>Al particles with a niobium core has been produced via RHC. The fracture toughness of the composites has been determined to be 3.5 MPa.m<sup>1/2</sup>, compared with 1.9 MPa.m<sup>1/2</sup> for the monolithic matrix [14,15]. The improvement can be attributed to crack deflection and crack trapping.

In order to further improve the fracture toughness of NbAl<sub>3</sub>, Nb filaments were incorporated into the matrix during RHC process [16]. To prevent chemical interaction between the matrix and reinforcements, a novel technique was developed to produce alumina coating *in situ* during the RHC processing. This *in situ* alumina coating is described in Patent 1. Briefly, the process involved pre-oxidizing Nb filaments to form Nb<sub>2</sub>O<sub>5</sub> scale, and converting the Nb<sub>2</sub>O<sub>5</sub> scale into Al<sub>2</sub>O<sub>3</sub> layer at the matrix/reinforcement interface via an interface reaction during the subsequent RHC process. The coating thickness was varied from 3 to 8 μm by changing the oxidation time of the Nb filaments. Long term annealing at 1200°C indicated that the *in situ* Al<sub>2</sub>O<sub>3</sub> coating was stable and effective in suppressing the interactions between the matrix and ductile reinforcement [16].

Fracture toughness of 20 vol% Nb-reinforced NbAl<sub>3</sub> composites was measured to be 9.4 Mpa.m<sup>1/2</sup>, five times higher than the matrix. Fracture surface analysis indicated that partial decohesion had occurred at the matrix/filament interface allowing the Nb filaments to fail in a ductile manner. The *in situ* Al<sub>2</sub>O<sub>3</sub> coating, therefore, not only acts as an effective diffusion barrier, but also imparts a desirable interfacial strength to allow for a limited debonding at the interface [16].

### **Publications**

- (1) L. Xiao, Y.S. Kim and R. Abbaschian, "Ductile Phase Toughening of MoSi<sub>2</sub> - Chemical Compatibility and Fracture Toughness," in Intermetallic Matrix Composites, edited by D.L. Anton, P.L. Martin, D.B. Miracle and R. McMeeking, Proceeding of MRS Meeting, 1990, vol. 194, pp. 399-404.

- (2) L. Xiao, Y.S. Kim, R. Abbaschian and R.J. Hecht, "Processing and Mechanical Properties of Nb Reinforced  $\text{MoSi}_2$  Composites", *Material Science Engineering*, 1991, vol. A144, pp. 277-85.
- (3) L. Xiao and R. Abbaschian, "Control of the Interfacial Reactions in Nb Reinforced  $\text{MoSi}_2$  Composites", to be published.
- (4) L. Xiao and R. Abbaschian "Evaluating a Technique for Determining the Toughening of Brittle Matrix Ductile Reinforcements", in *Advanced Metal-Matrix Composites for Elevated Temperatures*, edited by M.N. Gungor, E.J. Lavernia and S.G. Fishman, (ASM International, 1991), pp. 33-40.
- (5) L. Xiao, "Flow Behavior of Constrained Ductile Phases", recipient of the 1992 ASM International Graduate Student Paper Contest, and accepted for publication in *Metall. Trans.*
- (6) L. Xiao, "Study of the Flow Behavior of Constrained Ductile Phases---I. Experiment", in *Developments in Ceramic- and Metal-Matrix Composites*, edited by K. Upadhyya, (A Publication of TMS, 1992), pp. 115-124.
- (7) L. Xiao, "Study of the Flow Behavior of Constrained Ductile Phases --- II. Modeling", in *Developments in Ceramic-and Metal-Matrix Composites*, edited by K. Upadhyya, (A Publication of TMS, 1992, pp. 359-369.
- (8) L. Xiao and R. Abbaschian, "Ductile Phase Toughening --- Large Scale Bridging", in preparation.
- (9) L. Xiao and R. Abbaschian, "The Role of Matrix/Reinforcement Interfaces in the Fracture Toughness of Ductile Phase Reinforced  $\text{MoSi}_2$  Composites", *Metall. Trans.*, 1992, vol. 23A(10).
- (10) L. Xiao and R. Abbaschian, "Microstructure and Properties of  $\text{MoSi}_2/\text{Nb}$  Interfaces with and without Alumina Coating", in *Structure and Properties of Interfaces in Materials*, MRS Symposium Proceedings, 1992, vol 238, pp. 567-73.
- (11) L. Xiao and R. Abbaschian, "Toughening  $\text{MoSi}_2$  with Niobium Metal --- Effects of Size and Orientation of Ductile Laminae", in preparation.
- (12) L. Xiao and R. Abbaschian, "On the Strength and Stiffness of Ductile Phase Reinforced  $\text{MoSi}_2$  Composites", in *Advanced Metal-Matrix Composites for Elevated Temperatures*, edited by M.N. Gungor, E.J. Lavernia and S.G. Fishman, (ASM International, 1991), pp. 21-31.

- (13) L. Xiao and R. Abbaschian, "Interfacial Modification in Nb/MoSi<sub>2</sub> Composites and its Effects on Fracture Toughness", *Materials Science Engineering*, 1992, vol. A155, pp. 135-45.
- (14) L. Lu, Y.S. Kim, A.B. Gokhale and R. Abbaschian, "Reactive Synthesis of NbAl<sub>3</sub> Matrix Composites", in *Intermetallic Matrix Composites*, edited by D.L. Anton, P.L. Martin, D.B. Miracle and R. McMeeking, *Proceeds of MRS Meeting*, 1990, vol. 194, pp. 79-87.
- (15) L. Lu, A.B. Gokhale, M.J. Kaufman and R. Abbaschian, "Niobium Aluminide Matrix Composites Produced by the Reactive Hot Compaction of Elemental Powders", in *Powder Metallurgy: Key to Advanced Materials Technology*, ASM International, 1990, pp. 32-6.
- (16) L. Lu, A.B. Gokhale and R. Abbaschian, "*In-situ* Formation of and Alumina Interface Coating in Reactively Synthesized NbAl<sub>3</sub>-Nb Composites", *Materials Science Engineer*, 1991, vol. A144, pp. 11-23.

#### Patents

- (1) L. Lu, A.B. Gokhale and R. Abbaschian, "An 'In-Situ' Coating Process of Reinforcements Used in Reactively Synthesized Metal, Intermetallic, and Ceramic Matrix Composites", 1991, patent disclosure.

Copies of publications 1, 2, 4, 6, 7, 9, 10, 12, 13, 14 and 16 are attached.

## DUCTILE PHASE TOUGHENING OF $\text{MoSi}_2$ -CHEMICAL COMPATIBILITY AND FRACTURE TOUGHNESS

L. XIAO, Y. S. KIM, AND REZA ABBASCHIAN  
Department of Materials Science and Engineering, University of Florida, Gainesville, FL, 32611

### ABSTRACT

Chemical compatibility between oxide coated Nb filament reinforcements and  $\text{MoSi}_2$  was investigated. It was determined that  $\text{ZrO}_2$ ,  $\text{Al}_2\text{O}_3$ , and mullite coatings were chemically compatible with both Nb and  $\text{MoSi}_2$ . Comparison between coated and uncoated filaments indicated that the coatings reduced the thickness of the interaction zone. The fracture toughness of the Nb filament reinforced composites showed an increase, while W filament reinforced composite showed a decrease, in the toughness compared to that of the matrix. The results are discussed in terms of the mismatches in the coefficients of thermal expansion and the bonding characteristics of the reinforcement/matrix interface.

### INTRODUCTION

Molybdenum disilicide ( $\text{MoSi}_2$ ) is an attractive candidate material for elevated-temperature structural applications because of its high melting temperature (2030°C), and excellent oxidation resistance at elevated temperatures. However, it has a low fracture toughness at ambient temperatures like most of other intermetallics and a high creep rate at high temperatures. Previous studies on  $\text{MoSi}_2$  matrix composites have shown appreciable improvements in the fracture toughness by reinforcing the matrix with SiC whiskers [1-3] and  $\text{ZrO}_2$  particles [4]. The fracture toughness of these composites was determined to be in the range of 5-8  $\text{MPa}\cdot\text{m}^{1/2}$ , compared to 3-5  $\text{MPa}\cdot\text{m}^{1/2}$  for unreinforced matrix. In addition, it has been also shown that the ambient temperature fracture strength of  $\text{MoSi}_2$  can be increased by a factor of two by reinforcing with 30 vol.% of Nb filaments [5]. However, as will be shown later, the Nb filament reinforced  $\text{MoSi}_2$  composite is unstable at elevated temperatures because Nb reacts with  $\text{MoSi}_2$ , forming other brittle intermetallic compounds such as  $(\text{Mo,Nb})_5\text{Si}_3$ . The formation of the brittle reaction products as well as degradation of the reinforcements deteriorate the toughness of the composites. Therefore, a protective coating of the reinforcement is necessary for high temperature applications of these composites.

The purpose of the current work is to investigate the ductile phase toughening of the  $\text{MoSi}_2$  matrix using coated Nb and W filaments. It will be shown that based on the thermodynamic calculations and experimental chemical compatibility tests that  $\text{Al}_2\text{O}_3$  and  $\text{ZrO}_2$  are stable in contact with Nb and  $\text{MoSi}_2$  up to 1700 °C. The fracture toughness of the composites containing coated and uncoated Nb were evaluated using four-point bending test. In addition, composites containing uncoated W filaments were produced in order to elucidate the effect of the mismatches in coefficient of thermal expansion (CTE) on the fracture toughness of the composites.

### EXPERIMENTAL

Alumina coating on Nb filaments were produced by dipping the filaments into an aluminum-alkoxide-derived sol solution developed by Clark et al [6], followed by drying at 500°C. The dipping and the drying process were repeated twice in order to obtain a dense and uniform coating. On the other hand,  $\text{ZrO}_2$  coatings were applied by dipping the filaments into a coating solution consisting of 97%  $\text{ZrO}_2$  and

3%  $\text{Al}_2\text{O}_3$ . After hot pressing, the thickness of  $\text{Al}_2\text{O}_3$  and  $\text{ZrO}_2$  coating were determined to be in the range 3 to 20  $\mu\text{m}$ . The mullite ( $3\text{Al}_2\text{O}_3 \cdot 2\text{SiO}_2$ ) fibers used for the compatibility studies were produced by sol-gel processing at the University of Florida [7].

In order to produce a unidirectionally aligned composite, Nb filaments were pre-aligned in a plane and set with acrylic resins. The Nb filaments sheets were then stacked together with  $\text{MoSi}_2$  powders (-325 mesh) in an appropriate thickness ratio and vacuum hot pressed at 1700°C for 40 minutes under 30MPa pressure. The diameter of the filaments used were 0.25 mm, and the volume fraction of Nb filaments in the composites was 10%. The composites containing discontinuous W filaments (aspect ratio 20:1) were produced by mixing the filaments with  $\text{MoSi}_2$  powders and hot pressing under the same conditions. The theoretical densities of the  $\text{MoSi}_2$ ,  $\text{MoSi}_2/\text{Nb}$ , and  $\text{MoSi}_2/\text{W}$  composites were measured to be 98.6, 98.5 and 97.0% respectively. The fracture toughness of the composites was measured by four point bending on 3.81x5.08x25.4 mm Chevron notched samples with an inner and outer span of 10 and 20 mm, using a hydro-servo controlled MTS machine with a cross-head speed of  $4 \times 10^{-4}$  mm/sec. The chevron notches were cut perpendicular to the alignment direction of the filaments using a diamond wafering saw.

## RESULTS AND DISCUSSION

### Chemical Compatibility

Experimental study on the compatibility between the coating materials and  $\text{MoSi}_2$  matrix were carried out. Fig. 1 shows (a) microstructural morphology and (b) corresponding elemental profiles near the  $\text{Al}_2\text{O}_3/\text{MoSi}_2$  interface. This samples was produced by hot pressing at 1700°C for 40 minutes followed by annealing at 1400°C for 100 hours. The compositional profile indicates that the interface is "sharp" (approximately 2  $\mu\text{m}$  thick). Similar results were obtained for  $\text{MoSi}_2/\text{ZrO}_2$  and  $\text{MoSi}_2/\text{mullite}$ . For instance, the interface of  $\text{MoSi}_2/\text{mullite}$  is very sharp as shown in Fig. 2 and its thickness was measured to be around 1  $\mu\text{m}$ . These results indicate that  $\text{Al}_2\text{O}_3$ ,  $\text{ZrO}_2$ , and mullite are chemically compatible with  $\text{MoSi}_2$ .

To support the above findings, thermodynamic calculations were performed in order to predict the chemical stabilities of  $\text{Al}_2\text{O}_3$  and  $\text{ZrO}_2$  with Nb and  $\text{MoSi}_2$ . Using the thermodynamic data available [8], the free energy changes for possible reactions between the coating materials ( $\text{Al}_2\text{O}_3$  and  $\text{ZrO}_2$ ),  $\text{MoSi}_2$  and Nb were calculated at 1400K and 2000K. The reaction components considered in these calculations included Mo,  $\text{MoSi}_2$ ,  $\text{Mo}_5\text{Si}_3$ ,  $\text{Mo}_3\text{Si}$ ,  $\text{MoO(g)}$ ,  $\text{MoO}_2$ ,  $\text{MoO}_3(l)$ , Si,  $\text{SiO(g)}$ ,  $\text{SiO}_2$ , Al,  $\text{Al}_2\text{O}_3$ ,  $\text{AlO(g)}$ ,  $\text{Al}_2\text{O(g)}$ , Zr,  $\text{ZrO}_2$ ,  $\text{ZrO(g)}$ , Nb,  $\text{NbO}$ ,  $\text{NbO}_2$ ,  $\text{Nb}_2\text{O}_5$ ,  $\text{ZrSi}_2$ ,  $\text{ZrSi}$ .

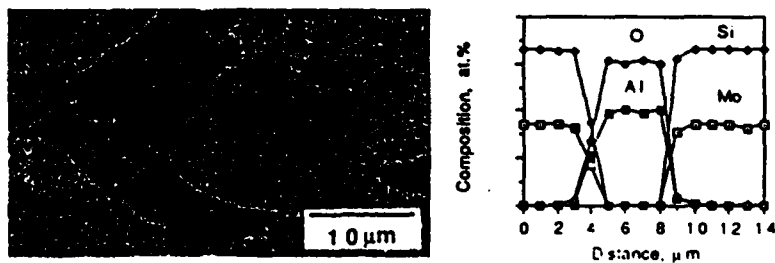


Fig.1 The interface microstructure and the corresponding composition profiles of a  $\text{MoSi}_2/\text{Al}_2\text{O}_3$  composite.

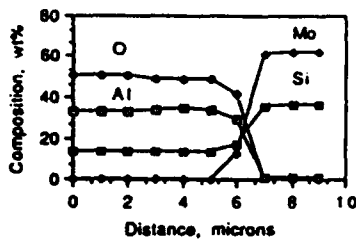


Fig 2 The composition profiles of a  $\text{MoSi}_2$ /mullite fiber composite, hot pressed at  $1700^\circ\text{C}$ .

extensively during the processing, forming an intermetallic compound at the interface. The reaction product was determined to be  $(\text{Mo,Nb})_5\text{Si}_3$  and its thickness was measured to be about  $30\ \mu\text{m}$ . The thickness of the interaction layer between Nb and  $\text{MoSi}_2$ , however, was reduced to  $4\ \mu\text{m}$  upon coating of filaments with  $\text{ZrO}_2$ , as shown in Fig. 4. In addition, the reaction product at the Nb/ $\text{ZrO}_2$  interface was determined to be  $\text{Nb}_5\text{Si}_3$ , instead of  $(\text{Mo,Nb})_5\text{Si}_3$  for the uncoated samples, suggesting that appreciable reduction in diffusion of Nb and Mo across the coating as indicated by the composition profiles in Fig. 4.

The growth rate of the interaction layer ( $\text{Nb}_5\text{Si}_3$ ) in the  $\text{ZrO}_2$  coated Nb filament reinforced composites were determined by annealing the samples for 25 and 100 hours at  $1300^\circ\text{C}$ . As shown in Fig. 5, the thickness of  $\text{Nb}_5\text{Si}_3$ , which increased to  $6\ \mu\text{m}$  after annealing for 100 hours, followed a parabolic function of the annealing time. The results indicated that the growth of the  $\text{Nb}_5\text{Si}_3$  is controlled by the diffusion of the elemental species through the  $\text{Nb}_5\text{Si}_3$  rather than the diffusion of Si through  $\text{ZrO}_2$ . In other words, the diffusion of Si is relatively fast in  $\text{ZrO}_2$ . Thus, even though  $\text{ZrO}_2$  is chemically compatible with Nb and  $\text{MoSi}_2$ , the coating is not a perfect barrier for diffusion of elemental species between Nb and  $\text{MoSi}_2$ . Nevertheless the coating is effective in reducing Nb or Mo diffusion, and substantially reduces growth of the reaction layers.

Similar observations were made for the  $\text{Al}_2\text{O}_3$  coated Nb filament reinforced composites. The composition profiles at the Nb filament/ $\text{Al}_2\text{O}_3$ / $\text{MoSi}_2$  interface for a sample produced by hot pressing at  $1400^\circ\text{C}$  for 40 minutes is shown in Fig. 6. Similar to the  $\text{ZrO}_2$  coated Nb filaments, the formation of  $\text{Nb}_5\text{Si}_3$  at the Nb side of the Nb/ $\text{Al}_2\text{O}_3$  interface was observed.

Table I. The standard free energy changes for some possible reactions among the coating materials, matrix and reinforcements.

| Reactions   | $\Delta G_{1400\text{K}}$<br>(Kcal) | $\Delta G_{2000\text{K}}$<br>(Kcal) |
|---|-------------------------------------|-------------------------------------|
| $6\text{MoSi}_2 + 5\text{ZrO}_2 = 5\text{Zr} + 2\text{Mo}_3\text{Si} + 10\text{SiO}(\text{g})$                      | 614.028                             | 372.126                             |
| $5\text{MoSi}_2 + 7\text{ZrO}_2 = 7\text{Zr} + \text{Mo}_5\text{Si}_3 + 7\text{SiO}_2$                              | 384.819                             | 371.332                             |
| $\text{MoSi}_2 + 4\text{ZrO}_2 = 2\text{Zr}_2\text{Si} + \text{MoO}_2 + 3\text{O}_2(\text{g})$                      | 646.815                             | 569.275                             |
| $2\text{Nb} + \text{ZrO}_2 = 2\text{NbO} + \text{Zr}$   | 58.56                               | 55.599                              |
| $4\text{Nb} + 5\text{ZrO}_2 = 2\text{Nb}_2\text{O}_5 + 5\text{Zr}$  | 378.656                             | 358.345                             |
| $9\text{MoSi}_2 + 5\text{Al}_2\text{O}_3 = 10\text{Al} + 3\text{Mo}_3\text{Si} + 15\text{SiO}(\text{g})$            | 894.567                             | 490.583                             |
| $5\text{MoSi}_2 + 7\text{Al}_2\text{O}_3 = 14\text{AlO}(\text{g}) + \text{Mo}_5\text{Si}_3 + 7\text{SiO}(\text{g})$ | 1709.968                            | 1186.314                            |
| $5\text{MoSi}_2 + 7\text{Al}_2\text{O}_3 = 7\text{Al}_2\text{O}(\text{g}) + \text{Mo}_5\text{Si}_3 + 7\text{SiO}_2$ | 627.166                             | 432.176                             |
| $6\text{Nb} + 5\text{Al}_2\text{O}_3 = 10\text{Al} + 3\text{Nb}_2\text{O}_5$  | 530.379                             | 469.91                              |
| $2\text{Nb} + \text{Al}_2\text{O}_3 = \text{Al}_2\text{O}(\text{g}) + 2\text{NbO}$                                  | 93.181                              | 64.291                              |

$\text{Zr}_5\text{Si}_3$ ,  $\text{Zr}_2\text{Si}$ , and  $\text{O}_2(\text{g})$ . All the compounds were assumed to be stoichiometric. Table I shows some reactions which have lower standard free energy changes among the various reactions considered. It is clear from the table that  $\text{Al}_2\text{O}_3$  and  $\text{ZrO}_2$  are chemically stable with  $\text{MoSi}_2$ /Nb system within the temperature range considered.

The microstructure and composition profiles of the uncoated Nb filaments/ $\text{MoSi}_2$  interface which was vacuum hot pressed at  $1700^\circ\text{C}$  for 40 minutes are shown in Fig. 3. As seen in the figure, Nb and  $\text{MoSi}_2$  reacted

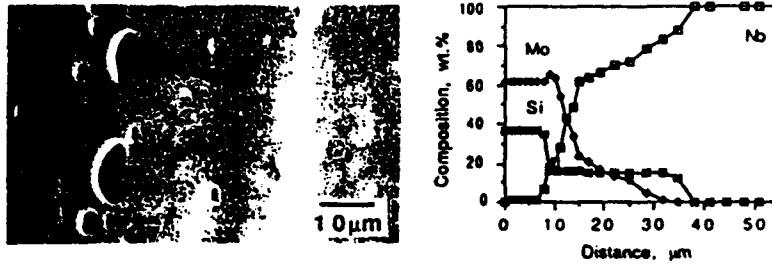


Fig.3 The microstructure and the corresponding composition profiles of a  $\text{MoSi}_2$ /uncoated Nb filament interface.

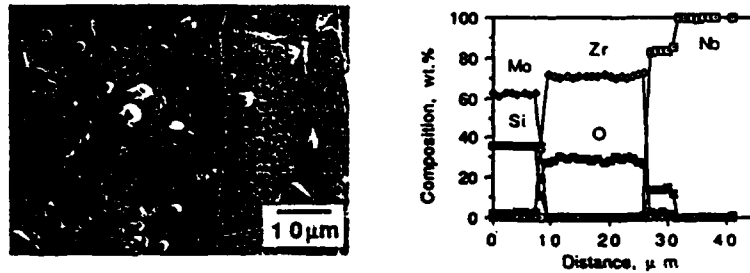


Fig.4 The microstructure and the corresponding composition profiles of a  $\text{MoSi}_2 / \text{ZrO}_2$  coated Nb filament interface.

Its thickness was measured to be around  $5 \mu\text{m}$ , compared with  $15 \mu\text{m}$  of  $(\text{Mo,Nb})_5\text{Si}_3$  formed around uncoated Nb filaments in composites produced under the same hot pressing conditions. In addition, it was observed that when the hot pressing temperature was increased to  $1700^\circ\text{C}$ , the  $\text{Al}_2\text{O}_3$  coating became discontinuous and extensive reaction between Nb and  $\text{MoSi}_2$  occurred. The thickness of intermetallics formed was increased to  $20 \mu\text{m}$ . Nevertheless electron microprobe analysis on the interface did not reveal any evidence of reaction of  $\text{Al}_2\text{O}_3$  with Nb,  $(\text{Mo,Nb})_5\text{Si}_3$  and  $\text{MoSi}_2$ . This suggests that the breakdown of the  $\text{Al}_2\text{O}_3$  coating is possibly due to the Kirkendal shift caused by the extensive Si diffusion across the coating.

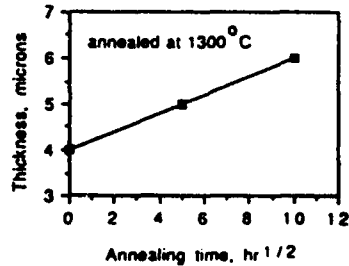


Fig.5 The thickness of  $\text{Nb}_5\text{Si}_3$  vs the square root of the annealing time in  $\text{MoSi}_2/\text{ZrO}_2$  coated Nb composites.

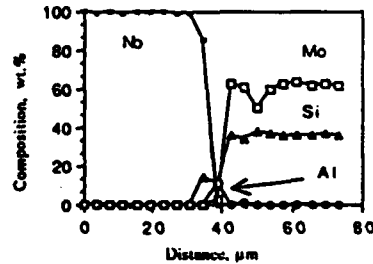


Fig.6 The composition profiles of  $\text{MoSi}_2$  reinforced by  $\text{Al}_2\text{O}_3$  coated Nb, hot pressed at  $1400^\circ\text{C}$ .

An order of magnitude calculation of Si diffusivity through  $ZrO_2$  and  $Al_2O_3$  coatings made from the thickness of the intermetallics formed. The results indicated that the apparent diffusivity of Si estimated to be larger than  $1.0 \times 10^{-9}$   $cm^2/sec$  in  $ZrO_2$  at  $1300^\circ C$  and larger than  $2.0 \times 10^{-8}$   $cm^2/sec$  in  $Al_2O_3$  at  $1400^\circ C$ . These values are considerably higher than the bulk diffusion of Si in the ceramic materials, suggesting that Si diffusion might have occurred via different diffusion paths rather than bulk diffusion. The most feasible fast diffusion route may be through the grain boundary. Since the grain size of the coating produced by the sol-gel technique is small, the diffusion flux from grain boundary diffusion may dominate the diffusion process because of the large grain boundary area. Another potential fast diffusion path is the free surface generated by the porosities in the coating. The porosities may also provide a probable path for gaseous diffusion of SiO. Therefore, in order to minimize the Si diffusion, grain boundary area and processing defects must be minimized in the coating.

### Fracture toughness

The fracture toughness ( $K_{Ic}$ ) values of  $MoSi_2$  matrix composites reinforced by uncoated Nb or W filaments are shown in Fig. 7. As seen in the figure,  $K_{Ic}$  values of the composites reinforced with Nb filaments was  $5 \text{ MPa}\cdot\text{m}^{1/2}$ , which shows 52% increase over that of the matrix. Analysis of fracture surface of the composites using SEM showed that the failure mode of the Nb filaments was a brittle cleavage in nature and the decohesion at the filament/matrix interface was minimal (Fig. 8). The brittle fracture of the filaments may be mainly due to the limited decohesion and this may have led to the limited improvement of the fracture toughness of the Nb filament reinforced composites. Fracture surface analysis of the alumina coated Nb filament reinforced composites also indicated that the failure mode of the Nb filaments was brittle cleavage in character, and without appreciable decohesion at the interface. Further studies are being conducted to improve the characteristics of the filament-matrix bonding by modifying the coating parameters.

W filament reinforced composites showed, on the other hand, considerably lower  $K_{Ic}$  than the Nb filament reinforced composites and slightly lower than the matrix. According to the micromechanical model of ductile phase reinforced composites [9-10], the fracture toughness of the W filament reinforced composites is expected to be higher than that of the Nb filament reinforced composites because W filaments have a higher elastic modulus and fracture strength than Nb filaments. The discrepancy between the theoretical predictions and experimental results seems to result from microcracks observed in the composites. These cracks have been observed when the CTE of filament is smaller than that of matrix and are due to a residual tensile hoop stress in the matrix near the filaments [12]. The residual stress can not only induce thermal cracks in the matrix but also increase the stress intensity in the composites, thus leading to the reduced  $K_{Ic}$ .

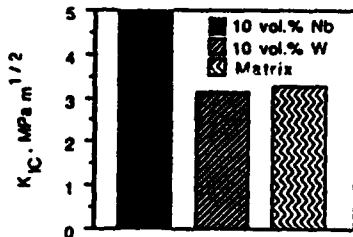


Fig.7 The  $K_{Ic}$  values of  $MoSi_2$  matrix and the composites containing 10 vol.% of Nb or W filaments.

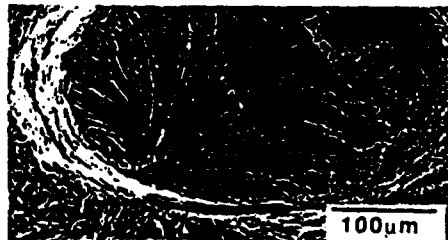


Fig.8 Fracture surface of the uncoated Nb reinforced composites.

The residual tensile stresses in the W filament reinforced composites were estimated by the equations proposed by Poritsky [11]. For a temperature difference of 1000°C, the calculated hoop stress was 2200 MPa and the axial stress was 160 MPa in the MoSi<sub>2</sub> matrix near the interface. The calculated tensile hoop stress is much higher than the tensile strength of MoSi<sub>2</sub>, 150 MPa, at ambient temperatures [13]. Thus, the matrix microcracking and the high level of residual stresses in the matrix are thought to be responsible for the reduced fracture toughness of the W filament reinforced composites.

#### CONCLUSIONS

(1) MoSi<sub>2</sub> matrix composites reinforced with uncoated Nb filaments exhibited significant matrix/filament interactions leading to the formation of the three-component intermetallic, (MoNb)<sub>5</sub>Si<sub>3</sub>. (2) Stability tests for Al<sub>2</sub>O<sub>3</sub>, ZrO<sub>2</sub>, and mullite indicated that they were chemically compatible with Nb and MoSi<sub>2</sub> up to 1700°C. However, upon coating the filaments with the ceramic oxides (ZrO<sub>2</sub> and Al<sub>2</sub>O<sub>3</sub>), a limited interaction was observed, leading to the formation of the binary intermetallic Nb<sub>5</sub>Si<sub>3</sub>. From these two observations, it was inferred that accelerated Si diffusion along the grain boundaries and processing defects in the coatings was responsible for the filament/matrix interaction. (4) The fracture toughness of the Nb filaments reinforced composites was 50 % higher than the unreinforced matrix, but the fracture toughness of W filament reinforced composites was lower than that of the matrix. The latter was attributed to the W/matrix thermal expansion coefficient mismatch, resulting in radial microcracks in the matrix near the interface. (5) The failure of Nb filament reinforcements in four-point bend tested chevron-notched samples occurred in a brittle cleavage mode, indicating a strong bonding at the filament/matrix interface.

**Acknowledgements** The research has been supported under DARPA contract number MDA972-88-J-1006. The authors express sincere appreciation to D. Folz for technical assistance in sol-gel coating process, and to M. R. Johnson for his assistance through the experiments.

#### REFERENCES

1. W.S. Gibbs, J.J. Petrovic and R.E. Honnell, *Ceram. Eng. Sci. Proc.*, **8** (7-8), 645-648 (1988).
2. F. D. Gac and J. J. Petrovic, *J. Am. Ceram. Soc.*, **68** (8), C200-C201 (1985).
3. D. H. Carter and G. F. Hurley, *J. Am. Ceram. Soc.*, **70** (4), C79-81 (1987).
4. J.J. Petrovic and R.E. Honnell, to be published.
5. E. Fitzer, in *Whisker-and Fiber-Toughened Ceramics*, edited by R. A. Bradley, D. E. Clark, D. C. Larsen and J. O. Stiegler, (ASM International TM, 1988), p165.
6. D. E. Clark, W. J. Dalzell and D. C. Folz, *Ceram. Eng. Sci. Proc.*, **9** (10), 1111-1118 (1988).
7. K. R. Venkatachari, L. T. Mocti, M. D. Sacks and J. H. Simmons, to be published in the Proceedings of the 14th Annual Conference on Composites and Advanced Ceramics, Cocoa Beach, Florida, January 1990.
8. I. Barin, O. Knacke and O. Kubaschewski, *Thermodynamical Properties of Inorganic Substances*, (Springer-Verlag Berlin Heidelberg New York, 1977).
9. J. Eberhardt and M. F. Ashby, Cambridge University Engineering Department Report CUED/C-MATS/TR 140, December 1987.
10. L. S. Sigl, P. A. Mataga, B. J. Dalgleish, R. M. McMeeking and A. G. Evans, *Acta Metall.*, **36** (4), 945-953 (1988).
11. H. Poritsky, *Physics*, **2**, 406 (1934).
12. A.B. Gokhale, L.Lu, and R. Abbaschian, to be published in *Solidification of Metal Matrix Composites I: Fundamentals* (Proc. Symp.), ASM/TMS Fall Meeting, Indianapolis, IN, Oct. 1-5, 1989.
13. D. H. Carter, Master thesis, Massachusetts Institute of Technology, 1988.

# Processing and mechanical properties of niobium-reinforced MoSi<sub>2</sub> composites

L. Xiao, Y. S. Kim and R. Abbaschian

*Department of Materials Science and Engineering, University of Florida, Gainesville, FL 32611 (U.S.A.)*

R. J. Hecht

*Pratt and Whitney, West Palm Beach, FL 33410-9600 (U.S.A.)*

## Abstract

In this paper, we describe a framework for the processing of niobium-reinforced MoSi<sub>2</sub> composites. As a part of the program, composites containing coated and uncoated niobium reinforcements were produced. Chemical compatibility between the coatings and the matrix was studied and the effect of the interface modification by the coating on the fracture toughness of the composites was investigated via four-point bending tests on chevron-notched samples. The results indicated that the coatings have a significant effect on the debonding at the reinforcement-matrix interface, which in turn can affect the damage tolerance of the composite. Also observation of the crack propagation in the composites suggests that the matrix failed at the early stages of loading. The results are discussed in terms of the mismatch between the elastic constants of the composite constituents.

## 1. Introduction

MoSi<sub>2</sub> heating elements have been used since the early 1950s because of a combination of properties: proper electrical resistivity, high melting temperature (2030 °C) and excellent oxidation resistance up to 1700 °C in oxidizing environment. In addition, MoSi<sub>2</sub> has a relatively low density (6.4 g cm<sup>-3</sup>) and can retain a significant part of its ambient temperature strength up to 1200 °C. These properties make MoSi<sub>2</sub> an excellent candidate as a structural material for high temperature applications. However, its poor room temperature fracture toughness imposes a severe limitation on its use in practical applications.

The toughness of MoSi<sub>2</sub> can be improved by the incorporation of ductile reinforcements such as refractory metal filaments or particles. Since the ductile reinforcements commonly have a lower elastic modulus than MoSi<sub>2</sub>, the composite was termed an "inverse composite" [1, 2]. The principal mechanism of toughness improvements in these composites is attributed to crack shielding or crack bridging by the ductile reinforcements. Results of independent theoretical modeling also indicate that the ductile phase toughening can be an effective tool in improving the fracture toughness of brittle matrices [3, 4].

The major difficulty in using ductile reinforcements, especially pure refractory metals, is that they tend to react with the matrix at high temperatures, leading to the formation of brittle interfacial products. For example, when Nb-MoSi<sub>2</sub> composites were annealed at high temperatures, (Mo, Nb)<sub>5</sub>Si<sub>3</sub>, among other compounds, formed at the reinforcement-matrix interface at a relatively rapid rate [1, 5]. The formation of the interfacial compounds at the expense of the ductile reinforcement not only degrades the ductile phase toughening effect but also can cause a notch effect on the ductile phase as the compound grows thicker [6]. Therefore the use of an inert diffusion barrier coating on the reinforcements prior to processing of the composites is essential for minimizing the matrix-reinforcement interactions during processing and service at elevated temperatures.

In this study, the effect of various oxide coatings on the decohesion length at the reinforcement-matrix interface and consequently the fracture toughness of the composites were investigated. It will be shown not only that the coatings have a significant effect on the fracture toughness of the composites but also that the magnitude of the effect changes according to the reinforcement geometry. Furthermore, the crack propagation

and crack-reinforcement interactions at various stages of loading were explored to understand the role of ductile reinforcements which have an elastic modulus lower than that of the matrix in determining the fracture toughness of the composites.

## 2. Experimental details

The chemical compatibility of various oxide coating materials ( $\text{Al}_2\text{O}_3$ ,  $\text{ZrO}_2$  and mullite) with  $\text{MoSi}_2$  was investigated by compositional and microstructural analysis of vacuum hot-pressed  $\text{MoSi}_2$  samples containing the oxide powders. The hot pressing was carried out  $1700^\circ\text{C}$  for 30 min under 40 MPa pressure.

Laminated composites containing uncoated and coated niobium foils were produced by vacuum hot pressing. Details of coating niobium foils with  $\text{Al}_2\text{O}_3$  or  $\text{ZrO}_2$  via the sol-gel route can be found elsewhere [5]. In order to fabricate the laminated composites, niobium foils 0.25 mm thick and -325 mesh  $\text{MoSi}_2$  powder were stacked to produce 20 vol.% of niobium foils in the final composite. The thickness of each  $\text{MoSi}_2$  layer was kept constant by using the same amount of  $\text{MoSi}_2$  powder between the layers. These stacked samples were vacuum hot pressed at  $1700^\circ\text{C}$  for 40 min under a pressure of 40 MPa. Similarly, fibrous aligned composites containing coated and uncoated niobium filaments (0.127 and 1.0 mm in diameter) were also fabricated. Compositional analysis was performed using a JEOL JXA 733 microprobe and pure molybdenum, silicon, nickel, aluminum and zirconium as standards: the oxygen content was determined as the balance.

The fracture toughness of the composites was determined by a four-point bending test on chevron-notched specimens using a hydro-servo-controlled MTS machine at a cross-head speed of  $4 \times 10^{-4} \text{ mm s}^{-1}$ . The dimensions of the specimen were  $3.81 \text{ mm} \times 5.08 \text{ mm} \times 25.4 \text{ mm}$ ; the chevron notch on the laminated composites was cut perpendicular to the foil plane using a diamond wafering saw. The crack propagation process in the chevron-notched sample during the four-point bending test was investigated by unloading the samples at various loads. The unloaded samples were sectioned and investigated for crack geometry.

## 3. Results and discussion

### 3.1. Chemical compatibility between $\text{MoSi}_2$ and coating materials

The chemical compatibility of the coating materials ( $\text{Al}_2\text{O}_3$ ,  $\text{ZrO}_2$  and mullite) with an  $\text{MoSi}_2$  matrix was assessed experimentally via microstructural and compositional analyses of the samples after hot pressing powder mixtures of commercial  $\text{MoSi}_2$  and the coating materials. Figure 1 shows the microstructural and the corresponding elemental compositional profiles near the  $\text{Al}_2\text{O}_3$ - $\text{MoSi}_2$  interface of a sample annealed at  $1600^\circ\text{C}$  for 100 h after hot pressing at  $1700^\circ\text{C}$  for 40 min. The compositional profiles show two very distinctive types of interface: a relatively sharp interface with a thickness less than the distance between two consecutive scanning points of the electron microprobe ( $2 \mu\text{m}$ ), and a relatively diffuse interface about  $7 \mu\text{m}$  thick. Also, the diffuse interface layer is rich in silicon, aluminum

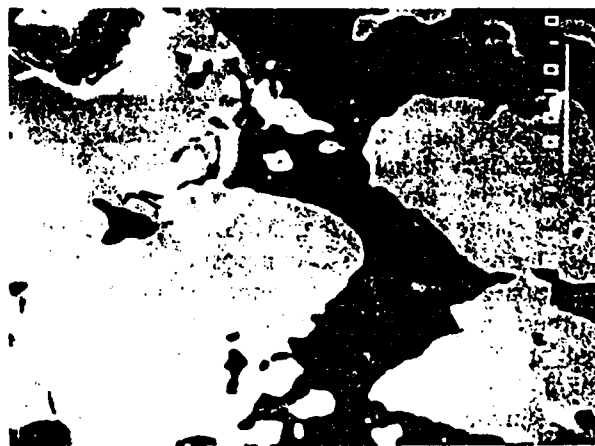
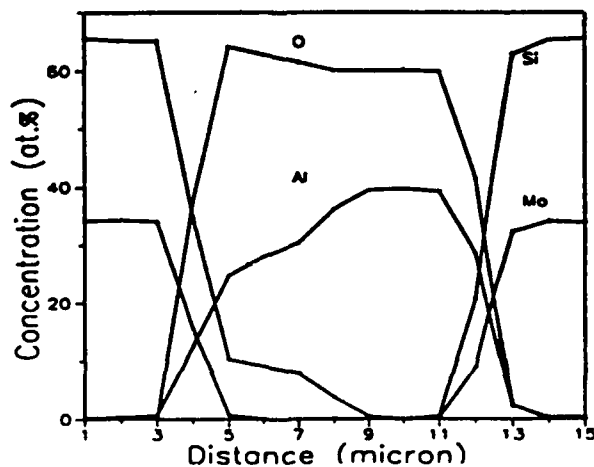


Fig. 1. Compositional profiles across an  $\text{Al}_2\text{O}_3$  particle in an  $\text{MoSi}_2$  matrix.

and oxygen, with little or no molybdenum. When the annealing temperature was varied from 1400 to 1600 °C, the general appearance of both interfaces and their thicknesses remained almost the same. In a related study, microstructural analysis of vacuum hot-pressed  $\text{MoSi}_2$  samples, fabricated from the commercial  $\text{MoSi}_2$  powders, revealed the presence of small second-phase particles distributed randomly throughout the matrix, as shown in Fig. 2. Transmission electron microscopy analysis indicated that these particles were amorphous  $\text{SiO}_2$  [7]. Consequently, it is believed that the interaction layer at the diffuse interface is due to a reaction between  $\text{Al}_2\text{O}_3$  and  $\text{SiO}_2$  impurity particles. This suggests that  $\text{MoSi}_2$  and  $\text{Al}_2\text{O}_3$  may be chemically compatible within the temperature range considered (1400–1600 °C).

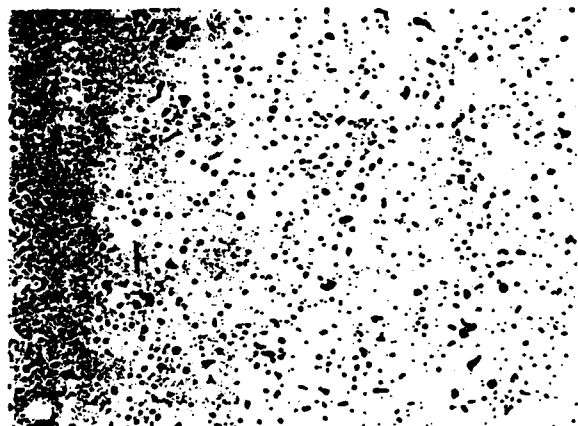


Fig. 2. Optical micrograph of  $\text{MoSi}_2$  produced by the hot pressing of commercial powders.

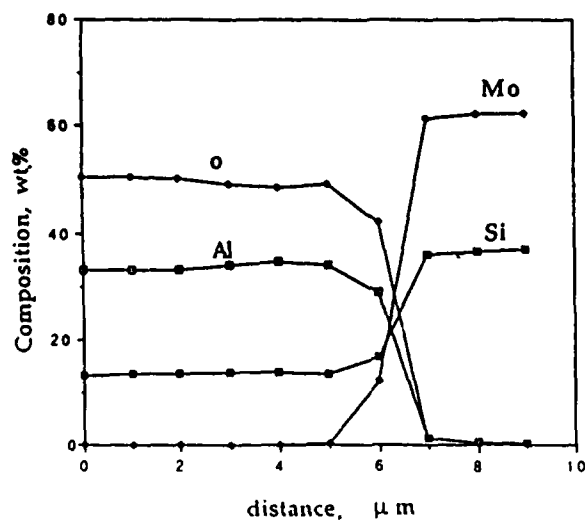


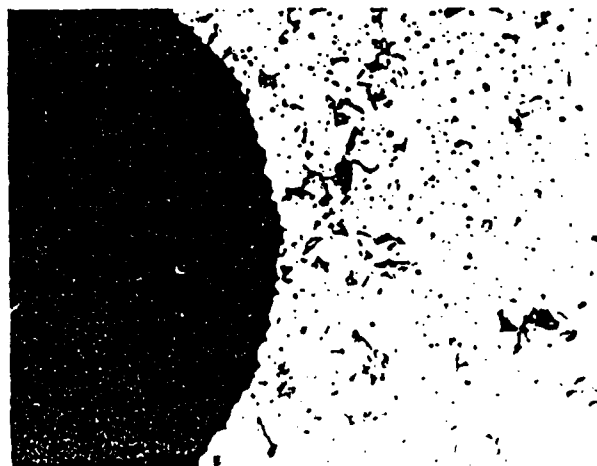
Fig. 3. The interface microstructure and the corresponding compositional profiles of an  $\text{MoSi}_2$ -mullite composite.

Compositional analysis of  $\text{MoSi}_2$ - $\text{ZrO}_2$  and  $\text{MoSi}_2$ -mullite fiber\* composites indicated a very sharp particle-matrix interface, with no apparent interaction zone. This is illustrated by the compositional profile and the corresponding microstructure of an  $\text{MoSi}_2$ -mullite composite (Fig. 3). Similar to  $\text{MoSi}_2$ - $\text{Al}_2\text{O}_3$ , the interface remained sharp with no appreciable increase in its thickness upon annealing.

### 3.2. Effectiveness of the inert coatings as a diffusion barrier

In addition to the chemical compatibility of a coating with the matrix and the reinforcement, it must act as a diffusion barrier for the elemental constituents of the composite. In order to evaluate the effectiveness of the various oxide coatings as diffusion barriers, niobium filaments coated with  $\text{ZrO}_2$  and  $\text{Al}_2\text{O}_3$  were mixed with  $\text{MoSi}_2$  powder and hot pressed at 1700 °C for 40 min.  $\text{ZrO}_2$ -coated niobium filaments (Fig. 4) exhibited a limited interaction layer on the niobium side of the coating, but not on the  $\text{MoSi}_2$  side. The thickness of the interaction layer was around 4 μm, which is considerably less than that observed for the uncoated filament-matrix interface produced under similar hot-pressing conditions. For the latter, the layer thickness was 30 μm. In addition, compositional analysis indicated that the reaction product at the Nb- $\text{ZrO}_2$  interface was  $\text{Nb}_5\text{Si}_3$ .

\*The mullite fibers were produced by M. D. Sacks *et al.* at the University of Florida.



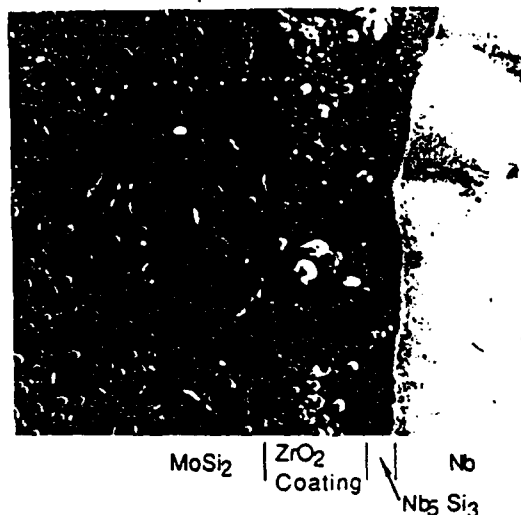
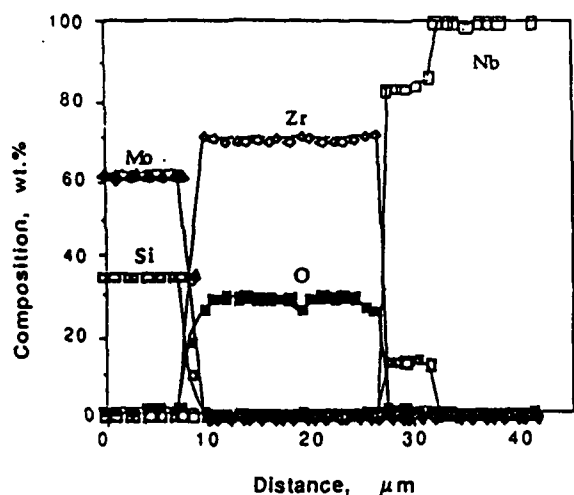


Fig. 4. The microstructure and the corresponding compositional profiles across a  $(\text{ZrO}_2\text{-coated Nb})\text{-MoSi}_2$  interface.

compared with  $(\text{MoNb})_5\text{Si}_3$  which formed at the uncoated Nb-MoSi<sub>2</sub> interface.

The growth of the interaction layer ( $\text{Nb}_5\text{Si}_3$ ) at 1300 °C was measured after annealing the samples for 25 and 100 h. As shown in Fig. 5, the layer thickness was increased to 6 μm after annealing for 100 h and followed a parabolic function of the annealing time. The results indicated that the growth rate of the  $\text{Nb}_5\text{Si}_3$  at the Nb-ZrO<sub>2</sub> interface is controlled by the diffusion of silicon through the  $\text{Nb}_5\text{Si}_3$ , rather than through the ZrO<sub>2</sub> coating.

A similar interfacial interaction was observed upon coating niobium with Al<sub>2</sub>O<sub>3</sub>, as shown in Fig. 6. The thickness of the interaction layer formed on the niobium side of the Nb-Al<sub>2</sub>O<sub>3</sub> interface was measured to be around 5 μm after hot pressing and the layer was again determined to be  $\text{Nb}_5\text{Si}_3$ . These results indicate that, even though ZrO<sub>2</sub> and Al<sub>2</sub>O<sub>3</sub> are chemically compatible with niobium and MoSi<sub>2</sub>, the coatings are not perfect barriers for silicon diffusion. Nevertheless, the coatings are effective in retarding the niobium and molybdenum diffusions and hence substantially reduce the growth rate of the reaction layers.

An order-of-magnitude calculation of silicon diffusivity through ZrO<sub>2</sub> and Al<sub>2</sub>O<sub>3</sub> made from the growth rate of the interaction layers indicates that the apparent silicon diffusivity must be larger than  $1.0 \times 10^{-9} \text{ cm}^2 \text{ s}^{-1}$  in ZrO<sub>2</sub> at 1300 °C and larger than  $2.0 \times 10^{-8} \text{ cm}^2 \text{ s}^{-1}$  in Al<sub>2</sub>O<sub>3</sub> at 1400 °C. These values are considerably higher

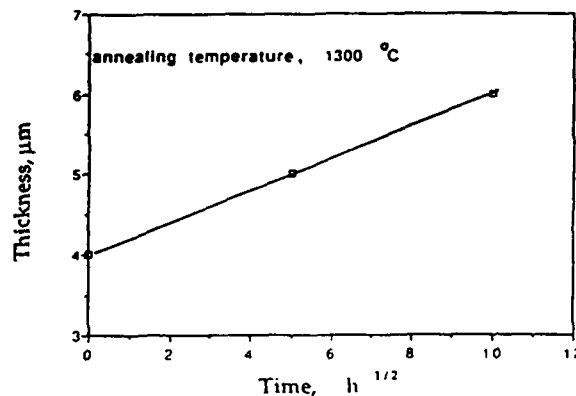


Fig. 5. The thickness of the interaction product in an  $\text{MoSi}_2\text{-(ZrO}_2\text{-coated Nb)}$  composite as a function of the square root of the annealing time.

than the bulk diffusivities of silicon in these ceramic materials [8]. It is possible that silicon diffusion in the coatings was enhanced along the grain boundaries, or processing defects such as pinholes generated during the sol-gel coating process.

### 3.3. Fracture toughness of ductile-phase-reinforced composites

The fracture toughness of the brittle matrix composite was calculated from the peak load of the load-displacement curves of chevron-notched samples tested in four-point bending. Typical load-displacement curves for an unreinforced matrix and an uncoated composite reinforced with 20 vol% Nb foil are shown in Fig. 7.

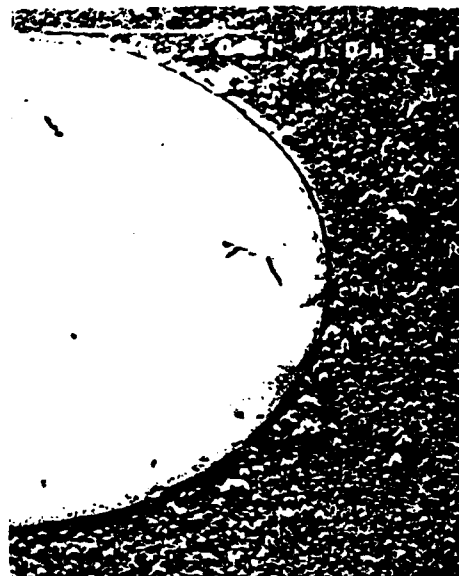
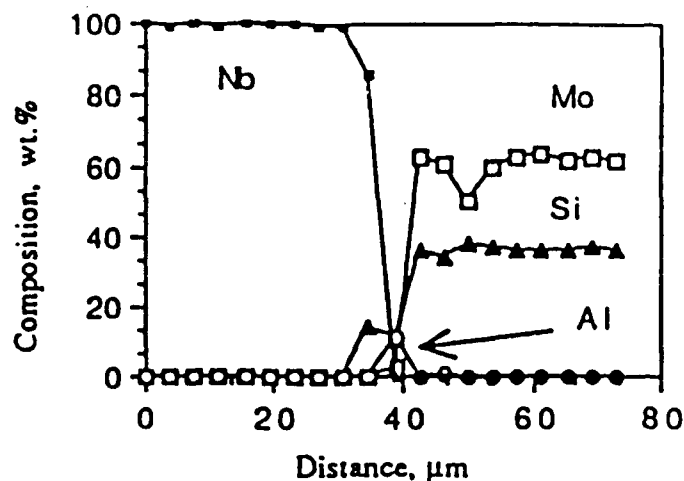


Fig. 6. The microstructure and the corresponding compositional profiles of  $\text{Al}_2\text{O}_3$ -coated niobium filaments in  $\text{MoSi}_2$ .

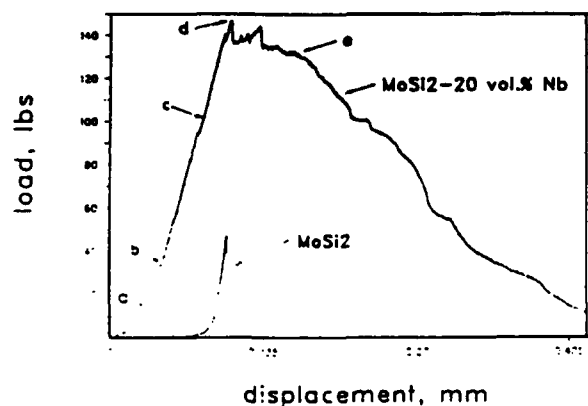


Fig. 7. Typical load-displacement curves of chevron-notched monolithic  $\text{MoSi}_2$  matrix and uncoated niobium-foil-reinforced composite specimens. The letters on the composite curve indicate the approximate unloading load levels for the microstructures shown in Fig. 8.

As can be seen, the peak load of the composite specimen is more than three times higher than that of the matrix. The fracture toughness calculated using a model derived by Munz *et al.* [9] indicated that the fracture toughness  $K_{Ic}$  of the composite was around  $15 \text{ MPa m}^{1/2}$  compared with  $3.3 \text{ MPa m}^{1/2}$  for monolithic  $\text{MoSi}_2$ . Also the work of fracture of the composite specimen has increased significantly over that of the matrix.

In order to investigate the crack propagation in the matrix, the chevron-notched composite specimens were unloaded at five different load levels,

indicated by points a-e in Fig. 7. The unloaded specimens were sectioned parallel to the crack propagation but perpendicular to the direction of the foil alignment and then examined for the extent of crack propagation. Figures 8(a)-(e) show the nature of crack propagation in the samples at the corresponding load levels indicated in Fig. 7. For the sample loaded up to 15 lbf (point a in Fig. 7) which is approximately 10% of the peak load of the composite, a crack was observed at the tip of the chevron notch, which had propagated in a stable manner as shown in Fig. 8(a). When the load was increased to 35 lbf (point b in Fig. 7), which is about 25% of the peak load, the result indicated that the crack had already propagated throughout the entire thickness of the matrix.

The extensive cracking of the matrix at a load level considerably below the peak load of the composite may be explained using the principle of strain compatibility in composite materials. During the initial loading and prior to cracking of the matrix, most of the applied load is carried by the matrix because the elastic modulus of  $\text{MoSi}_2$  matrix (380 GPa) is much higher than that of niobium foils (105 GPa). For the niobium foils to carry the same stress as the matrix, they need to be elongated three times more than the matrix (assuming no constrained deformation). On the basis of the strain compatibility criteria, this is clearly impossible unless the matrix fractures.

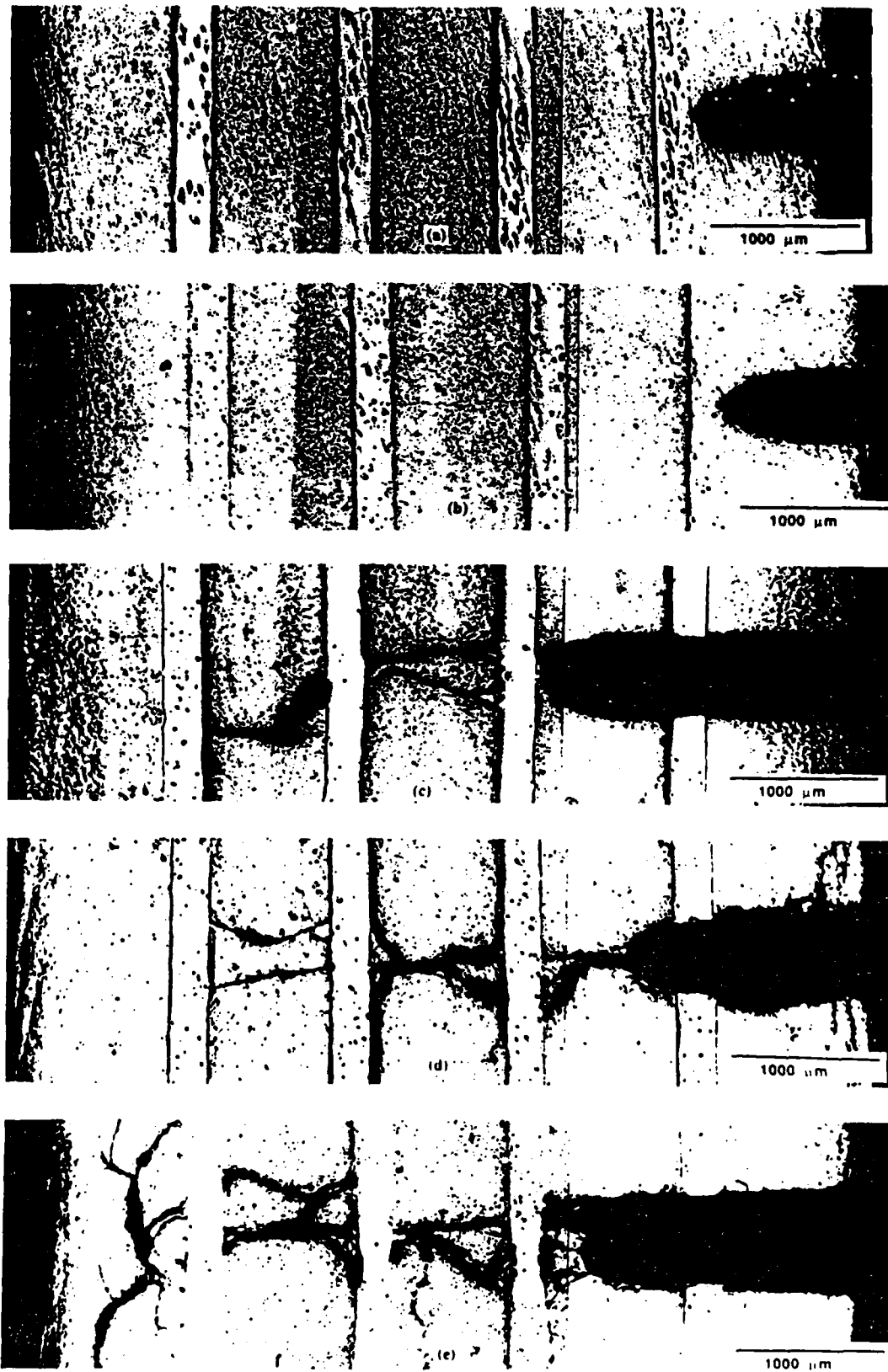


Fig. 8. The propagation of the cracks in uncoated molybdenum-foil-reinforced MoSi<sub>2</sub> composites at various load levels in Fig. 7

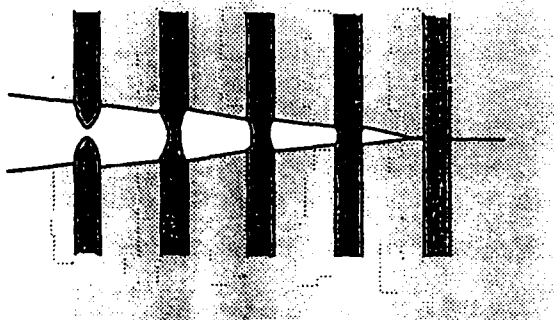


Fig. 9. Crack propagation in a ductile-phase-reinforced brittle matrix composite. The reinforcements located farther behind the crack tip are strained much more to carry the applied stress.

Therefore the reinforcement with a lower elastic modulus will carry a minor part of the load until a matrix crack has opened appreciably to allow the reinforcement to strain. This is schematically shown in Fig. 9, where the reinforcements which are farther behind the crack tip are strained much more than those closer to the tip or ahead of the crack. Obviously, the required level of the crack opening for the additional straining of the reinforcement will depend on the length of debonded section of the reinforcement: the larger the debonding length, the larger is the reinforcement section which is being strained, and the larger is the required crack opening. Moreover, the latter will also depend on the relative values of the elastic moduli of the matrix and the reinforcement. The thick (0.25 mm) niobium foils and the large distance between the foils (about 800  $\mu\text{m}$ ) may also have contributed to the premature failure of the matrix. It is clear that the value calculated from the peak load (point d in Fig. 7) may be interpreted as an indicator of the damage tolerance of the composite.

#### 3.4. Interaction of cracks with uncoated niobium reinforcements

Closer examination of Fig. 8 reveals interesting aspects of the interaction between cracks and niobium foils in the composites reinforced by the uncoated niobium foils. At the early stages of loading, there is only one primary crack propagating in the matrix. This primary crack propagates through the matrix in a stepwise manner, instead of propagation on one crack plane (Fig. 8(b)). The stepwise crack propagation in the matrix may be explained through geometrical

effects of the niobium reinforcement foils. In these laminated composites, as a crack ends on one side of the niobium foils, it needs to renucleate on the other side, making the crack propagation discontinuous in nature. Let us consider, moreover, the crack nucleation mechanism: because of a statistical distribution of crack nucleation sites on the other side of the foil, it is not necessary that the renucleation be coplanar with the original crack. In fact, it may be expected that the renucleated crack will most probably not be coplanar with the original crack. The net result is the observed stepwise crack propagation.

As the load level is increased, the niobium foils at the opening of the primary crack become stretched and secondary cracks start to nucleate as shown in Fig. 8(c). On further increase in load, additional secondary cracks continue to form and propagate throughout the matrix, creating a region at the interface which may be termed "virtual debonding" as shown in Fig. 8(e). In this area, the matrix-imposed constraints are relaxed and the foil can deform freely in a unidirectional tensile stress state until it fails in a ductile manner.

When the geometry of the niobium reinforcements is changed from foils to filaments, the crack propagation in the matrix is also expected to change. For filament-reinforced composites, the crack can propagate continuously throughout the matrix without the need for renucleation. Therefore the crack will propagate on the plane of the maximum stress intensity and the secondary cracks are not expected to form. Figure 10 shows the fracture surface of an uncoated niobium-filament-reinforced composite. As seen in the figure, there is no appreciable debonding at the reinforcement-matrix interface and the filaments have failed in a brittle cleavage manner. The brittle fracture of the filaments is believed to occur because of the lack of decohesion at the reinforcement-matrix interface due to strong bonding and because of the absence of the virtual decohesion by secondary cracks as in the laminated composites. As a result, the filaments are constrained by the matrix and, under a triaxial state of stress, lead to a brittle fracture of the filaments.

#### 3.5. Effect of coating on the crack-reinforcement interaction

When niobium foils were coated with  $\text{Al}_2\text{O}_3$ , the cracks in the laminated composites propagated in a manner similar to the uncoated

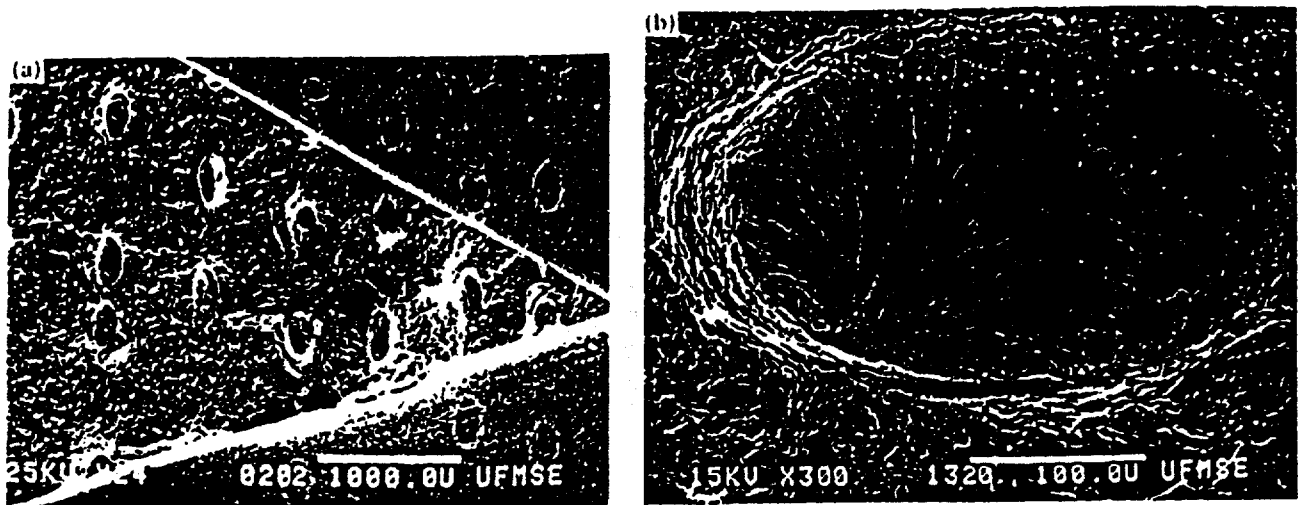


Fig. 10. Fracture surface of an uncoated niobium-filament-reinforced  $\text{MoSi}_2$  composite, showing limited decohesion at the interface and brittle cleavage fracture of the niobium filament: (a) fractured chevron-notched specimen; (b) fractured niobium filament

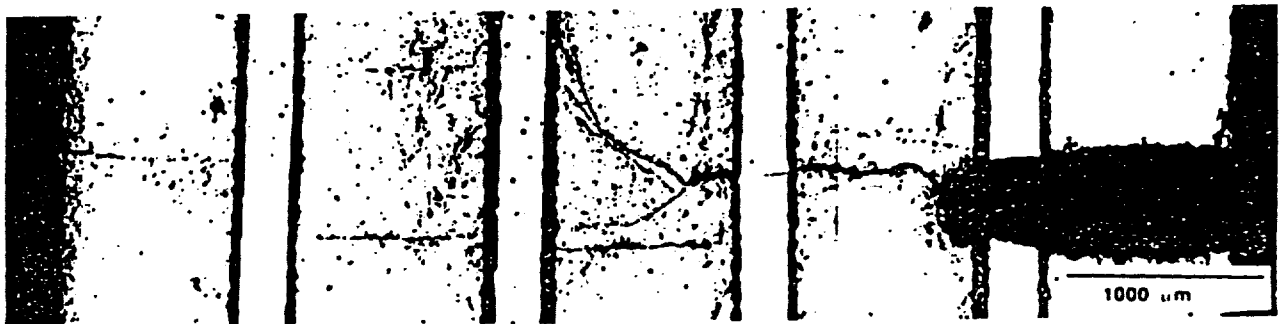


Fig. 11. The crack propagation in a  $\text{ZrO}_2$ -coated niobium-foil-reinforced  $\text{MoSi}_2$  composite. The niobium foils failed in a brittle manner

niobium-foil-reinforced composite: stepwise propagation of the primary crack, extensive secondary cracking and ductile failure of niobium foils. However, when niobium foils were coated with  $\text{ZrO}_2$ , cracks propagated in a different mode, as shown in Fig. 11. In this composite, there was no extensive secondary cracking and niobium foils failed in a brittle manner, even though the primary crack propagated in the stepwise manner. The brittle fracture of niobium foil may be due to several factors such as embrittlement of the niobium foils, the notch effect from the thick coating and the reaction layer, and/or residual stresses build up owing to the mismatches in thermal expansion coefficients. The measurement of the Vickers microhardness of the niobium foils in the composites indicated that the Vickers microhardness of the  $\text{ZrO}_2$ -coated niobium foils was increased slightly (236 HV) over that of the uncoated niobium foils (145 HV)

and the  $\text{Al}_2\text{O}_3$ -coated foils (164 HV). This hardness increase is believed to be due to a slight increase in the oxygen concentration in the niobium foils. At present, the most probable cause for the observed fracture behavior appears to be related to the high degree of constraint imposed by the strong interface. However, further studies will be continued to investigate the exact cause of the brittle fracture of  $\text{ZrO}_2$ -coated Nb foils.

Table 1 summarizes the effect of the crack-reinforcement interaction on the damage tolerance of the composites. These values may be compared with the fracture toughness of the monolithic matrix (about  $3.3 \text{ MPa m}^{1/2}$ ). As expected, the damage tolerance of the composites in which niobium foils failed in a ductile manner is higher than that of the composites with a brittle niobium failure. On the contrary, when the niobium reinforcements failed in a brittle manner, the damage tolerance with uncoated niobium fila-

TABLE I  
Damage tolerance of the niobium-reinforced MoSi<sub>2</sub> matrix composites

|                      | Damage tolerance (MPa m <sup>1/2</sup> ) |                                       |                         | Remarks                   |
|----------------------|--|---------------------------------------|-------------------------|---------------------------|
|                      | Uncoated                                 | Al <sub>2</sub> O <sub>3</sub> coated | ZrO <sub>2</sub> coated |                           |
| Laminated composites | 15.5                                     | 14.0                                  | 8.6                     | Nb foil reinforcement     |
| Fibrous composite    | 12.2                                     |                                       |                         | Nb filament reinforcement |

ment composite was higher than the ZrO<sub>2</sub>-coated niobium-foil-reinforced composite, which may again be related to the character of the interface bond.

#### 4. Summary and conclusions

The main effort in this study was focused on the control of the reinforcement-matrix interface interactions as well as the interface mechanical properties in Nb-MoSi<sub>2</sub> composites. The approach was to coat the niobium reinforcements with inert diffusion barriers. A chemical compatibility study of MoSi<sub>2</sub> with Al<sub>2</sub>O<sub>3</sub> as a potential coating material showed that they are chemically compatible in the absence of SiO<sub>2</sub> impurity particles. The presence of SiO<sub>2</sub> was found to cause extensive reaction between the second phase (SiO<sub>2</sub>) and Al<sub>2</sub>O<sub>3</sub>. ZrO<sub>2</sub> and mullite were also found to be chemically compatible with MoSi<sub>2</sub>.

When Al<sub>2</sub>O<sub>3</sub> and ZrO<sub>2</sub> coatings were applied on niobium prior to incorporation in MoSi<sub>2</sub>, they were effective in eliminating niobium and molybdenum diffusion, and retarding the interaction between niobium and MoSi<sub>2</sub>.

Investigation on the crack propagation in the niobium-reinforced MoSi<sub>2</sub> composite indicated that the matrix cracked at a load level considerably below the peak load of the load-displacement curve. This early crack propagation through the matrix is believed to be due to low elastic modulus of the niobium reinforcement compared with that of the matrix and the strain compatibility requirements in the composite. Thus it was suggested that the fracture toughness of the composite determined from the peak load of the four-point bending test should be interpreted as

an indicator of the damage tolerance of the composite.

Composites containing uncoated and Al<sub>2</sub>O<sub>3</sub>-coated niobium foils showed an improved damage tolerance, with  $K_{Ic}$  around 14-15 MPa m<sup>1/2</sup>. On the contrary, the composites reinforced by ZrO<sub>2</sub>-coated niobium foils showed a lower damage tolerance (8.6 MPa m<sup>1/2</sup>) with a brittle cleavage fracture of the foils.

The geometry of the reinforcements was also found to affect the crack propagation in the matrix. In the laminated composites, the crack propagation was discontinuous, leading to a step-wise crack propagation of a primary crack and nucleation of secondary cracks. On the contrary, the crack in a fibrous composite propagated continuously on one plane, and the filaments failed in a brittle cleavage manner.

#### Acknowledgments

The authors thank A. B. Gokhale for his valuable discussions and critical reading of the manuscript. The support of this research by Defense Advanced Research Projects Agency, under Contract MDA972-88-J-1006, is greatly appreciated.

#### References

- 1 E. Fitzer, in R. A. Bradley, D. E. Clark, D. C. Larsen and J. O. Stiegler (eds.), *Whisker- and Fiber-Toughened Ceramics*, American Society for Metals, Metals Park, OH, 1988, 165.
- 2 C. K. Elliott, G. R. Odette, G. E. Lucas and J. W. Shekherd, *DARPA Annu. Rep.*, 1987 (University of California, Santa Barbara, CA) (Defense Advanced Research Projects Agency Contract).
- 3 L. S. Sigl, P. A. Mataga, B. J. Dalgleish, R. M. McMeeking and A. G. Evans, *Acta Metall.*, **36** (1988) 945-953.
- 4 S. Kunz-Douglass, P. W. R. Beaumont and M. F. Ashby, *J. Mater. Sci.*, **15** (1980) 1109-1123.
- 5 L. Xiao, Y. S. Kim and R. Abbaschian, *Intermetallic Matrix Composites, Proc. Materials Research Society Spring Meet., San Francisco, CA, April 16-21, 1990*, Materials Research Society, Pittsburgh, PA, 1990, p. 399.
- 6 A. G. Metcalfe and M. J. Klein, *Composite Materials, Vol. 1, Interfaces in Metal Matrix Composites*, Academic Press, New York, 1974, p. 146.
- 7 J. D. Cotton, Y. S. Kim and M. J. Kaufman, *Mater. Sci. Eng.*, **144** (1991) 281.
- 8 W. D. Kingery, H. K. Bowen and D. R. Uhlman, *Introduction to Ceramics*, Wiley, New York, 1976, p. 240.
- 9 D. G. Munz, J. L. Shannon, Jr., and R. T. Bussey, *Int. J. Fracture*, **16** (1980) R137-141.

# Evaluating a Technique for Determining the Toughening of Brittle Matrix by Ductile Reinforcements

L. Xiao and R. Abbaschian  
University of Florida  
Gainesville, FL, USA

## EVALUATING A TECHNIQUE FOR DETERMINING THE TOUGHENING OF BRITTLE MATRIX BY DUCTILE REINFORCEMENTS

Lingang Xiao and Reza Abbaschian  
Department of Materials Science and Engineering, University of Florida,  
Gainesville, FL 32611

### ABSTRACT

Substantial toughening of intermetallics and ceramics by ductile reinforcements has been established. To evaluate the toughening by ductile reinforcements, it is necessary to know the stress-displacement curve of the ductile phase constrained by the brittle matrix. In the present study, tensile tests involving the specimen with a ductile reinforcement imbedded in the notched brittle matrix have been used. Effects of experimental variables, notch geometry in the vicinity of the ductile phase, depth of the notches and size of ductile reinforcement, on the measured stress-displacement curves have been evaluated. The experimental results showed that these variables played important roles in the stress-displacement curves. The results are analyzed using theory of notch stresses and finite element method. A formula to estimate these effects of the variables has been put forward.

### 1. INTRODUCTION

It has been established that substantial toughening of brittle matrices can be achieved by incorporating ductile reinforcements [1-9]. The primary

mechanism responsible for the enhanced toughness has been attributed to be bridging by intact ligaments of the ductile phase behind the advancing crack tip [10-14]. The physical mechanism of toughening by intact ligaments of the ductile phase is straightforward. If ductile ligaments span the advancing crack, they must stretch as the crack opens until they fracture or decohere. The work of stretching contributes to the toughness of the composite and the increased fracture toughness of the composite can be obtained directly from the  $J$ -integral around the traction zone as [11,12]

$$\Delta G = V_f \int_0^{u^*} \sigma(u) du \quad \dots \quad (1)$$

where  $u$  is the crack opening,  $\sigma(u)$  the nominal stress on the ligament,  $u^*$  the crack opening at the end of the traction zone and  $V_f$  is the area fraction of reinforcements on the crack plane. Once  $\sigma(u)$  as a function of crack opening is known, the increase in toughness of the composite can be evaluated through eq. (1).

Recognizing that  $\sigma(u)$  is different from that measured in a simple tensile test, several investigators [15-17] have used a test procedure to

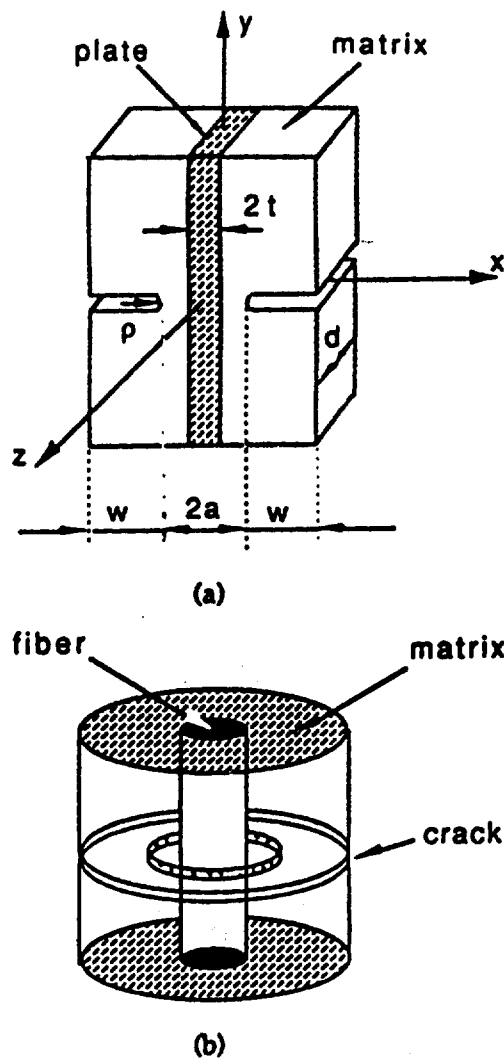


Fig. 1 (a) Schematic of a composite laminate test specimen;  
 (b) Schematic of a composite cylinder test specimen.

evaluate  $\sigma(u)$ . The test procedure is based on the concept that the stress-displacement relationship obtained from one ductile reinforcement imbedded in a brittle matrix can be used to describe the mechanical characteristics of the reinforcements in the composites. The basic test specimen consists of one ductile filament or foil imbedded in a precracked brittle matrix, as shown in Fig. 1, and a tensile test is conducted to evaluate the  $\sigma(u)$ . Clearly, in order to accurately simulate constrained condition of the reinforcements in the matrix, it is necessary to be aware of effects of experimental variables, such as depth of the notch and geometry of the notch tip, on the measured stress-

displacement relation. In the present study, effects of these two variables are evaluated and appropriate combination of these two variables with size of ductile reinforcement is also evaluated. The experimental results are analyzed using theory of notch stresses and finite element method. A formula to estimate the effects of the variables is established and will provide guideline for the future design of proper test specimens to obtain the intrinsic properties of the reinforcements.

## II. EXPERIMENTAL

**2.1 THE TEST SPECIMEN** - The test specimens used in this study were laminated composites with pure Nb foil sandwiched between  $\text{MoSi}_2$  matrices, as shown in Fig. 1(a). The specimens were prepared by stacking a Nb foil with two layers of  $\text{MoSi}_2$  powder of -325 mesh at an appropriate ratio, and then vacuum hot pressing at  $1400^\circ\text{C}$  for 1 hour under a pressure of 40 MPa to get the composite discs. Three different thicknesses of Nb foils ( 0.25, 0.5 and 1.0 mm) were used to prepare the composite discs. The discs were then cut into rectangular tensile test bars with dimensions of  $5.0 \times 3.8 \times 30.0$  mm. In order to obtain the relation between crack propagation and stresses, surfaces of the tensile test bars perpendicular to the plane of the Nb foil were polished before notching. The notches in the  $\text{MoSi}_2$  matrix were introduced using diamond wafering blades. The variation in radius of the notch tip was obtained by using different sizes of diamond wafering blades. Three different radii of notch tips used in the present study were 0.075, 0.165 and 0.270 mm. Fig. 2 shows typical precracks in a test specimen and a close-up image of one of the notch tips with a radius of 0.075 mm. The notches on the both sides were symmetrical with respect to the central Nb foil. Depth of the notches was measured in terms of the width of the narrowest cross section,  $2a$ , as shown in Fig. 1(a). The reason for that will become obvious in Section 3.

**2.2 TEST PROCEDURE** - Displacement controlled tensile tests were conducted with INSTRON. Wedge-type grips were used to clamp the specimens and load train alignment was achieved by coupling the top grip to a universal joint. Strictly speaking, to simulate the interaction between ductile reinforcements and cracks, very sharp precracks should be introduced in the matrix. However, this is difficult to do or very tedious procedure has to be



Fig. 2 (a) A general view of precracks in a composite laminate test specimen with a 0.5 mm thick Nb lamina and 0.075 mm notch tip radius; (b) A close-up image of one of the notch tips in (a).

taken, such as initiating cracks by fatigue or by introducing a chevron form of notch. In the present study, a very slow displacement speed, 0.005 in/min, was used to alleviate this conflict. With such low speed, it was easy to unload the specimens at the load level desired for examining the specimens with SEM to identify the critical stress for initiating a crack at the notch tip and to observe sharpness of cracks and crack propagation.

For comparison, the critical stress for initiating a crack at the notch tip was also detected by conducting tensile tests on some notched monolithic MoSi<sub>2</sub> specimens.

### III. RESULTS AND DISCUSSION

**3.1 STRESS DISTRIBUTION IN A MONOLITHIC MATERIAL SPECIMEN** - Because of geometry of the specimens in the present study, stress distribution in the specimens consisting of a

monolithic material can be approximately treated as a problem of a flat bar with a deep notch on each side. H. Neuber [18] has already derived a formula to calculate stress distribution over the narrowest cross section of such specimen under a tensile loading (Fig.3). The stress distribution in question is only a function of  $a/\rho$  and not affected by depth of the notch,  $w$  (Fig.1). The formula proposed is

$$\sigma_v = \frac{A}{h^2} \cosh v \cos u \left( 2 + \frac{\cos^2 u_0 - \cos^2 u}{h^2} \right) \dots \dots \dots (2)$$

where A and h are defined as

$$A = \frac{F}{2ad} \frac{\sin u_0}{v_0 + \sin u_0 \cos v_0} \dots \dots \dots (3)$$

$$h^2 = \sinh^2 v + \cos^2 u \dots \dots \dots (4)$$

Meanings of the symbols used in eqs. (2)-(4) are as follows.  $v$  and  $u$  are elliptical coordinates and the relations between elliptical coordinates and Cartesian coordinates are

$$y = \sinh v \cos u$$

$$x = \cosh v \sin u$$

$\sigma_v$  is stress in  $v$  direction at any position in the plane of the narrowest cross section,  $F$  the tensile loading,  $F/2ad$  the nominal stress in  $y$  direction over the narrowest cross section,  $v_0$  a constant which defines contour of the notches with a formula of  $v = v_0$  (a hyperbola contour). The reason the contour of the notches was assumed as a hyperbola in the derivation of eq. (2) was because curvature of the notch tip had much more considerable effect on the stress distribution than the additional contour of the notch and the assumption of a hyperbola contour permitted the simplest possible calculation. Due to such an assumption, the contour of the notch is related to the width of the narrowest cross section and curvature of the notch tip with a formula of  $v_0 = \arccos(1/\sqrt{(a/\rho+1)})$ . The stress component,  $\sigma_y$ , over the narrowest cross section can be obtained from eq. (2) when setting  $v=0$ .

The tensile tests on the notched monolithic MoSi<sub>2</sub> specimens showed that the nominal stress over the narrowest cross section for initiating cracks at the notch tips,  $\sigma_{crack(nom)}$  was  $66.2 \pm 13.6$  MPa for

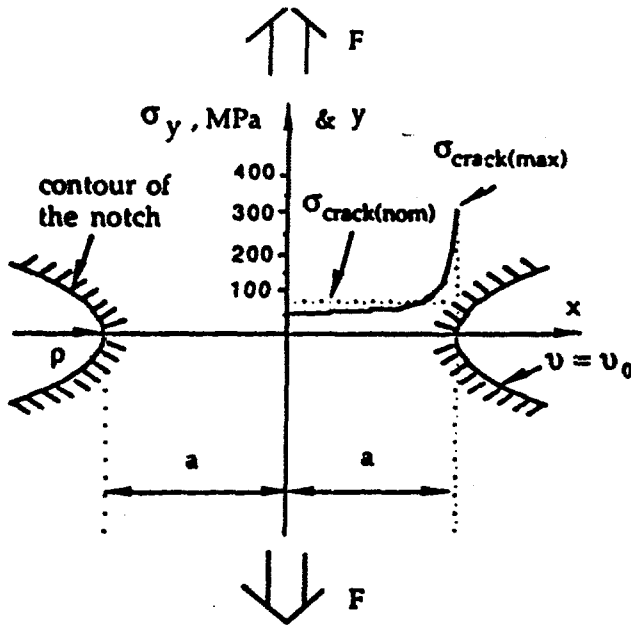


Fig. 3 Stress distribution over the narrowest cross section and the corresponding contour of the notches in a notched bar consisting of a monolithic MoSi<sub>2</sub>

specimens with a width of 2.0 mm at the narrowest cross section and a notch tip radius of 0.075 mm. Inserting the  $\sigma_{crack(nom)}$  measured and the specimen's dimensions into eq. (2) and setting  $v = 0$ , it was found that the stress at the notch tip at the point of crack initiation,  $\sigma_{crack(max)}$ , was  $310.4 \pm 60.6$  MPa, as shown in Fig. 3. It is noteworthy that  $\sigma_{crack(max)}$  calculated in the present study is very close to the flexural strength (319MPa) of monolithic MoSi<sub>2</sub> measured using four-point bend tests in a related study [19]. The physical meanings of these two quantities are the same, i.e., both of them are the maximum tensile stress the MoSi<sub>2</sub> can sustain before a crack is initiated. The results suggest that with a proper design of the notched specimen, tensile strength of brittle materials can be evaluated with such precracked specimen geometry.

**3.2 STRESS ANALYSIS OF THE SANDWICHED SPECIMEN** - In the case of sandwiched specimens, eq. (2) can still be utilized provided some assumptions are made. It is noted that there is a deformation continuity across the matrix/reinforcement interface before the debonding at the interface occurs. Therefore, it is assumed that the stress  $\sigma_y$  in the Nb side at the

interface is 3.6 times less than that in the MoSi<sub>2</sub> side during the elastic stage because the elastic modulus of MoSi<sub>2</sub> (379GPa) is 3.6 times larger than that of Nb (105GPa). It is also assumed that the stress distribution described by eq. (2) is still valid even inside the Nb reinforcement but with all the stresses being only 1/3.6 of the stresses calculated using eq. (2). With the above assumptions, the stress distribution in the sandwiched specimens can be calculated using eq. (2). Errors introduced with the assumptions are estimated using finite element analysis and the results are presented in the Appendix.

Measured  $\sigma_{crack(nom)}$  for laminated composites with 0.5 mm thick Nb lamina as a function of width of the narrowest cross section is shown in Fig. 4. If  $\sigma_{crack(max)}$  of 310.4 MPa measured from the monolithic MoSi<sub>2</sub> is taken as the stress to initiate cracks at the notch tips in the laminated composite specimens,  $\sigma_{crack(nom)}$  for the laminated specimens can be calculated using eq. (2) with the aforementioned assumptions. The calculated  $\sigma_{crack(nom)}$  is also included in Fig. 4 for comparison. As seen in the figure, the theory of notch stresses predicts that  $\sigma_{crack(nom)}$  increases with decreasing width of the narrowest cross section and such trend is confirmed by the measurement when the narrowest cross section is wide. However, the predicted value deviates from the experimental data when width of the narrowest cross section is small. Such deviation is caused by the residual thermal stresses, as discussed below. Using eq. (2) and the aforementioned assumptions,

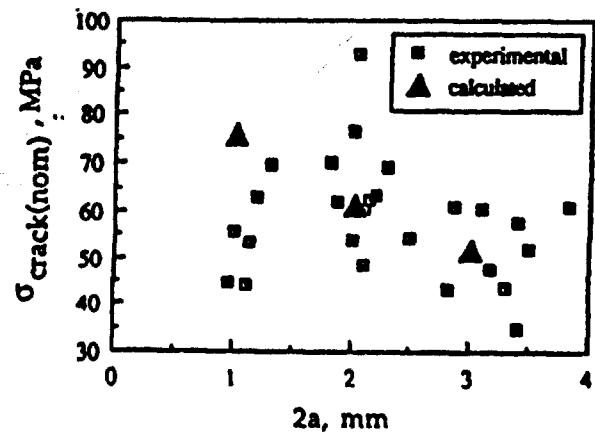


Fig. 4 A plot of  $\sigma_{crack(nom)}$  vs width of the narrowest cross section for composite laminates with 0.5 mm thick Nb lamina and 0.075 mm notch tip radius.

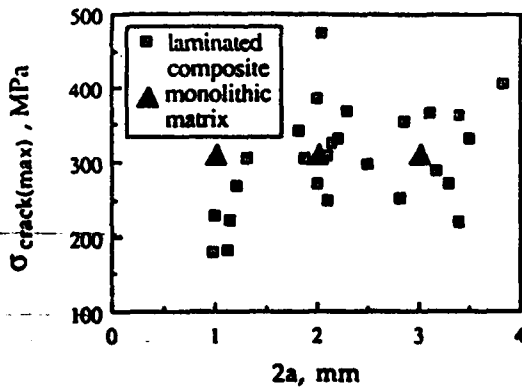


Fig. 5 A plot of  $\sigma_{crack(max)}$  vs width of the narrowest cross section. The data for the laminated composites are calculated from the data in Fig. 4.

the measured  $\sigma_{crack(nom)}$  in Fig. 4 can be used to calculate  $\sigma_{crack(max)}$  for the laminated specimens. The calculated  $\sigma_{crack(max)}$  are presented in Fig. 5 as a function of width of the narrowest cross section. In principle, the stress to initiate cracks at notch tips for all the specimens should be the same in spite of different notch depths. However, Fig. 5 shows that the measured  $\sigma_{crack(max)}$  is lower for deeply notched specimens than other specimens. It is believed that this conflict is caused by the residual thermal stresses which contribute a tensile stress in y direction (Fig.1) of about 19 MPa to the MoSi<sub>2</sub> adjacent to the interfaces [19]. Superposition of the residual stresses to the external stress results in a drop of  $\sigma_{crack(max)}$  when width of the narrowest cross section is small.

Effect of notch size on the measured  $\sigma_{crack(nom)}$  is shown in Fig. 6. Taking 310.4 MPa as the stress to initiate cracks at the notch tips in the laminated specimens,  $\sigma_{crack(nom)}$  has been calculated using eq. (2) as a function of notch size and the results are also presented in Fig. 6. As expected, the theory of notch stresses predicts increase of  $\sigma_{crack(nom)}$  with increasing radius of notch tip. However, the measured  $\sigma_{crack(nom)}$  shows no increase or a very small increase from  $65.86 \pm 12.48$  to  $71.15 \pm 16.32$  and then to  $69.62 \pm 10.14$  MPa as radius of the notch tip increases from 0.075 to 0.165 and then to 0.27 mm. The results suggest that when radius of the notch tip is large, such as 0.165 and 0.27 mm, the stress to initiate cracks at the notch tips is no longer controlled by radius of the notch tips, but by intrinsic defects such as porosity

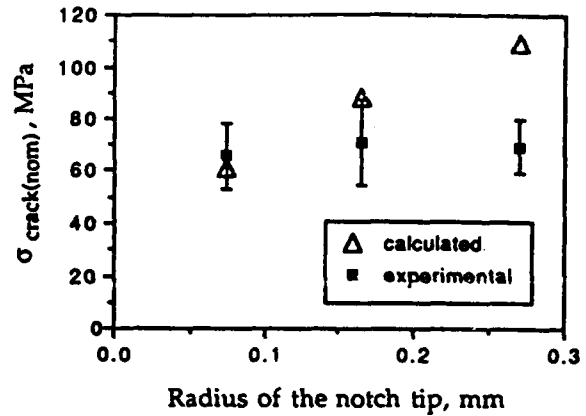


Fig. 6 Effect of notch size on the nominal stress for initiating cracks in the matrix.

in the matrix or the defects introduced during the notching. Close examination of Fig. 2(b) reveals that some defects are indeed introduced at the notch tip. Such defects could become decisive factors when radius of the notch tip is large. The results indicate that a small radius of notch tip should be used if the stress to initiate cracks at the notch tips is to be controlled.

**3.3 LOAD-DISPLACEMENT CURVES** - Fig. 7 shows effect of notch depth (0.075 mm tip radius) on the load-displacement curves of laminated composites with 0.5 mm thick Nb lamina. Sudden load drops in curves A and B correspond to the load for initiating cracks at the notch tips. The load for initiating cracks in curve C is about 40 lbs and it is hard to ascertain from the curve because of small load drop. The reason the load drop in curve C is

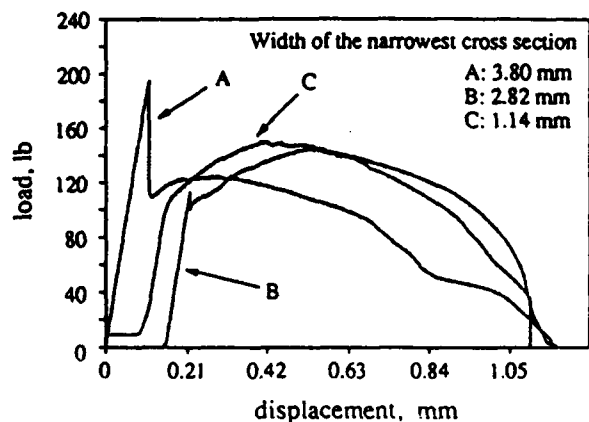


Fig. 7 Effect of notch depth on the load-displacement curves of constrained Nb

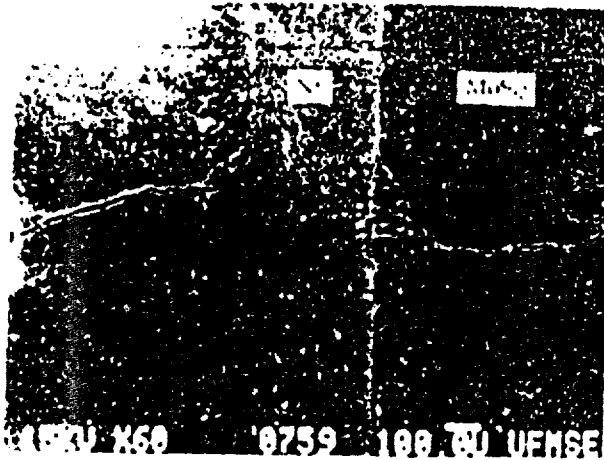


Fig. 8 A SEM micrograph of a laminated specimen unloaded after the specimen has passed the sudden load drop in the load-displacement curve.

small is because the matrix only carries a small portion of the tensile loading when the width of the narrowest cross section is small. It is noteworthy that when width of the narrowest cross section is large, the stress to initiate cracks could be high enough to distort intrinsic load-displacement curves of the constrained ductile reinforcement, as in the cases of curves A and B.

A proper design of notch depth should remain an appropriate degree of elastic constraints on the ductile phase, and on the other hand it should prevent distortion of the load-displacement curves of the constrained ductile phase. Based on this guideline, the width of the narrowest cross section for curve C is deemed as an appropriate

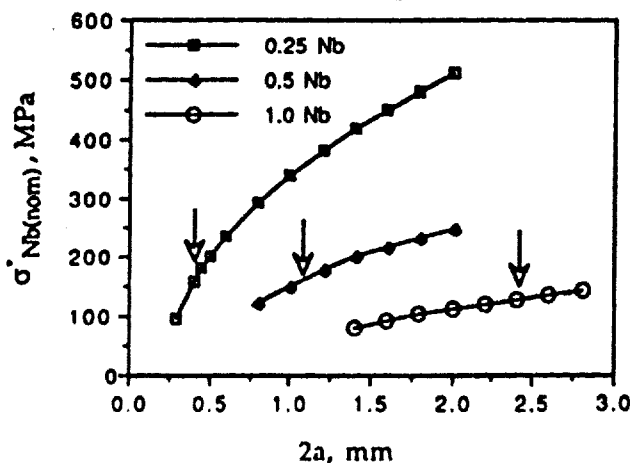


Fig. 9 A plot of notch depth vs the nominal stress carried by different sizes of constrained Nb laminae right after the crack propagation through the whole matrix.

notch depth and the area under curve C is regarded as a truly representative of the contribution of the ductile reinforcements to the toughness of a brittle matrix composite.

The present experiments showed that cracks propagated through the whole matrix as soon as the cracks were initiated at the notch tips, and from that point on the load was carried only by the central Nb lamina. Fig. 8 shows such a typical crack propagation. Nominal stress carried by the central Nb lamina right after the crack propagation through the whole matrix,  $\sigma^*_{Nb(nom)}$ , is calculated using eq. (2) by assuming that 310.4 MPa is the stress to initiate cracks at the crack tips and the load reached at the point of initiating cracks is carried totally by the Nb lamina. The calculated results for different thicknesses of Nb laminae are plotted as a function of width of the narrowest cross section in Fig. 9. The maximum stress reached by the constrained Nb measured from the load-displacement curves are  $351.3 \pm 25.7$ ,  $320.4 \pm 14.6$  and  $259.9 \pm 22.9$  MPa for Nb laminae with a thickness of 0.25, 0.5 and 1.0 mm, respectively. The present experiments showed that if  $\sigma^*_{Nb(nom)}$  was below about half of the maximum stress reached by the constrained Nb lamina, then the stress to initiate cracks was not high enough to distort the intrinsic load-displacement curves of the constrained ductile phase. Half of the maximum stress reached by each size of constrained Nb lamina is indicated by arrows in Fig. 9. Thus, a proper combination of size of ductile reinforcement and depth of notch can be found in Fig. 9.

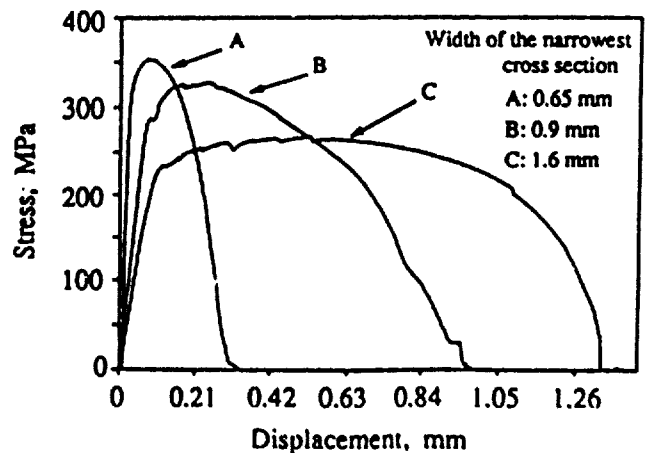


Fig. 10 Stress-displacement curves for different sizes of constrained Nb laminae. The thickness of the Nb laminae is 0.25, 0.5 and 1.0 mm for curves A, B and C, respectively.

Examples of stress-displacement curves resulted from a proper combination of reinforcement size and notch depth are showed in Fig. 10. The widths of the narrowest cross section in the figure are 0.65, 0.9 and 1.6 mm for 0.25, 0.5 and 1.0 mm thick Nb laminae, respectively. It can be seen that with such combinations the load drop in the curves is at the lower stress level and very hard to ascertain. Thus, the area under the curves can be regarded as the contribution of Nb to the toughness of MoSi<sub>2</sub> matrix composites. From Fig. 10 and eq. (1), it is concluded that toughness of ductile-phase-reinforced brittle matrix composites increases with increasing size of ductile phases.

#### IV. CONCLUDING REMARKS

The present set of experiments demonstrate that the formula proposed by H. Neuber to describe the stress distribution of a flat bar with a deep notch on each side can be used to estimate the stress distribution for both notched monolithic and composite laminate tensile specimens. The stress to initiate cracks at the notch tips in the brittle matrix can be predicted using the formula and such stress has been found to be equal to the flexural strength of the basic matrix.

Evaluation of notch size effect indicates that a small radius of notch tip should be used for a better control of the stress to initiate cracks in the matrix. It is shown that in order to remain an appropriate degree of elastic constraints on the ductile phase and at the same time prevent the distortion of the stress-displacement curve of the constrained ductile phase, the nominal stress on the ductile phase at the point of crack initiation in the matrix should be below about half of the maximum stress reached by the constrained ductile phase. Thus, to avoid the distortion of the stress-displacement curve, notch depth should increase with decreasing size of constrained ductile reinforcement.

Although no experiment on composite cylinder specimens has been conducted, it is recommended that the formula proposed by H. Neuber to describe the stress distribution for a tensile rod with a deep circumferential notch could be used to analyze the notched composite cylinder specimen using an approach analogous to the present analysis of composite laminate specimens.

Acknowledgements ---- The authors are grateful to the support of the Defense Advanced Research Projects Agency (DARPA) through contract MDA972-88-J-1006.

#### REFERENCES

1. J. L. Chermant and F. Osterstock, *J. Mater. Sci.*, **11**, 1939-51(1976).
2. J. Gurland, *Trans. ASM*, **50**, 1063-71(1958).
3. A. V. Virkar and D. L. Jognson, *J. Am. Ceram. Soc.*, **60**, 514-19(1977).
4. D. T. Rankin, *J. Am. Ceram. Soc.*, **54**, 277-81(1971).
5. P. Hing and G. W. Groves, *J. Mater. Sci.*, **7**, 427-34 (1972).
6. V. V. Kristie and P. S. Nicholins, *J. Am. Ceram. Soc.*, **64**, 499-504(1981).
7. C. K. Elliott, G. R. Odette, G. E. Lucas and J. W. Sheckherd, "High Temperature, High Performance Composites", edited by F. D. Lemkey et al., *MRS Proc.*, **120**, 95-102(1988).
8. E. Fitzer, "Whisker- and Fiber-Toughened Ceramics", edited by R. A. Bradley, D. E. Clark, D. C. Larsen and J. O. Stiegler, pp. 165-83, *ASM International TM* (1988).
9. L. Xiao, Y. S. Kim and R. Abbaschian, "Intermetallic Matrix Composites", edited by D. L. Anton, P. L. Martin, D. B. Miracle and R. McMeeking, *MRS Proc.*, **194**, 399-404(1990).
10. L. R. F. Rose, *J. Mech. Phys. Solids*, **35**, 383-405 (1987).
11. L. S. Sigl, P. A. Mataga, B. J. Dalgleish, R. M. McMeeking and A. G. Evaris, *Acta Metall.*, **36**, 945-53(1988).
12. A. G. Evans and R. M. McKeeking, *Acta Metall.*, **34**, 2435-41(1986).
13. P. A. Mataga, *Acta Metall.*, **37**, 3349-59(1989).
14. B. Budiansky, J. C. Amazigo and A. G. Evans, *J. Mech. Phys. Solids*, **36**, 167-87(1988).
15. M. F. Ashby, F. J. Blunt and M. Bannister, *Acta Metall.*, **37**, 1847-57(1989).
16. H. C. Cao, B. J. Salgleish, H. E. Deve, C. Elliott, A. G. Evans, R. Mehrabian and G. R. Odette, *Acta Metall.*, **37**, 2969-77(1989).
17. H. E. Deve, A. G. Evans, G. R. Odette, R. Mehrabian, M. L. Emiliani and R. J. Hecht, *Acta Metall.*, **38**, 1491-1502(1990).
18. H. Neuber, "Theory of Notch Stresses - Principles for Exact Stress Calculation", pp. 38-42, *Edwards Brothers, Inc., Ann Arbor, Michigan* (1946).
19. L. Xiao and R. Abbaschian, "On the Strength and

Stiffness of Ductile Phase Reinforced MoSi<sub>2</sub> Composites", to be presented in TMS Fall Meeting, Cincinnati, OH, Oct. 1991.

### APPENDIX

Finite element analysis (FEA) of the stress distribution in the notched composite laminates during the elastic deformation was implemented using the finite element software package ANSYS. Due to the symmetry, only one quarter of the specimen was analyzed using both two-dimensional 4-node isoparametric and 6-node triangular elements with an assumption of plane stress deformation. Fig. 11 shows the mesh used in the analysis. A total of 184 elements were used. The displacement at the central plane along y-axis was allowed only in the y-direction, and the plane of the narrowest cross section was allowed to displace only in x-direction.

Stress distributions over the narrowest cross section from analysis of the theory of notch stresses and FEA are shown in Fig. 12. The input data for the analysis are as follows: the Nb lamina is 0.5 mm thick, width of the narrowest cross section is 1.0 mm, radius of notch tips is 0.075 mm and the nominal stress over the narrowest cross section is 66.75 MPa. It is noted that the stress distributions analyzed using both methods are very similar with

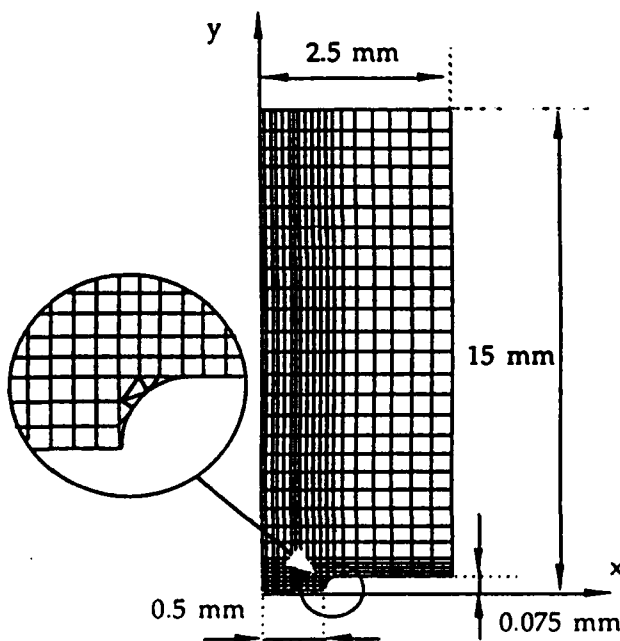


Fig. 11 Mesh used in the FEA.

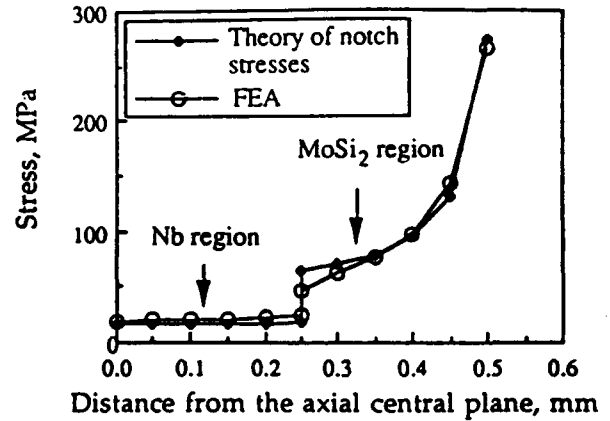


Fig. 12 Comparison between FEA and the theory of notch stresses on the stress distribution over the narrowest cross section.

the maximum stress at the notch tip predicted from the theory of notch stresses 3% higher than that predicted from FEA. The results indicate that the assumptions mentioned in Section 3.2 only introduce 3% error either to the calculation of the maximum stress at the notch tips or to the calculation of the nominal stress over the narrowest cross section.

It is also noted that ratio of the stress in the MoSi<sub>2</sub> side to that in the Nb side at the interface is not 3.6 (ratio of the Poisson's ratios of MoSi<sub>2</sub> to Nb), but equals to 2.01 for FEA. It is believed that the deviation of the stress ratio from 3.6 is due to the presence of the precracks because if there are no precracks in the FEA, the ratio of the stresses becomes 3.6.

## STUDY OF THE FLOW BEHAVIOR OF CONSTRAINED DUCTILE PHASES

### ----- I. EXPERIMENT

Lingang Xiao

Department of Materials Science and Engineering, University of Florida,  
Gainesville, FL 32611

#### Abstract

Effects of the matrix/reinforcement interface, and the mechanical properties and size of the ductile reinforcement on the flow behavior of the constrained ductile reinforcement have been evaluated using a tensile test on a single Nb lamina imbedded in  $\text{MoSi}_2$  matrix. Three different thicknesses of Nb foils (1.0, 0.5 and 0.25 mm) have been tested. Variation of interfacial bonding was achieved by depositing an oxide coating ( $\text{Al}_2\text{O}_3$  or  $\text{ZrO}_2$ ) or by the development of a reaction product layer between the reinforcement and matrix. It was found that work of rupture of the ductile reinforcement increased with size of the ductile reinforcement and with decreasing bonding strength at the matrix/reinforcement interface. Such results suggested that both of increasing size of ductile reinforcement and obtaining a relatively weak interface were conducive to toughness of the composites. It was also found that the work of rupture normalized by size and yield strength of the reinforcement was dependent on the interfacial properties and size of the reinforcement. The results were interpreted in terms of the dependence of the decohesion length on the interfacial properties and size of the reinforcement.

## I. Introduction

Numerous studies have shown that improved fracture toughness can be achieved by the incorporation of a ductile second phase into a brittle matrix. Examples of current or potential technological significance are tungsten carbide toughened with cobalt network [1,2], zirconia toughened with zirconium network [3], alumina toughened with dispersed molybdenum [4], magnesia toughened with cobalt and nickel particles or fibers [5], and glass-enamels toughened with dispersed aluminum and nickel particles [6]. Successful toughening has also been observed in titanium aluminide [7] and molybdenum disilicide [8,9] reinforced with niobium pancake or filament.

The primary toughening mechanism of ductile reinforcement has been attributed to the bridging of ductile ligaments [10-14]. The contribution to fracture toughness from bridging can be estimated by extending cohesive force model [15] to ligament bridging [11,12] and can be written as

$$\Delta G = v_f \int_0^{U^*} \sigma(U) dU \quad \dots\dots\dots (1)$$

where  $\sigma(U)$  is the nominal stress carried by the constrained ductile reinforcement for a given crack opening  $U$ ,  $v_f$  is volume fraction of the ductile reinforcement,  $U^*$  is the crack opening at the point when the ductile reinforcement fails and the definite integral, designated as  $\xi$ , is the work of rupture of the constrained ductile ligament. Thus, the key to predict the increased fracture toughness is to calculate  $\sigma(u)$  as a function of crack opening. Recognizing that  $\sigma(u)$  is different from that measured in a simple tensile test, several investigators [16-18] have used a test procedure to evaluate  $\sigma(u)$ . The test procedure is based on the concept that the stress-displacement relationship obtained from one ductile reinforcement imbedded in a brittle matrix can be used to describe the mechanical characteristics of the reinforcements in the composites. Their results demonstrated that flow behavior of constrained ductile phases was governed by the yield strength,  $\sigma_0$ , work hardening coefficient,  $n$ , and the decohesion length,  $d$ , at the matrix/reinforcement interface. Clearly, more work needs to be done in this area to evaluate the effect on  $\sigma(u)$  of the intrinsic properties of the ductile reinforcement (yield strength, work hardening and ductility), interfacial properties and size of the ductile phases.

The principle intent of the present study is to experimentally examine the effects of properties of the matrix/reinforcement interface and size of ductile phase on its flow behavior, and therefore on the enhanced fracture toughness of the composite. The system selected for investigation was MoSi<sub>2</sub> matrix reinforced with Nb. Since the two components used have similar coefficients of thermal expansion, the residual thermal stresses were minimized, thus simplifying the present stress analysis. Specimens with laminated form have been used, because of the ease of producing the composites with controlled properties, but it still serves the purpose of the present study. The results showed that work of rupture of the ductile reinforcement increased with size of the ductile reinforcement and with decreasing bonding strength at the matrix/reinforcement interface. Such results suggested that both of increasing size of ductile reinforcement and having a relatively weak interface are conducive to toughness of the composites.

## II. Experimental

Disc shaped laminated specimens were prepared by stacking a Nb foil with two layers of MoSi<sub>2</sub> powder (-325 mesh) at an appropriate ratio, and then vacuum hot pressing at 1400°C for 1 hour under a pressure of 40 MPa. In order to minimize residual thermal stresses, the hot pressed discs were held in the hot pressing chamber at 800°C for 1 hour before cooling down to room temperature. The residual thermal stresses induced with such processing have been estimated to be small with a tensile stress of 19 MPa in the matrix and a compressive stress of 79 MPa in the Nb on the lamina plane [19]. Three different thicknesses of Nb foils (1.0, 0.5 and 0.25 mm) with a purity of 99.8% were used to prepare the laminated specimens. Variation of the

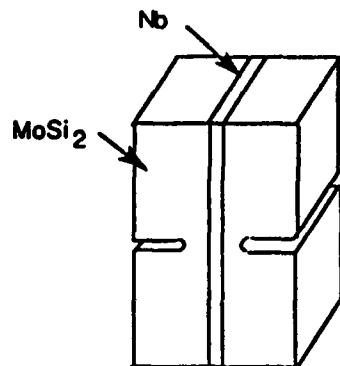


Fig. 1 Schematic of a composite laminate test specimen.

matrix/reinforcement interfaces was achieved by depositing different oxide coatings ( $\text{Al}_2\text{O}_3$  or  $\text{ZrO}_2$ ) to the Nb surface prior to the hot pressing or by the development of a reaction product layer between the matrix and reinforcement. Details of the coating procedures can be found in Reference [9].

The hot pressed discs were cut into rectangular tensile test bars with dimensions of 5.0x3.9x30.0 mm, as shown in Fig. 1. Straight-through notches in the  $\text{MoSi}_2$  matrix were introduced using a diamond wafering blade with a thickness of 0.15 mm. Distance from the notch tip to the laminate interface is 300  $\mu\text{m}$  for 1.0 mm thick Nb

lamina and 200  $\mu\text{m}$  for 0.5 and 0.25 mm thick Nb laminae. Such distances have been found to be small enough not to distort the

stress-displacement curve of the constrained ductile reinforcement and at the same time remain an appropriate degree of elastic constraint from the matrix [20].

Displacement controlled tensile tests were conducted using INSTRON with a displacement speed of 0.005 in/min. The wedge type grips were used to clamp the specimens and load train alignment was achieved by coupling the top grip to a universal joint. The load was recorded as a function of cross head displacement.

To obtain the intrinsic mechanical properties of Nb used, tensile and hardness tests were conducted on the as-received and processed Nb foils. The processed Nb foils were obtained from hot pressed  $\text{ZrO}_2$  coated Nb/ $\text{MoSi}_2$  composites by breaking all the  $\text{MoSi}_2$  on both sides of the Nb foil. This is not very difficult to do due to a relative weak bonding between Nb and  $\text{MoSi}_2$  at the presence of a  $\text{ZrO}_2$  coating layer (it is described in Section 3.2).

### III. Results and Discussion

#### 3.1 Mechanical Properties of Unconstrained Niobium

Properties measured from the processed Nb and as-received Nb are summarized in Table 1. The data show that strength of Nb has increased after hot pressing except for the 1.0 mm Nb foils, but the rate of strain hardening increased for all the niobium. Such changes are believed to be due

Table 1. Mechanical properties of the niobium used

| Processing condition                 | As received |       |       | Hot pressed<br>( $\text{ZrO}_2$ coated, 1400°C, 40 MPa for 1 hr) |       |       |
|--------------------------------------|-------------|-------|-------|--|-------|-------|
|                                      | 1.0         | 0.5   | 0.25  | 1.0  | 0.5   | 0.25  |
| Thickness of Nb foil (mm)            | 1.0         | 0.5   | 0.25  | 1.0  | 0.5   | 0.25  |
| Microhardness (HV)                   | 110         | 79.4  | 82.3  | 104  | 114   | 131   |
| Yield strength ( $\sigma_0$ , MPa)   | 204         | 121   | 123   | 180  | 211   | 236   |
| Tensile strength ( $\sigma_u$ , MPa) | 277         | 195   | 204   | 221  | 260   | 285   |
| Elongation ( $\delta$ )              | 0.403       | 0.523 | 0.468 | 0.317  | 0.175 | 0.103 |
| Strength coefficient (MPa)           | 454         | 353   | 370   | 356  | 363   | 386   |
| Strength hardening coefficient (n)   | 0.173       | 0.245 | 0.243 | 0.165  | 0.085 | 0.076 |
| $\sigma_0/\text{HV}$                 | 1.85        | 1.52  | 1.49  | 1.73   | 1.85  | 1.80  |
| $\sigma_u/\text{HV}$                 | 2.52        | 2.45  | 2.48  | 2.12   | 2.28  | 2.1   |

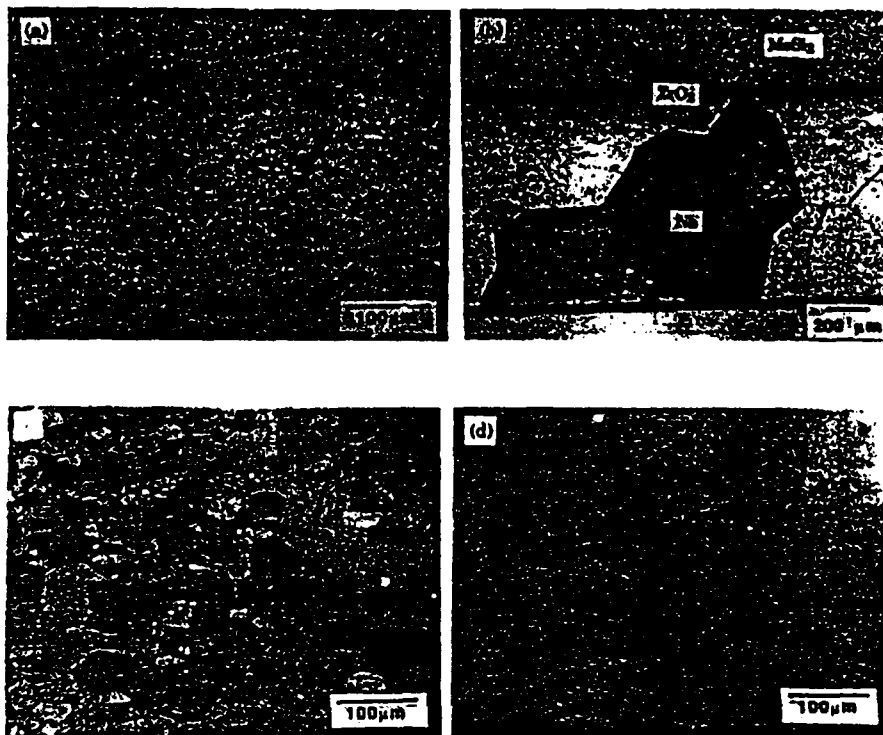


Fig. 2 Optical microstructures of Nb foils. (a) as-received, 1.0 mm thick; (b) processed, 1.0 mm thick; (c) as-received, 0.5 mm thick and (d) processed, 0.5 mm thick. Note that different magnifications are used.

to a combination of two competitive processes during hot pressing: (1) grain growth of Nb, as shown in Fig. 2; (2) solid solution strengthening because of the equilibrium of Nb with the silicides formed at the matrix/reinforcement interface, as shown in Fig. 3. For 1.0 mm Nb foils, grain size has changed from 15 to  $\sim 500 \mu\text{m}$ , which leads to a large decrease in strength and overshadows the increase due to the solid solution hardening. For 0.5 and 0.25 mm Nb foils, grain size has changed from 50 to  $\sim 370 \mu\text{m}$  and from 48 to  $\sim 300 \mu\text{m}$ , respectively. However, shorter diffusion distance to the center of the niobium has made solid solution hardening dominate over the softening due to the grain growth. Therefore, 0.5 and 0.25 mm Nb foils show an increased strength after hot pressing.

It is noted in Table 1 that the tensile strength and Vicker's hardness exhibit a definite relationship, i. e.,  $\sigma_y/HV$  equals to  $2.48 \pm 0.04$  and  $2.19 \pm 0.08$  for the as-received and processed Nb, respectively. Such definite relation has also been reported for other materials [21]. Ratio of the yield strength to the Vicker's hardness is also approximately a constant, as shown in Table 1. The results indicate that it is reasonable to infer the strength of the niobium from the hardness measured. Hardnesses of Nb hot pressed with different conditions are summarized in Table 2. The table shows that the hardnesses are almost the same for each group of Nb based on the size. Due to such hardness results, the stress-strain relations for the unconstrained uncoated and  $\text{Al}_2\text{O}_3$  coated Nb can be assumed to be the same as that of the processed Nb which is the  $\text{ZrO}_2$  uncoated Nb before  $\text{MoSi}_2$  on both sides of the Nb foils has been broken away.

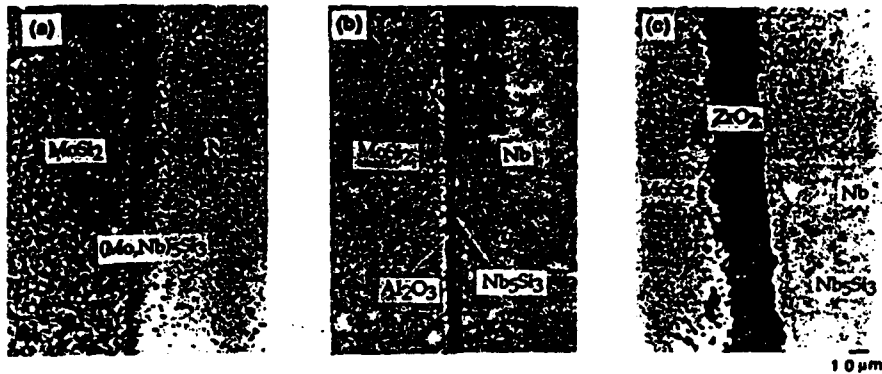


Fig. 3 Interfacial microstructures of (a) uncoated, (b)  $\text{Al}_2\text{O}_3$  coated and (c)  $\text{ZrO}_2$  coated Nb/MoSi<sub>2</sub> laminated composites.

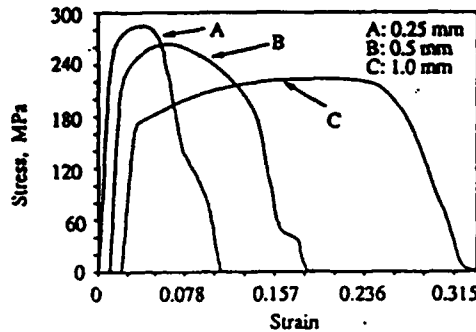


Fig. 4 Typical engineering stress-strain curves for three different thicknesses of the processed Nb foils.

Typical engineering stress-strain curves for different sizes of the processed Nb foils are shown in Fig. 4. As seen in the figure, strengths and rate of work hardening are different for different sizes of Nb. It is believed that such difference is mainly due to the differences in grain size and solid solution strengthening, as discussed above.

From the above discussion, it is clear that the intrinsic mechanical properties of the Nb reinforcement in the composites are different from those of the Nb before the compositing. It is believed that such change in properties due to hot compaction processing is a common phenomenon for ductile-phase-reinforced brittle matrix composites, because most of them have to be fabricated with high temperature processing techniques. Even in chemically compatible composites, change of grain size will cause property change of the ductile reinforcements. Such change imposes difficulty on the prediction and modeling of the composite properties.

### 3.2 Failure Mechanism and Related Observation on Constrained Niobium

An edge view of the unconstrained and constrained uncoated Nb foils after tensile test is shown in Fig. 5. As seen in the figure, Nb foils fail by drawing down to a wedge for both the constrained and unconstrained conditions. All three different sizes of Nb foils show the same failure mechanism, as shown in Fig. 5. Furthermore, such necking is also observed for all the coated Nb.

Details of the interfaces for the coated and uncoated foils are shown in Fig. 3. As seen in the figure, the coated foils contain three interfaces between the matrix and reinforcement:

Table 2. Microhardness of Nb with different processing conditions (hot pressed at  $1400^\circ\text{C}$ , 40MPa for 1 hr)

| Thickness of Nb foil (mm) | 1.0      |                                |                       | 0.5      |                                |                       | 0.25     |                                |                       |
|---------------------------|----------|--------------------------------|-----------------------|----------|--------------------------------|-----------------------|----------|--------------------------------|-----------------------|
| Processing condition      | Uncoated | $\text{Al}_2\text{O}_3$ coated | $\text{ZrO}_2$ coated | Uncoated | $\text{Al}_2\text{O}_3$ coated | $\text{ZrO}_2$ coated | Uncoated | $\text{Al}_2\text{O}_3$ coated | $\text{ZrO}_2$ coated |
| HV                        | 104      | 106                            | 104                   | 118      | 116                            | 114                   | 131      | 134                            | 131                   |

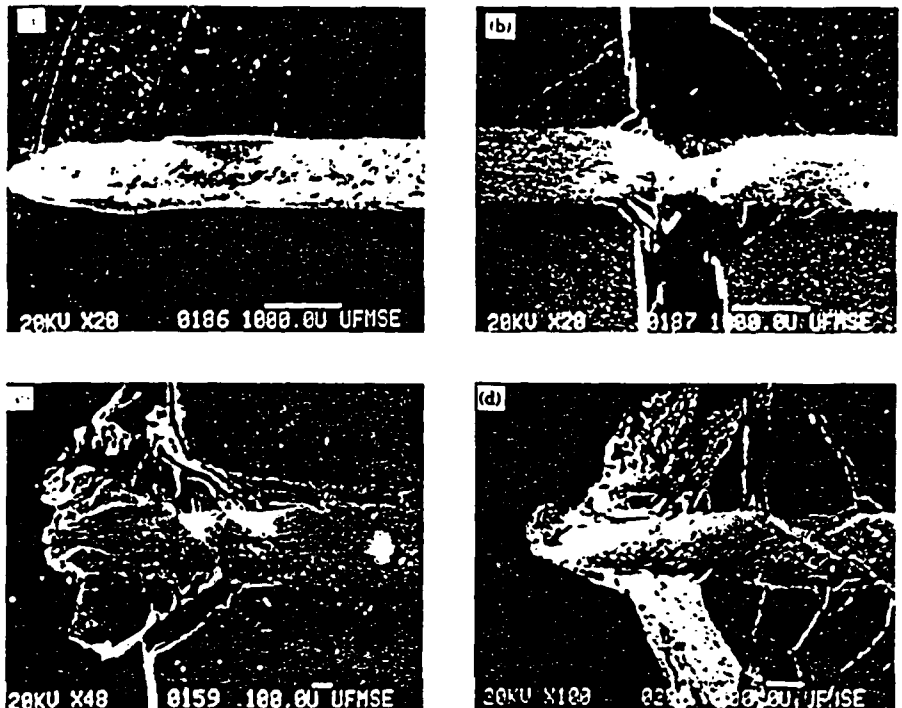


Fig. 5 An edge view of fractured specimens, showing contour of the neck. (a) is a unconstrained, processed Nb foil with a thickness of 1.0 mm, (b), (c) and (d) are constrained Nb with thicknesses of 1.0, 0.5 and 0.25 mm, respectively. Note that different magnifications are used.

MoSi<sub>2</sub>/coating/Nb<sub>5</sub>Si<sub>3</sub>/Nb; whereas, the uncoated foils contain two interfaces : MoSi<sub>2</sub>/(Mo,Nb)<sub>5</sub>Si<sub>3</sub>/Nb. Examination of the microstructures on the tested specimens show that decohesion of the Al<sub>2</sub>O<sub>3</sub> and ZrO<sub>2</sub> coated Nb from the matrix was largely due to debonding at the interfaces, as shown in Fig. 6, while decohesion in the uncoated Nb came largely from the matrix fracture, as shown in Fig. 5. This is in agreement with a related study [22], which shows that the uncoated interface has a higher interfacial fracture energy than the fracture energy of the matrix, while the oxide coated interfaces have a lower interfacial fracture energy than the matrix. Thus, it is expected the matrix would fracture before the interface fails in the case of the uncoated Nb, as contrasted with predominance of interfacial failure in the case of the coated Nb.

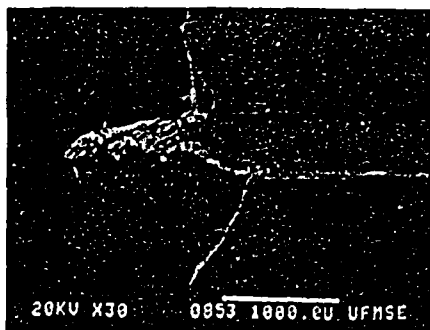


Fig. 6 An edge view of a fractured Al<sub>2</sub>O<sub>3</sub> coated Nb/MoSi<sub>2</sub> composites laminate, showing interfacial debonding.

Both interfacial failure and matrix fracture create a "gauge length" at the matrix/reinforcement interface which is virtually a region free from constraints of the matrix and is called decohesion length in the text. The measured decohesion lengths are

Table 3. Decohesion length in the MoSi<sub>2</sub>/Nb composites  
(hot pressed at 1400°C, 40MPa for 1 hour)

| Thickness of Nb foil (mm) | 1.0      |                                       |                         | 0.5       |                                       |                                      | 0.25        |                                       |                         |
|---------------------------|----------|---------------------------------------|-------------------------|-----------|---------------------------------------|--------------------------------------|-------------|---------------------------------------|-------------------------|
| Processing condition      | Uncoated | Al <sub>2</sub> O <sub>3</sub> coated | ZrO <sub>2</sub> coated | Uncoated  | Al <sub>2</sub> O <sub>3</sub> coated | ZrO <sub>2</sub> coated              | Uncoated    | Al <sub>2</sub> O <sub>3</sub> coated | ZrO <sub>2</sub> coated |
| Decohesion length (mm)    | 10 ± 5   | Decohesion all the way to the grips.  |                         | 2.9 ± 0.4 | 3.3 ± 0.4                             | Decohesion all the way to the grips. | 0.86 ± 0.09 | 0.94 ± 0.23                           | 1.30 ± 0.61             |

summarized in Table 3. The data show that within each size group, decohesion length increases from the uncoated to Al<sub>2</sub>O<sub>3</sub> coated and then to ZrO<sub>2</sub> coated Nb/MoSi<sub>2</sub> composites. Such results are consistent with the measurement of the interfacial fracture energy [22], which shows that the uncoated Nb/MoSi<sub>2</sub> has the highest interfacial fracture energy, followed by the Al<sub>2</sub>O<sub>3</sub> coated and then ZrO<sub>2</sub> coated Nb/MoSi<sub>2</sub> composites.

Increase of the decohesion length with the thickness of Nb foils, as shown in Table 3, is believed to be mainly related to the necking of the Nb. Fig. 7 shows schematically effect of the necking on the decohesion length. Length of the Nb region affected by necking, 2H, is proportional to the thickness of the Nb, as shown in Fig. 5. Approximately, H is 1.3 times of the thickness of Nb, measured from Fig. 5. Large lateral displacement of Nb in the necking affected region gives rise to large transverse stresses which lead to the interfacial debonding and/or matrix fracture. Thus, the thicker the niobium, the longer the necking affected region, and therefore the longer the decohesion length. If the interface bonding is relatively weak, such as the Al<sub>2</sub>O<sub>3</sub> and ZrO<sub>2</sub> coated interfaces, the transverse stresses aroused by lateral displacement of the Nb during uniform strain can be large enough to cause the interfacial debonding all the way to the test grips. During the uniform strain, the lateral displacement of Nb right at the interface is proportional to thickness of the Nb. Therefore, decohesion by this mechanism is easier to occur in thick Nb composites than in thin Nb counterparts, as indicated in Table 3.

The failure mechanism observed in the present study suggests that flow behavior of the constrained Nb can be simplified into three stages: (1) elastic deformation; (2) plastic deformation within the decohesion region; (3) localized plastic deformation within the necking region. Such processes are illustrated in Fig. 8. The crack opening of the matrix can be directly related to the deformation of Nb in the decohesion zone. At the early stage of crack opening, Nb only

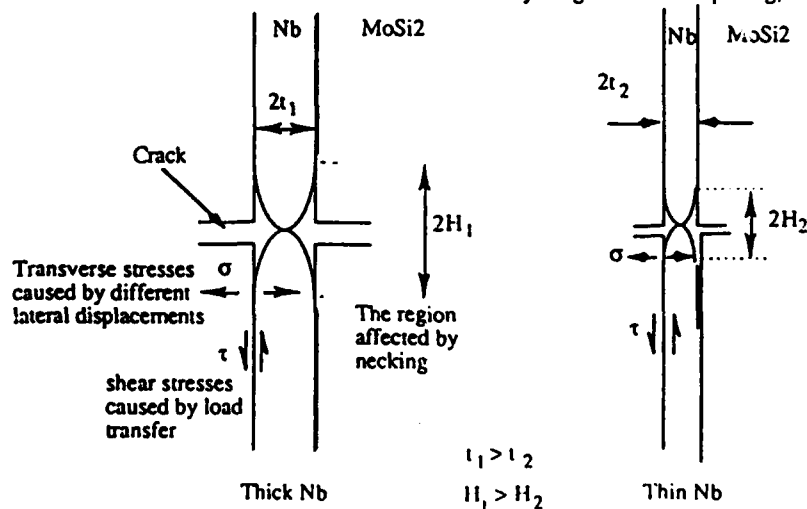


Fig. 7 A schematic showing effect of necking on the decohesion length.

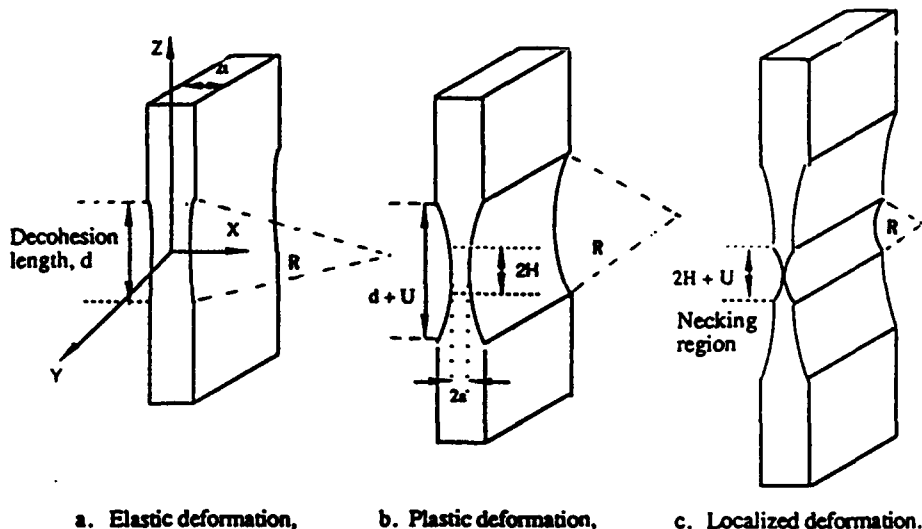


Fig. 8 A schematic of three stages of deformation for constrained Nb.  $2H$  is the length of the necking affected region,  $2a$  is remaining thickness of the reinforcement and  $U$  is displacement.

undergoes elastic deformation, as shown in Fig. 8a. As crack opening increases, Nb enters the stage of plastic deformation (Fig. 8b). At last, the work hardening rate of the niobium at the central portion of the decohesion region is lower than stress increase rate due to decrease in the cross section area of the reinforcement, the localized deformation begins (Fig. 8c), which lead to the final failure of the Nb lamina. Such simplified deformation processes can be used to model stress-displacement behavior of the constrained Nb, as presented in a related study [23].

### 3.3 Stress-Displacement Curves of Constrained Niobium

Fig. 9 shows typical stress-displacement curves for the uncoated Nb foils with different thicknesses constrained in  $\text{MoSi}_2$  matrix. The parameters measured are summarized in Table 4. The work of rupture normalized by the yield strength,  $\sigma_0$ , and half thickness of ductile phase,  $t$ ,

$$\int_0^{u^*} \frac{\sigma(U)}{\sigma_0} \frac{dU}{t}$$

is presented as  $E_1$  in the table and is called the normalized work of rupture in the text for convenience. As seen in the figure and table, due to the different intrinsic properties, the maximum stresses reached by the constrained Nb,  $\sigma_{\max}$ , are different for different sizes of Nb. However, if the  $\sigma_{\max}$  is normalized by its own yield strength, the normalized maximum stress,  $\sigma_{\max}/\sigma_0$ , exhibits an independence on size of Nb. This result suggests that the maximum stress reached is not a function of size of the ductile phase. It is noted that the work of rupture increases with size of Nb, indicating that large size of ductile reinforcement is more effective in improving toughness of the brittle matrix composites. Such size dependence of work of rupture is believed to be due to the increase of decohesion length with increasing size of the ductile phase. It is also noted that the normalized work of rupture shows a dependence on size of Nb.  $E_1$  increases with increasing size of the niobium. The size dependence of the normalized work of rupture is again attributed to the size dependence of the decohesion length [23]. This result suggests that the data of the normalized work of rupture obtained from the test on large size of ductile reinforcements

Table 4. Parameters measured from the uncoated Nb/MoSi<sub>2</sub> laminates

| 2t (mm) | $\sigma_{max}$ (MPa) | $\sigma_{max}/\sigma_0$ | $\xi$ (J/m <sup>2</sup> ) | $E_1$ |
|---------|----------------------|-------------------------|---------------------------|-------|
| 1.0     | 259                  | 1.44                    | 477,000                   | 5.3   |
| 0.5     | 320                  | 1.54                    | 239,000                   | 4.5   |
| 0.25    | 351                  | 1.49                    | 85,000                    | 2.8   |

Table 5. Parameters measured from the composites with 0.5 mm thick Nb lamina

| Processing condition                  | $\sigma_{max}$ (MPa) | $\sigma_{max}/\sigma_0$ | $\xi$ (J/m <sup>2</sup> ) | $E_1$ |
|---------------------------------------|----------------------|-------------------------|---------------------------|-------|
| uncoated                              | 320                  | 1.54                    | 239,000                   | 4.5   |
| Al <sub>2</sub> O <sub>3</sub> coated | 310                  | 1.47                    | 243,000                   | 4.6   |
| ZrO <sub>2</sub> coated               | 275                  | 1.31                    | 429,000                   | 8.1   |

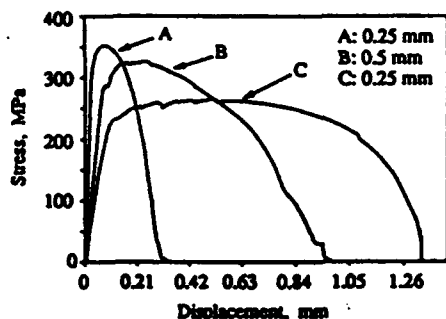


Fig. 9 Typical stress-displacement curves of constrained, uncoated Nb laminae with different thicknesses.

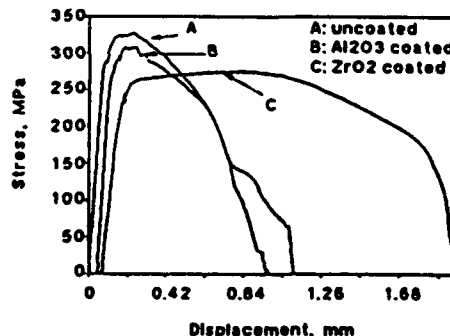


Fig. 10 Effect of the coatings on the stress-displacement curve, measured from composite laminates with 0.5 mm thick Nb lamina.

cannot be extended to small size of the reinforcements directly.

Effect of coatings on the stress-displacement curves is shown in Fig. 10. The parameters measured are summarized in Table 5. The data show that as the decohesion length increases, i.e., the constraints on the reinforcement decreases, the work of rupture increases. This is not surprising since the longer the decohesion length, the more ductile material participates in the plastic deformation, and therefore the more energy is consumed before fracture occurs. It is noted that as the decohesion length increases, the normalized maximum stress decreases, indicating that increasing constraints on the ductile phase increases the  $\sigma_{max}$ . This is consistent with theoretical analyses [11,13,16]. Table 5 also shows that the normalized work of rupture is dependent on the interfacial bonding strength. This is believed to be due to the increase of work of rupture with increasing decohesion length. The above results indicate that limited decohesion enhances the energy consumed to fracture the constrained ductile reinforcement, and therefore improves toughness of the composites.

#### IV. Concluding Remarks

The present set of experiments demonstrate that flow behavior of constrained ductile reinforcement depends strongly on the intrinsic properties and size of the reinforcement and the properties of the matrix/reinforcement interface. The maximum stress reached by the constrained reinforcement increases as the strength of the reinforcement and constraints increase. Constraints, indicated by decohesion length, are found to be related to the interfacial properties and size of the reinforcement. Decohesion length increases from the uncoated to the oxide coated laminates and increases with increasing size of the reinforcement. Dependence of decohesion length on size of the reinforcement is attributed to the dependence on size of the reinforcement of the length of the necking affected region and the lateral displacement difference between the matrix and reinforcement at the interface. The results indicate that both weak interface and large size of reinforcement improve toughness of the composites.

The normalized work of rupture,  $E_1$ , is found dependent on size of the reinforcement.  $E_1$  decreases with decreasing size of the reinforcement and increases with decohesion length. This result suggests that more work needs to be done before the data of the normalized work of rupture obtained from the test on large size of ductile reinforcements can be extended to small size of the the reinforcements.

Based on the observation, the flow behavior of the constrained reinforcement has been simplified into three stages: (1) elastic deformation; (2) plastic deformation within the decohesion region; (3) localized plastic deformation within the necking region. Such simplified deformation processes enable the modeling of the stress-displacement relation to be implemented.

**Acknowledgements** --- The author is deeply indebted to Dr. Reza Abbaschian for his constant guidance, support and encouragement. The financial support of the Defense Advanced Research Projects (DARPA) through contract MDA972-88-J-1006 is gratefully appreciated.

#### References

1. J. L. Chermant and F. Osterstock, *J. Mater. Sci.*, 1976, vol. 11, pp. 1939-51.
2. J. Gurland, *Trans. ASM*, 1958, vol. 50, pp. 1063-71.
3. A. V. Virkar and D. L. Jognson, *J. Am. Ceram. Soc.*, 1977, vol. 60, pp. 514-19.
4. D. T. Rankin, *J. Am. Ceram. Soc.*, 1971, vol. 54, pp. 277-81.
5. P. Hing and G. W. Groves, *J. Mater. Sci.*, 1972, vol. 7, pp. 427-34.
6. V. V. Kristie and P. S. Nicholisin, *J. Am. Ceram. Soc.*, 1981, vol. 64, pp. 499-504.
7. C. K. Elliott, G. R. Odette, G. E. Lucas and J. W. Shekherd, High Temperature, High Performance Composites, edited by F. D. Lemkey et al., *MRS Proc.*, 1988, vol. 120, pp. 95-102.
8. E. Fitzer, Whisker and Fiber-Toughened Ceramics, edited by R. A. Bradley, D. E. Clark, D. C. Larsen and J. O. Sügler, (ASM International TM, 1988), pp. 165-83.
9. L. Xiao, Y. S. Kim and R. Abbaschian, Intermetallic Matrix Composites, Edited by D. L. Anton, P. L. Martin, D. B. Miracle and R. McMeeking, *MRS Proc.*, 1990, vol. 194, pp. 399-404.
10. L. R. F. Rose, *J. Mech. Phys. Solids*, 1987, vol.35, pp. 383-405.
11. L. S. Sigl, P. A. Mataga, B. J. Dalgleish, R. M. McMeeking and A. G. Evans, *Acta Metall.*, 1988, vol.36, pp. 945-53.
12. A. G. Evans and R. M. McMeeking, *Acta Metall.*, 1986, vol.34, pp. 2435-41.
13. P. A. Mataga, *Acta Metall.*, 1989, vol.37, pp. 3349-59.
14. B. Budiansky, J. C. Amazigo and A. G. Evans, *J. Mech. Phys. Solids*, 1988, vol.36, pp. 167-87.
15. J. R. Rice, Fracture, edited by H. Liebowitz, 1968, vol. 2, pp.191-311.
16. M. F. Ashby, F. J. Blunt and M. Bannister, *Acta Metall.*, 1989, vol. 37, pp. 1847-57.
17. H. C. Cao, B. J. Salgleish, H. E. Deve, C. Elliott, A. G. Evans, R. Mehrabien and G. R. Odette, *Acta Metall.*, 1989, vol. 37, pp. 2969-77.
18. H. E. Deve, A. G. Evans, G. R. Odette, R. Mehrabien, M. L. Emiliani and R. J. Hecht, *Acta Metall.*, 1990, vol. 38, pp. 1491-1502.
19. L. Xiao and R. Abbaschian, "On the Strength and Stiffness of Ductile Phase Reinforced  $MoSi_2$  Composites", to be published in Advanced Metal Matrix Composites for Elevated Temperatures, Proc. in 1991 TMS Fall Meeting, Cincinnati, OH, Oct. 1991.
20. L. Xiao and R. Abbaschian, "Evaluating A Technique for Determining the Toughening of Brittle Matrix by Ductile Reenforcement", to be published in Advanced Metal Matrix Composites for Elevated Temperatures, Proc. in 1991 TMS Fall Meeting, Cincinnati, OH, Oct. 1991.
21. F. C. Lea, Hardness of Metals, Charles Griffin and Company, Ltd, 42 Drury Lane, W. C. 2., London, 1936, pp. 91-105.
22. L. Xiao and R. Abbaschian, "Role of Matrix/Reinforcement Interfaces in the Fracture Toughness of Brittle Materials Toughened by Ductile Reinforcements", presented in TMS Fall Meeting, Cincinnati, OH, Oct. 22, 1991.
23. L. Xiao, "Study of the Flow Behavior of Constrained Ductile Phases ---- II. Modeling", published in this Proceedings.

## STUDY OF THE FLOW BEHAVIOR OF CONSTRAINED DUCTILE PHASES

### ..... II. MODELING

Lingang Xiao

Department of Materials Science and Engineering, University of Florida,  
Gainesville, FL 32611

#### Abstract

Brittle materials can be toughened by incorporating ductile reinforcements into them. To evaluate the toughening by ductile reinforcements, it is necessary to know the stress-displacement relation of the ductile phase constrained by the brittle matrix. In the present study, based on the observations from tensile tests on the specimens of a single Nb lamina imbedded in MoSi<sub>2</sub> matrix, an analytical model is developed which gives insight into the influence on the stress-displacement curve of yield strength, work hardening, matrix/reinforcement interfacial bonding strength and size of the reinforcement. A characteristic decohesion length, which is a function of size of the reinforcement, has been identified by the model and related to the measured decohesion length. The results allow the extrapolation of the work of rupture measured from large size of constrained ductile phases to small size of the ductile phases. As the reinforcements used in composites are usually smaller in size than those tested in such tensile tests, the extrapolation of the work of rupture allows the contribution of ductile reinforcements to the toughness of a brittle matrix composite to be calculated.

## I. Introduction

It has been established that substantial toughening of brittle matrices can be achieved by incorporating ductile reinforcements [1-9]. The primary toughening mechanism of ductile reinforcement has been attributed to the bridging of ductile ligaments [10-14], although the ductile reinforcements may also increase toughness by crack deflection and by trapping mechanisms. The contribution to fracture toughness from bridging can be estimated by extending cohesive force model [15] to ligament bridging [11,12] and can be written as

$$\Delta G = v_f \int_0^{U^*} \sigma(U) dU \quad \dots\dots\dots (1)$$

where  $\sigma(U)$  is the nominal stress carried by the constrained ductile reinforcement for a given crack opening  $U$ ,  $v_f$  is volume fraction of the ductile reinforcement,  $U^*$  is the crack opening at the point when the ductile reinforcement fails, and the definite integral, designated as  $\xi$  in the text, is the work of rupture of the constrained ductile ligament. Thus, the key point to predict the increased fracture toughness is to calculate  $\sigma(U)$  as a function of crack opening. Due to the difference between  $\sigma(U)$  and that measured in a simple tensile test, several investigators have attempted to relate  $\sigma(U)$  to the uniaxial stress-strain properties of the ductile phase. The methods used included a slip line field analysis [11,12], finite element methods [11,13], spring models [10,14] and geometric models [11,13,16]. Their results indicated that  $\sigma(U)$  was dependent on the intrinsic properties of the ductile phase and the constraint conditions. However, direct comparison of stress-displacement curves between the models and experimental results is not very satisfying in magnitude, although the general trends are the same for the models and experiments. The extrapolation of the work of rupture measured from large size of constrained ductile phases to small size of the ductile phases also needs to be investigated.

The present study is aimed to model the stress-displacement relation and to examine the feasibility of extrapolation of the work of rupture measured from large size of constrained ductile phases to small size of the ductile phases. Based on the observations from tensile tests on the specimens of a single Nb lamina imbedded in MoSi<sub>2</sub> matrix, an analytical model is developed which gives insight into the influence on the stress-displacement curve of yield strength, work hardening, matrix/reinforcement interfacial bonding strength and size of the reinforcement. A characteristic decohesion length, which is a function of size of the reinforcement, has been identified by the model and related to the measured decohesion length. The results allow the extrapolation of the work of rupture measured from large size of constrained ductile phases to small size of the ductile phases and allows the contribution of ductile reinforcements to the toughness of a brittle matrix composite to be calculated.

The symbols used in the text are defined in Table 1.

## II. Modeling

### 2.1 Experimental Observations

It has been shown [17,18] that the failure of the constrained Nb laminae in MoSi<sub>2</sub> matrix involves the following scenario. When an advancing crack just impinges a Nb reinforcement, no debonding at the matrix/reinforcement interface occurs. As external load continues to increase, debonding at the interface and/or multiple fracture of the matrix near the interface occur due to a relatively large lateral deformation of the Nb reinforcement compared to the matrix and load transfer from the matrix to the reinforcement. Then come the necking and fracture of the niobium as the load continues to increase. The observations [17] lead to a simplified flow behavior of the constrained Nb which can be divided into three stages: (1) elastic deformation; (2) plastic deformation within the decohesion region; (3) localized plastic deformation within the necking region. Such deformation processes are illustrated in Fig. 1. At the early stage of crack opening, Nb only undergoes elastic deformation, as shown in Fig. 1a. As crack opening increases, Nb enters the stage of plastic deformation (Fig. 1b). At last, the work hardening rate of the niobium

at the central portion of the decohesion region is lower than stress increase rate due to decrease in the cross section area of the reinforcement, the localized deformation begins (Fig. 1c), which lead to the final failure of the Nb lamina.

In the present study, displacement of the stress-displacement curve is assumed to only come from the deformation of Nb lamina inside the decohesion region because the Nb outside the decohesion region is bonded to the matrix and only undergoes elastic deformation. Contour of the Nb lamina in the decohesion region is assumed to be part of the outside surface of a cylinder with a varied radius of R for all the stages of the deformation, as shown in Fig. 1. Such assumption is a good approximation to the real contour of the Nb observed in the experiments [17] and makes the calculation possible. To generate data of the nominal axial stress-displacement curve ( $\sigma$ -U), U is measured as the axial displacement of the matrix point at the boundary of the decohesion region, while  $\sigma$  is computed from the total force exerted on the remaining cross section of the midplane at the neck, normalized by the original midplane area. Plane strain is assumed for the computation in all the stages.

Table 1. Symbols and definition

|                    |   |
|--------------------|---|
| 2a                 | remaining thickness of reinforcement  |
| d                  | decohesion length   |
| d <sub>c</sub>     | characteristic decohesion length  |
| d <sub>m</sub>     | measured decohesion length  |
| E                  | Young's modulus   |
| E <sub>t</sub>     | normalized work of rupture  |
|                    | $\int_0^{u^*} \frac{\sigma(U) dU}{\sigma_0 t}$                                    |
| $\epsilon_t$       | true strain   |
| $\bar{\epsilon}_x$ | mean strain in x-direction at the midplane of the neck during elastic deformation |
| $\Delta G$         | increment in toughness caused by ductile reinforcement                            |
| 2H                 | length of reinforcement affected by necking                                       |
| n                  | work hardening coefficient  |
| $\mu$              | Poisson's ratio   |
| R                  | radius of contour of the neck   |
| $\sigma$           | stress  |
| $\bar{\sigma}$     | effective stress  |
| $\sigma_0$         | yield strength  |
| $\sigma_{max}$     | maximum stress reached by constrained reinforcement                               |
| $\sigma_y$         | yield stress of constrained reinforcement   |
| $\sigma_{za}$      | stress in z-direction at the free surface of neck                                 |
| 2t                 | initial thickness of reinforcement  |
| U                  | axial extension equal to crack-opening displacement                               |
| U*                 | crack opening displacement at failure of ductile reinforcement                    |
| V <sub>f</sub>     | volume fraction of ductile reinforcement  |
| $\xi$              | work of rupture, $\int_0^{u^*} \sigma(U) dU$                                      |

The true stress-strain relations of the Nb laminae used in the calculation are

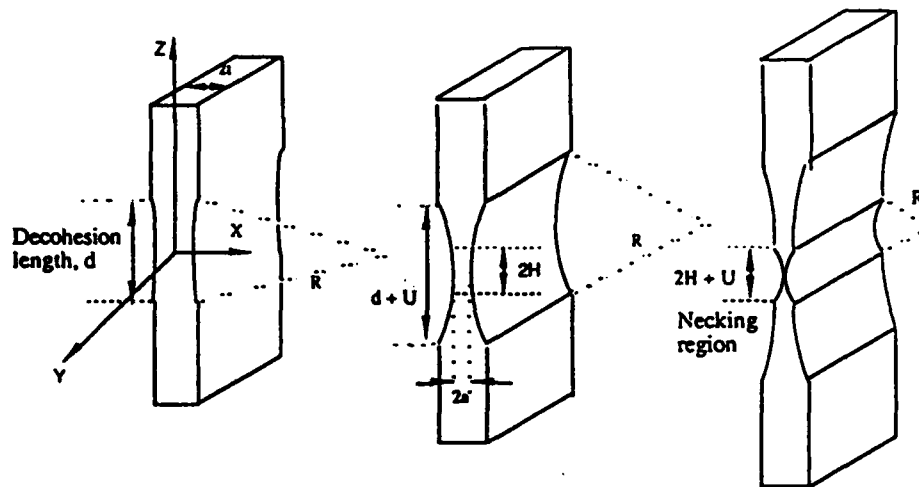
$$\begin{aligned} \sigma_t &= 356 \epsilon_t^{0.165} \text{ (MPa)} && \text{for 1.0 mm Nb} \\ \sigma_t &= 363 \epsilon_t^{0.085} \text{ (MPa)} && \text{for 0.5 mm Nb} \\ \sigma_t &= 386 \epsilon_t^{0.076} \text{ (MPa)} && \text{for 0.25 mm Nb} \end{aligned} \quad \dots\dots\dots (2)$$

The above equations are obtained from the direct measurement on the unconstrained hot pressed Nb which is different from the Nb prior to the compositing because of change of the properties of the Nb during hot compaction. Use of the above equations allow us to compare the model to the experiment directly. Details of the measurement of the true stress-strain relations for the unconstrained hot pressed Nb can be found in Reference [17]. The yield strengths,  $\sigma_0$ , of three different sizes of Nb laminae measured are also different due to different grain sizes and solid solution strengthening [17]. The yield strengths are 180, 211 and 236 MPa for Nb laminae with a thickness of 1.0, 0.5 and 0.25 mm, respectively.

### 2.2 Stage of Elastic Deformation

To compute  $\sigma$ -U data for elastic deformation, two more assumptions are made: (1) the volume-conserving nature of large scale plastic deformation is also applicable to this stage; (2) the effective stress across the midplane of the neck is constant.

Assumption (1) and the assumed contour relate the displacement, U, to the radius of the cylinder, R, as



a. Elastic deformation, b. Plastic deformation, c. Localized deformation.

Fig. 1 A schematic of three stages of deformation for constrained Nb.

$$R = \frac{(d + U)^3}{12 \tau U} + \frac{4}{3} \frac{\tau U}{(d + U)} \quad \dots \quad (3)$$

Assumption (2) renders Bridgman formula for a necking plate [19]

$$\sigma_z \left( \frac{x}{a} \right) = \sigma_x \left( \frac{x}{a} \right) \cdot \left[ R + \frac{a}{2} \left( 1 - \frac{x^2}{a^2} \right) \frac{\partial \sigma_x}{\partial x} \right] \quad \dots \quad (4)$$

computable even for elastic deformation.  $x$  and  $a$  in the above equation are defined in Fig. 1. Although the assumed contour and constant effective stress do not represent the real situation of the decohesion region, they introduce negligible error to the work of rupture (see the Appendix).

With the assumption (2), boundary conditions at the neck and plane strain assumption, the stress component  $\sigma_z$  at the midplane of the neck can be related to the stress  $\sigma_{2a}$ , which is  $\sigma_z$  at the free surface of the neck, as follows

$$\sigma_{2a}^2 = \sigma_x^2 + \sigma_z^2 - \frac{(1 + 2\mu - 2\mu^2)}{(1 - \mu + \mu^2)} \sigma_x \sigma_z \quad \dots \quad (5)$$

Introduction of the Poisson's ratio of Nb ( $\mu=0.39$ ) into eq. (5) yields

$$\sigma_z = 0.968 \sigma_x + \sigma_{2a} \quad \dots \quad (6)$$

Substituting eq. (6) into eq. (4) and solving for  $\sigma_x$  yield

$$\sigma_x = \sigma_{2a} \left[ 31.25 - 31.25 \frac{\left( \frac{R}{a} \right)^{0.032}}{\left( \frac{R}{a} + \frac{1}{2} - \frac{x^2}{2a^2} \right)^{0.032}} \right] \quad \dots \quad (7)$$

where  $\sigma_{2a}$  is related to the average strain,  $\bar{\epsilon}_x$ , measured from the neck with the following

equation

$$\begin{aligned} \bar{\epsilon}_x &= \frac{\int_0^a \epsilon_x(\sigma_x, \sigma_y, \sigma_z) dx}{a} \\ &= \sigma_{2a} \frac{1}{aE} \left[ 9.5579 a - \int_0^a \frac{10.1 \left(\frac{R}{a}\right)^{0.032}}{\left(\frac{R}{a} + \frac{1}{2} - \frac{x^2}{2a^2}\right)^{0.032}} dx \right] \dots\dots\dots (8) \end{aligned}$$

where E is Young's modulus of Nb, and  $\bar{\epsilon}_x$  can be measured from the dimension of the neck using the relation of  $\bar{\epsilon}_x = \ln(a/t)$ . Thus, by numerical integration of eq. (8),  $\sigma_{2a}$  can be found for any specific R and a. Using eqs. (3), (6), (7) and (8),  $\sigma$ -U data can be calculated for the elastic deformation.

### 2.3 Stage of Plastic Deformation

Von Mises yield criterion is used to monitor the initial yielding. Thus, when the effective stress reaches the yield strength of the Nb, plastic deformation begins. Now, Bridgman formula for a necking plate [19]

$$\sigma_z = \sigma_{2a} \left\{ 1 + \ln \left[ 1 + \frac{1}{2} \frac{a}{R} \left( 1 - \frac{x^2}{a^2} \right) \right] \right\} \dots\dots\dots (9)$$

can be used directly to compute the nominal axial stress. By applying boundary conditions at the neck, a relation between  $\sigma_{2a}$  and the effective stress,  $\bar{\sigma}$ , can be found, which is

$$\sigma_{2a} = 1.1547 \bar{\sigma} \dots\dots\dots (10)$$

where  $\bar{\sigma}$  is determined by the effective strain.

In the computation, the effective strain at the initial yield is assigned as zero, while the effective stress has a value of the yield strength of the unconstrained Nb. After the initial yield, the niobium is assumed to be perfect isotropy of strain hardening and the power law, eq. (2), is used to compute the effective stress.

### 2.4 Stage of Localized Plastic Deformation

The localized plastic deformation is assumed to begin when the nominal axial stress is about to decrease. The length of the region affected by necking, 2H, shown in Fig.1, is chosen as 2t. After necking down to a point at the neck, the region with such dimension gives two triangles with the height equal to the base. The base is assumed to have no more deformation when the localized deformation begins. The assumptions give rise to a contour as shown in Fig. 1c, and such contour is an approximation for the contour of Nb in the decohesion region observed in the experiments [17]. The displacement in the stage of the localized deformation is assumed to come only from the deformation of the necking affected region and the computation of the nominal axial stress is carried out using eqs. (9) and (10).

## III. Results of the Model

### 3.1 Effect of the Decohesion Length

Dependence of the stress-displacement curve on the decohesion length is shown in Fig. 2 which

Table 2. Decohesion length in the MoSi<sub>2</sub>/Nb composites (hot pressed at 1400°C, 40MPa for 1 hour)

| Thickness of Nb foil (mm) | 1.0      |                                       | 0.5                     |           |                                       | 0.25                                 |          |                                       |                         |
|---------------------------|----------|---------------------------------------|-------------------------|-----------|---------------------------------------|--------------------------------------|----------|---------------------------------------|-------------------------|
| Processing condition      | Uncoated | Al <sub>2</sub> O <sub>3</sub> coated | ZrO <sub>2</sub> coated | Uncoated  | Al <sub>2</sub> O <sub>3</sub> coated | ZrO <sub>2</sub> coated              | Uncoated | Al <sub>2</sub> O <sub>3</sub> coated | ZrO <sub>2</sub> coated |
| Decohesion length (mm)    | 10 ± 5   | Decohesion all the way to the grips.  |                         | 2.9 ± 0.4 | 3.3 ± 0.4                             | Decohesion all the way to the grips. |          | 0.94 ± 0.23                           |                         |

is generated using the true stress-strain data of 0.5 mm Nb. The results indicate that the maximum stress reached by the constrained Nb,  $\sigma_{max}$ , increases with increasing constraints on the ductile reinforcement; but increasing constraints decreases the work of rupture. Such results suggest that a relatively weak bond at the interface enhances the work of rupture and therefore is conducive to toughness of the brittle matrix composites. Similar results are obtained by other investigators using different models [11,13,16].

When the data measured in the experiment [17], as shown in Table 2, are put into the model, the results show that the maximum stresses are nearly constant for each size of Nb, although the work of rupture increases with increasing decohesion length. The work of rupture normalized by the yield strength,  $\sigma_0$ , and half thickness of ductile phase,  $t$ ,

$$\int_0^{u^*} \frac{\sigma(U) dU}{\sigma_0 t}$$

called as the normalized work of rupture,  $E_t$ , in the text, also exhibit an increase with increasing decohesion length. The computed parameters for the constrained Nb lamina with a thickness of 0.5 mm are summarized in Table 3. The results suggest that the present coated and uncoated Nb/MoSi<sub>2</sub> laminates are in the range of low constraints because in the high constraint range (i.e., short decohesion length),  $\sigma_{max}$  is very sensitive to the decohesion length, as shown in Fig. 2. An experimental evidence indicating that the present laminates are in the range of low constraints is that the maximum stress reached by the laminate composites with 1.0 mm Nb lamina are almost the same for different decohesion lengths ranging from ~ 5 to ~ 15 mm.

### 3.2. Effect of Reinforcement Size

A comparison on the size effect between the model and experiments for the uncoated Nb/MoSi<sub>2</sub> laminates is showed in Fig. 3. The input data for the model are from eq. (2) and Table 2 with each size of Nb having its own measured parameters and properties. The input of Young's

Table 3. Calculated parameters for the composite laminates with 0.5 mm thick Nb lamina

| Processing condition                  | $\sigma_{max}$ (MPa) | $\sigma_{max}/\sigma_0$ | $\xi$ (J/m <sup>2</sup> ) | $E_t$ |
|---------------------------------------|----------------------|-------------------------|---------------------------|-------|
| uncoated                              | 329.3                | 1.56                    | 196,000                   | 3.707 |
| Al <sub>2</sub> O <sub>3</sub> coated | 328.4                | 1.55                    | 203,000                   | 3.860 |
| ZrO <sub>2</sub> coated               | 328.2                | 1.55                    | 339,000                   | 6.435 |

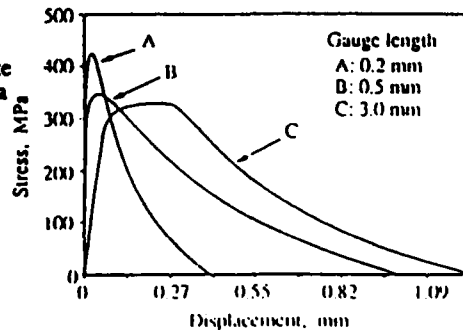


Fig. 2 Effect of decohesion length on the stress displacement curves

Table 4. Summary of parameters calculated from the model and measured for the uncoated Nb/MoSi<sub>2</sub> laminates

| 2t<br>(mm) | Calculated              |                         |                              |       | Measured                |                         |                              |       |                         |
|------------|-------------------------|-------------------------|------------------------------|-------|-------------------------|-------------------------|------------------------------|-------|-------------------------|
|            | $\sigma_{max}$<br>(MPa) | $\sigma_{max}/\sigma_0$ | $\xi$<br>(J/m <sup>2</sup> ) | $E_t$ | $\sigma_{max}$<br>(MPa) | $\sigma_{max}/\sigma_0$ | $\xi$<br>(J/m <sup>2</sup> ) | $E_t$ | $E_{t(cal)}/E_{t(exp)}$ |
| 1.0        | 292                     | 1.62                    | 400,000                      | 4.4   | 259                     | 1.44                    | 477,000                      | 5.3   | 0.838                   |
| 0.5        | 329                     | 1.56                    | 196,000                      | 3.7   | 320                     | 1.54                    | 239,000                      | 4.5   | 0.814                   |
| 0.25       | 354                     | 1.50                    | 88,000                       | 2.9   | 351                     | 1.49                    | 85,000                       | 2.8   | 1.025                   |

modulus is from the slope of the stress-strain curve of the unconstrained Nb in a simple tensile test. As shown in Fig. 3, the model fits the experimental data reasonably well except the stage of the localized plastic deformation. The deviation in this stage is believed to be due to the difference between the real and assumed contours of the neck. The parameters calculated from the model are summarized in Table 4. For comparison the measured parameters [17] are also included in the table. Ratios of the calculated and measured normalized work of rupture,  $E_{t(cal)}/E_{t(exp)}$ , is also included in the table. It is noted that the calculated maximum stress, the work of rupture and the normalized work of rupture are all close to the measured counterparts. It is quite clear that the maximum stress, the work of rupture and the normalized work of rupture can be estimated from the model.

Reinforcements used in composites are usually smaller in size than those tested in the present study. To predict the work of rupture for small size of reinforcements, it is necessary to know the decohesion length in advance for computation of the model. A plot of  $\sigma_{max}$  vs decohesion length computed from the model for the composites with 0.25 mm Nb lamina is shown in Fig. 4. It is noted that there exists a characteristic decohesion length,  $d_c$ , below which  $\sigma_{max}$  becomes very sensitive to the decohesion length. Computation of the model shows that the characteristic decohesion length is equal to twice of the thickness of the niobium and the normalized work of rupture with the characteristic decohesion length, called as the characteristic normalized work of rupture, is constant regardless of size of the reinforcement.

The measured decohesion lengths,  $d_m$ , in the present study are all larger than  $d_c$ . However, ratio of  $d_m$  to  $d_c$  is found to be a linear function of size of the reinforcement, as shown in Fig. 5. The relations found are

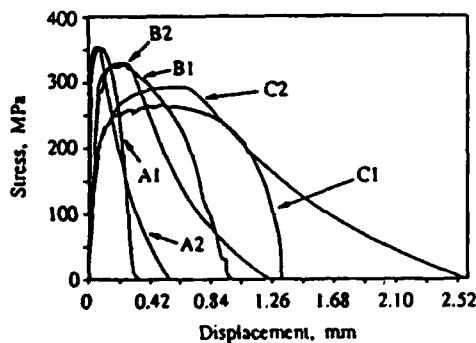


Fig. 3 Effect of reinforcement size on the stress displacement curve. A1, B1 and C1 are experimental curves of the composites with 0.25, 0.5 and 1.0 mm thick Nb laminae, respectively; A2, B2 and C2 are results from the model for composites with 0.25, 0.5 and 1.0 mm thick Nb laminae, respectively.

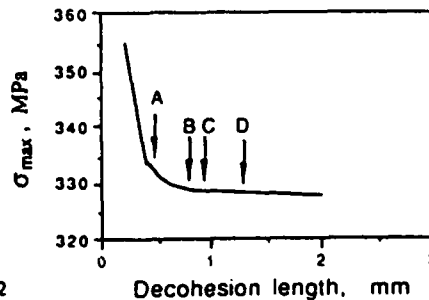


Fig. 4 A plot of  $\sigma_{max}$  vs decohesion length. Arrow A shows characteristic decohesion length, and arrows B, C and D show the measured decohesion lengths of the composites containing uncoated, Al<sub>2</sub>O<sub>3</sub> coated and ZrO<sub>2</sub> coated Nb laminae, respectively.

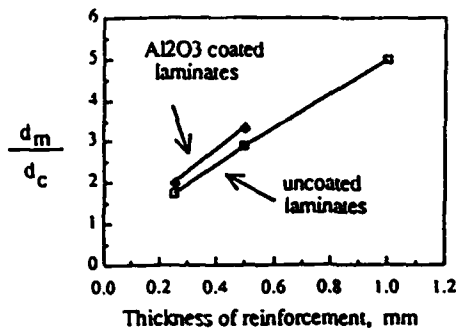


Fig. 5 A plot of ratio of the measured to characteristic decohesion length as a function of reinforcement size.

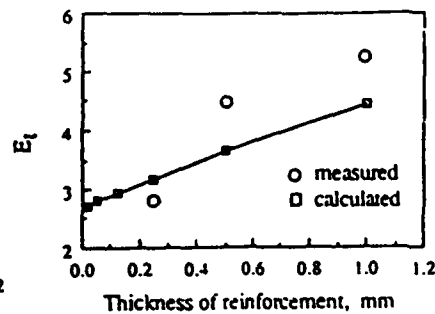


Fig. 6 Normalized work of rupture as a function of reinforcement size.

$$\begin{aligned} d_m/d_c &= 0.66 + 10.72 t && \text{(for Al}_2\text{O}_3 \text{ coated laminates)} \\ d_m/d_c &= 0.66 + 8.70 t && \text{(for uncoated laminates)} \end{aligned}$$

$$\dots\dots\dots (11)$$

It is noted that  $d_m$  becomes closer to  $d_c$  as size of the reinforcement decreases, suggesting that the normalized work of rupture becomes smaller and closer to the characteristic normalized work of rupture. The oxide coating changes the slope of the line, indicating that the coating enhances decohesion and such effect becomes larger as size of the reinforcement increases. With eq. (11), the decohesion length of small size of the reinforcement can be predicted and the work of rupture be calculated from the model. A plot generated in this way is shown in Fig. 6 which shows that  $E_t$  decreases with decreasing size of the reinforcement, as found in the experiments [17]. Thus, to estimate the contribution of ductile reinforcements to the toughness of a brittle matrix composite, the model can be used.

### 3.3 Effect of Yield Strength and Work Hardening

Effects of yield strength and work hardening on the work of rupture are evaluated by putting the properties of several different materials into the model. The properties are obtained from Reference [20] and the true stress-strain curves for some materials are shown in Fig. 7. It is noted that both 4340 steel and 70/30 brass have a higher work hardening rate than the Nb used in the present study. The computed stress-displacement curves are shown in Fig. 8, and the input and output data are summarized in Table 5. It is clear that work of rupture increases with increasing work hardening rate. Although 70/30 brass has the lowest yield strength, its high work hardening rate enables it to have a much higher work of rupture than both 4340 steel and Nb both of which have a higher yield strength than the brass. Reason for such phenomenon is that a high work hardening rate reinforcement have a higher increase rate in the load-carrying ability, and instability (i.e., the localized plastic deformation within the necking region), therefore, comes relatively later than a low work hardening rate reinforcement, when the two

Table 5. The input and output data for computing the stress-displacement curves shown in Fig. 8 (the thickness of all materials is assumed as 0.5 mm)

| Material       | Input Data                          |                     |            |       | Output Data             |                              |       |
|----------------|-------------------------------------|---------------------|------------|-------|-------------------------|------------------------------|-------|
|                | $\sigma_t = K\epsilon_t^n$<br>(MPa) | $\sigma_0$<br>(MPa) | E<br>(GPa) | $\mu$ | $\sigma_{max}$<br>(MPa) | $\xi$<br>(J/m <sup>2</sup> ) | $E_t$ |
| Nb             | $363\epsilon_t^{0.085}$             | 210                 | 105        | 0.39  | 329                     | 196.000                      | 3.7   |
| SAE 4340 steel | $642\epsilon_t^{0.15}$              | 230                 | 193        | 0.29  | 496                     | 351.000                      | 6.1   |
| 0.6% C steel   | $1573\epsilon_t^{0.10}$             | 500                 | 199        | 0.29  | 1337                    | 801.000                      | 6.4   |
| 70/30 brass    | $897\epsilon_t^{0.49}$              | 80                  | 111        | 0.30  | 483                     | 662.000                      | 33.1  |

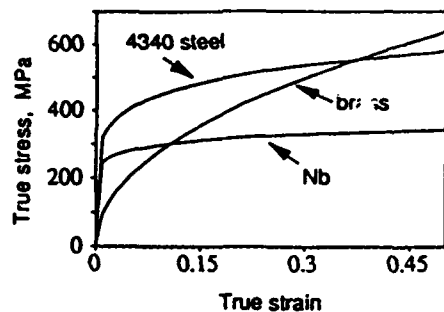


Fig. 7 The true stress-strain curves of the some materials used for evaluating effects of yield strength and work hardening.

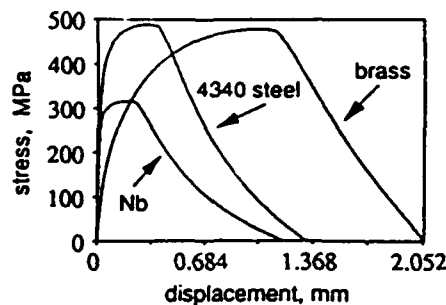


Fig. 8 Computed stress-displacement curves using the data in Fig. 7 and Table 5.

reinforcements have the same increase rate in stress due to decrease in the cross-sectional area of the reinforcements. Thus, high work hardening rate reinforcements have a relatively longer stage of plastic deformation in the whole decohesion region, leading to more energy to be dissipated and higher work of rupture. It is noteworthy that the brass has a very high normalized work of rupture, which suggests that the normalized work of rupture could probably be used as an indicator of the efficiency with which the work hardening contributes to enhancing the work of rupture.

When yield strength is very high, such as 0.6 % C steel in Table 5, work of rupture would be also very high. As shown in Table 5, 0.6% C steel has a much higher work of rupture than 70/30 brass although it has a lower work hardening rate than the brass. Contribution of yield strength to work of rupture is mainly to increase the maximum stress reached by the constrained reinforcement. From the above discussion, it is concluded that both high work hardening rate and yield strength are beneficial to work of rupture. Work hardening is more effective in enhancing the work of rupture than yield strength because high work hardening rate delays the instability of deformation for constrained ductile reinforcements, therefore more material of the reinforcements participates in plastic deformation and more energy has to be consumed.

#### IV. Concluding Remarks

Based on the observation, the flow behavior of the constrained reinforcement has been divided into three stages: (1) elastic deformation; (2) plastic deformation within the decohesion region; (3) localized plastic deformation within the necking region. An analytical model has been developed to describe these three stages. The model gives insight into the influence of decohesion, yield strength, work hardening and size of the reinforcement on the stress-displacement curve. The overall shape of the  $\sigma$ - $U$  curves generated by the model fits the measured curves reasonably well.

Computation of the model indicates that work of rupture is enhanced by a relatively weak bond at the matrix/reinforcement interface, by large size of reinforcement, and by a high yield strength and high work hardening rate. High work hardening rate is more effective in enhancing work of rupture than high yield strength.

Computation of the model suggests that there is a characteristic decohesion length,  $d_c$ , with which the normalized work of rupture,  $E_t$  is constant regardless of size of the reinforcement. It is found that the deviation of the measured decohesion length from  $d_c$  increases with increasing size of the reinforcement, which leads to  $E_t$  increases with increasing size of the reinforcement. A relation between  $d_m$  and  $d_c$  is found which allows the prediction of the real decohesion length for small size of the reinforcement and therefore the calculation of the work of rupture for

specific size of the reinforcement.

**Acknowledgements** --- The author is deeply indebted to Dr. Reza Abbaschian for his constant guidance, support and encouragement. The financial support of the Defense Advanced Research Projects (DARPA) through contract MDA972-88-J-1006 is gratefully appreciated.

#### References

1. J. L. Chermant and F. Osterstock, *J. Mater. Sci.*, 1976, vol. 11, pp. 1939-51.
2. J. Gurland, *Trans. ASM*, 1958, vol. 50, pp. 1063-71.
3. A. V. Virkar and D. L. Jognson, *J. Am. Ceram. Soc.*, 1977, vol. 60, pp. 514-19.
4. D. T. Rankin, *J. Am. Ceram. Soc.*, 1971, vol. 54, pp. 277-81.
5. P. Hing and G. W. Groves, *J. Mater. Sci.*, 1972, vol. 7, pp. 427-34.
6. V. V. Kristie and P. S. Nicholas, *J. Am. Ceram. Soc.*, 1981, vol. 64, pp. 499-504.
7. C. K. Elliott, G. R. Odette, G. E. Lucas and J. W. Sheckherd, *High Temperature, High Performance Composites*, edited by F. D. Lemkey et al., *MRS Proc.*, 1988, vol. 120, pp. 95-102.
8. E. Fitzer, *Whisker- and Fiber-Toughened Ceramics*, edited by R. A. Bradley, D. E. Clark, D. C. Larsen and J. O. Stiegler, (*ASM International TM*, 1988), pp. 165-83.
9. L. Xiao, Y. S. Kim and R. Abbaschian, *Intermetallic Matrix Composites*, Edited by D. L. Anton, P. L. Martin, D. B. Miracle and R. McMeeking, *MRS Proc.*, 1990, vol. 194, pp. 399-404.
10. L. R. F. Rose, *J. Mech. Phys. Solids*, 1987, vol.35, pp. 383-405.
11. L. S. Sigl, P. A. Mataga, B. J. Dalgleish, R. M. McMeeking and A. G. Evans, *Acta Metall.*, 1988, vol.36, pp. 945-53.
12. A. G. Evans and R. M. McMeeking, *Acta Metall.*, 1986, vol.34, pp. 2435-41.
13. P. A. Mataga, *Acta Metall.*, 1989, vol.37, pp. 3349-59.
14. B. Budiansky, J. C. Amazigo and A. G. Evans, *J. Mech. Phys. Solids*, 1988, vol.36, pp. 167-87.
15. J. R. Rice, *Fracture*, edited by H. Liebowitz, 1968, vol. 2, pp.191-311.
16. C. A. Anderson and M. K. Aghajanian, *Ceram. Eng. Sci. Proc.*, 1988, vol. 9, pp. 621-26.
17. L. Xiao, "Study of the Flow Behavior of Constrained Ductile Phases --- I. Experiment", published in this Proceedings.
18. L. Xiao and R. Abbaschian, "Role of Matrix/Reinforcement Interfaces in the Fracture Toughness of Brittle Materials Toughened by Ductile Reinforcements", presented in TMS Fall Meeting, Cincinnati, OH, Oct. 22, 1991.
19. P. W. Bridgman, *Studies in Large Plastic Flow and Fracture*, 1st ed., McGraw-Hill Book Comp., Inc., New York, NY, 1952, pp. 32-37.
20. G. E. Dieter, Jr., *Mechanical Metallurgy*, McGraw-Hill Kogakusha, Ltd., Tokyo, 1961, p. 248.

#### Appendix

Finite element analysis (FEA) of the stress distribution across the neck and the contour of the decohesion region during the elastic deformation was implemented using the finite element software package ANSYS. Due to the symmetry, only one quarter of the specimen was analyzed using two-dimensional 4-node isoparametric elements with an assumption of plane strain deformation. A typical finite element model for the constrained Nb is shown in Fig. 9. The displacement at the midplane of the neck was allowed only in the x-direction, and the bonded boundary of Nb to the matrix and the axial central plane were allowed to displace only in z-direction, as shown in Fig. 9.

Results from the FEA for the case of constrained 1.0 mm Nb lamina with 2.28 mm decohesion length under a nominal axial stress of 150 MPa are presented in Figures 10-12. Fig. 10 compares the assumed contour of the decohesion region with the FEA result. The data show that the assumed contour deviates from the FEA result, leading to a smaller crack opening displacement compared to the finite element analysis. However, the difference is so small that it introduces negligible errors to the computation of the work of rupture.

Evaluation of effective stress distribution across the midplane of the neck is shown in Fig. 11.

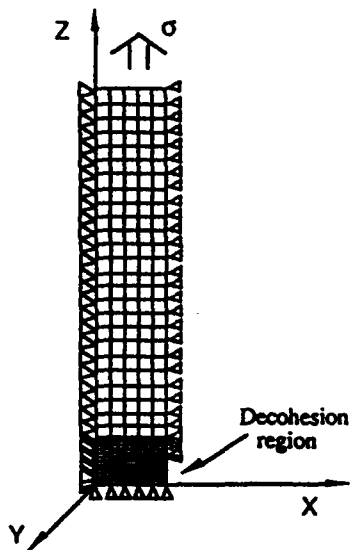


Fig. 9 Mesh and boundary conditions used for analysis of constrained Nb.

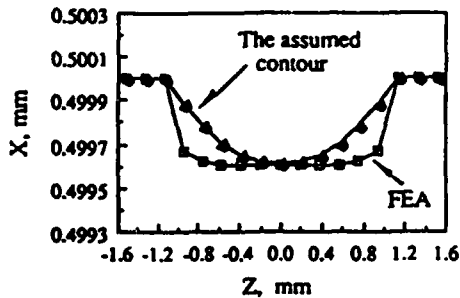


Fig. 10 A comparison between the assumed contour and finite element analysis of decohesion region during the stage of elastic deformation. X and Z are defined in Fig. 17.

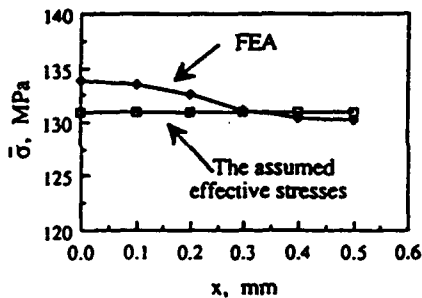


Fig. 11 Effective stress distribution at the midplane of neck.

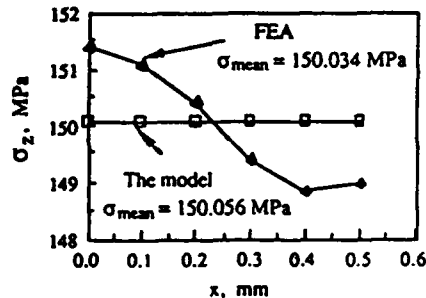


Fig. 12 A comparison of the axial stresses at the midplane of neck between the model and FEA. Note that mean axial stresses,  $\sigma_{mean}$ , are almost the same.

Clearly, the effective stress is not constant across the midplane, but increases from the free surface to the center of the neck. Although the assumed constant effective stress does not represent the real stress distribution, the mean axial stresses across the midplane are almost the same for the model and FEA, as shown in Fig. 12. The axial stress calculated from the model increases monotonously from the free surface to the center, which is hard to tell from Fig. 12 because of the scale used. Similar results were also obtained from calculation of constrained 0.25 and 0.5 mm Nb laminae. Thus, it is concluded that the assumed constant effective stress and contour of the decohesion region impose negligible errors on the calculation of  $\sigma$ -U curve and the work of rupture.

# Role of Matrix/Reinforcement Interfaces in the Fracture Toughness of Brittle Materials Toughened by Ductile Reinforcements

L. XIAO and R. ABBASCHIAN

Crack interactions with ductile reinforcements, especially behavior of a crack tip at the interface, have been studied using  $\text{MoSi}_2$  composites reinforced with Nb foils. Effects of fracture energy of interfaces on toughness of the composites have also been investigated. Variation of interfacial bonding was achieved by depositing an oxide coating or by the development of a reaction product layer between the reinforcement and matrix. Toughness was measured using bend tests on chevron-notched specimens. It has been established that as a crack interacts with a ductile reinforcement, three mechanisms compete: interfacial debonding, multiple matrix fracture, and direct crack propagation through the reinforcement. Decohesion length at the matrix/reinforcement interface depends on the predominant mechanism. Furthermore, the results add to the evidence that the extent to which interfacial bonding is conducive to toughness of the composites depends on the criterion used to describe the toughness and that ductility of the ductile reinforcement is also an important factor in controlling toughness of the composites. Loss of ductility of the ductile reinforcement due to inappropriate processing could result in little improvement in toughness of the composites.

## I. INTRODUCTION

THE interface between matrix and reinforcements plays an important role in the mechanical performance of composites. It is commonly accepted that a relatively weak interface is desirable for improving fracture toughness of brittle materials reinforced by ceramic fibers.<sup>[1-4]</sup> The reason for this is that such an interface when present in the path of an advancing crack would fail locally and blunt the crack. Otherwise, if the interface is strong, the propagating crack is unlikely to "see" the fiber and little improvement in toughness will be realized. This toughening concept has become a dogma in design of brittle materials to be reinforced by ceramic fibers. However, when the reinforcement is a ductile fiber with a high strain to failure, the requirement for the interfacial bonding may be different. This is because occurrence of fracture for the two different fibers is based on different criteria. For a brittle fiber, the occurrence of fracture is simply based on the magnitudes of the maximum tensile stresses which are enhanced by the presence of stress concentration. In contrast, since ductile fibers can yield locally by dislocation slip and thus blunt the crack, the fracture occurs only after exhaustion of ductility of the fiber in the presence of triaxial stresses at the crack tip (particularly in plane strain). As such, there may be different requirements for the interfaces in ductile-fiber-reinforced brittle matrix composites.

The responsibility for the ductile phase toughening has been attributed to bridging of intact ligaments of the ductile phase behind the advancing crack tip.<sup>[5-12]</sup> Based on this mechanism, the increased toughness of the composites in the case of small-scale bridging can be related

to the work of stretching and fracturing the ductile phases,  $\Delta G$ , by the following equation:<sup>[6,9]</sup>

$$\Delta G = V_f \int_0^{u^*} \sigma(u) du \quad [1]$$

where  $u$  is the crack opening,  $\sigma(u)$  the nominal stress on the ligament,  $u^*$  the crack opening at the end of the traction zone, and  $V_f$  the area fraction of reinforcements on the crack plane. It is clear that the increased toughness depends on the stress-displacement function of the ductile ligament,  $\sigma(u)$ , which in turn relies on the extent of decohesion at the matrix/reinforcement interface and can be determined independently using a simple tensile test on a single constrained ductile reinforcement.<sup>[7,12-16]</sup> These experiments indicated that a high work of rupture of ductile reinforcements was encouraged by a partial decohesion at the interface.<sup>[7,12-13]</sup> Deve *et al.*,<sup>[16]</sup> however, found that whether or not extensive decohesion was desirable for a high work of rupture depended on the work-hardening capability of the reinforcements, suggesting that contributions of decohesion were complicated and interdependent with other material properties. Theoretical analysis of stress-displacement function,  $\sigma(u)$ , has also been attempted. Numerical models<sup>[3,4]</sup> showed that partial decohesion was beneficial to a high work of rupture, and therefore, a high toughness. Similar conclusions have also been drawn from analytical models.<sup>[6,7,17]</sup>

In the present work, effects of interfacial coating and decohesion on the toughness of ductile-phase-reinforced brittle matrix composites were measured directly using a four-point bend test on chevron-notched specimens rather than measuring the stress-displacement function and deducing the toughness increment *via* Eq. [1]. The composite system selected for the investigation was laminated  $\text{MoSi}_2$  matrix reinforced with coated or uncoated Nb foils. The composite system was selected, because  $\text{MoSi}_2$  is

L. XIAO, Research Assistant, and R. ABBASCHIAN, Chairman and Professor, are with the Department of Materials Science and Engineering, University of Florida, Gainesville, FL 32611.

Manuscript submitted November 12, 1991.

among the most promising candidates for high-temperature structural applications. In addition, the two components used have similar coefficients of thermal expansion, thus minimizing the residual thermal stresses and simplifying the fracture toughness analysis. The use of Nb foil rather than filaments allowed for the ease of producing the composites with controlled properties, but it still served the main purpose of the present study.

## II. EXPERIMENTAL

### A. Measurement of Fracture Toughness

Disc-shaped laminated composites were produced by hot pressing MoSi<sub>2</sub> powder (-325 mesh) with 20 vol pct of coated or uncoated Nb foils at 1400 °C for 1 hour or 1700 °C for 40 minutes under a pressure of 40 MPa. In order to minimize residual thermal stresses, the hot-pressed discs were held in the hot-pressing chamber at 800 °C for 1 hour before cooling down to room temperature. The thickness of the Nb foils was 0.25 mm. The interface coatings were produced by depositing Al<sub>2</sub>O<sub>3</sub> or ZrO<sub>2</sub> to the Nb surface prior to the hot pressing or by the development of a reaction product layer between the matrix and reinforcement. Details of the coating procedures can be found in Reference 18.

One way to evaluate the ductile phase toughening is to generate a resistance curve (*R*-curve) of the composites, as done by Elliott *et al.*<sup>[19]</sup> and Venkateswara Rao *et al.*<sup>[20]</sup> To generate this curve, however, the dimensions of the specimens should be at least as large as the bridging length. For the present model composites, based on the equilibrium stress distribution across the crack face, the bridging length has been estimated to be at least 50 mm.<sup>[21]</sup> To avoid using such a large specimen, the toughness of the present composites was measured by four-point bending of chevron-notched specimens.<sup>[22,23]</sup> The samples had inner and outer spans of 10 and 20 mm, respectively, and were tested using a hydro-servo-controlled MTS with a crosshead speed of  $4 \times 10^{-4}$  mm/s. In order to prepare the chevron-notched bending specimens, the hot-pressed discs were cut into rectangular bars with dimensions of  $3.81 \times 5.08 \times 25.4$  mm. The notch on each sample was cut perpendicular to the foil plane using a diamond wafering blade. To investigate interactions between cracks and reinforcements, some specimens were unloaded at various levels of load during the bending tests. A cross section perpendicular to the chevron notch of the unloaded specimens was cut, polished, and examined using scanning electron microscopy (SEM) to measure decohesion length and the crack geometry and position.

The peak load of the bending tests was used to calculate fracture toughness with the aid of the following equation:<sup>[22]</sup>

$$K_{max} = \frac{P_{max}}{B\sqrt{W}} Y_{min}^* \quad [2]$$

where  $P_{max}$  is the maximum test load,  $B$  and  $W$  the width and height of the bending bar, respectively, and  $Y_{min}^*$  the minimum value of the dimensionless stress intensity factor coefficient as a function of relative crack length for

the particular specimen used. The present experiments revealed that  $P_{max}$  was reached when the crack was inside the chevron. However, because of the rising crack-growth resistance for ductile-phase-toughened composites,  $P_{max}$  and  $Y_{min}^*$  do not occur coincidentally at the same crack length, and therefore,  $P_{max}$  does not exactly correspond to the stress-intensity factor at failure but is a good approximation to it.<sup>[23,24,25]</sup> Thus, the value calculated using Eq. [2] is called "damage tolerance" in this article and is designated as  $K_{max}$  rather than  $K_{Ic}$ .

### B. Interface Fracture Energy Measurement

The measurement of the fracture energy of matrix/reinforcement interfaces was conducted on chevron-notched short bars using the procedures recommended in Reference 26. The technique involves determining the critical stress intensity factor from the peak load of the notched bars and then converting the critical stress intensity factor to the fracture energy of the interface (bond toughness of the interface). In the present study, however, a modified specimen geometry, as shown in Figure 1, was used. An advantage of the present geometry is that there is no need for compliance calibration due to symmetry of compliance of the specimen with respect to the interface.

The short bar specimens were produced by hot pressing. The hot-pressing temperature and coating procedures were the same as for preparing the composite laminates mentioned in Section A. The Nb foils used for the short bar specimens were 0.127 mm<sup>thick</sup> and the notch was cut parallel to the foil using a diamond wafering blade with a thickness of 0.4 mm. The thickness of the notch was chosen to be slightly larger than that of the foil to insure that the initiation and propagation of the crack were at the weakest positions among various interfaces between matrix/coating/reinforcement.

The fracture energy of the interface,  $G_{max}$ , was calculated using the following equation:<sup>[26]</sup>

$$G_{max} = \frac{K_{Icr}^2}{E} \quad [3]$$

where  $E$  is the elastic modulus of MoSi<sub>2</sub> and  $K_{Icr}$  is the critical stress intensity factor determined from the peak load of the short bar bending test.

### C. Tensile Tests on a Single Constrained Reinforcement

A schematic of a tensile test specimen used to determine the crack behavior near the reinforcement is shown in Figure 2. The specimens, consisting of a single Nb foil sandwiched between two MoSi<sub>2</sub> layers, were produced by hot pressing with the same processing conditions as for the composite laminates and short bar specimens. The straight-through notches on the MoSi<sub>2</sub> matrix were introduced using a diamond wafering blade with a thickness of 0.15 mm. The tensile specimens were polished on both sides perpendicular to the Nb foil before testing. The specimens were unloaded at various levels of load during testing and examined with SEM to observe the interactions and behavior of ductile reinforcement at the near-tip region.

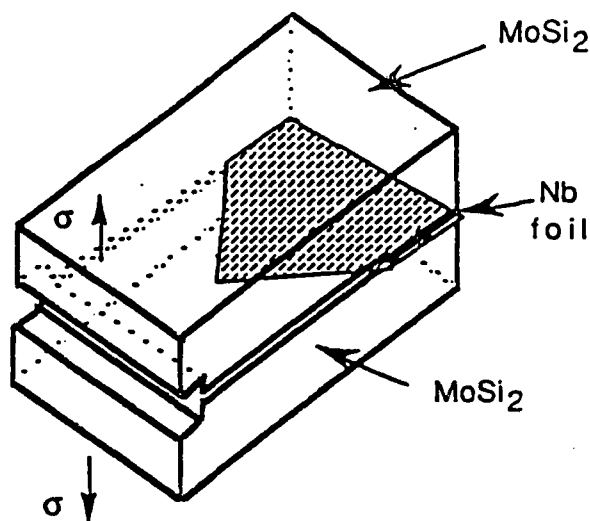


Fig. 1—Short bar specimen geometry.

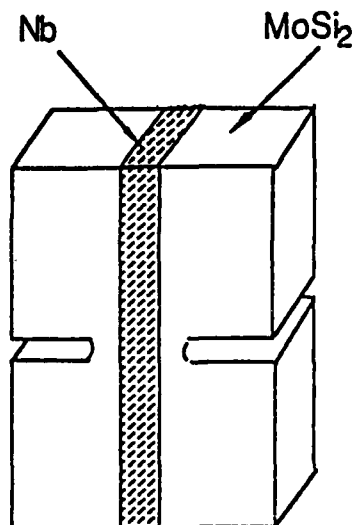


Fig. 2—Schematic of a composite laminate tensile test specimen.

### III. RESULTS AND DISCUSSION

#### A. Fracture Energy of Interfaces

Microstructures of the matrix/reinforcement interfaces for the coated and uncoated foils are shown in Figure 3. The thicknesses of  $\text{Al}_2\text{O}_3$  and  $\text{ZrO}_2$  coatings produced are about 5 and 25  $\mu\text{m}$ , respectively. For the uncoated foils, as shown in Figure 3(a), the interaction between the matrix and reinforcement causes formation of  $(\text{Mo}, \text{Nb})_3\text{Si}_2$ , the thickness of which depends on the compositing and annealing conditions.<sup>[10]</sup> For the coated foils, no interaction between the composite constituents was observed. However, because of the diffusion of Si through the coatings, a  $\text{Nb}_3\text{Si}_2$  layer was produced near the surface of the foil. Therefore, as can be seen in the figure, the coated foils contain three interfaces between

the matrix and reinforcement:  $\text{MoSi}_2/\text{coating}/\text{Nb}_3\text{Si}_2/\text{Nb}$ ; whereas, the uncoated foils contain two interfaces:  $\text{MoSi}_2/(\text{Mo}, \text{Nb})_3\text{Si}_2/\text{Nb}$ .

When the hot-pressing temperature was 1400 °C, the interfaces between the uncoated Nb and  $\text{MoSi}_2$  became  $\text{MoSi}_2/(\text{Nb}, \text{Mo})\text{Si}_2/\text{Nb}_3\text{Si}_2/\text{Nb}$ . Detailed mechanisms of the interphase formation for the uncoated Nb/ $\text{MoSi}_2$  system at different temperatures are described in Reference 27. Despite the different interfacial microstructures, mechanical behavior was observed to be the same for the specimens hot-pressed at 1400 °C and 1700 °C. For the  $\text{ZrO}_2$  coated Nb, the same interfacial microstructure was produced at both hot-pressing temperatures. However, for the  $\text{Al}_2\text{O}_3$  coated Nb, the coating became discontinuous when the hot-pressing temperature was 1700 °C. Such phenomenon has been attributed to the Kirkendall shift caused by the extensive Si diffusion across the coating.<sup>[10]</sup>

A typical load-displacement curve of the chevron-notched short bar for a  $\text{ZrO}_2$  coated Nb/ $\text{MoSi}_2$  laminate is shown in Figure 4. Some stable crack propagation has been achieved, as indicated by the fluctuation in the curve near the maximum load. Therefore, the maximum load was used to calculate  $G_{\text{max}}$  with the aid of Eq. [3]. The corresponding fracture surface at the chevron crack is also presented in Figure 4. By examining both fracture surfaces of a broken sample with SEM and an energy-dispersive spectrometer (EDS), the failure location at the interface was determined. The measured fracture energies of interfaces and failure locations for the uncoated and coated Nb/ $\text{MoSi}_2$  composites are summarized in Table I. In the case of coated Nb systems, failure occurred along the oxide/ $\text{Nb}_3\text{Si}_2$  interface or inside the oxide coating. For the uncoated system, on the other hand, the failure was observed to take place inside  $\text{MoSi}_2$  rather than at the interfaces or inside the interphases formed, indicating that the interfacial region has a higher toughness than the matrix. Indeed, the value of  $G_{\text{max}}$  of  $\text{MoSi}_2$  measured in the present study is 33.7  $\text{J}/\text{m}^2$ , and all the measurements conducted on  $\text{MoSi}_2/\text{uncoated Nb}$  system showed that fracture energies for failure of the notched short bars were about 36.4  $\text{J}/\text{m}^2$  because the crack in  $\text{MoSi}_2$  failed to follow the chevron-notched plane strictly. The data in Table I also show that the fracture energy of the interface has been reduced by the oxide coatings. Furthermore, the zirconia coating exhibits a lower fracture energy of the interface than the alumina. This is attributed to the existence of residual tensile stresses in the zirconia coating caused by the thicker coating layer and a higher coefficient of thermal expansion of the zirconia than that of the matrix and reinforcement.

#### B. Behavior of Cracks at the Interface

Details of cracks impinging on Nb foils for uncoated and coated composite systems are shown in Figure 5. The micrographs were taken from the cross sections of laminated composites unloaded at about 20 pct of the peak load of the composites during the four-point bending tests. It is noted from the figures that debonding at the interface does not occur when a crack approaches the interface or just impinges on it for both uncoated and coated reinforcement systems. Similar observations were

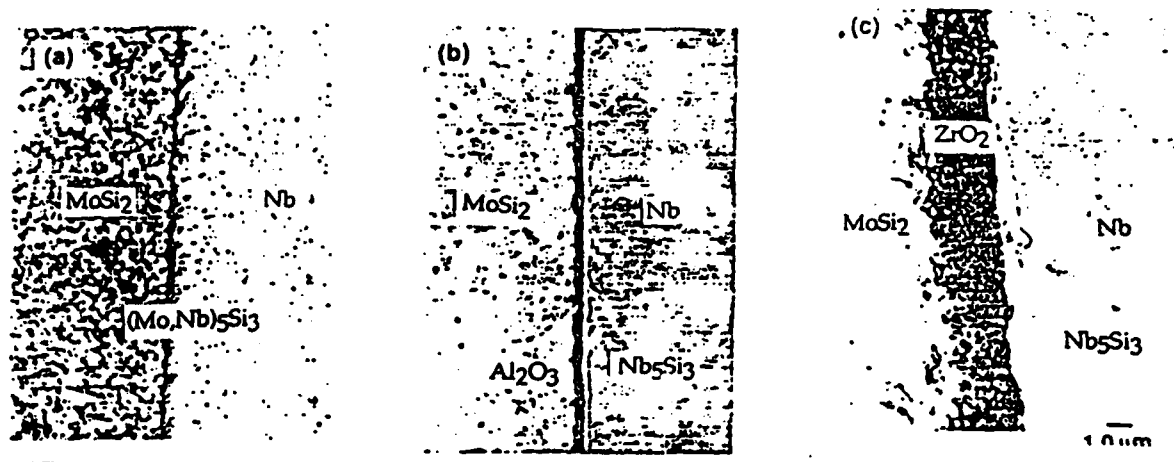


Fig. 3—Interfacial microstructures of the laminated composites reinforced by (a) uncoated Nb, hot-pressed at 1700 °C; (b) Al<sub>2</sub>O<sub>3</sub> coated Nb, hot-pressed at 1400 °C; and (c) ZrO<sub>2</sub> coated Nb, hot-pressed at 1700 °C.

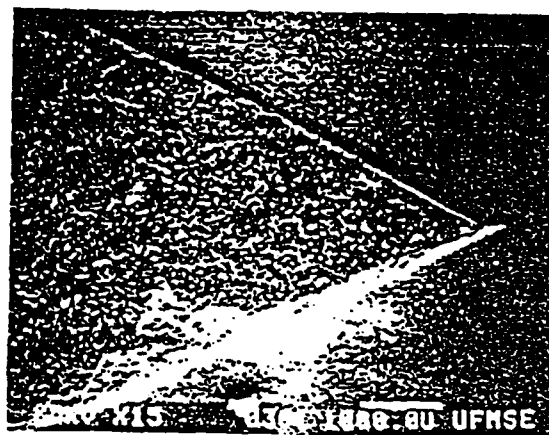
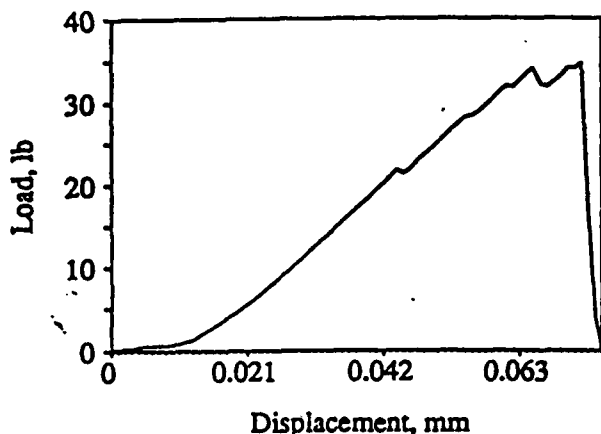


Fig. 4—A typical load-displacement curve of the chevron notched short bar for a ZrO<sub>2</sub> coated Nb/MoSi<sub>2</sub> laminate and the corresponding fracture surface at the chevron crack.

Table I. Fracture Energy of Interfaces in Coated and Uncoated Nb/MoSi<sub>2</sub> Systems\*

| System  | Processing Conditions | Failure Location   | Fracture Energy of Interface ( $G_{max}$ , J/m <sup>2</sup> ) |
|---|-----------------------|--|---|
| MoSi <sub>2</sub> /uncoated Nb                              | 1400 °C and 1700 °C   | inside the MoSi <sub>2</sub>   | $>33.7 \pm 1.4$   |
| MoSi <sub>2</sub> /Al <sub>2</sub> O <sub>3</sub> coated Nb | 1400 °C               | Al <sub>2</sub> O <sub>3</sub> /Nb <sub>5</sub> Si <sub>3</sub> interface                  | $16.1 \pm 1.3$  |
| MoSi <sub>2</sub> /ZrO <sub>2</sub> coated Nb               | 1400 °C and 1700 °C   | ZrO <sub>2</sub> /Nb <sub>5</sub> Si <sub>3</sub> interface or inside the ZrO <sub>2</sub> | $12.8 \pm 1.0$  |

\*Four specimens for each condition were tested.

made from tensile tests on a single constrained Nb foil. This is not surprising, since all the fracture energies of the interfaces measured in the present study are higher than 1/5 of the matrix fracture energy. The observation is consistent with an estimation made by Cook and Gordon.<sup>(20)</sup> They found that for an elliptical crack, an interfacial fracture energy of 1/5 or less of the matrix fracture energy would cause interfacial debonding in advance of the crack.

Figure 6 shows a typical microstructure of an uncoated Nb tensile test specimen. A notch tip can be seen at the left side of Figure 6(a), which shows that a crack initiates at the notch tip and ends at the Nb foil. Figure 6(b) is a close-up of one of the crack tips in Figure 6(a). As seen in the figure, the impingement of the crack on the interface causes local dislocation slip of the reinforcement instead of interfacial failure, leading to the release of the stress concentration. In addition, there are also

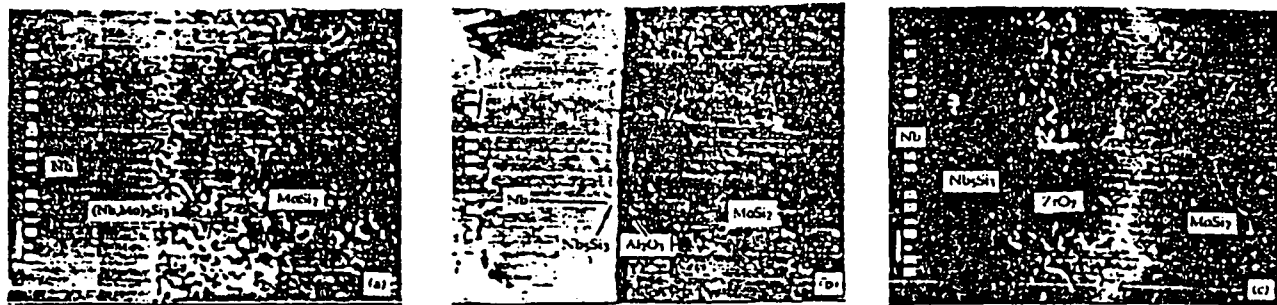


Fig. 5—Optical microstructures of composite laminates showing that cracks end at the front of the reinforcement without causing interfacial debonding. (a) Uncoated Nb, (b)  $\text{Al}_2\text{O}_3$  coated Nb, and (c)  $\text{ZrO}_2$  coated Nb reinforced composites.

multiple cracks at the interface which add to relaxation of tip stress intensity and effectively enlarge the initial plastic zone in the ductile phase. The result shows that interfacial failure is not the only mechanism of blunting cracks in the case of ductile reinforcements. The slip capability of ductile reinforcement can play an important role, as will be discussed further in the following sections.

A general view of the cross section of a composite laminate reinforced with 20 vol pct of  $\text{Al}_2\text{O}_3$  coated Nb laminae unloaded at about 20 pct of the peak load is shown in Figure 7. As seen in the figure, the crack propagation is discontinuous in nature, *i.e.*, after a crack stops at one side of a Nb lamina in the laminated composites, its propagation is accomplished by renucleation of another crack at the other side. Also, around a load level of 20 pct of the peak load, the crack has already propagated throughout the entire thickness of the matrix. Beyond this level, the load is carried exclusively by Nb laminae. Owing to the extensive cracking of the matrix at a load level considerably below the peak load of the composite, the value calculated from the peak load of a bending test on the chevron-notched specimen using Eq. [2] was actually a reflection of the bridging capability of the ductile phases and was interpreted as an indicator of the damage tolerance of the composite.<sup>[29]</sup>

### C. Debonding, Multiple Matrix Fracture, and Direct Crack Propagation through the Reinforcement

As load continues to increase during the tensile tests after the cracks have impinged on the Nb foil, debonding at the interfaces and/or multiple fracture of the matrix near the interfaces occur due to a relatively large lateral deformation of the Nb reinforcement compared to the matrix and load transfer from the matrix to the reinforcement. Typical features of debonding at the interface and multiple fracture of the matrix near the interface for the coated and uncoated specimens are shown in Figure 8. It is noted that interfacial debonding has occurred at the oxide coated systems (Figure 8(a)) as contrasted with multiple matrix fracture near the interface for the uncoated systems (Figure 8(b)). This is in agreement with the interface fracture energy measurement, since the interfaces in the uncoated composites have a higher fracture energy than the matrix; as such, the matrix is expected to fail more easily than the interfaces in these composites. On the other hand, for the oxide coated

composites, the fracture energy of the interfaces is lower than the fracture energy of the matrix. Thus, interfacial debonding prevailed in these composites. Similar results were also observed in a related study on bending tests of chevron-notched composite laminates,<sup>[29]</sup> which showed that debonding at the interfaces prevailed in the  $\text{Al}_2\text{O}_3$  coated Nb composites while multiple matrix fracture dominated in the uncoated Nb composites.

Both interfacial debonding and multiple matrix fracture create a "gage length" at the matrix/reinforcement interface which is a region virtually free from constraints of the matrix and is called "decohesion length" in the text. Measurement of the decohesion length was conducted for laminated composites, and the results are shown in Table II. Since the decohesion length of the laminated composites varies with load and position of the reinforcement, the values reported in Table II are measured at the peak load and for the second foil from the notch tip. Microhardness of the Nb reinforcements after hot pressing is also included in Table II to show how hardness of the Nb foils was effected by the processing conditions. Little change in microhardness across the whole Nb foil was observed so that the microhardness was taken as a constant for each specific condition. The results for the specimens hot-pressed at 1400 °C show that the lower the fracture energy of the interface, the longer the decohesion length. This is the result we would expect, since lower interfacial fracture energy means lower resistance to interfacial decohesion. However, in the case of  $\text{ZrO}_2$  coated systems, when hot-pressing temperature is increased to 1700 °C, the decohesion length becomes negligible in contrast with the general trend exhibited by the composites processed at lower temperatures. Figure 9 shows two typical load-displacement curves of bending tests on  $\text{ZrO}_2$  coated Nb/ $\text{MoSi}_2$  laminated composites hot-pressed at 1400 °C and 1700 °C. It is noted that fracture toughness of the composites is reduced and the failure becomes catastrophic when hot-pressing temperature changes from 1400 °C to 1700 °C. Observation of fracture surfaces also shows a change of fracture modes from quasi-cleavage to cleavage, as shown in Figure 10. As indicated in Table II, microhardness of the Nb foils increases from 131 to 236 as the processing temperature is increased, indicating an increase in the slip resistance of the Nb foils. The embrittlement of Nb is probably due to the diffusion of interstitial oxygen into the foils at higher processing temperatures from the decomposition of  $\text{ZrO}_2$ .

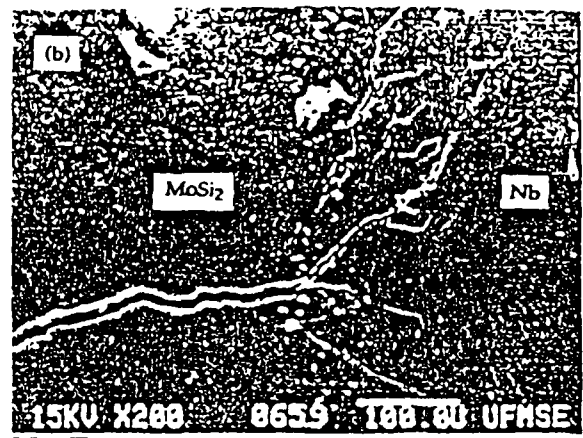
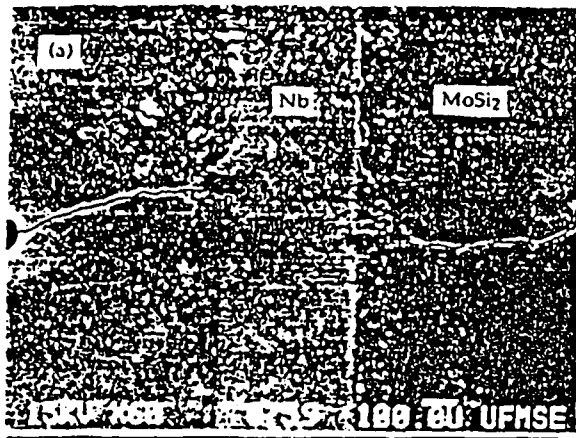
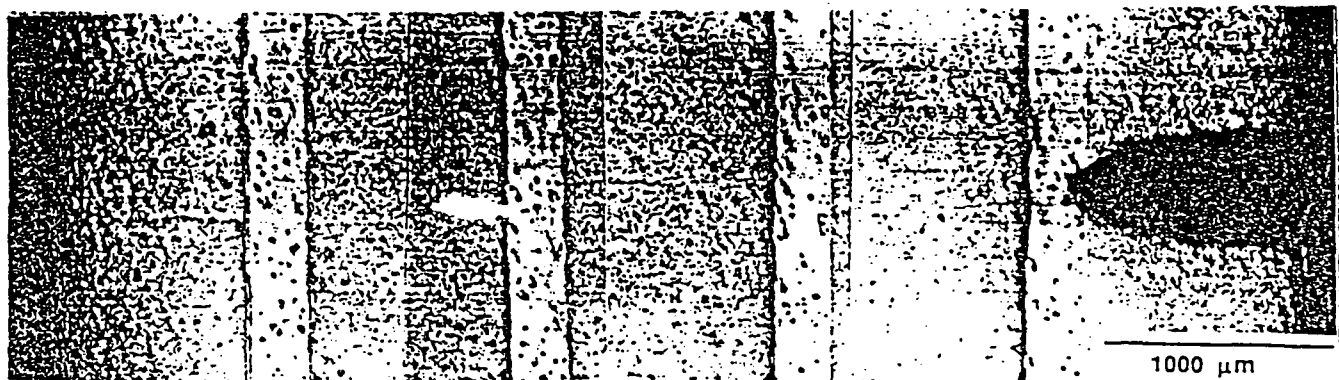


Fig. 6—An edge view of a unloaded tensile test specimen. (a) A general view of the cracks and (b) a close-up of the crack tips showing dislocation slip of the Nb at the crack tips.



3 Fig. 7—A cross section of a laminated composite reinforced by 20 vol pct of uncoated Nb foils showing the characteristics of crack propagation in the composites.

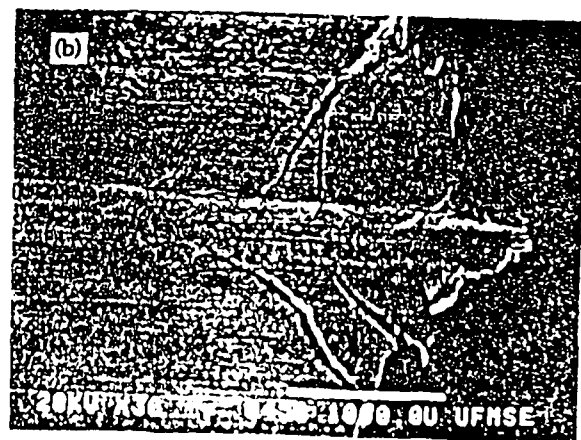
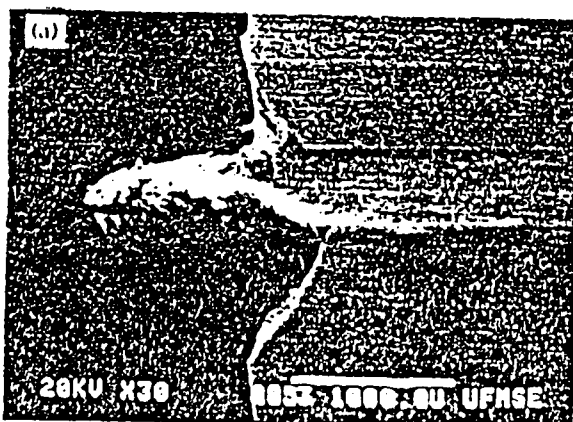


Fig. 8—An edge view of tensile tested specimens. (a) Debonding at the interface in a specimen with  $Al_2O_3$  coated Nb. (b) Multiple matrix fracture near the interface in a specimen with uncoated Nb.

Table II. Decohesion Length and Microhardness Measured from the Laminated Composites Reinforced with 20 Vol Pct of Nb Foils with a Thickness of 0.25 mm\*

| Composite System                       | Uncoated Nb |             | Al <sub>2</sub> O <sub>3</sub> Coated Nb | ZrO <sub>2</sub> Coated Nb |         |
|--|-------------|-------------|--|----------------------------|---------|
| Hot-pressing temperature               | 1700 °C     | 1400 °C     | 1400 °C                                  | 1400 °C                    | 1700 °C |
| Decohesion length (mm)                 | 0.75 ± 0.08 | 0.76 ± 0.06 | 0.80 ± 0.12                              | 1.06 ± 0.23                | 0       |
| Vickers hardness (Kg/mm <sup>2</sup> ) | 145         | 131         | 134                                      | 131                        | 236     |

\*Four specimens for each condition were tested except for Al<sub>2</sub>O<sub>3</sub> coated Nb system for which eight specimens were tested.

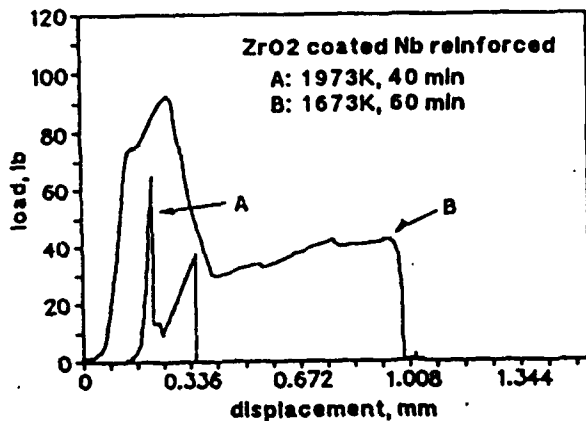


Fig. 9—Typical load-displacement curves of bending tests on chevron notched composite laminates reinforced by ZrO<sub>2</sub> coated Nb foils.

Loss of ductility of the foil leads to little lateral deformation of the Nb and resultant transverse stresses and, therefore, results in negligible decohesion length. To support this inference, tensile tests on single constrained reinforcement specimens were conducted and the results showed that whenever Vickers hardness of uncoated Nb foils increased to about 200 by controlling hot-pressing conditions, fracture mode was always by cleavage even if the notches were cut directly into the Nb foils. This result shows clearly that brittle fracture of the Nb foils is due to embrittlement of the foils.

From the previous discussion, it can be summarized

that as a crack approaches the ductile reinforcements in these systems, there exist three competitive mechanisms: interfacial debonding, multiple matrix fracture, and direct crack propagation through the ductile reinforcement. Figure 11 shows schematically these interactions. In the case of high ductility of the reinforcement, the crack is blunted by local dislocation slip of the ductile phase. The present experiments showed that extensive debonding did not occur at the early stage of the crack/ductile phase interaction, so that the interaction could be approximated as the case of no debonding at this stage. Thus, to fail the ductile reinforcement, a much higher tensile stress has to be applied which increases shear stresses at the interface due to load transfer and transverse stresses caused by the difference between lateral displacements of the matrix and reinforcement. Both shear and transverse stresses enhance interfacial debonding and/or multiple matrix fracture. Thus, whether interfacial debonding or multiple matrix fracture predominates depends on the values of the fracture energies of the matrix and interface. On the other hand, for the case of low ductility of the reinforcements, the crack can relatively easily propagate through the reinforcement before occurrence of the interfacial debonding or multiple matrix fracture. The decohesion length, which results from the competition of the three above-mentioned mechanisms, is controlled by a combination of three material properties: interface fracture energy, toughness of the matrix, and slip capability of the reinforcement.

#### D. Fracture Toughness of the Laminated Composites

Typical load-displacement curves of bending tests on chevron-notched composite laminates hot-pressed at

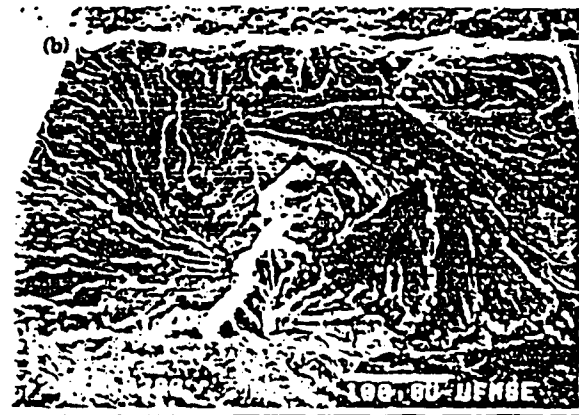
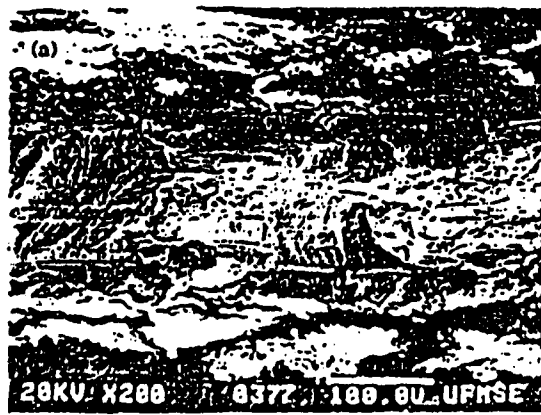


Fig. 10—Fracture surfaces of the Nb foils in composite laminates reinforced by ZrO<sub>2</sub> coated Nb: (a) hot-pressed at 1400 °C for 1 hour and (b) hot-pressed at 1700 °C for 40 min.

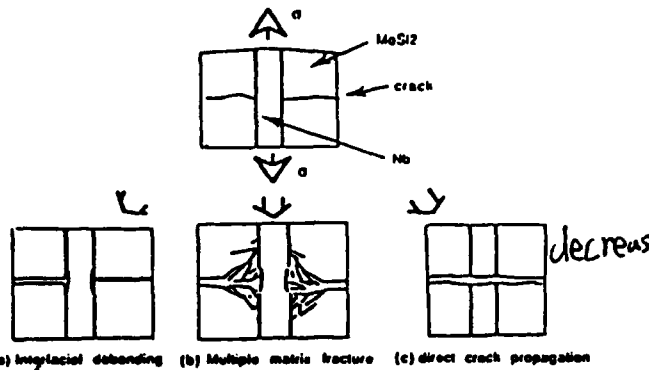


Fig. 11 — Schematic of the three competitive mechanisms at the interface. Conditions for the process to dominate shown in (a) are high toughness reinforcement and weak interface, (b) are high toughness reinforcement and strong interface, (c) are low toughness reinforcement and strong or weak interface.

1400 °C are shown in Figure 12. There are two prominent features in the figure: (1) uncoated Nb reinforced composites exhibit the highest peak load and (2) mechanical behaviors of ZrO<sub>2</sub> and Al<sub>2</sub>O<sub>3</sub> coated systems are similar, both of them showing an increase in the carried load in the last part of the displacement curves. The latter observation is caused by the extensive delamination at the interface, and correspondingly, more niobium participates in deformation and deforms under much less constrained condition. Because of this feature, the total energy consumed to break a specimen (area under the curve) for the coated composites is larger than that to break the uncoated ones. The work of fracture, defined as the total energy normalized with respect to the generated crack area,<sup>[30]</sup> for the various composites is presented in Table III. As seen in the table, the coated composites show the higher work of fracture, indicating that the low interfacial fracture energy and, thus, long decohesion length are beneficial to improving the toughness of the composite. This result is consistent with

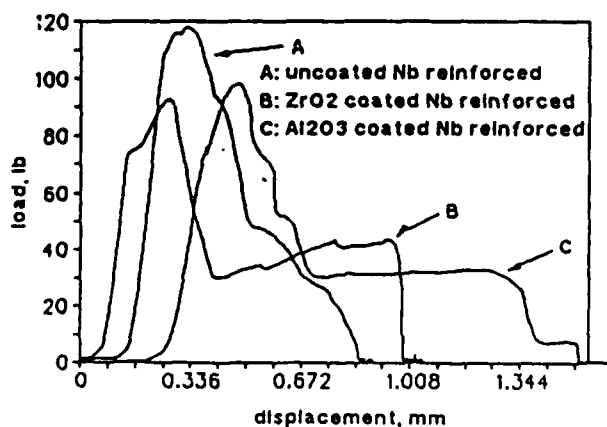


Fig. 12 — Typical load-displacement curves of bending tests on chevron notched laminates reinforced by 20 vol pct of coated and uncoated Nb foils, hot-pressed at 1400 °C for 1 hour.

predictions based on the numerical and analytical studies.<sup>[5-7,9,17]</sup>

However, damage tolerance determined from the peak load of the chevron-notched specimens shows an opposite trend. The damage tolerance determined in this way is also included in Table III. The data show that uncoated Nb reinforced composites exhibit the highest damage tolerance, followed by Al<sub>2</sub>O<sub>3</sub> coated and then ZrO<sub>2</sub> coated composites. This sequence is parallel to the increase in the interfacial fracture energy of the composites; that is, the higher the interfacial fracture energy, the higher the damage tolerance of the composites.

The data in Table III also indicate that loss of ductility of the ZrO<sub>2</sub>-coated Nb foils hot-pressed at 1700 °C results in a large drop of toughness of the laminated composites. Therefore, the damage tolerance data suggest that a high degree of constraints is conducive to toughness as long as the ductile reinforcement has a high slip capability. When the reinforcement does not have the slip capability, as in the case of ZrO<sub>2</sub> coated composites processed at 1700 °C, decreasing the constraint (*i.e.*, increasing the gage length by decreasing the interfacial bonding) is more beneficial to improving the toughness.

In summary, the results from the bend test of chevron-notched specimens indicate that the role of the interface for ductile reinforcement and debonding in the toughness depends on the criterion used to describe the toughness of the composites. If the peak load of the chevron-notched specimen is used as an indicator of the toughness, a strong bonding and, therefore, a high degree of constraints, would be desirable. On the other hand, if the total energy consumed to break a specimen is used as indicative of that specimen's toughness, then a relatively weak bonding is required.

The aforementioned dual effects of interfacial properties on the toughness of the composites are further supported using the data obtained from the simple tensile test on a single constrained Nb foil. Representative stress-displacement curves for 0.5-mm-thick Nb lamina are shown in Figure 13, and the corresponding decohesion lengths with different coating conditions for different sizes of Nb laminae are summarized in Table IV. It is noted that the area under the stress-displacement curve, called "work of rupture of the constrained ductile phase," increases with increasing decohesion length. As given by Eq. [1], the steady state toughness of the composites is proportional to the work of rupture of the constrained ductile phase. Thus, increasing decohesion length is conducive to improving steady state toughness of the composites, a trend also shown by the work of fracture measured from chevron-notched specimens (Table III). Figure 13, at the same time, also reveals that the maximum stress reached by the constrained Nb decreases with increasing decohesion length, a trend similar to that exhibited by the damage tolerance measured from the chevron-notched specimens. These apparently different roles of the interface can be explained by relating the maximum stress reached by the constrained ductile phases to the crack propagation resistance in the case of large-scale bridging (*i.e.*, crack length is at the same order of magnitude as bridging length), as observed in the present composites (Figure 7). A recent calculation based on the equilibrium stress distributions across the crack face<sup>[11]</sup>

Table III. Measured Toughness of the Laminated Composites Reinforced with 20 Vol Pct of Nb Foils with a Thickness of 0.25 mm\*

| Material                                   | Monolithic MoSi <sub>2</sub> | Uncoated Nb Reinforced | Al <sub>2</sub> O <sub>3</sub> Coated Nb Reinforced | ZrO <sub>2</sub> Coated Nb Reinforced | ZrO <sub>2</sub> Coated Nb Reinforced |
|--|------------------------------|------------------------|---|---------------------------------------|---------------------------------------|
| Hot-pressing temperature                   | 1700 °C                      | 1700 °C and 1400 °C    | 1400 °C   | 1400 °C                               | 1700 °C                               |
| Damage tolerance (MPa · m <sup>1/2</sup> ) | 3.3 ± 0.3                    | 15.2 ± 1.3             | 14.0 ± 1.5  | 12.8 ± 1.5                            | 8.6 ± 1.3                             |
| Work of fracture (J/m <sup>2</sup> )       | 690 ± 30                     | 21,600 ± 3000          | 28,700 ± 1900                                       | 28,700 ± 4600                         | 2800 ± 300                            |
| Interfacial fracture energy**              | —                            | high                   | medium  | low                                   | low                                   |
| Ductility of the reinforcement**           | —                            | high                   | high  | high                                  | low                                   |

\*Four specimens for each condition were tested except for Al<sub>2</sub>O<sub>3</sub> coated Nb system for which eight specimens were tested.  
\*\*For details, see Tables I and II.

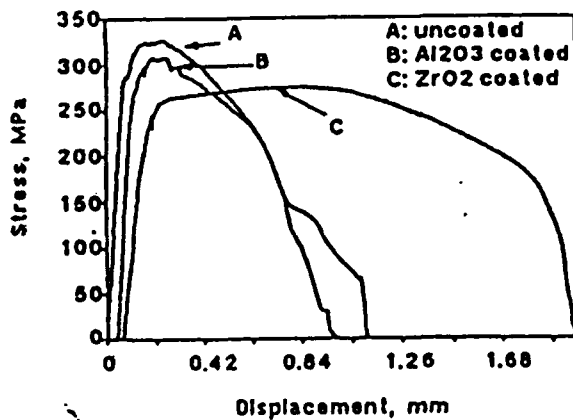


Fig. 13—Effect of the coatings on the stress-displacement curves, measured from tensile test on the single constrained Nb laminae (thickness of the Nb laminae = 0.5 mm).

indicates that the maximum crack propagation resistance of the composites increases with increasing decohesion length. However, the maximum crack propagation resistance is achieved only after the crack has propagated extensively. At the small crack size, the composites with less decohesion show a higher crack propagation resistance than their counterparts with more decohesion. Therefore, it seems that the choice of weak or strong interface in describing fracture behavior of ductile-phase-toughened composites depends on the criterion used to describe the toughness of the composites.

## VI. SUMMARY AND CONCLUSIONS

The present set of experiments clarifies the role a matrix/reinforcement interface plays in brittle materials toughened by ductile reinforcements. It has been disclosed that influence of interfaces on fracture toughness of brittle matrix/ductile reinforcement composites is not as crucial as in brittle matrix/ceramic fiber composites due to the local dislocation slip of ductile phase at the crack tip. Furthermore, it has been established that as a crack impinges a reinforcement, there exist three competitive mechanisms: interfacial debonding, multiple matrix fracture, and direct crack propagation through the reinforcement. The mechanism that prevails is decided not only by fracture energies of the interface and toughness of the matrix but also by the slip capability of the ductile reinforcement. Decoherence length at the matrix/reinforcement interface is a result of the competition. In the case of high slip capability of the reinforcements, the higher the fracture energy of interfaces, the shorter the decohesion length.

The toughness measurement has revealed that whether or not a strong interfacial bonding is conducive to toughness depends on the criterion used to describe the toughness of the composites. If the peak load of the chevron-notched specimen is used as an indicator of the toughness, a strong bonding would be desirable. On the other hand, if the work of fracture is used as indicative of its toughness, then a relatively weak bonding is required. Ductility of the ductile reinforcement is also an important factor in controlling toughness of the composites. It has been demonstrated that loss of ductility of

Table IV. Decoherence Length Measured from Single Constrained Nb Foil Specimens (Hot-Pressed at 1400 °C, 40 MPa for 1 Hour)\*

| Thickness of Nb Foil (mm) | 1.0                  |                                       |                         | 0.5       |                                       |                                     | 0.25        |                                       |                         |
|---------------------------|----------------------|---------------------------------------|-------------------------|-----------|---------------------------------------|-------------------------------------|-------------|---------------------------------------|-------------------------|
|                           | Processing condition | Al <sub>2</sub> O <sub>3</sub> coated | ZrO <sub>2</sub> coated | uncoated  | Al <sub>2</sub> O <sub>3</sub> coated | ZrO <sub>2</sub> coated             | uncoated    | Al <sub>2</sub> O <sub>3</sub> coated | ZrO <sub>2</sub> coated |
| Decoherence length (mm)   | 10 ± 5               | decohesion all the way to the grips   |                         | 2.9 ± 0.4 | 3.3 ± 0.4                             | decohesion all the way to the grips | 0.86 ± 0.09 | 0.94 ± 0.23                           | 1.30 ± 0.61             |

\*Four specimens for each condition were tested except for 0.5-mm-thick Nb foils for which eight specimens were tested.

the ductile reinforcement during processing could result in little improvement in toughness of the composites.

### ACKNOWLEDGMENTS

The authors are grateful to the support of the Defense Advanced Research Projects Agency (DARPA) and Office of Naval Research (ONR) through Grant No. N00014-91-J-4075.

### REFERENCES

1. K.M. Prew: *Mater. Res. Soc. Symp. Proc.*, 1988, vol. 120, pp. 145-56.
2. R.J. Dieffendorf and R.P. Boisvert: *Mater. Res. Soc. Symp. Proc.*, 1988, vol. 120, pp. 157-62.
3. A.G. Evans and D.B. Marshall: in *High Tech Ceramics*, P. Vincenzini, ed., Elsevier Science Publishers B.V., Amsterdam, 1987, pp. 213-46.
4. R.W. Davidge: in *High Tech Ceramics*, P. Vincenzini, ed., Elsevier Science Publishers B.V., Amsterdam, 1987, pp. 763-77.
5. P.A. Mataga: *Acta Metall.*, 1989, vol. 37, pp. 3349-59.
6. L.S. Sigl, P.A. Mataga, B.J. Dalgleish, R.M. McMeeking, and A.G. Evans: *Acta Metall.*, 1988, vol. 36, pp. 945-53.
7. M.F. Ashby, F.J. Blunt, and M. Bannister: *Acta Metall.*, 1989, vol. 37, pp. 1847-57.
8. L.R.F. Rose: *J. Mech. Phys. Solids*, 1987, vol. 35, pp. 383-405.
9. A.G. Evans and R.M. McMeeking: *Acta Metall.*, 1986, vol. 34, pp. 2435-41.
10. B. Budiansky, J.C. Amazigo, and A.G. Evans: *J. Mech. Phys. Solids*, 1988, vol. 36, pp. 167-87.
11. B.N. Cox: *Acta Metall. Mater.*, 1991, vol. 39, pp. 1189-1201.
12. B.N. Cox and C.S. Lo: *Acta Metall. Mater.*, 1992, vol. 40, pp. 69-80.
13. H.C. Cao, B.J. Dalgleish, H.E. Deve, C. Elliott, A.G. Evans, R. Mehrabian, and G.R. Odette: *Acta Metall.*, 1989, vol. 37, pp. 2969-77.
14. L. Xiao and R. Abbaschian: in *Advanced Metal Matrix Composites for Elevated Temperatures*, M.N. Gungor, E.J. Laverna, and S.G. Fishman, eds., ASM INTERNATIONAL, Metals Park, OH, 1991, pp. 33-40.
15. L. Xiao: in *Developments in Ceramic and Metal-Matrix Composites*, K. Upadhy, ed., TMS, Warrendale, PA, 1992, pp. 115-24.
16. H.E. Deve, A.G. Evans, G.R. Odette, R. Mehrabian, M.L. Emiliani, and R.J. Hecht: *Acta Metall.*, 1990, vol. 37, pp. 1491-1502.
17. L. Xiao: in *Developments in Ceramic and Metal-Matrix Composites*, K. Upadhy, ed., TMS, Warrendale, PA, 1992, pp. 359-69.
18. L. Xiao, Y.S. Kim, and R. Abbaschian: in *Intermetallic Matrix Composites*, Proc. MRS Meeting, D.L. Anton, P.L. Martin, D.B. Miracle, and R. McMeeking, eds., 1990, vol. 194, pp. 399-404.
19. C.K. Elliott, G.R. Odette, G.E. Lucas, and J.W. Shockherd: in *High Temperature/High Performance Composite*, MRS Proc., F.D. Lemkey, A.G. Evans, S.G. Fishman, and J.R. Strife, eds., 1988, vol. 120, pp. 95-102.
20. K.T. Venkateswara Rao, G.R. Odette, and R.O. Ritchie: *Acta Metall. Mater.*, 1992, vol. 40, pp. 353-61.
21. L. Xiao and R. Abbaschian: University of Florida, Gainesville, FL, unpublished research, 1992.
22. D.G. Munz, J.L. Shannon, Jr., and R.T. Buscy: *Int. J. Fract.*, 1980, vol. 16, pp. R137-R141.
23. J.C. Newman, Jr.: in *Chevron-Notched Specimens: Testing and Stress Analysis*, ASTM STP 855, J.H. Underwood, S.W. Freiman, and F.I. Baratta, eds., ASTM, Philadelphia, PA, 1984, pp. 5-31.
24. L.M. Barker and F.I. Baratta: *J. Test. Eval.*, 1980, vol. 8, pp. 97-102.
25. D. Munz: *Eng. Fract. Mech.*, 1981, vol. 15, pp. 231-36.
26. J.J. Mecholsky and L.M. Barker: in *Chevron-Notched Specimens: Testing and Stress Analysis*, ASTM STP 855, J.H. Underwood, S.W. Freiman, and F.I. Baratta, eds., ASTM, Philadelphia, PA, 1984, pp. 324-36.
27. L. Xiao and R. Abbaschian: *Mater. Sci. Eng.*, in press.
28. J. Cook and J.E. Gordon: *Proc. R. Soc. London A*, 1964, vol. 282, pp. 508-20.
29. L. Xiao, Y.S. Kim, R. Abbaschian, and R.J. Hecht: *Mater. Sci. Eng.*, 1991, vol. A144, pp. 277-85.
30. H.G. Tatterall and G. Tappin: *J. Mater. Sci.*, 1966, vol. 1, pp. 296-301.

## MICROSTRUCTURE AND PROPERTIES OF $\text{MoSi}_2/\text{Nb}$ INTERFACES WITH AND WITHOUT ALUMINA COATING

L. Xiao and R. Abbaschian  
Department of Material Science and Engineering, University of Florida, Gainesville,  
FL 32611

### ABSTRACT

This study explores the relations between processing routes, microstructures and mechanical properties of the matrix/reinforcement interfaces in  $\text{MoSi}_2/\text{Nb}$  composites. It was found that the fracture energy of the interfacial region depended on the interfacial bond strength, roughness of interface, and the nature of the interfacial compounds. The fracture energy between the oxide coating and intermetallic interfacial compounds was found to be lower than that between two intermetallics or between Nb and an intermetallic. Processing routes were found to affect the fracture energy of the interfacial region by changing interphase formation, changing microstructure of materials adjacent to the interface, or changing roughness of interface.

### INTRODUCTION

It is commonly accepted that a relatively weak interface is desirable for improving fracture toughness of ceramics and intermetallics reinforced by ceramic fibers [1-4]. The reason for this is that such an interface when present in the path of an advancing crack would fail locally and blunt the crack. A relatively weak interface is also beneficial to fracture toughness of polymer-matrix composites. An example is provided by Harris et al. [5], who used different fiber surface treatments to change the bond strength of the interface in carbon fiber-reinforced polyester composites, and demonstrated that higher fracture energy was achieved in the case of the weakest interface, resulting from greater pullout length of the carbon fibers. Similar results are found in carbon fiber-reinforced epoxies [6] and a boron epoxy composite [7]. Metal-matrix composites also exhibit a strong dependence of toughness on the fiber-matrix debonding, as exemplified by tungsten wire-reinforced aluminum composites [8]. In this case, the toughness is proportional to the energy to break the debonded fibers.

The above examples show that debonding at the interface play an important role in the mechanical performance of composites. A recent study [9] has shown that debonding length in the composites depends strongly on the fracture energy of the matrix/reinforcement interface. The latter is expected to be affected by various factors, such as the extent of chemical interaction at the interface, roughness of interface, dissipation of strain energy by ductile reinforcements, thermal expansion mismatch, and bond strength of the interface. Therefore, parameters affecting interfacial fracture energy must be evaluated and understood in order to control the mechanical behavior of interfaces in composites. In the present study, the relations between processing routes, microstructures and fracture energy of the matrix/reinforcement interfaces in  $\text{MoSi}_2/\text{Nb}$  composites were explored. The composites were fabricated by hot pressing  $\text{MoSi}_2$  powder with  $\text{Al}_2\text{O}_3$  coated or uncoated Nb reinforcement. Deposition of the oxide coating on Nb was achieved via different processing routes, i. e., sol-gel coating technique, physical vapor deposition and hot dipping Nb in a molten Al bath, followed by an anodizing process to form  $\text{Al}_2\text{O}_3$ . Interfacial fracture energy was evaluated using chevron-notched-short-bar specimens. Variation in the fracture energy of the interfacial region is discussed in terms of the microstructures and types of the interfacial bonding.

### EXPERIMENTAL

#### Coating Techniques

The sol solution for the sol-gel coating was an aluminum-alkoxide-derived sol (using aluminum-sec-butoxide (ASB)), hydrolyzed in excess water and peptized with aluminum

nitrate,  $\text{Al}(\text{NO}_3)_3$ . The procedures for preparing the sol solution developed by Clark et al. [10] were used. The  $\text{Al}_2\text{O}_3$  coating was produced by electrophoretic deposition on to the Nb foils. Once the coating was applied, the coated Nb foils were suspended vertically for 48 hrs at the ambient temperature, and then further dried in a furnace at  $500^\circ\text{C}$  for 1 hr with a heating rate of  $3^\circ\text{C}/\text{min}$  before the hot pressing.

Physical vapor deposition of  $\text{Al}_2\text{O}_3$  on to Nb foils was conducted using Thermionics 100-0030 with a electron beam heated source. The emission current was 200 mA with a potential difference between the cathode and the anode being 3 KV. The resulting deposition rate was  $10 \text{ \AA}/\text{sec}$ . The thickness of the  $\text{Al}_2\text{O}_3$  deposit in the present study was  $1 \mu\text{m}$ .

The hot dipping and anodizing technique for the formation of  $\text{Al}_2\text{O}_3$  coating consisted of the following steps. First, Nb foils were hot dipped into a molten aluminum bath for 2 minutes which was kept at a temperature of  $930^\circ\text{C}$ . Second, the hot dipped Nb foils was anodized in an electrolyte containing 5 wt.% of sulfuric acid to convert the aluminum into alumina. The anodizing was conducted at ambient temperature, and a constant DC voltage ranging from 10 to 20 volts was applied to produce current densities ranging from 5 to 25  $\text{mA}/\text{cm}^2$ . Anodizing time was 30 minutes. More detailed description of the coating techniques can be found elsewhere [11].

#### Fabrication of Laminate Composites

The test specimens were three layer composites with the coated or uncoated Nb foil sandwiched in between two layers of  $\text{MoSi}_2$ . The thickness of the Nb foils used was 0.127 mm. The specimens were prepared by stacking the coated or uncoated Nb foil with two layers of commercially pure  $\text{MoSi}_2$  powder of -325 mesh and then vacuum hot pressing at  $1400^\circ\text{C}$  for 1 hr with a pressure of 40 MPa. In order to minimize residual thermal stresses, the hot pressed discs were held in the hot pressing chamber at  $800^\circ\text{C}$  for 1 hour before cooling down to room temperature. The discs were then cut into rectangular short bar with dimensions of  $8.28 \times 9.25 \times 14.29 \text{ mm}$  to prepare the specimens for the measurement of interfacial fracture energy.

#### Measurement of Interfacial Fracture Energy

The measurement of the interfacial fracture energy was conducted on chevron notched short bars using the procedures recommended in reference [12]. The technique involves determining the critical stress intensity factor from the peak load of the notched bars and then converting the critical stress intensity factor to the fracture energy of the interface. The equation used to calculate the fracture energy of the interface,  $G_{\text{IC}}$ , is [12]

$$G_{\text{IC}} = \frac{K_{\text{ICSR}}^2}{E} \quad \dots \quad (1)$$

where  $E$  is the elastic modulus of  $\text{MoSi}_2$  and  $K_{\text{ICSR}}$  is the critical stress intensity factor determined from the peak load of the short bar test.

In the present study, however, a modified specimen geometry, as shown in Fig. 1, was used. An advantage of the present geometry is that there is no need for compliance calibration due to symmetry of compliance of the specimen with respect to the interface. The notch in the short bar was cut parallel to the foil using a diamond cutting blade with a thickness of  $0.4 \text{ mm}$ . The thickness of the notch was chosen to be slightly larger than that of the foil to insure that the

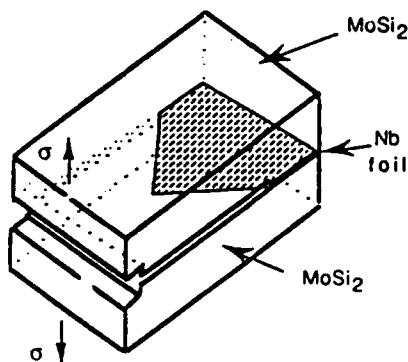


Fig. 1 Short bar specimen geometry

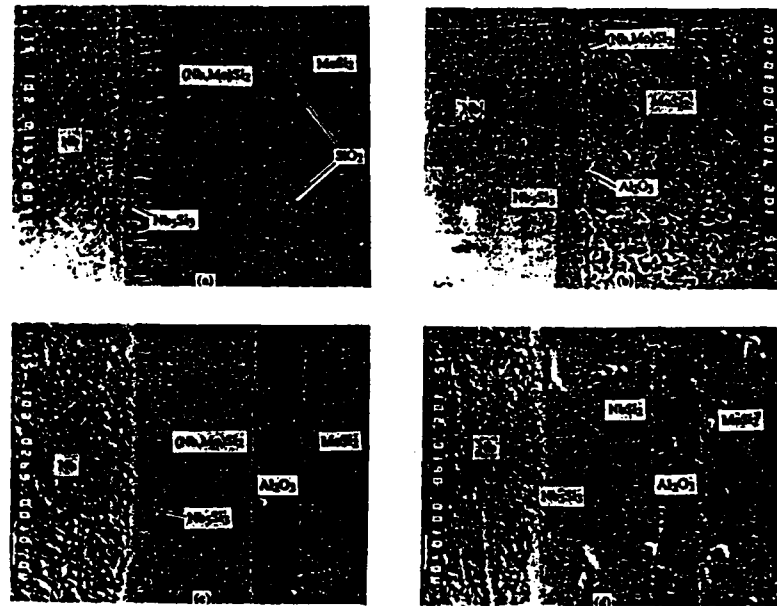


Fig. 2 Interfacial Microstructures of MoSi<sub>2</sub>/Nb laminate composites with different processing conditions.  
 (a) uncoated Nb, (b) PVD coated Nb, (c) sol-gel coated Nb, and (d) hot-dipping-and-anodizing coated Nb.

initiation and propagation of the crack is at the weakest position among various interfaces between matrix/coating/reinforcement. The specimen was loaded at a constant test machine crosshead speed of 0.005 in/min using a hydro-servo controlled MTS. The load was recorded as a function of the crosshead displacement.

## RESULTS

Interfacial microstructures of MoSi<sub>2</sub>/Nb laminate composites with different processing conditions are shown in Fig. 2. The detailed mechanism for the formation of the interfacial compounds (interphases) between MoSi<sub>2</sub> and Nb and the effect of the coatings on the interphase formation can be found elsewhere [11,13,14]. Extensive interphase formation was observed in MoSi<sub>2</sub>/uncoated Nb composites, resulting in the formation of intermetallics of (Nb,Mo)Si<sub>2</sub> and Nb<sub>5</sub>Si<sub>3</sub>. When the Al<sub>2</sub>O<sub>3</sub> coating was applied, either the thickness of the interphases was reduced or the composition of the interphase was changed (Fig. 2d). Such changes have been attributed to the retardation of Si diffusion and the suppression of Mo and Nb interdiffusion across the coatings [14].

A typical load displacement curve of the hot-dipping-and-anodizing coated Nb/MoSi<sub>2</sub> laminate and the corresponding fracture surface at the chevron crack are shown in Fig. 3. A stable crack propagation has been achieved, as indicated by the fluctuation in the curve near the maximum load. Therefore, the maximum load was used to calculate G<sub>IC</sub> with the aid of eq. (1). By examining the two fracture surfaces of a broken short bar with SEM and EMP, the failure location at the interface could be determined. Depending on the processing conditions, the crack propagates along an interface in some cases, or by kinking between two interfaces, or only inside MoSi<sub>2</sub> matrix in other cases. Owing to this feature, the measured fracture energy of interface using the notched short bar has been referred to as fracture energy of the interfacial region of the laminates. The measured fracture energies of the interfacial region and failure locations for laminate composites with different processing conditions are summarized in

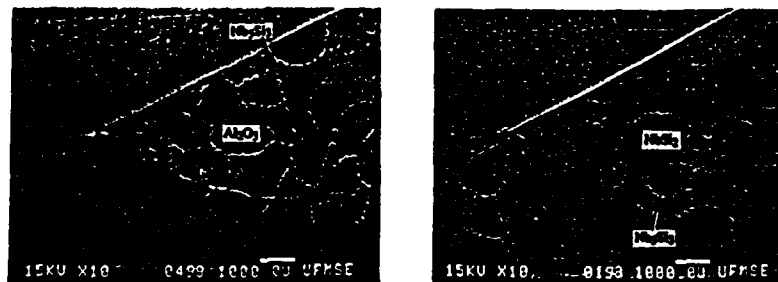
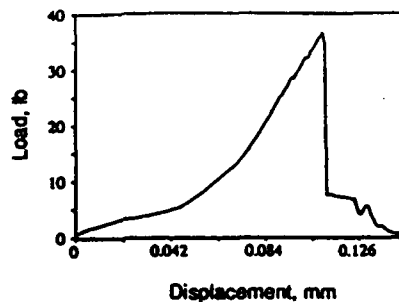


Fig. 3 A typical load displacement curve of the hot-dipping-and-anodizing coated Nb/MoSi<sub>2</sub> laminate and the corresponding fracture surfaces at the chevron crack.

Table 1. For comparison, fracture energy for MoSi<sub>2</sub> alone is also included in the table.

In the case of the hot-dipping-and-anodizing, the failure of the laminate occurred mainly along the Al<sub>2</sub>O<sub>3</sub>/NbSi<sub>2</sub> interface. A small portion of the failure also occurred in the Nb<sub>5</sub>Si<sub>3</sub> phase, as shown in Fig. 3, which was probably due to the discontinuity of the oxide coating generated during the anodizing process and/or the roughness of the interface. Similar fracture surface was observed for the sol-gel coated Nb/MoSi<sub>2</sub> laminate. Correspondingly, the specimens using the two coating techniques mentioned above exhibited a similar fracture energy of the interfacial region. By changing the sol-gel processing control parameters, the interphase formed can be limited to be only one phase, i. e., Nb<sub>5</sub>Si<sub>3</sub>, instead of (Nb,Mo)Si<sub>2</sub> and Nb<sub>5</sub>Si<sub>3</sub> [11,13]. However, the measured fracture energy of the interfacial region in this case is the same as Al<sub>2</sub>O<sub>3</sub>/(Nb,Mo)Si<sub>2</sub> interface, as shown in Table 1.

Quite different fracture surface was observed for the PVD coated specimens. As shown in Fig. 4, failure location in this case was partially in MoSi<sub>2</sub> and partially at the interface of

Table 1. Fracture energy and failure location of the interfacial region in the coated and uncoated Nb/MoSi<sub>2</sub> systems

| System   | Failure location   | Toughness, G <sub>IC</sub> , J/m <sup>2</sup> |
|--|--|---|
| MoSi <sub>2</sub> alone                                |  | 33.7 ± 1.4                                    |
| MoSi <sub>2</sub> /uncoated Nb                         | inside the MoSi <sub>2</sub>   | > 33.7  |
| MoSi <sub>2</sub> /sol-gel coated Nb                   | Al <sub>2</sub> O <sub>3</sub> /(Nb,Mo)Si <sub>2</sub> interface<br>or Al <sub>2</sub> O <sub>3</sub> /Nb <sub>5</sub> Si <sub>3</sub> interface | 16.1 ± 1.3                                    |
| MoSi <sub>2</sub> /hot-dipping-and-anodizing coated Nb | Al <sub>2</sub> O <sub>3</sub> /NbSi <sub>2</sub> interface  | 15.5 ± 1.6                                    |
| MoSi <sub>2</sub> /PVD coated Nb                       | partially inside the MoSi <sub>2</sub> and<br>partially at Al <sub>2</sub> O <sub>3</sub> /(Nb,Mo)Si <sub>2</sub><br>interface                   | 31.7 ± 3.4                                    |

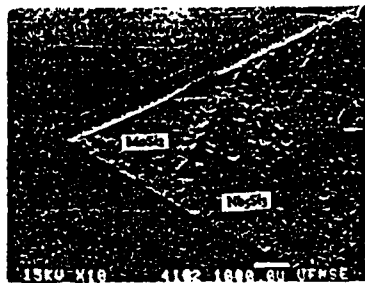


Fig. 4 Fracture surface at the chevron crack of a PVD coated Nb/MoSi<sub>2</sub> specimen

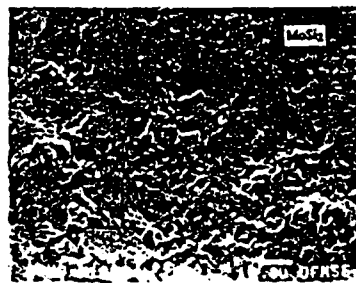


Fig. 5 An enlarged fracture surface of the tip area in Fig. 4.

Al<sub>2</sub>O<sub>3</sub>/(Nb,Mo)Si<sub>2</sub>. This is believed to be due to the small and frequent discontinuity of the oxide coating (Fig. 2b) caused by the presence of the SiO<sub>2</sub> and free Si in the commercially pure MoSi<sub>2</sub> powder, as shown in Fig. 2(a) and reported in elsewhere [15,16]. Because of such small and frequent discontinuity of the coating, the fracture resistance along the Al<sub>2</sub>O<sub>3</sub>/(Nb,Mo)Si<sub>2</sub> interface has been increased. Combining the effect of the roughness of the interface (Fig. 2b), crack is unable to propagate along the Al<sub>2</sub>O<sub>3</sub>/(Nb,Mo)Si<sub>2</sub> interface, but have to kink between the interface and MoSi<sub>2</sub> matrix to obtain crack propagation with minimum energy consumption.

For the uncoated Nb/MoSi<sub>2</sub> laminates, the failure was observed to take place inside MoSi<sub>2</sub> rather than at the interfaces, indicating that the interfacial region has a higher fracture energy than the matrix. The fracture energy of MoSi<sub>2</sub> measured in the present study is 33.7 J/m<sup>2</sup>. Thus, the fracture energy of the interfacial region in uncoated Nb/MoSi<sub>2</sub> laminates must be higher than this value. Indeed, all the measurements conducted on uncoated Nb/MoSi<sub>2</sub> laminates were about 36.4 J/m<sup>2</sup> because the crack in MoSi<sub>2</sub> failed to follow the chevron notched plane strictly.

## DISCUSSION

Various interphases were formed in the present study due to the diffusion of Si, Mo and/or Nb through the coating. The thickness and the nature of the interphases were found to depend on the processing temperature and time [13,14]. Because of the presence of the various interphases, the interfaces at the interfacial region have been divided into three categories, as shown in Table 2. Category I consists of an interface (bonding) between the oxide coating and intermetallics. Category II is composed of a bond between two intermetallics. Category III is the interfaces which have a bond between a metal and an intermetallic. Because of the interaction, no direct bonding between oxide and metal was observed. By examining the failure locations and fracture energy of the interfacial region measured, the fracture energy for the interfaces present in this study can be estimated and summarized in Table 2.

It is noted that fracture energy for the oxide bond, category I, is lower than the bonds between intermetallics or between a metal and an intermetallic (categories II and III). It is at a level of 16 J/m<sup>2</sup> in the present instance, which is even lower than the fracture energy of the alumina itself (~ 20-40 J/m<sup>2</sup>). The low fracture energy of the oxide bond is attributed to the low bond strength between alumina and silicides involved. As concluded by Sutton and Feingold [17], the bond strength between oxide and other materials is directly related to the amount of interaction between the two materials, and the free energy of formation of the other materials' oxide is an important criterion in determining the interaction. Weak bonding will form when the conditions are unfavorable for the formation of other oxides. In the present case, elemental Mo, Nb and Si have a lower free energy of formation of their oxides in comparison with Al<sub>2</sub>O<sub>3</sub> [18]. As such, formation of silica, niobium and molybdenum oxides,

Table 2. Fracture energy of the interfaces

| System (category)   | $G_{IC}$ , J/m <sup>2</sup> |
|---|-----------------------------|
| MoSi <sub>2</sub>   | 33.7                        |
| Al <sub>2</sub> O <sub>3</sub> /(Nb,Mo)Si <sub>2</sub> (I)          | ~ 16                        |
| Al <sub>2</sub> O <sub>3</sub> /NbSi <sub>2</sub> (I)               | ~ 16                        |
| Al <sub>2</sub> O <sub>3</sub> /Nb <sub>5</sub> Si <sub>3</sub> (I) | ~ 16                        |
| Al <sub>2</sub> O <sub>3</sub> /MoSi <sub>2</sub> (I)               | > 16 ?                      |
| MoSi <sub>2</sub> /(Nb,Mo)Si <sub>2</sub> (II)                      | ≥ 33.7                      |
| Nb <sub>5</sub> Si <sub>3</sub> /(Nb, Mo)Si <sub>2</sub> (II)       | ≥ 33.7                      |
| Nb <sub>5</sub> Si <sub>3</sub> /Nb (III)                           | ≥ 33.7                      |

Moreover, the fracture energy of category I interface was found to be insensitive to the change in the composition of the silicides, as shown in Table 2. This is probably due to the similarity of Nb and Mo in their atomic structures. If this is true, Al<sub>2</sub>O<sub>3</sub>/MoSi<sub>2</sub> interface should show similar fracture energy. However, no failure at Al<sub>2</sub>O<sub>3</sub>/MoSi<sub>2</sub> interface was observed in the present study. As shown in Fig. 2(c) and (d), one major difference of Al<sub>2</sub>O<sub>3</sub>/MoSi<sub>2</sub> interface from the Al<sub>2</sub>O<sub>3</sub>/NbSi<sub>2</sub> and Al<sub>2</sub>O<sub>3</sub>/(Nb,Mo)Si<sub>2</sub> interfaces is that the former is rougher than the latter. Such roughness of the interface can increase fracture resistance by the mechanism of interlocking and crack deflection. Thus, Al<sub>2</sub>O<sub>3</sub>/MoSi<sub>2</sub> interface shows a higher fracture resistance than Al<sub>2</sub>O<sub>3</sub>/NbSi<sub>2</sub> and Al<sub>2</sub>O<sub>3</sub>/(Nb,Mo)Si<sub>2</sub> interfaces, although their bond strengths may be similar.

Category II and III interfaces all exhibit higher fracture resistance than MoSi<sub>2</sub> matrix, indicating the bond strength between two intermetallics or between a metal and an intermetallic is high. In this case, crack was observed to propagate inside the MoSi<sub>2</sub> matrix instead of inside the interphases formed. However, this does not necessarily mean that MoSi<sub>2</sub> has a lower inherent fracture resistance than that of the interphases, (Nb,Mo)Si<sub>2</sub> and Nb<sub>5</sub>Si<sub>3</sub>. It is believed that the low apparent fracture resistance of MoSi<sub>2</sub> in the present instance is partially related to the high porosity and SiO<sub>2</sub> in MoSi<sub>2</sub> adjacent to the interface, as shown in Fig. 2(a). High porosity is due to the fast diffusion of Si into Nb and segregation of vacancy onto the opening channel of MoSi<sub>2</sub> powder compact. In contrast, the interphases formed are very dense, as shown in Fig. 2. Because the pores distribute along the grain boundary of MoSi<sub>2</sub>, it is expected that crack would propagate along the grain boundary and an intergranular fracture results. Indeed, this is confirmed by SEM observation. Fig. 5 shows an enlarged fracture surface of the tip area in Fig. 4. Similar intergranular fracture was observed in MoSi<sub>2</sub> specimens, consistent with the report by Kaufman et al. [15]. Therefore, low apparent fracture resistance of MoSi<sub>2</sub> is partially caused by the presence of porosity and SiO<sub>2</sub>.

Different processing routes have shown little effect on the fracture energy of the interfacial region as long as the oxide coating is thick enough to prevent the breakdown of the coating by the attack of SiO<sub>2</sub> and free Si. Fracture energies for the interfacial region generated by sol-gel technique and the hot-dipping-and-anodizing technique are similar because a thick and continuous coating has been formed in general by these two techniques. The results indicate that bond strength merely depends on chemical bonding rather than on a long range interaction force. For the PVD coated laminates, a frequent discontinuity in the coating results in a partial oxide bond and a partial intermetallic bond interface, leading to an increase in fracture resistance of the interfacial region.

#### CONCLUDING REMARKS

The present set of experiments have demonstrated that fracture energy of an interfacial region depends on the interfacial bond strength, roughness of interface and microstructure of the two component materials at the interface. Weak bond strength leads to a low interfacial fracture energy. Roughness of the interface increases the interfacial fracture energy. Porosity in one of the two component materials at the interface could lead to a low fracture energy of the interfacial region due to the crack propagation along the weak path in one of the component materials instead of along the interface. Processing routes can affect fracture energy of the

directly or by decomposition of MoSi<sub>2</sub>, is unfavorable in terms of free energy change. Therefore, it is expected that the reactivity of the silicides with alumina would be very low, resulting in a low bond strength. On the otherhand, if the free energy of formation is more favorable for forming other oxides instead of alumina, strong bond may form. An example is given by the work of Dagleish et al. [19]. They found that crack always initiated in the alumina adjacent to the interface of a Al-Mg alloy bonded to an alumina. High bond strength in this case can be attributed to a much more negative free energy of formation for MgO than that of Al<sub>2</sub>O<sub>3</sub>.

interfacial region by changing interphase formation, changing roughness of interface, or by changing microstructure of materials adjacent to the interface. However, if such changes have not been brought out during processing, there will be little effect of processing routes on fracture energy of the interfacial region.

**Acknowledgements** ---- The authors are grateful to the support of the Defense Advanced Research Projects Agency (DARPA) and Office of Naval Research (ONR) through grant N00014-91-J-4075.

#### REFERENCES

1. K. M. Prewo, in High Temperature/High Performance Composites, edited by F. D. Lemkey, et al. (Mater. Res. Soc. Symp. Proc., 120, Pittsburgh, PA, 1988), pp. 145-56.
2. R. J. Diefendorf and R. P. Boisvert, in High Temperature/High Performance Composites, edited by F. D. Lemkey, et al. (Mater. Res. Soc. Symp. Proc., 120, Pittsburgh, PA, 1988), pp. 157-62.
3. A. G. Evans and D. B. Marshall, in High Tech Ceramics, edited by P. Vincenzini, (Elsevier Science Publishers B. V., Amsterdam, 1987), pp. 213-46.
4. R. W. Davidge, in High Tech Ceramics, edited by P. Vincenzini, (Elsevier Science Publishers B. V., Amsterdam, 1987), pp. 763-77.
5. B. Harris, P. W. R. Beaumont and E. Moncuill de Ferran, *J. Mater. Sci.*, **6**, 238(1971).
6. G. R. Sidey and F. J. Brandshaw, presented at Int. Conf. Carbon Fibers: Their Composites Appl., London, (1971).
7. J. Fitz-Randolph, D. D. Phillips, P. W. R. Beaumont and A. S. Tetelman, presented at St. Louis Symp. Advan. Fiber Composites, 5th, St. Louis, Missouri, (1971).
8. E. F. Olster and R. C. Jones, Massachusetts Inst. of Technol. Tech. Rep., R70-75, (Nov. 1970).
9. L. Xiao and R. Abbaschian, submitted to *Metall. Trans.*, (1991).
10. D. E. Clark, W. J. Dalzell and D. C. Folz, *Ceram. Eng. Sci. Proc.*, **2**, 1111(1988).
11. L. Xiao and R. Abbaschian, to be published.
12. J. J. Mecholsky and L. M. Barker, in Chevron-Notched Specimens: Testing and Stress Analysis, ASTM STP 855, edited by J. H. Underwood, S. W. Freiman and F. I. Baratta, (ASTM 1916 Race Street, Philadelphia, PA, 1984), pp. 324-36.
13. L. Xiao, Y. S. Kim and R. Abbaschian, in Intermetallic Matrix Composites, edited by D. L. Anton, P. L. Martin, D. B. Miracle and K. McMeeking, *MRS Proc.*, **194**, 399(1990).
14. L. Xiao and R. Abbaschian, submitted to *Mater. Sci. Eng.*, (1991).
15. J. D. Cotton, Y. S. Kim and M. J. Kaufman, *Mater. Sci. Eng.*, **A144**, 287(1991).
16. J. D. A. Lofvander, J. Y. Yang, C. G. Levi and R. Mehrabian, in Advanced Metal Matrix Composites for Elevated Temperatures, edited by M. N. Gungor, E. J. Lavernia and S. G. Fishman, (ASM International, 1991), pp. 1-10.
17. W. H. Sutton and E. Feingold, *Mater. Sci. Res.*, **3**, 577(1966).
18. C. T. Lynch and H. M. Burte, in Metal Matrix Composites, ASTM STP 438, (Amer. Soc. Test. Mater., Philadelphia, PA, 1968), pp. 3-25.
19. B. J. Dalgleish, K. P. Trumble and A. G. Evans, *Acta Metall.*, **37**, 1923(1989).

# On the Strength and Stiffness of Ductile Phase Reinforced MoSi<sub>2</sub> Composites

L. Xiao and R. Abbaschian  
University of Florida  
Gainesville, FL, USA

## ABSTRACT

It has been established that substantial toughening of brittle matrices can be achieved by incorporating ductile reinforcements. However, in most cases the ductile reinforcements have lower elastic moduli than matrices, which would affect the stiffness and strength of the composites. In the present study, laminated composites of MoSi<sub>2</sub> reinforced by Nb foils were used to explore the effects of ductile reinforcement on the stiffness and strength of the composites. The effects of reinforcement size were also studied by changing thickness of the Nb laminae from 0.127 mm to 1.0 mm. Four point bending tests were conducted to measure the flexural strengths of the laminates. The results were analyzed in terms of the theory of laminated composites. It was found that residual thermal stresses had influence on the stiffness of the composites, and the strength of the composites relied heavily on the microstructure of the MoSi<sub>2</sub> matrix. Furthermore, it was found that both of stiffness and strength of the composites could be predicted from the theory of laminated composites provided that the residual thermal stresses and the microstructure of the MoSi<sub>2</sub> matrix were taken into account.

## 1. INTRODUCTION

Most ceramics and intermetallics have high elastic

moduli, low densities, and can withstand high temperatures and hostile environments. These properties make them attractive candidates for high temperature structural applications. Nevertheless, intrinsic brittleness of these materials impedes their applications as structural materials. Recent progresses in composite technology have significantly improved toughness of ceramics and intermetallics. Among various toughening approaches, ductile phase toughening has been shown to be an effective way to improve toughness of ceramics and intermetallics [1-8]. Ductile reinforcements used usually have lower elastic moduli than ceramic and intermetallic matrices, such as TiAl/Nb [1], ZrO<sub>2</sub>/Zr [2], MoSi<sub>2</sub>/Nb [7] and WC/Co [8]. With the incorporation of a ductile phase into a matrix, stiffness of the composite would be lower than that of the matrix due to the lower elastic modulus of the ductile phase used. Similarly, strength of the composite would be lower than that of the matrix because of load transfer from the ductile phase to the matrix. Small decreases in these two properties are desirable because both stiffness and strength are crucial properties for structural materials.

In the present study, how strength and stiffness are affected by the addition of ductile reinforcements to brittle matrix has been investigated. Comparison between the experimental results and the laminate plate theory has been emphasized to examine any special

characteristics of ductile-phase-reinforced brittle matrix composites. The system selected for investigation was MoSi<sub>2</sub> matrix reinforced by Nb foils because a significant improvement in fracture toughness of the composites has been achieved in a related study [9]. Also, Nb metal has a lower elastic modulus (105 GPa) than MoSi<sub>2</sub> matrix (379 GPa). Due to such a combination, lower strength and stiffness of the composites are anticipated compared to the basic matrix. Another objective of the study is to explore the effects of reinforcement size on the stiffness and strength of the composites, which has been achieved by changing thickness of the Nb laminae from 0.127 to 1.00 mm.

## II. REVIEW OF LAMINATED PLATE EQUATIONS

In order to quantitatively analyze the experimental results and illustrate some consequence, the laminated plate equations used in the present study are reviewed briefly. For laminated beams having ratios of inplane dimensions to thickness less than ten as in the present study, beam deflection is considerably larger than predicted by classical laminated plate theory owing to the effects of transverse shear deformation and rotatory inertia [10,11]. Therefore, the effects of transverse shear deformation and rotatory inertia on beam deflection have been taken into account in the present study.

**2.1 ELASTIC MODULI OF LAMINATES** - For four point bending of a symmetric laminate beam, Fig. 1, the relation between deflection of the laminated beam,  $W$ , and load is given by [12]

$$W = \frac{PL^3}{768 E_b I} \left[ 1 - 48 \left( \frac{x}{L} \right) + 48 \left( \frac{x}{L} \right)^2 - 8 S \right]$$

$$\text{for } L/4 \leq x \leq L/2 \quad \dots \quad (1)$$

where  $P$  and  $L$  are defined in Fig. 1,  $I$  is the moment of inertia of the cross section of the beam,  $E_b$  the effective bending modulus of the laminated beam,  $S$  is a shear correction factor given by

$$S = \frac{1}{K} \left( \frac{E_b}{G_{xz}} \right) \left( \frac{h}{L} \right)^2 \quad \dots \quad (2)$$

where  $K$  equals 5/6, a parameter introduced by Reissner [13] in the constitutive relation for transverse shear,  $G_{xz}$  is shear modulus of the

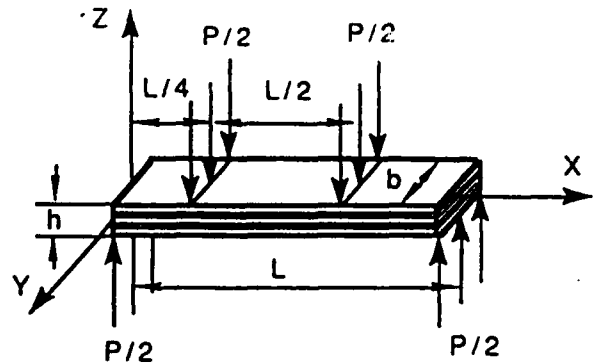


Fig. 1 Schematic of a laminated bend bar and the arrangement of a bend test.

laminates,  $h$  is thickness of the beam and  $E_b$  has the same meaning as in eq (1), which in the case of laminates consisting of isotropic laminae has been shown by Pagano [14] to be equal to

$$E_b = \frac{\sum_{k=1}^N E^k I^k}{I} \quad \dots \quad (3)$$

where  $E^k$  is the modulus of the  $k$ th layer relative to the beam axis,  $I^k$  is the moment of inertia of the  $k$ th layer relative to the midplane, and  $N$  the number of layers in the laminate.

By solving equations (1) and (2) simultaneously, the effective bending modulus in terms of the quarter point deflection can be obtained as

$$E_b = \frac{PL^3}{8 b h^3 \left[ Wq - \frac{PL}{8 K b h G_{xz}} \right]} \quad \dots \quad (4)$$

where  $Wq$  is the deflection at the quarter point and  $b$  the width of the beam. By using eq. (4), the effective bending modulus can be calculated from load-displacement data in 4-point bending tests.

**2.2 STRESS DISTRIBUTION IN LAMINATES** - Following Yang, Norris and Stavsky [10] and Whitney and Pagano [11], the constitutive equation for a layer in a laminate is given by

$$\begin{bmatrix} \sigma_x \\ \sigma_y \\ \sigma_{xy} \end{bmatrix} = \begin{bmatrix} Q_{11} & Q_{12} & Q_{16} \\ Q_{12} & Q_{22} & Q_{26} \\ Q_{16} & Q_{26} & Q_{66} \end{bmatrix} \begin{bmatrix} \epsilon_x^0 + z \kappa_x \\ \epsilon_y^0 + z \kappa_y \\ \epsilon_{xy}^0 + z \kappa_{xy} \end{bmatrix} \quad \dots \quad (5)$$

where  $[Q_{ij}]$  are the transformed reduced stiffness matrix for the layer in the laminate,  $\sigma_x$ ,  $\sigma_y$ , and  $\sigma_{xy}$  are stresses in the layer of the laminate at any position through the thickness  $z$ ,  $\epsilon_x^0$ ,  $\epsilon_y^0$  and  $\epsilon_{xy}^0$  are the midplane strains, and  $\kappa_x$ ,  $\kappa_y$  and  $\kappa_{xy}$  are derivatives defined as follows.

$$\kappa_x = \frac{\partial \phi_x}{\partial x}, \quad \kappa_y = \frac{\partial \phi_y}{\partial y}, \quad \kappa_{xy} = \frac{\partial \phi_x}{\partial y} + \frac{\partial \phi_y}{\partial x}$$

where  $\phi_x$  and  $\phi_y$  are the rotations about  $y$ -axis and  $x$ -axis, respectively. For bending of a symmetric laminate beam, derivative  $\kappa$ 's are expressed as

$$\begin{bmatrix} \kappa_x \\ \kappa_y \\ \kappa_{xy} \end{bmatrix} = \begin{bmatrix} D_{11} & D_{12} & D_{16} \\ D_{12} & D_{22} & D_{26} \\ D_{16} & D_{26} & D_{66} \end{bmatrix} \begin{bmatrix} M_x \\ M_y \\ M_{xy} \end{bmatrix} \quad \dots\dots\dots (6)$$

where  $M_x$ ,  $M_y$  and  $M_{xy}$  are the moment resultants at the midplane, and  $D_{ij}$  are elements of the inverse of stiffness matrix  $D$  of the laminate. For bending of a laminated beam, Fig. 1,

$$\epsilon_x^0 = \epsilon_y^0 = \epsilon_{xy}^0 = 0 \quad \dots\dots\dots (7)$$

$$M_y = M_{xy} = 0 \quad \dots\dots\dots (8)$$

Solving equations (5) - (8) simultaneously, the stresses in each layer of the beam at any position through the thickness  $z$  during four-point bending tests can be calculated and the resultant equation is

$$\sigma_x = -z [ Q_{11} D_{11}^* + Q_{12} D_{12}^* + Q_{16} D_{16}^* ] \{ PL/8b \} \text{ for } L/4 \leq x \leq L/2 \quad \dots\dots\dots (9)$$

The outer layer stresses during the bending test can be found from eq. (9) by setting  $z = -(h/2)$ .

**2.3 RESIDUAL THERMAL STRESSES IN LAMINATES** - Equation (5) can be utilized to calculate residual thermal stresses in laminates. Following Tsai and Hahn [15], the residual thermal stresses,  $[\sigma^R]_{xy}$ , and strains,  $[\epsilon^R]_{xy}$ , in a layer of the laminate at any position through the thickness  $z$  are expressed as

$$[\sigma^R]_{xy} = [Q'] [\epsilon^R]_{xy} \quad \dots\dots\dots (10)$$

where  $[Q']$  is defined in equation (5), and the notations

$$[\sigma^R]_{xy}^T = [ \sigma_x^R, \sigma_y^R, \sigma_{xy}^R ]$$

$$\text{and } [\epsilon^R]_{xy}^T = [ \epsilon_x^R, \epsilon_y^R, \epsilon_{xy}^R ]$$

The subscript  $xy$  denotes the  $X, Y, Z$  coordinate system used. We will use this notation in the following text unless otherwise mentioned. The residual thermal strains are given by

$$[\epsilon^R]_{xy} = [\epsilon^{0T}]_{xy} + z [\kappa^T]_{xy} - [e^T]_{xy} \quad \dots\dots\dots (11)$$

where  $[e^T]_{xy}$  are the unconstrained thermal strains,  $[\epsilon^{0T}]_{xy}$  the final midplane strains and  $[\kappa^T]_{xy}$  the final derivatives in the  $X, Y, Z$  coordinate system as temperature changes from  $T_1$  to  $T_2$ . The unconstrained thermal strains  $[e^T]_{xy}$  are related to the unconstrained thermal strains along the lamina principal axes,  $[e^T]_{12}$ , and coefficients of the thermal expansion of the lamina with the following equations

$$[e^T]_{xy} = [T_e]^{-1} [e^T]_{12} \quad \dots\dots\dots (12)$$

and

$$e_1^T = \alpha_1 \Delta T, \quad e_2^T = \alpha_2 \Delta T, \quad e_{12}^T = 0 \quad \dots\dots\dots (13)$$

where  $\alpha_i$  are the coefficients of the thermal expansion of the lamina in the lamina principal directions,  $[T_e]^{-1}$  is the inverse of the strain transformation matrix, and the subscript 12 denotes the lamina principal axis coordinate. The final strains, which are  $[\epsilon^{0T}]_{xy} + z [\kappa^T]_{xy}$ , are determined from

$$\begin{bmatrix} \epsilon^{0T} \\ \kappa^T \end{bmatrix} = \begin{bmatrix} A & B \\ B & D \end{bmatrix} \begin{bmatrix} N^T \\ M^T \end{bmatrix} \quad \dots\dots\dots (14)$$

where  $A, B$  and  $D$  are the stiffness matrices of the laminate, and  $N^T$  and  $M^T$  are the thermal stress and moment resultants which are defined as

$$(N_x^T, N_y^T, N_{xy}^T) = \int_{-h/2}^{h/2} (\sigma_x^T, \sigma_y^T, \sigma_{xy}^T) dz$$

$$(M_x^T, M_y^T, M_{xy}^T) = \int_{-h/2}^{h/2} (\sigma_x^T, \sigma_y^T, \sigma_{xy}^T) z dz$$

$$\dots\dots\dots (15)$$

with  $[\sigma^T]$  given by

$$[\sigma^T]_{xy} = [Q'] [e^T]_{xy} \quad \dots\dots\dots (16)$$

Solving equations (10) - (16) simultaneously, residual thermal stresses in the laminate can be calculated.

### III. EXPERIMENTS

MoSi<sub>2</sub> composite laminates with 20 vol.% of Nb foils were produced by vacuum hot pressing at 1400 ± 5°C under a pressure of 40 MPa for 1 hour. All hot pressed discs were held at 800°C for 1 hour before taking out the hot pressing chamber to reduce residual thermal stresses, and then furnace cooled to room temperature. Thickness of the Nb foils used ranged from 0.127 to 1.00 mm. The laminates produced were all symmetric relative to the midplane and the outside layers of the laminates were always MoSi<sub>2</sub> regardless of the thickness of the Nb foils used. For comparison, monolithic MoSi<sub>2</sub> specimens were also fabricated by hot pressing with the same condition as the composite laminates.

Flexural strengths of the monolithic MoSi<sub>2</sub> and composite laminates were measured using a 4-point bending fixture mounted on a hydro-servo controlled MTS. The inner and outer span of the bend fixture are 10 and 20 mm, respectively. The bend bars had a rectangular cross-section with nominal dimensions of 5.08 mm thick by 4.00 mm wide. These dimensions were limited essentially by the available size of the hot pressed specimens. The orientation of the specimens was such that the tensile and compressive faces of the bend bars lay perpendicular to the hot pressing direction and parallel to the lamina plane. The surfaces of the bend bars were ground using SiC abrasive paper up to 320 grit with the final grinding direction parallel to the bar axis. The testing was done at a cross-head speed of 0.005 in/min, and the load was recorded as a function of cross head displacement. Since objective of the study was to compare the stiffness and flexural strength of specimens with different sizes of Nb reinforcement and no Nb reinforcement, no effort was made to strain gage the specimens in as much as the testing condition was held constant.

To find out residual thermal stresses in the laminates, coefficients of the thermal expansion of the Nb foils used and hot pressed monolithic MoSi<sub>2</sub> were measured using a dilatometer with a

heating rate of 4°C/min and Ar atmosphere from room temperature to 1200°C. Microstructure examination of the laminates was conducted using an optical microscope. The volume fraction and size of the porosity and the grain size in the MoSi<sub>2</sub> matrix were determined using an image analyzer.

### IV. RESULTS AND DISCUSSION

4.1 STIFFNESS OF THE LAMINATES - Fig. 2 shows three typical load-displacement curves of 4-point bend test on MoSi<sub>2</sub> laminates reinforced by 20 vol.% of Nb laminae with a thickness of 0.5 mm. The first load drop in the curves of Fig. 2 corresponds to the initiation and rapid propagation of a crack through the outside layer of MoSi<sub>2</sub> and the ending of the crack propagation at the front of the first Nb lamina encountered. The rest of the curves reveal the characteristics of ductile phase bridging and crack propagation through the rest of the MoSi<sub>2</sub> matrix. Due to this feature, the initial linear portion of the load-displacement curve is used to calculate a quantity,  $(P/bh^3)(1/(Wq - PL/8KbhGxz))$ , in equation (4), which is linearly proportional to the effective bending modulus of the laminate. Since the displacements in the present study were based on measurement of only cross-head displacements, eq. (4) cannot be utilized directly. Thus, the quantity  $(P/bh^3)(1/(Wq - PL/8KbhGxz))$  is normalized by a quantity  $C(P/bh^3)/Wq$  which is obtained from the bend test of the monolithic MoSi<sub>2</sub> specimens and is also

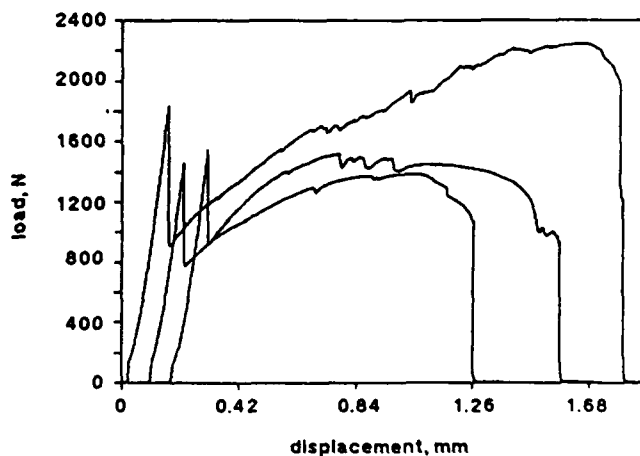


Fig. 2 Typical load-displacement curves of 4-point bend test on MoSi<sub>2</sub> laminates reinforced by 20 vol.% of Nb laminae with a thickness of 0.5 mm.

linearly proportional to the bending modulus of the specimens. The  $C$  in the aforementioned quantity is a constant taking into account the deflection due to the shear deformation of the beam and is derived from the stress function proposed by Ugural and Fenster [16]. The expression of  $C$  is

$$C = 1 + 2(1+\nu)(h/L)^2/0.84$$

where  $\nu$  is the Poisson's ratio of the beam, and  $L$  and  $h$  are defined in Fig. 1. The normalized quantity is called as normalized slope throughout the text for convenience. The normalized slopes measured are listed in table 1. For comparison, effective bending moduli calculated from eq. (3) are also normalized by elastic modulus of MoSi<sub>2</sub> and the results denoted as normalized modulus 1 are also included in table 1. The data of the normalized slope and modulus 1 versus thickness of the Nb

Table 1. Summary of the normalized stiffness of the laminates

| Material        | 1.0 mm Nb reinf. | 0.5 mm Nb reinf. | 0.25 mm Nb reinf. | 0.127 mm Nb reinf. |
|-----------------|------------------|------------------|-------------------|--------------------|
| Norm. slope     | 0.990            | 0.925            | 0.885             | 0.845              |
| Norm. modulus 1 | 0.995            | 0.941            | 0.913             | 0.884              |
| Norm. modulus 2 | 0.994            | 0.930            | 0.895             | 0.865              |

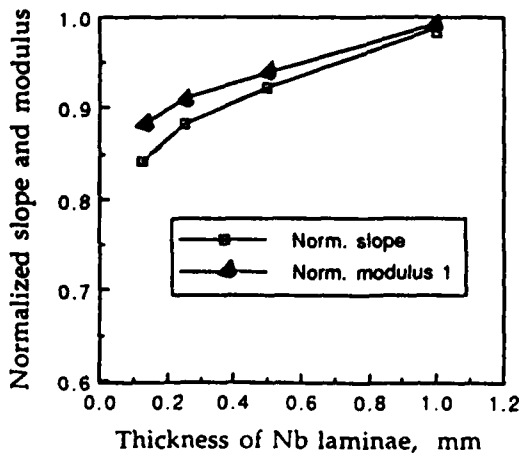


Fig. 3 Comparison between measured normalized slopes and calculated moduli as a function of the thickness of Nb laminae.

laminae are plotted in Fig. 3. As anticipated, Fig. 3 shows that the addition of Nb reinforcement decreases moduli of the laminates and the moduli of the laminates decrease with decreasing the thickness of the Nb laminae. The results are in good agreement with the fact that the moment of inertia of the cross section stemmed from MoSi<sub>2</sub> becomes smaller and smaller with decreasing Nb thickness while the volume fraction of Nb laminae is kept constant. It is noted that the normalized slopes and moduli show the same trend of stiffness variation with the thickness of the Nb laminae, indicating eq. (3) is an adequate equation to describe

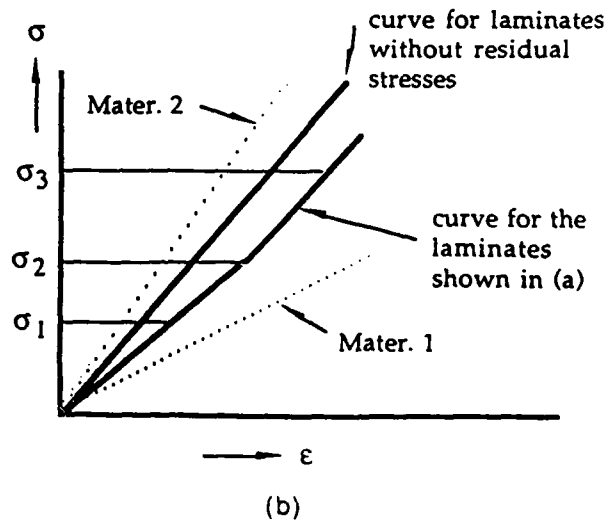
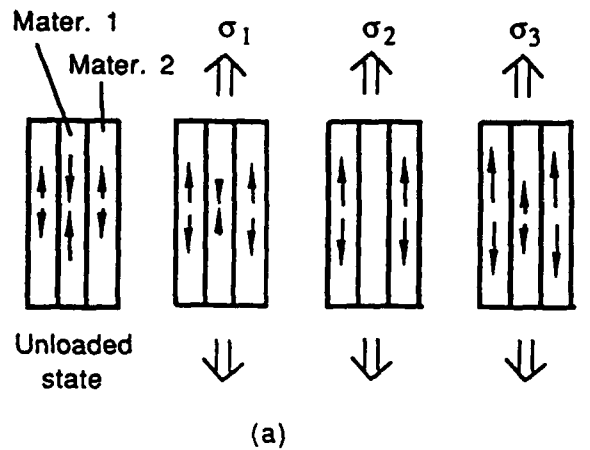


Fig. 4 A schematic showing how residual thermal stresses affect elastic modulus of the laminate. (a) Stress distribution in the laminate during a tensile loading, (b) the corresponding stress-strain curve of the laminate.

the effective bending moduli of the laminates.

By definition, the normalized slope should be exactly equal to the normalized modulus 1. However, Fig. 3 shows that the normalized moduli are always higher than the normalized slopes. The discrepancies are believed to be due to residual thermal stresses in the laminates. The effect of residual thermal stresses on the elastic modulus of laminates can be illustrated schematically in Fig. 4. Suppose the laminate shown in Fig. 4 has such residual stresses that material 1 is in compression and material 2 is in tension. When a tensile stress,  $\sigma_1$ , is applied to the laminate in a direction parallel to the lamina plane, the modulus of the laminate stems only from material 2 because material 1 does not carry any load at this stage, but simply change to less strained state. Only after the tensile stress is above  $\sigma_2$  which make material 1 restore to totally unstrained state, does material 1 begin to contribute modulus to the laminate. To verify this is the case in the present study, calculation of residual thermal stresses in the laminates were carried out using equations (10) - (16) with an assumption that no strain relaxation occurs during the cooling of the specimens from 800°C to room temperature. The coefficients of thermal expansion of the Nb and MoSi<sub>2</sub> used in the calculation for this temperature range were  $7.599 \times 10^{-6}/^\circ\text{C}$  and  $8.227 \times 10^{-6}/^\circ\text{C}$ , respectively, which were measured in the present study. The calculated results are listed in table 2. As seen from the table, Nb laminae are in compression while MoSi<sub>2</sub> matrix is in tension in the as-hot pressed laminates. Therefore, according to the hypothesis proposed earlier, the bending modulus of the tensile part of the beam comes only from MoSi<sub>2</sub>, and that of the compressive part of the beam comes only from Nb at least at early stage of the loading. More and more MoSi<sub>2</sub> and Nb

Table 2. Summary of the residual thermal stresses and strains in the as-hot pressed laminates

| Lamina                         | Nb                      | MOSi <sub>2</sub>       |
|--------------------------------|-------------------------|-------------------------|
| Unconstrained strain, $e^T$    | $-6.079 \times 10^{-3}$ | $-6.582 \times 10^{-3}$ |
| Final thermal strain, $e^T$    | $-6.539 \times 10^{-3}$ | $-6.539 \times 10^{-3}$ |
| Residual thermal strain, $e^R$ | $-4.599 \times 10^{-4}$ | $4.249 \times 10^{-5}$  |
| Residual thermal stress, $s^R$ | -79.16 MPa              | 19.40 MPa               |

contribute to the bending modulus of the laminate as the bending load is increased. The final bending modulus of the laminate depends on how much MoSi<sub>2</sub> and Nb make contributions. To find out this, the stress distribution in the laminates reinforced by different thicknesses of Nb laminae were calculated using equations (5) - (9). The maximum bending load in the calculation was determined with an assumption that the outer layer of MoSi<sub>2</sub> can only sustain a tensile stress of 319 MPa which is the mean strength of MoSi<sub>2</sub> measured in the present study. The residual thermal stresses were taken into account by superimposing them to the stress field induced by the bending moment. The results are plotted in Fig. 5. Note that all the laminates used did not have

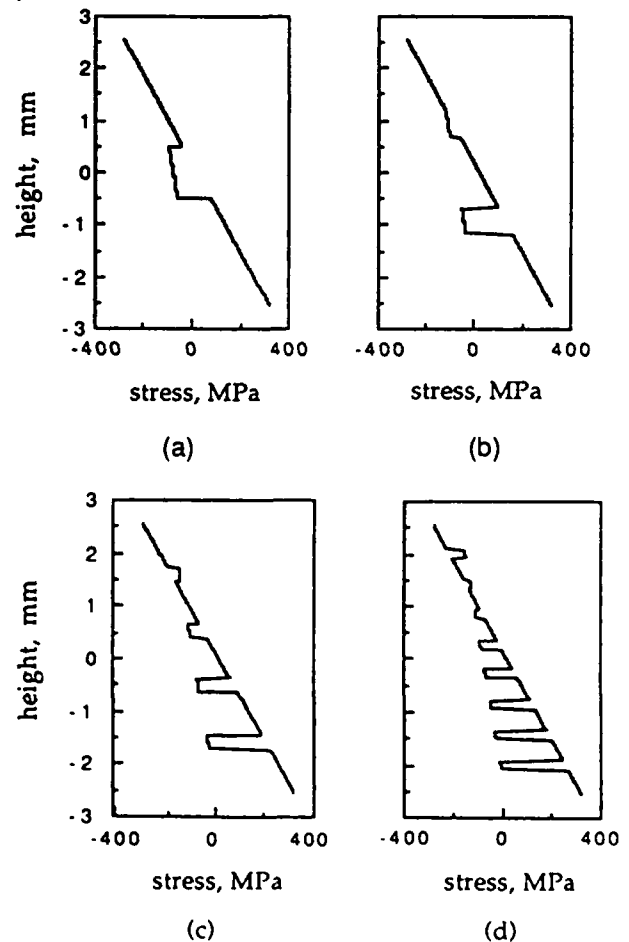


Fig. 5 Calculated stress distribution in the MoSi<sub>2</sub> laminates reinforced by 20 vol.% of Nb laminae with a thickness of (a) 1.0 mm, (b) 0.5 mm, (c) 0.25 mm and (d) 0.127 mm.

contributions from Nb foils in the tensile part of the beam because the Nb laminae still have not changed from compression to tension. In light of this reasoning, eq. (3) was used to calculate the moduli of the laminates without taking contributions of half Nb laminae into account. The moduli obtained were again normalized by the modulus of MoSi<sub>2</sub> and referred to as normalized modulus 2 as shown in table 1. Fig. 6 shows the comparison among the normalized slope, modulus 1 and modulus 2. It is obvious that the normalized modulus 2 fits the experimental data better than the normalized modulus 1, indicating that residual stresses indeed affect the moduli of the laminates. According to the hypothesis proposed, the bending moduli of the laminates should change gradually during the bending test, i. e. the slopes of the load-displacement curves should change gradually. This is very hard to ascertain in the present study because the change is very small and no strain gage is used.

#### 4.2 FLEXURAL STRENGTH OF THE LAMINATES

The measured mean strengths of all the laminates as a function of thickness of the Nb lamina are plotted in Fig. 7. For comparison, the predicted flexural strengths of the laminates calculated using eqs. (5) - (9) are also included in Fig. 7. In the calculation the residual thermal stresses are superimposed to the stresses field induced by the bending moment and an assumption is made that the outer layer of MoSi<sub>2</sub> can only sustain a tensile

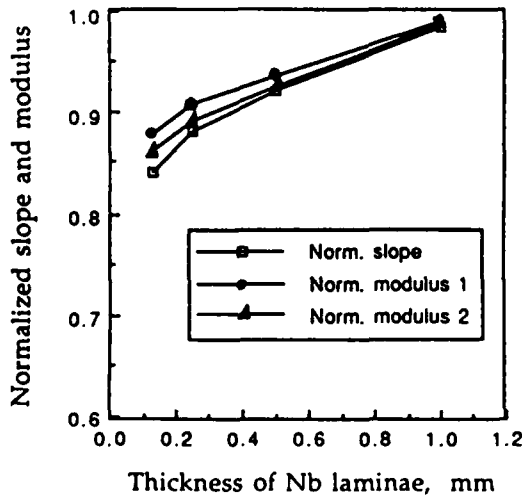


Fig. 6 Comparison among measured normalized slopes and calculated normalized moduli with contribution of all Nb laminae and of only half Nb laminae.

stress of 319 MPa which is the mean strength of MoSi<sub>2</sub> measured in the present study. Note that the laminate plate theory predicts a decrease in the strength with decreasing thickness of Nb lamina. However, the experimental results do not exhibit such behavior. Also note that there exist a large scatter in the data of the strengths. Each experimental datum point in Fig. 7 is the results of 12 specimens which come from 3 batches of hot pressing. If the strengths are examined in terms of each batch of the hot pressing, the scatter of the data becomes much smaller, suggesting processing factors play a role in the strength of the laminates.

Examination of microstructures of the MoSi<sub>2</sub> matrices in different laminates revealed that size and volume fraction of porosity and grain size varied from batch to batch. Fig. 8 (a) - (c) show some typical microstructures of MoSi<sub>2</sub> matrices from different laminates, and the quantitative measurement of the microstructure and the corresponding strength measured are summarized in table 3. The mean lineal intercept, L<sub>3</sub>, used in table 3 is not a diameter, but is frequently used to estimate diameters [17,18]. It is noted that the smallest grain size measured is close to the starting size of MoSi<sub>2</sub> powder used which is ~5 μm in diameter. Change of the grain size within controlled variation of hot pressing temperature of only ± 5°C indicates that the hot pressing temperature used in the present study is the critical temperature at which grain growth is about to occur. It is also noted that strength scatter becomes smaller when strength is reported based on the data from the subgroups. Such change of the strength is

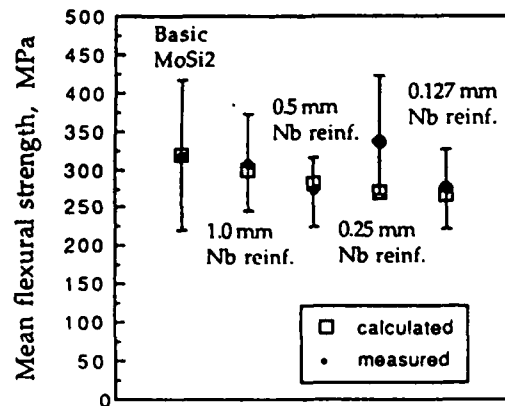
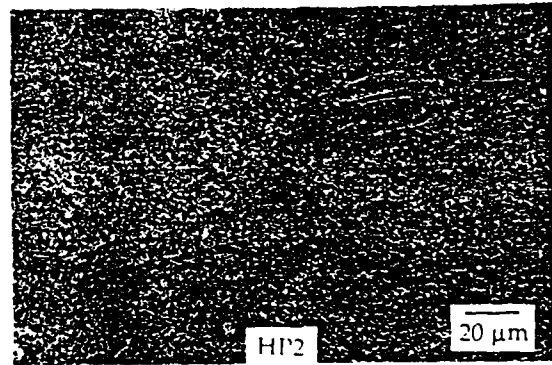
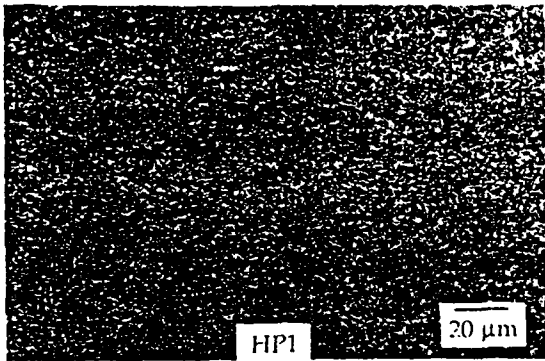
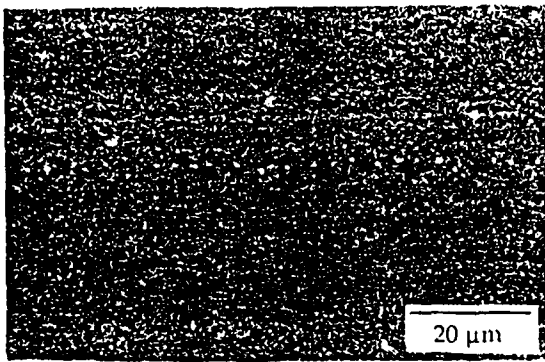
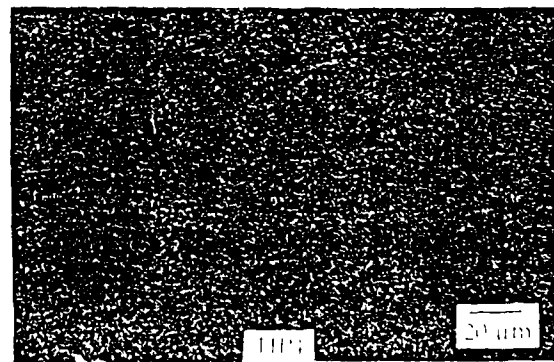
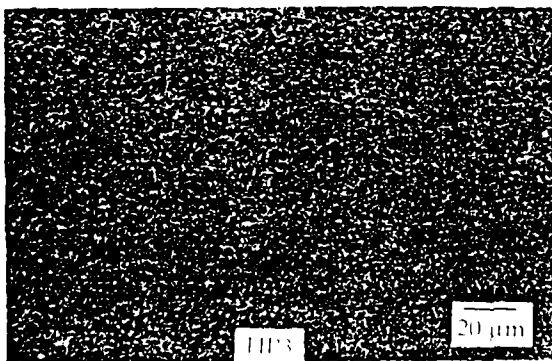
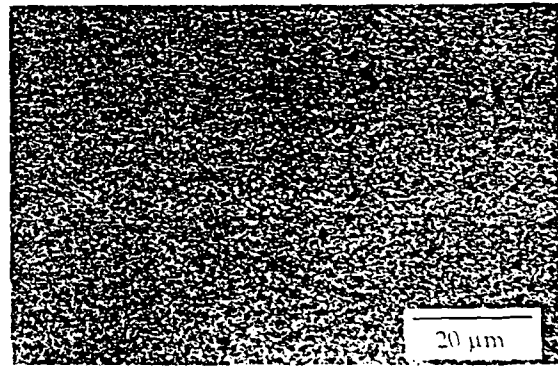
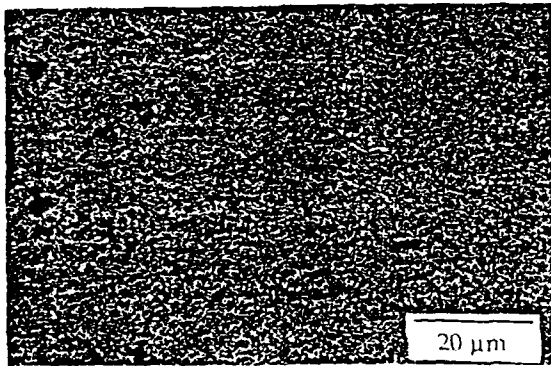


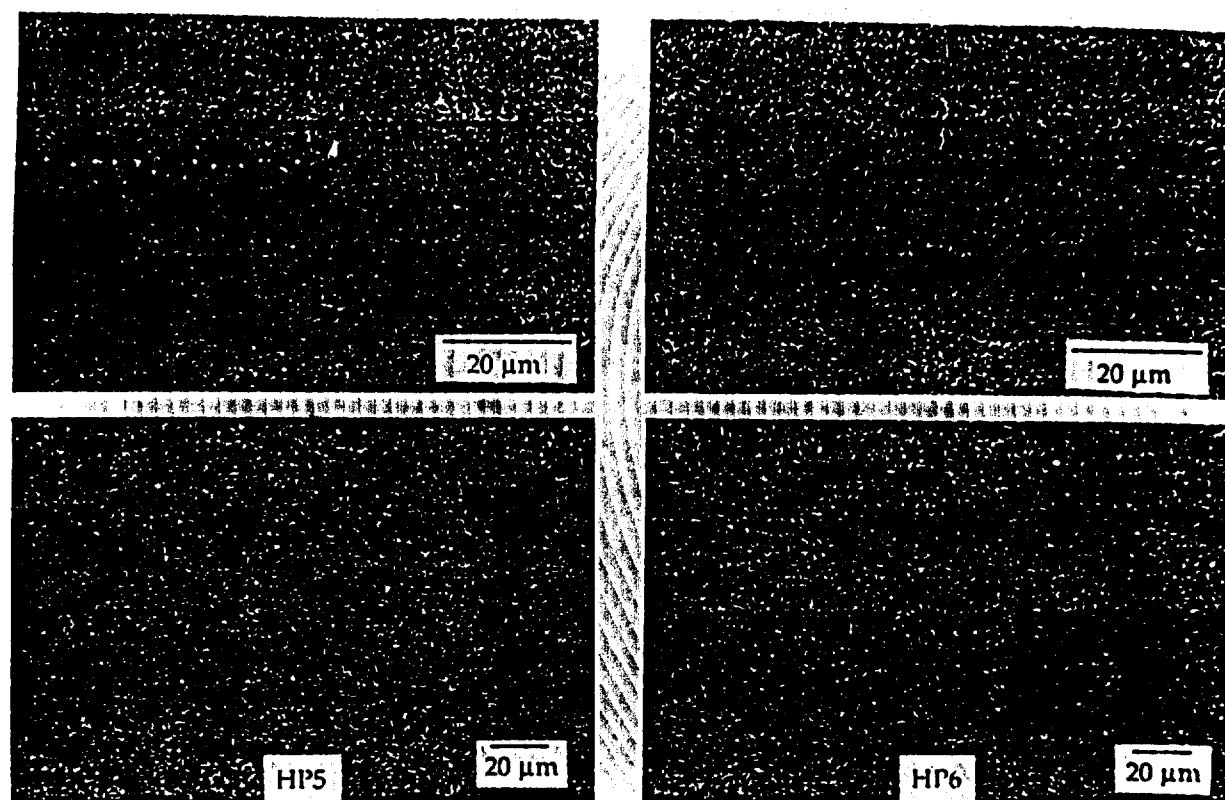
Fig. 7 A plot showing measured and calculated mean flexural strengths of MoSi<sub>2</sub> laminates reinforced by 20 vol.% of Nb laminae as a function of the thickness of the Nb laminae.



(a)



(b)



(c)

Fig. 8 Optical microstructures of MoSi<sub>2</sub>. Top micrographs are as-polished surfaces showing porosity features; bottom micrographs are the corresponding polarized light images showing grain features. (a) The monolithic MoSi<sub>2</sub>, (b) the MoSi<sub>2</sub> matrix in the laminates reinforced by 1.0 mm thick Nb laminae, and (c) the MoSi<sub>2</sub> matrix in the laminates reinforced by 0.5 mm thick Nb laminae.

believed due to the change of the microstructures as shown in Fig. 8 and table 3.

It is well known that the strength of brittle materials, especially ceramics, are controlled by two main sets of parameters, i. e. material parameters (such as composition, crystal structure, size and volume fraction of porosity, grain size, surface condition, cracks and internal stresses from thermal expansion anisotropy or phase transformation, etc. ) and environmental parameters (such as temperature, atmosphere, strain rate and loading methods, etc. ). The relevant variables in the present study are size and volume fraction of porosity, grain size, surface condition and internal stresses, because other parameters have been kept constant. Pores play a two-fold function in the strength of brittle materials; one is as fracture origin [19], the other is reduction of the effective solid area which resists fracture [20]. In the present case, the pores can not be controlling factor in the fracture origin because the size of the

porosity is much smaller than that of the machining flaw, ~30 μm, produced by grinding with 320 grit SiC abrasive paper [21,22]. Change of the volume fraction of porosity did not show systematic effects on the strength as seen in table 3. Thus, the change of the strength is attributed to change of the grain size. Table 3 shows that the strength decreases with increasing grain size within each group. Similar grain size dependence of strength were observed in other ceramics [20, 22-25]. Such grain size dependence of strength is believed due to internal stresses from thermal expansion anisotropy of the noncubic MoSi<sub>2</sub> and the change of resistance to crack propagation for such specific size of the machining flaw because the ratio of machining flaw to grain size is about 1 - 3 in the present case depending on whether the maximum or average grain size is used [23,26].

To avoid the effect of microstructure on the strength, the strengths measured from laminates with similar grain size of MoSi<sub>2</sub> matrix are plotted

Table 3. Microstructural properties of the matrices and the corresponding flexural strengths of the laminated composites

| Group Subgroup   | Monolithic MoSi <sub>2</sub> HP1 | MoSi <sub>2</sub> HP2 | 1.0 mm Nb reinf. HP3 HP4 |           | 0.5 mm Nb reinf. HP5 HP6 |            |
|--|----------------------------------|-----------------------|--------------------------|-----------|--------------------------|------------|
| Strength, MPa  | 393±60                           | 251±17                | 363±30                   | 288±67    | 284±38                   | 253±26     |
| Volume fraction of porosity (%)                          | 6.04±0.93                        | 6.78±1.11             | 9.28±0.99                | 5.82±0.47 | 6.18±0.66                | 6.87±1.70  |
| Mean lineal intercept of porosity, L <sub>3</sub> , (mm) | 0.81±0.07                        | 1.00±0.05             | 1.15±0.10                | 0.93±0.05 | 0.81±0.04                | 1.23±0.15  |
| Mean lineal intercept of grain, L <sub>3</sub> , (mm)    | 4.88±0.23                        | 9.75±2.88             | 4.94±0.53                | 7.32±2.46 | 6.09±1.47                | 10.97±2.74 |
| Largest grain diameter (mm)                              | 24.39                            | 48.78                 | 12.19                    | 46.34     | 24.39                    | 48.78      |

in Fig. 9. Calculated strengths from laminate plate theory are also included in the figure with an assumption that the outer layer of MoSi<sub>2</sub> can only carry a tensile stress of 393 MPa which is the mean strength of the monolithic MoSi<sub>2</sub> specimens with average grain size of 4.88 μm. Note that the experimental data of subgroup C is well below the prediction, which is attributed to a relatively large grain size of subgroup C specimens. Therefore, all the calculated data in Fig. 9 fit the experimental data better than in Fig. 7 which does not exclude the effect of grain size. Thus, it is concluded that when microstructure of the brittle matrix is kept constant, the laminate plate theory could be used to describe the strength of brittle matrix laminates reinforced by ductile phase.

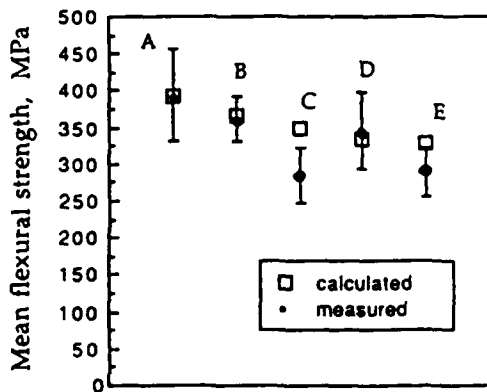


Fig. 9 A plot of mean flexural strengths measured and calculated from the laminates with similar grain size of MoSi<sub>2</sub> matrix. The grain size of the MoSi<sub>2</sub> matrices and the laminated composites are  
 A: 4.88 mm, monolithic MoSi<sub>2</sub>;  
 B: 4.94 mm, 1.0 mm Nb reinforced;  
 C: 6.09 mm, 0.5 mm Nb reinforced;  
 D: 4.86 mm, 0.25 mm Nb reinforced;  
 E: 5.74 mm, 0.127 mm Nb reinforced.

However, effect of the microstructure of the brittle matrix could be very strong and overshadows the effect of the addition of ductile phase.

## V. SUMMARY AND CONCLUSIONS

The present set of experiments show that toughening brittle matrix by incorporating a ductile phase with a low elastic modulus is accompanied by a reduction in the stiffness of the composites. As much as 15% reduction in flexural stiffness is observed in the MoSi<sub>2</sub> laminates toughened by 20 vol.% of Nb laminae with a thickness of 0.127 mm. The magnitude of the reduction in flexural stiffness is a function of the thickness of the Nb laminae, as predicted by the laminate plate theory and confirmed in the present investigation. At a constant volume fraction of the reinforcement, the thicker the Nb laminae, the higher the stiffness of the laminates. Residual thermal stresses in the laminates is found to have influence on the stiffness of the laminates. Such effect always decreases the stiffness of the composites regardless of the loading methods. The use of the laminate plate theory is found to predict the stiffness of the MoSi<sub>2</sub>/Nb laminates quite well as long as the residual thermal stresses is taken into account.

The measurement of the flexural strengths indicates that flexural strength is also decreased with the incorporation of a ductile phase with a low elastic modulus. Such decrease becomes larger as the Nb laminae become thinner at a constant volume fraction of the Nb reinforcement. The observed decrease in the strength can be estimated using the laminate plate theory so long as the microstructure of the matrix is kept constant. In the present instance, the microstructure of the matrix shows a strong influence on the flexural

strength of the laminated composites and in fact overshadows the effect of the incorporation of the ductile phase. These results suggest that the controlling factor in the strength of ductile-phase-reinforced brittle matrix composites is the microstructure of the matrix. Therefore, a good control of the microstructure of the brittle matrix is crucial to obtaining high strength composites containing a ductile phase with a lower elastic modulus.

**Acknowledgements** --- The authors are grateful to the support of the Defense Advanced Research Projects Agency (DARPA) through contract MDA972-88-J-1006.

#### REFERENCES

1. C. K. Elliott, G. R. Odette, G. E. Lucas and J. W. Sheckherd, "High Temperature, High Performance Composites", Edited by Lemkey et al., *MRS Proc.*, 120, 95-102(1988).
2. A. V. Virkar and D. L. Johnson, *J. Am. Ceram. Soc.*, 60, 514-19(1977).
3. M. I. Mendelson and M. E. Fine, *J. Am. Ceram. Soc.*, 57, 154-59(1974).
4. J. Gurland, *Trans. ASM*, 50, 1063-71(1958).
5. V. V. Kristie and P. S. Nicholisin, *J. Am. Ceram. Soc.*, 64, 499-504(1981).
6. C. A. Anderson and M. K. Aghajanian, *Ceram. Eng. Sci. Proc.*, 2, 621-26(1988).
7. L. Xiao, Y. S. Kim and R. Abbaschian, "Intermetallic Matrix Composites", Edited by D. L. Anton, P. L. Martin, D. B. Miracle and R. McMeeking, *Proc. M. R. S. Meeting*, 194, 399-404(1990).
8. J. L. Chermant and F. Osterstock, *J. Mater. Sci.*, 11, 1939-51(1976).
9. L. Xiao, Y. S. Kim, R. Abbaschian and R. J. Hecht, to be published in *Mater. Sci. Eng.*, 1991.
10. P. C. Yang, C. H. Horris and Y. Stavsky, *International J. of Solids and Structures*, 2, 665-84(1966).
11. J. M. Whitney and N. J. Pagano, *J. of applied Mech.*, 37, 1031-36(1970).
12. J. M. Whitney, "Structural Analysis Of Laminated Anisotropic Plates", p. 288, Technomic Publishing Company, Inc., Lancaster, Pennsylvania (1987).
13. E. Reissner, *J. of Applied Mech.*, 12, 69-77(1945).
14. N. J. Pagano, *J. of composite Mater.*, 1, 336-42 (1967).
15. S. W. Tsai and H. T. Hahn, "Introduction to Composite Materials", p. 345, Technomic Publishing Company, Inc., Westport, CT (1980).
16. A. C. Ugural and S. K. Fenster, "Advanced Strength and Applied Elasticity", p. 67, Elsevier North Holland, Inc., New York, NY (1981).
17. R. T. Dehoff, *Metals Forum*, 5, 4-12(1982).
18. ASTM Standards, *Physical and Mechanical Testing of Metals*, p. 448, Philadelphia, PA. (1967).
19. D. R. Biswas and R. M. Fulrath, "Fracture Mechanics of Ceramics", Vol. 4, pp. 933-43, Edited by R. C. Bradt, D. P. H. Hasselman and F. F. Lange, Plenum, New York (1978).
20. R. W. Rice, S. W. Freiman, R. C. Pohsna, J. J. Mecholsky, Jr. and C. Cm. Wu, "Fracture Mechanics of Ceramics", Vol. 4, pp. 840-76, Edited by R. C. Bradt, D. P. H. Hasselman and F. F. Lange, Plenum, New York (1978).
21. R. W. Rice, J. J. Mecholsky, Jr. and P. F. Becher, *J. Mater. Sci.*, 16, 853-62(1981).
22. R. W. Rice and J. J. Mecholsky, Jr., "Science of Ceramic Machining and Surface Finishing, II", pp. 351-78, Edited by B. J. Hockey and R. W. Rice, *Nat. Bur. Stand. (U. S.) Spe. Publ.*, No. 562, Washington, D. C. (1979).
23. R. W. Rice, "Science of Ceramic Machining and Surface Finishing, II", pp. 429-52, Edited by B. J. Hockey and R. W. Rice, *Nat. Bur. Stand. (U. S.) Spe. Publ.*, No. 562, Washington, D. C. (1979).
24. R. W. Rice, "Ceramics for High-Performance Applications", pp. 287-343, Edited by J. J. Burke, A. E. Gorum and R. N. Katz, Brook Hill, Chestnut Hill, Mass. (1974).
25. R. E. Tressler, R. A. Langensiepen and R. C. Bradt, *J. Am. Ceram. Soc.*, 57, 226-27(1974).
26. J. P. Singh, A. V. Virkar, D. L. Shetty and R. S. Gordon, *J. Am. Ceram. Sci.*, 62, 179-183 (1979).

# Interfacial modification in Nb/MoSi<sub>2</sub> composites and its effects on fracture toughness

L. Xiao and R. Abbaschian

*Department of Materials Science and Engineering, University of Florida, Gainesville, FL 32611 (USA)*

## Abstract

Niobium-reinforced MoSi<sub>2</sub> composites have shown a large improvement in fracture toughness over the MoSi<sub>2</sub> matrix. However, the chemical incompatibility of niobium with MoSi<sub>2</sub> has to be solved for high-temperature structural applications of the composite. In addition, the effects of interfacial coatings on the fracture toughness of ductile-phase-reinforced composites need to be investigated to find the optimum toughening effect of niobium reinforcement. In the present study different oxide coatings, Al<sub>2</sub>O<sub>3</sub> and ZrO<sub>2</sub>, were applied to niobium reinforcement and effectiveness of the coatings as diffusion barriers was evaluated. The mechanical behavior and the fractographic characteristics of constrained niobium were also examined. Finally, the effect of the coatings on fracture toughness of the composites was studied and compared with predictions based upon tensile tests on a single constrained niobium reinforcement. The results are discussed in terms of the interfacial fracture energy and micromechanical models of ductile-phase-reinforced composites.

## 1. Introduction

Molybdenum disilicide is an attractive candidate material for elevated-temperature structure applications because of its high melting temperature (2030 °C), and excellent oxidation resistance at elevated temperatures. However, it has a low fracture toughness at ambient temperatures and a high creep rate at high temperatures. Toughening of the material can be achieved by the incorporation of a ductile second phase [1-6]. Previous studies [7, 8] have shown that incorporating niobium filaments or foils into the MoSi<sub>2</sub> matrix is a feasible approach to improving the toughness. For example, it has been shown [8] that the fracture toughness of MoSi<sub>2</sub> can be increased to around 12 MPa m<sup>1/2</sup> by the incorporation of 20 vol.% of niobium filaments. However, the resulting composites are unstable at elevated temperatures because niobium reacts with MoSi<sub>2</sub>, forming other brittle intermetallic compounds such as (Mo,Nb)<sub>3</sub>Si<sub>3</sub> at the interface. The formation of the interfacial compounds at the expense of the ductile reinforcement not only degrades the toughening effect of the ductile phase, but also causes a notch effect on the ductile phase [9]. Therefore, the use of an inert diffusion barrier coating on the reinforcement is essential to decrease the interface interactions during processing, and also to maintain the integrity of the ductile phase at elevated service temperatures.

In the present study, oxide coatings (Al<sub>2</sub>O<sub>3</sub> and ZrO<sub>2</sub>) were applied to the surface of the niobium reinforcement prior to compositing. The effectiveness

of the coatings as a diffusion barrier was evaluated. Effects of the coatings on the diffusion path of the composites and the fractographic characteristics of the ductile reinforcement were also examined. Furthermore, effects of the coatings on the toughness of the composites were studied and compared with predictions based upon tensile tests on a single constrained niobium reinforcement.

## 2. Experimental details

Al<sub>2</sub>O<sub>3</sub> coating on niobium foils was produced by a sol-gel technique and ZrO<sub>2</sub> coating was obtained by dipping the foils into a ZrO<sub>2</sub> coating solution. Details of the coating procedures can be found elsewhere [7]. Model composites of MoSi<sub>2</sub> reinforced by 20 vol.% of uncoated or coated niobium foils were produced by hot pressing at 1400 °C for 1 h under a pressure of 40 MPa. The thickness of niobium foils used was 0.25 mm and the volume fraction of niobium reinforcements was controlled by stacking niobium foils with MoSi<sub>2</sub> powders in an appropriate thickness ratio.

The fracture toughness of the composites was measured by four-point bending on 3.81 × 5.08 × 25.4 mm<sup>3</sup> chevron notched specimens with an inner and outer span of 10 and 20 mm, using a hydro-servo controlled MTS with a cross-head speed of 4 × 10<sup>-4</sup> mm s<sup>-1</sup>. The chevron notch on the laminated composites was cut perpendicular to the foil plane using a diamond wafering blade.

The investigation of the effect of the coatings on the mechanical behavior of the constrained ductile phase was achieved by tensile tests on precracked specimens, as shown in Fig. 1. The test specimens were prepared by stacking a niobium foil with two layers of MoSi<sub>2</sub> powder at an appropriate ratio to form niobium foil sandwiched discs and then hot pressing under the same conditions as described for the laminated composites. The discs were then cut into rectangular tensile test bars with dimensions of 5.0 × 3.9 × 30.0 mm<sup>3</sup>. Niobium foils with thicknesses of 0.25 and 0.5 mm were used in this study. The notches in the MoSi<sub>2</sub> matrix were introduced using a diamond wafering blade. The distance from the notch tip to the laminate interface was 200 μm. This distance has been found to be small enough not to distort the stress-displacement curve of the constrained ductile reinforcement and at the same time maintain an appropriate degree of elastic constraint from the matrix [10]. The radius of the notch tip was 0.075 mm. The tensile tests were conducted using MTS with a displacement speed of 2.1 × 10<sup>-3</sup> mm s<sup>-1</sup>. The fracture surfaces of both chevron notched and precracked specimens were examined with scanning electron microscopy (SEM) to find the relationship between constraining conditions and fracture surfaces of ductile phases.

### 3. Results and discussion

#### 3.1. Interactions between Nb and MoSi<sub>2</sub>

The microstructure and compositional profiles of an MoSi<sub>2</sub>-uncoated-niobium interface hot pressed at 1400 °C are shown in Fig. 2. As seen in the figure, niobium and MoSi<sub>2</sub> reacted extensively during the processing, forming three new intermetallic compounds at

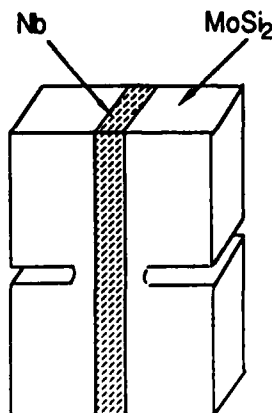
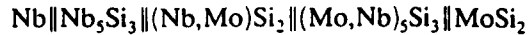


Fig. 1. Schematic diagram of a composite laminate tensile test specimen.

the interface. The resulting interaction region consisted of



However, it was found that (Mo,Nb)<sub>5</sub>Si<sub>3</sub> existed in a discrete form rather than a continuous layer. Most (Mo,Nb)<sub>5</sub>Si<sub>3</sub> was formed around the dark areas in Fig. 2 which were porosities or SiO<sub>2</sub>. A high magnification of the (Mo,Nb)<sub>5</sub>Si<sub>3</sub> microstructure at the MoSi<sub>2</sub>-(Nb,Mo)Si<sub>2</sub> interface is shown in Fig. 3. The thickness of the interaction zone formed was measured to be about 30 μm for hot pressing at 1400 °C for 1 h. In addition, the nature of the reaction products was found to depend on the processing temperature and time. For example, Fig. 4 shows the interfacial microstructure and the corresponding composition profiles of an MoSi<sub>2</sub>/Nb sample which was hot pressed at 1700 °C for 30 min. As seen in the figure, at this processing temperature only one (Nb,Mo)<sub>5</sub>Si<sub>3</sub> interphase

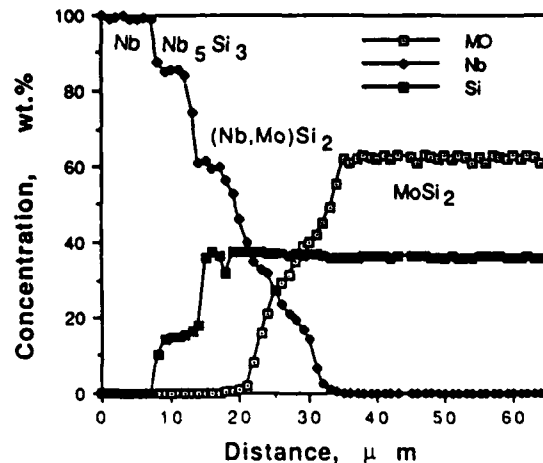
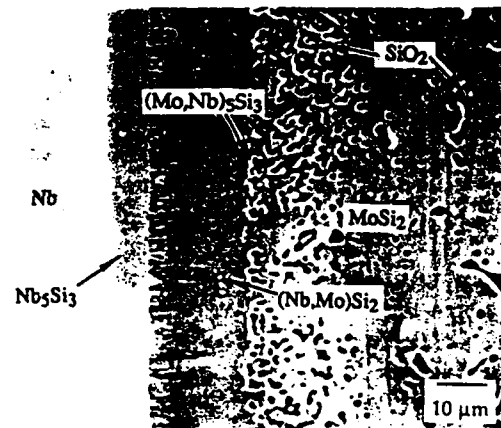


Fig. 2. Microstructure and composition profile across the interface in the MoSi<sub>2</sub>/uncoated Nb composite, hot pressed at 1400 °C.

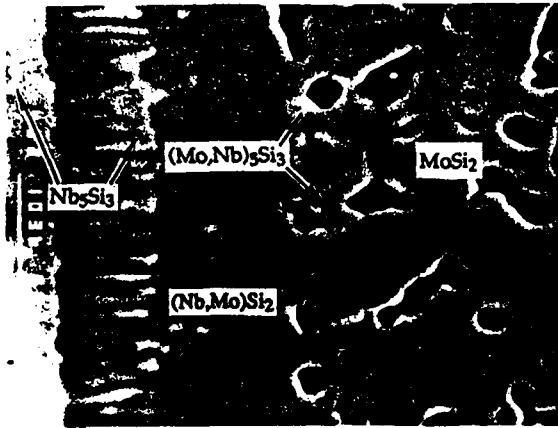


Fig. 3. Microstructure of  $(\text{Mo,Nb})_5\text{Si}_3$  at the  $\text{MoSi}_2$ - $(\text{Nb,Mo})\text{Si}_2$  interface in the  $\text{MoSi}_2$ /uncoated-niobium composite, hot pressed at  $1400^\circ\text{C}$ .

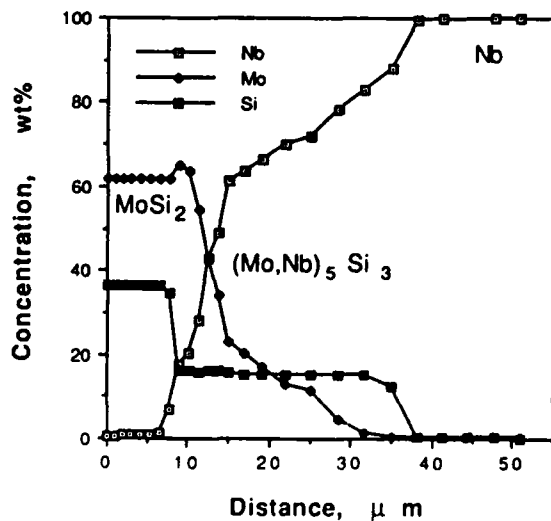
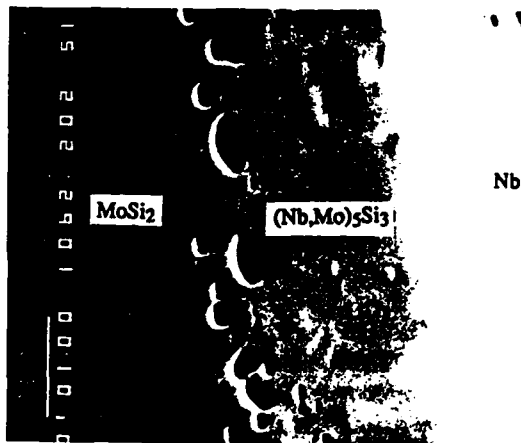
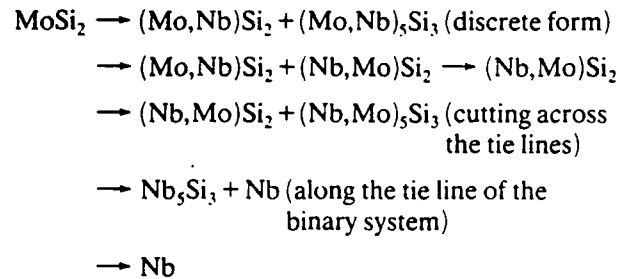


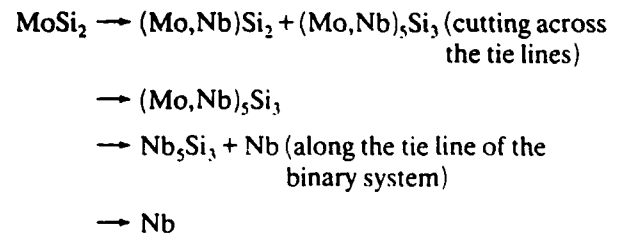
Fig. 4. Microstructure and composition profile across the interface in the  $\text{MoSi}_2$ /uncoated-niobium composite, hot pressed at  $1700^\circ\text{C}$ .

was formed instead of the three intermetallics,  $\text{Nb}_5\text{Si}_3$ ,  $(\text{Nb,Mo})\text{Si}_2$  and  $(\text{Mo,Nb})_5\text{Si}_3$ , formed at  $1400^\circ\text{C}$ .

Such temperature dependence of interphase formation can be explained in terms of the Mo-Si-Nb ternary phase diagram and temperature dependence of the diffusivity of each elemental species. The available isopleth through  $\text{MoSi}_2/\text{Nb}$  [11] shows that there are two four-phase equilibria, at  $1730$  and  $1740^\circ\text{C}$ , associated with the  $\text{MoSi}_2/\text{Nb}$  vertical section. The isopleth [11] also shows that the relevant phase fields remain essentially unchanged below the two four-phase equilibria. Therefore, the composition path in the present study can be analyzed on the basis of the  $800^\circ\text{C}$  isothermal section [12], which has been slightly modified by Lu *et al.* [13] to eliminate the  $\text{Nb}_4\text{Si}$  phase [14] and is shown in Fig. 5. The composition paths for hot pressing at  $1400^\circ\text{C}$  and  $1700^\circ\text{C}$  are also shown in Fig. 5 by lines A and B respectively. The non-planar interface of  $\text{Nb}_5\text{Si}_3$ - $(\text{Nb,Mo})\text{Si}_2$  in Fig. 2 (hot pressed at  $1400^\circ\text{C}$ ) suggests that the composition path crosses the corresponding two-phase region by cutting across the tie lines. However, the sharp interface of  $\text{Nb}$ - $\text{Nb}_5\text{Si}_3$  indicates that the composition path runs along the tie line in the corresponding two-phase region. Therefore, the composition path for  $1400^\circ\text{C}$  is shown in the following route:



Similarly, based on the microstructure examination and composition analysis, the composition path for hot pressing at  $1700^\circ\text{C}$  (Fig. 4) is



Since the isopleth of the Mo-Nb-Si system [11] shows that the relevant phase fields remain essentially unchanged below  $1730^\circ\text{C}$ , the difference in the microstructures at different processing temperatures below  $1730^\circ\text{C}$  might be due to the changes in the interface reaction rate which is proportional to the free energy of formation of these compounds or due to changes in diffusion kinetics of the elemental species to the reaction

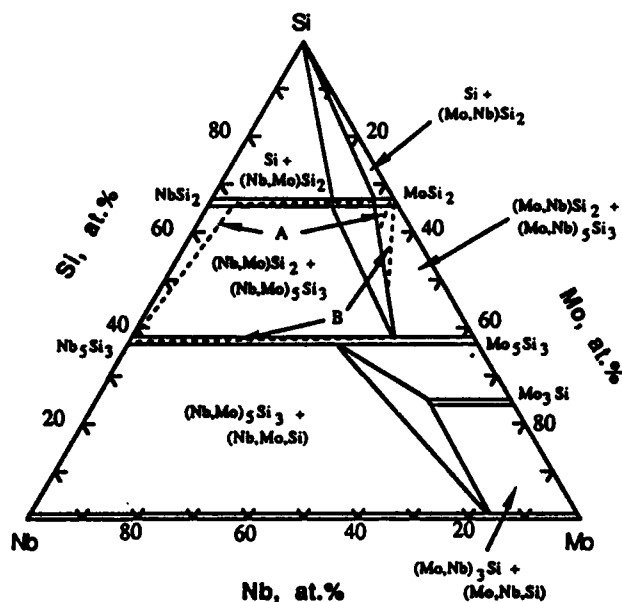
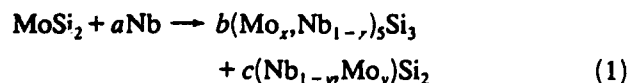
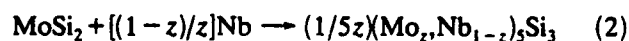


Fig. 5. Isothermal section of the Mo-Si-Nb ternary diagram [12] at 800 °C, showing the composition path of Nb/MoSi<sub>2</sub> systems. Line A is for 1400 °C and line B for 1700 °C.

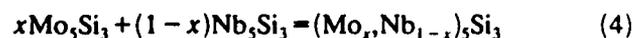
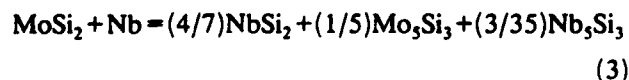
sites. According to the phase diagram shown in Fig. 5, the compounds formed in the MoSi<sub>2</sub>/Nb diffusion couple may be described, depending on whether or not (Nb,Mo)Si<sub>2</sub> forms, by the following formulae:



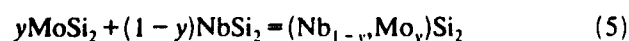
or



where the coefficients  $a$ ,  $b$ ,  $c$ ,  $x$ ,  $y$  and  $z$  depend on the composition and relative amounts of the products. For the above equations, it is assumed that 1 mol of MoSi<sub>2</sub> reacts completely with the required amount of niobium to form the compounds listed on the right-hand side of the equations. The free energy for reaction (1) can be calculated by considering several intermediate steps, such as the following



and



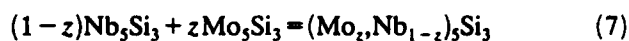
Similarly, reaction (2) can be broken down into



TABLE 1. The standard free energy of formation for some possible reactions in the MoSi<sub>2</sub>/Nb diffusion couple

| Reaction | $\Delta G_{1400}$<br>(kcal mol <sup>-1</sup> ) | $\Delta G_{1700}$<br>(kcal mol <sup>-1</sup> ) |
|----------|--|--|
| 3        | -44.46   | -49.76   |
| 6        | -37.45   | -38.20   |

and



Reactions (4), (5) and (7) correspond to the formation of the solid solutions from mixing of the pure components. Based on the available thermodynamic data [15], free energies of formation for consuming 1 mol of MoSi<sub>2</sub> in reactions (3) and (6) were calculated for two different temperatures, 1400 °C and 1700 °C, and the results are listed in Table 1. As seen in the table, free energies of formation for reactions (3) and (6) do not change much as the hot pressing temperature increases from 1400 °C to 1700 °C. It should be noted that depending on the amounts of MoSi<sub>2</sub> and niobium participating in reaction (3), the ratio of the products NbSi<sub>2</sub> to Nb<sub>5</sub>Si<sub>3</sub> may not be fixed as indicated in the equation. Other possibilities such as the formation of much more Nb<sub>5</sub>Si<sub>3</sub> than NbSi<sub>2</sub> or a similar amount have also been considered. However, the calculations show that the same conclusion mentioned above (for the case of more NbSi<sub>2</sub> than Nb<sub>5</sub>Si<sub>3</sub>) still holds for these cases. Since no data on the free energy of mixing for reactions (4) and (7) are available, the free energy of mixing can be assumed to be ideal. This may not be an unreasonable approximation since (Mo<sub>z</sub>, Nb<sub>1-z</sub>)<sub>5</sub>Si<sub>3</sub> is a continuous solid solution as shown in Fig. 5. For this case, the free energy of mixing is proportional to temperature for a fixed composition. Thus, the change in the free energy of mixing for reactions (4) and (7) from 1400 °C to 1700 °C should not change the order of the free energy of formation for reactions (1) and (2). A similar argument may apply to reaction (5), since the isopleth of the Mo-Nb-Si system [11] shows that the relevant phase fields remain essentially unchanged below 1730 °C, i.e. the phase relations between (Nb,Mo)Si<sub>2</sub>, (Mo,Nb)Si<sub>2</sub> and (Nb,Mo)<sub>5</sub>Si<sub>3</sub> remain unchanged (Fig. 5), implying that (Nb<sub>1-y</sub>, Mo<sub>y</sub>)<sub>5</sub>Si<sub>2</sub> behaves more or less like an ideal solid solution. Thus, although the free energies of formation for reactions (1) and (2) change with temperature, the order of the free energy of formation for reactions (1) and (2) does not vary with temperature in the range of interest. Therefore, the effect of the free energy of formation of these compounds on the reaction kinetics may not explain the observed microstructural changes from 1400 °C to 1700 °C.

In contrast, the microstructural changes in the interaction zone at different processing temperatures could be due to the change in the diffusion kinetics of silicon, niobium and molybdenum, as will be discussed below. The composition profile in Fig. 2 (1400 °C) shows clearly that silicon diffuses far deeper into the niobium-rich region than molybdenum, indicating that silicon has a higher mobility than molybdenum. This is consistent with the available literature data [16, 17], which show that diffusivities of silicon and molybdenum in niobium can be expressed as follows:

$$D_{\text{Si}} = 0.51 \times 10^{-2} \exp(-48000/RT) \quad 700\text{--}1500\text{ }^{\circ}\text{C}$$

$$D_{\text{Mo}} = 92 \exp(-122000/RT) \quad 1725\text{--}2182\text{ }^{\circ}\text{C}$$

The above equations indicate that the diffusion coefficients of silicon in niobium at 1400 °C and 1700 °C are  $2.73 \times 10^{-9}$  and  $2.45 \times 10^{-8}$  cm<sup>2</sup> s<sup>-1</sup> respectively. For molybdenum, the corresponding values are  $1.56 \times 10^{-14}$  and  $2.81 \times 10^{-12}$  cm<sup>2</sup> s<sup>-1</sup>. Because of the low mobility of molybdenum relative to silicon, the interphase formation at 1400 °C is expected to be dominated by the diffusion of silicon into the niobium region. This is supported by the formation of Nb<sub>5</sub>Si<sub>3</sub> adjacent to niobium instead of the formation of (Nb,Mo)<sub>5</sub>Si<sub>3</sub>. However, as the temperature increases, the diffusion of molybdenum becomes more pronounced relative to the diffusion of silicon because of its higher diffusion activation energy, and therefore a stronger temperature dependence of its diffusivity. Similarly, niobium diffusion becomes more competitive at high temperatures, which combined with the diffusion of molybdenum leads to the formation of (Nb,Mo)<sub>5</sub>Si<sub>3</sub> at 1700 °C, as shown in Fig. 4. The limited growth of the (Mo,Nb)Si<sub>2</sub> interphase at 1700 °C is probably due to the faster growth of (Mo,Nb)<sub>5</sub>Si<sub>3</sub> caused by the more pronounced diffusion of niobium relative to silicon at high temperatures. It should be noted that at 1400 °C, growth of Nb<sub>5</sub>Si<sub>3</sub> depends mainly on the transport of silicon through the (Nb,Mo)Si<sub>2</sub> layer. However, at 1700 °C, as niobium diffusion becomes more pronounced, the growth of (Mo,Nb)<sub>5</sub>Si<sub>3</sub> is enhanced not only in the direction of the niobium-rich region but also in the direction of the (Nb,Mo)Si<sub>2</sub> interphase. Thus, when the diffusion of niobium becomes competitive with respect to the diffusion of silicon, the growth of (Mo,Nb)<sub>5</sub>Si<sub>3</sub> will be enhanced and that of (Nb,Mo)Si<sub>2</sub> limited. In Section 3.2 where the hot pressing temperature is kept at 1400 °C, some more evidence will be provided that whenever diffusion of niobium becomes more competitive with respect to the diffusion of silicon, the growth of (Nb,Mo)Si<sub>2</sub> becomes limited.

Note that according to the conservation of mass, much more (Mo,Nb)<sub>5</sub>Si<sub>3</sub> should exist in the diffusion couple. However, only a small amount of (Mo,Nb)<sub>5</sub>Si<sub>3</sub>

has been observed, as shown in Fig. 2. This is believed to be due to the presence of SiO<sub>2</sub> and free silicon in the commercially pure MoSi<sub>2</sub> powder as shown in Fig. 2 and reported in refs. 18 and 19. The presence of SiO<sub>2</sub> and free silicon shifts the actual composition of the starting MoSi<sub>2</sub> powder to the MoSi<sub>2</sub>-Si two-phase field, instead of the single-phase MoSi<sub>2</sub> field. The presence of the extra silicon is also reflected in the composition profile. As shown in Fig. 2, Matano interfaces of three elements are not at the same position, with the silicon Matano interface far closer to the niobium-rich side than that of molybdenum. However, the difference in the position of the Matano interfaces becomes smaller at 1700 °C, as shown in Fig. 4. The results suggest that the presence of excess silicon and SiO<sub>2</sub> contributes more to the diffusion process at lower temperatures, whereas at high temperatures contributions from MoSi<sub>2</sub> and niobium became more pronounced.

### 3.2. Effect of the coatings on the diffusion path

Comparison of interfacial microstructures of MoSi<sub>2</sub> with coated and uncoated niobium is shown in Fig. 6. At 1700 °C the thickness of the interaction layer between niobium and MoSi<sub>2</sub> has been reduced from approximately 30 μm for the uncoated interface to about 6 μm for the ZrO<sub>2</sub> coated samples. In addition, the composition of the interphase formed was determined to be Nb<sub>5</sub>Si<sub>3</sub>, instead of (Mo,Nb)<sub>5</sub>Si<sub>3</sub> for the uncoated samples, suggesting a substantial reduction in the diffusion of niobium and molybdenum across the coating. For 1400 °C the thickness of the interaction layer has also been reduced from approximately 30 μm to about 4 μm upon coating of niobium foils with Al<sub>2</sub>O<sub>3</sub>. Furthermore, only one interphase (Nb<sub>5</sub>Si<sub>3</sub>) was observed, instead of the three interphases Nb<sub>5</sub>Si<sub>3</sub>, (Nb,Mo)Si<sub>2</sub> and (Mo,Nb)<sub>5</sub>Si<sub>3</sub> for the uncoated samples (Fig. 2). The reduction in the thickness and change in the composition of the interfacial compounds formed at 1700 and 1400 °C can again be attributed to the retardation of silicon diffusion and the suppression of niobium and molybdenum diffusion across the coatings. Note that the suppression of niobium diffusion across the coatings leads to the absence of interphase formation in the MoSi<sub>2</sub> side of the oxide coating, whereas suppression of molybdenum diffusion results in the formation of only the binary compound, instead of the ternary compound, in the niobium side. In addition, retardation of silicon diffusion in the coated samples favors the formation of niobium-rich compounds, such as Nb<sub>5</sub>Si<sub>3</sub>, instead of NbSi<sub>2</sub>.

The effectiveness of the coatings as a diffusion barrier was found to be affected not only by the quality and integrity of the coating itself, but also by the presence of SiO<sub>2</sub> and free silicon near the coating. A typical

microstructure of MoSi<sub>2</sub> hot pressed with sol-gel-coated niobium is shown in Fig. 7. As can be seen, the coating is discontinuous. This is believed to be due to the interaction of the coating with SiO<sub>2</sub> and free silicon

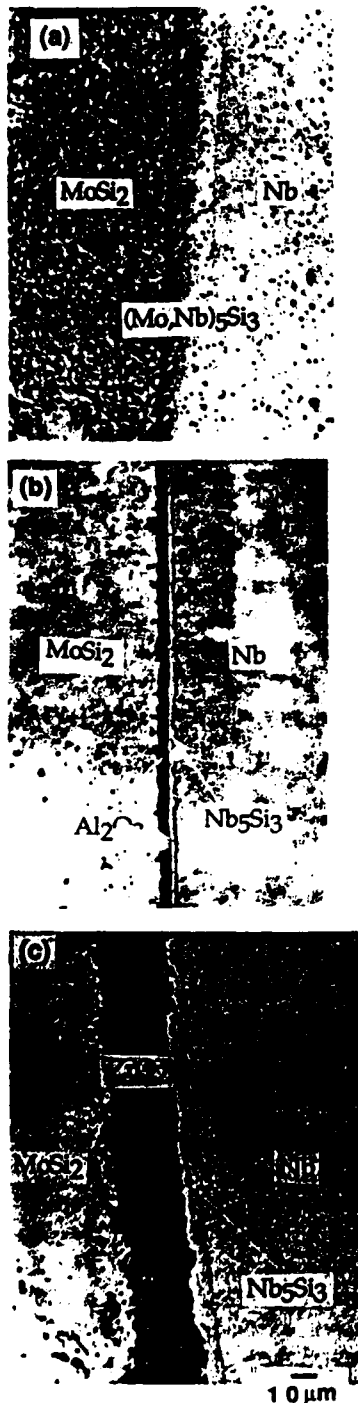


Fig. 6. Interfacial microstructures of MoSi<sub>2</sub> with (a) uncoated niobium, hot pressed at 1700 °C, (b) Al<sub>2</sub>O<sub>3</sub>-coated niobium, hot pressed at 1400 °C, (c) ZrO<sub>2</sub>-coated niobium, hot pressed at 1700 °C.

[20]. This coating degradation can be eliminated by improvements in the matrix chemistry. As has been shown by Kaufman and coworkers [21, 22], one promising approach is to convert SiO<sub>2</sub> and silicon into SiC by mechanically mixing elemental molybdenum and silicon powders with excess carbon. The formation of SiC by this method not only eliminates the detrimental effect of SiO<sub>2</sub> and free silicon, but also provides *in situ* compositing of MoSi<sub>2</sub> with SiC. Optimization of this processing technique is currently under development [22].

The extent of the retardation of silicon diffusion has been found to depend also on the quality of the coatings. For example, the apparent diffusivity of silicon in the sol-gel derived Al<sub>2</sub>O<sub>3</sub> coating has been estimated to be larger than  $2.0 \times 10^{-8} \text{ cm}^2 \text{ s}^{-1}$  at 1400 °C [7]. Such high diffusivity has been attributed to the grain boundary diffusion and vapor phase diffusion through the pinholes which are characteristic defects associated with sol-gel processing. Therefore, in order to reduce further the silicon diffusion, grain boundary area and processing defects must be minimized in the coating. Figure 8 shows a microstructure and the corresponding composition profile of an MoSi<sub>2</sub> and sol-gel coated niobium interface which is obtained via electrophoresis with optimized processing parameters. As seen in the figure, the thickness of the interphase has been reduced from approximately 30 μm to less than 1 μm, compared with the uncoated samples. The reaction product in this case could not be determined because its thickness was close to the beam size of the electron microprobe (approximately 1 μm). Nevertheless, the result indicates that if the coating is dense enough, the diffusion of silicon can be effectively limited, and therefore the interaction between niobium and MoSi<sub>2</sub> can be prevented.

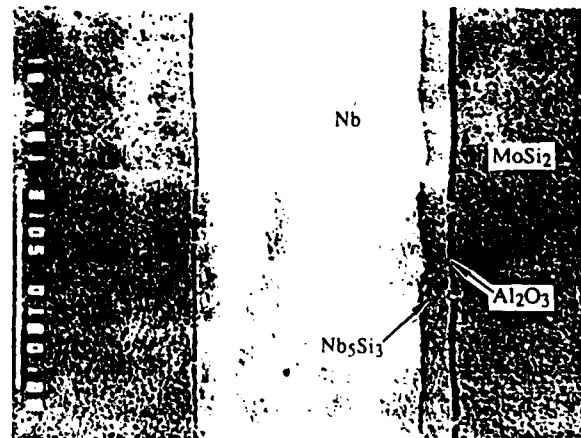


Fig. 7. A typical microstructure of MoSi<sub>2</sub> hot pressed with sol-gel-coated niobium.

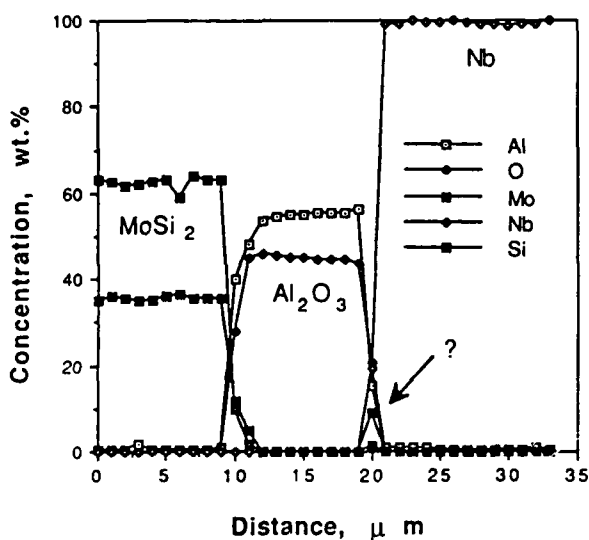
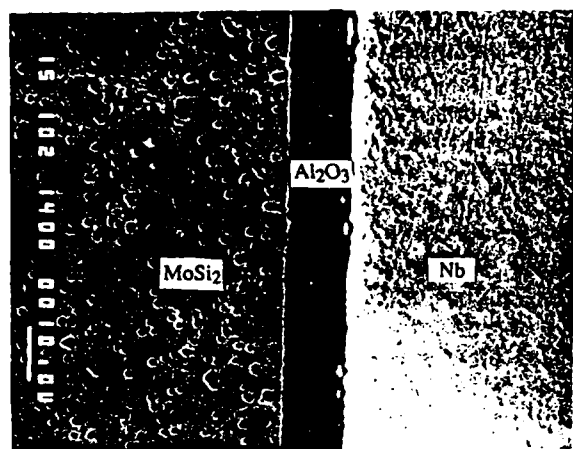


Fig. 8. Microstructure and composition profile across the interface in MoSi<sub>2</sub>/sol-gel-coated niobium composite, hot pressed at 1400 °C.

### 3.3. Effect of the coatings on fractographic characteristics of constrained ductile phases

The dependence of the fracture surface of niobium on the coating conditions is shown in Fig. 9. These fracture surfaces were taken from the same location with respect to the tip of the chevron notch of the laminated composites in order to eliminate the location effect on the fracture surface of niobium foil. A close examination of Fig. 9 shows that Al<sub>2</sub>O<sub>3</sub>-coated niobium exhibits a total dimple rupture, while ZrO<sub>2</sub>-coated and uncoated niobium fracture with a mixed mode. The differences in the fracture surfaces are a result of the difference in the interfacial fracture energy of these interfaces and the level of constraints—the reinforcement. Here, the constraint is referred to a phenomenon that when a ductile phase is imbedded in

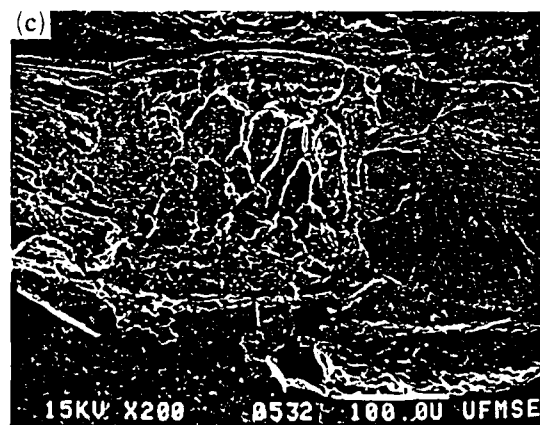
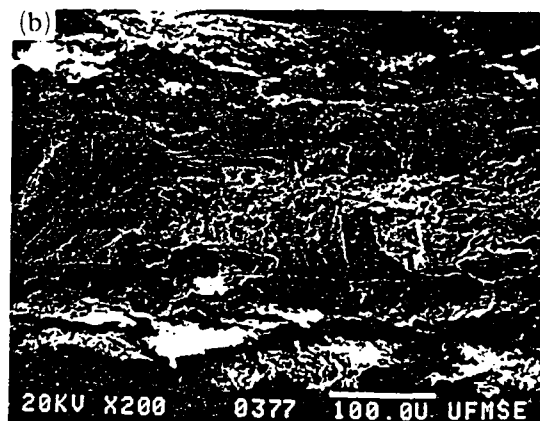
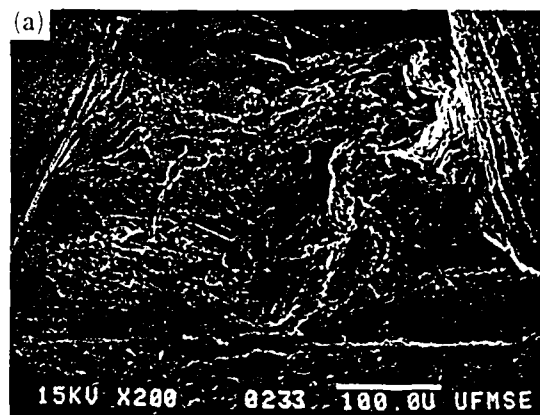


Fig. 9. Fracture surfaces of constrained niobium foils in the chevron notched specimens: (a) Al<sub>2</sub>O<sub>3</sub>-coated niobium, (b) ZrO<sub>2</sub>-coated niobium, (c) uncoated niobium, hot pressed at 1400 °C.

a brittle matrix, it can no longer deform freely, and instead it will deform under the restriction of the matrix. A recent study [23] shows that the oxide coating reduces the fracture energy of the MoSi<sub>2</sub>-Nb interface and the measured interfacial fracture energies are 13, 16 and greater than 33.7 J/m<sup>2</sup> for the ZrO<sub>2</sub>-coated,

Al<sub>2</sub>O<sub>3</sub>-coated and uncoated interfaces respectively. Moreover, the decohesion length at the matrix-reinforcement interface has been found to be inversely proportional to the interfacial fracture energy, *i.e.* the ZrO<sub>2</sub>-coated interface exhibits the longest decohesion length, followed by the Al<sub>2</sub>O<sub>3</sub>-coated and then the uncoated interface [23]. The constraint from the matrix on the deformation of niobium is related to the decohesion length. The longer the decohesion length is, the lower the constraint from the matrix. Thus, the uncoated composites have a larger constraint from the matrix on the ductile phase, indicated by a shorter decohesion length [23]. The fracture surfaces shown in Fig. 9(a) and (c) show that as the constraint increases, the fracture mode niobium changes from dimple to quasi-cleavage. Similar to the Al<sub>2</sub>O<sub>3</sub>-coated samples, the ZrO<sub>2</sub>-coated Nb/MoSi<sub>2</sub> system also has weak bonding at the interface. However, the fracture of ZrO<sub>2</sub>-coated niobium does not strictly follow the constraint-fracture mode relation observed in the

uncoated and Al<sub>2</sub>O<sub>3</sub>-coated systems. One possible reason is the embrittlement of niobium by the interstitial oxygen in the ZrO<sub>2</sub>-coated systems [23].

The fact that the fracture mode of the ductile phase depends on the constraint condition can be further illustrated by Fig. 10 which shows the fracture surfaces of uncoated niobium foils at different locations in the laminated composites. As seen in the figure, the fracture mode of niobium foils has changed from cleavage to dimple rupture as the location of the niobium foils changes from near the tip of the notch to the bottom of the notch. Between these two positions, a mixed mode of fracture is observed. Owing to the change in stress state during the bending test, a longer decohesion length was observed to occur at the bottom of the chevron notch than at the tip, which leads to a less constrained condition for the niobium foils at the bottom. Therefore, the fracture mode of the ductile phase changes from the total dimple to mixed mode, and even to cleavage, whenever the constraint increases either by

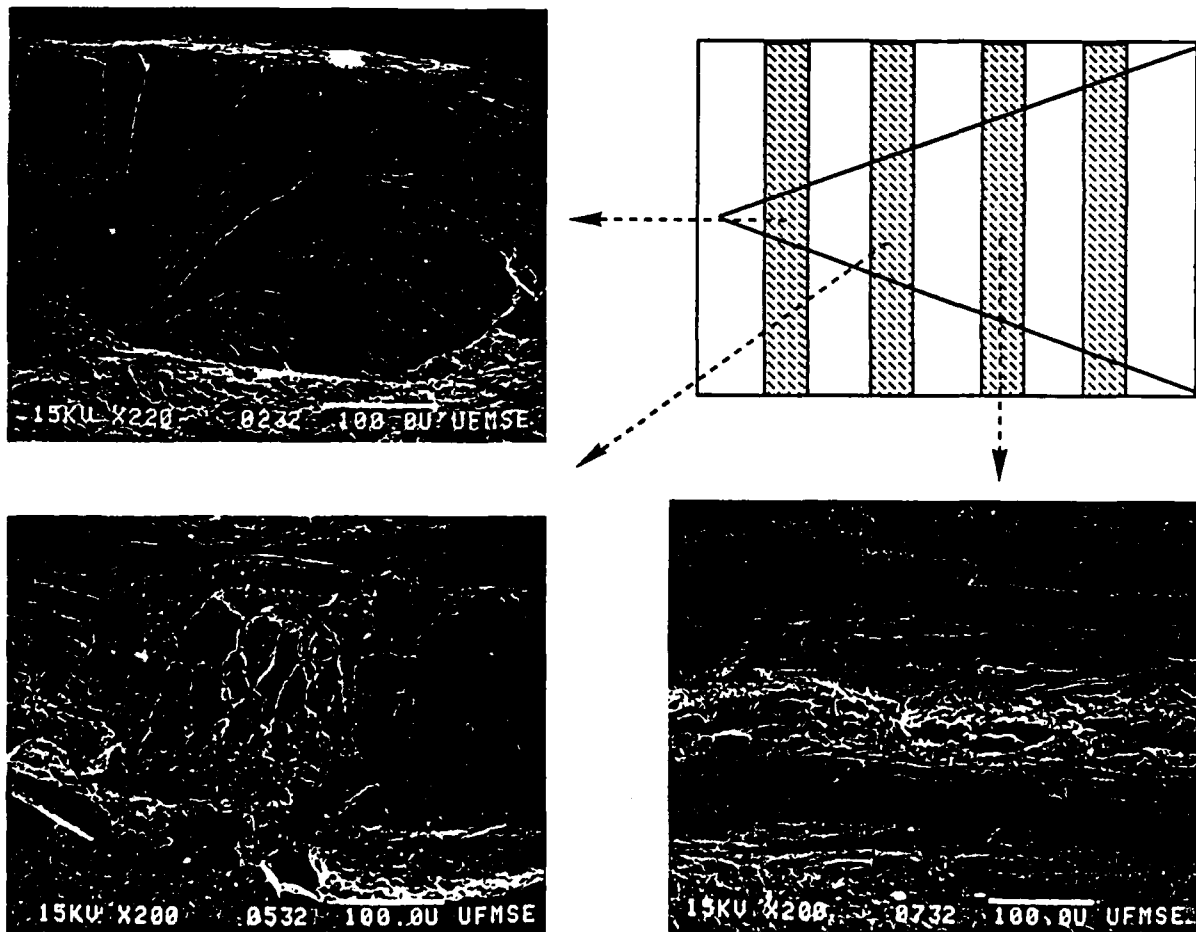


Fig. 10. Fracture surfaces of uncoated niobium foils in a chevron notched specimen, showing that the fracture mode of niobium foils changes with position.

changing the interfacial properties or by changing the stress state. Thus, fractographic analysis can be used to estimate the degree of constraint qualitatively.

### 3.4. Effect of the coatings on the mechanical behavior of constrained ductile phases

The effects of the coatings on the stress-displacement curves of the tensile test on precracked specimens (see Fig. 1) is shown in Fig. 11. It has been shown previously [10] that owing to the appropriate choice of notch depth in the precracked specimens, the cracks during tensile testing are initiated at the notch tips at very low stress levels. Thus, the curves in Fig. 11 are characteristic of the flow behavior of the constrained ductile phase. As shown in the figure, the uncoated niobium exhibits the highest peak stress, followed by the Al<sub>2</sub>O<sub>3</sub>-coated and then the ZrO<sub>2</sub>-coated niobium. In contrast, the ZrO<sub>2</sub>-coated niobium has the largest work of rupture (the area under the curve). The measured peak stress and work of rupture for 0.25 mm thick niobium lamina are summarized in Table 2. The decohesion length at the interface and the interfacial fracture energy measured using chevron notched short

bars of laminated composites [23] are also presented in Table 2 to illustrate the relation between the constraint condition and the mechanical characteristics. Also included in Table 2 is the microhardness of niobium in the precracked specimens, which shows the effect of the processing conditions on the hardness of the niobium foils.

Table 2 shows clearly that the degree of constraint on the ductile phase decreases with decreasing fracture energy of the interface, as indicated by the increase in decohesion length. In addition, as the degree of constraint decreases, the peak stress also decreases, but the work of rupture increases. These findings are consistent with theoretical analyses of Sigl *et al.* [24], Evans and McMeeking [25] and Ashby *et al.* [26].

Toughening of brittle materials by the bridging of ductile phases can be estimated with the aid of the following equation [24, 25]

$$\Delta G = V_f \int_0^{u^*} \sigma(u) du \quad (8)$$

where  $\sigma(u)$  is the nominal stress carried by the constrained ductile reinforcement for a given crack opening  $u$ ,  $V_f$  is the volume fraction of the reinforcement and  $u^*$  is the crack opening at the point when the ductile reinforcement fails. The integral in eqn. (8) corresponds to the area under the stress-displacement curve from the tensile test on a single constrained ductile reinforcement. The steady-state toughness of the composite  $K_c$  can be related to the fracture energy increase  $\Delta G$  by the use of the Rice J-integral [27], as follows:

$$\frac{(1 - \nu_c^2) K_c^2}{E_c} = \frac{(1 - \nu_m^2) K_m^2}{E_m} + \Delta G \quad (9)$$

where  $\nu$ ,  $E$  and  $K$  are Poisson's ratio, the elastic modulus and fracture toughness respectively. The subscripts

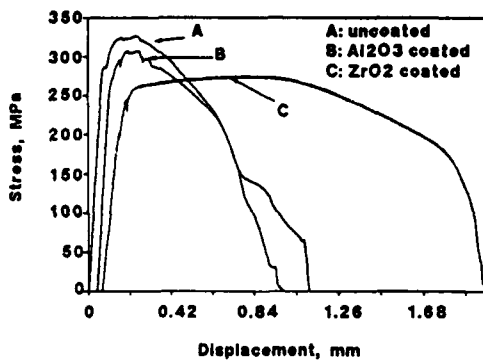


Fig. 11. Effect of the coatings on the stress-displacement curves, measured from precracked specimens with 0.5 mm thick niobium lamina.

TABLE 2. Measured damage tolerance, steady-state toughness and other relevant parameters from the tensile tests and bend tests

| Material  | Uncoated Nb  | Al <sub>2</sub> O <sub>3</sub> -coated Nb | ZrO <sub>2</sub> -coated Nb |
|---|--------------|---|-----------------------------|
| HV (kg/mm <sup>2</sup> )                                      | 131          | 134                                       | 131                         |
| Interfacial fracture energy <sup>a</sup> (J m <sup>-2</sup> ) | > 33.7 ± 1.4 | 16.1 ± 1.3                                | 12.8 ± 1.0                  |
| Decohesion length <sup>b</sup> (mm)                           | 0.86 ± 0.09  | 0.94 ± 0.23                               | 1.31 ± 0.61                 |
| Peak stress <sup>b</sup> (MPa)                                | 350 ± 15     | 340 ± 30                                  | 330 ± 15                    |
| Work of rupture <sup>b</sup> (J m <sup>-2</sup> )             | 85400 ± 7800 | 92400 ± 9500                              | 103200 ± 7300               |
| Steady-state toughness <sup>b</sup> (MPa m <sup>1/2</sup> )   | 88           | 92  | 97                          |
| Damage tolerance <sup>c</sup> (MPa m <sup>1/2</sup> )         | 15.2 ± 1.3   | 14.0 ± 1.5                                | 12.8 ± 1.5                  |
| Work of fracture <sup>c</sup> (J m <sup>-2</sup> )            | 21600 ± 3000 | 28700 ± 1900                              | 28700 ± 4600                |

<sup>a</sup>From chevron notched short bars of laminated composites [23].

<sup>b</sup>From tensile tests on a single constrained niobium foil (0.25 mm thick).

<sup>c</sup>From bend tests on chevron notched composite laminates reinforced with 20 vol.% of niobium laminae (0.25 mm thick).

c and m refer to the composite and matrix respectively. Using the experimental data from the tensile tests on the precracked specimens, the fracture toughness of the Nb/MoSi<sub>2</sub> system has been calculated using eqns. (8) and (9) and the results are compared with the measured fracture toughness presented in the next section.

### 3.5. Effect of the coatings on the fracture toughness of the laminated composites

Typical load-displacement curves of four-point bending tests on the chevron notched specimens of uncoated and coated niobium reinforced composites are shown in Fig. 12. As can be seen, the maximum load  $P_{max}$  increases with increasing the degree of constraint, that is uncoated niobium-reinforced laminates exhibit the highest maximum load. The maximum load reached by the chevron notched specimen can be used to calculate the fracture toughness with the aid of the following equation [28]

$$K_{Ic} = \frac{P_{max}}{B\sqrt{W}} Y^* \quad (10)$$

where  $P_{max}$  is the maximum test load,  $B$  and  $W$  are the width and height of the bending bar respectively, and  $Y^*$  is the dimensionless stress intensity factor coefficient. The latter is a function of the geometry of the specimen and bending test set-up. Substituting the measured  $P_{max}$  into eqn. (10), the calculated fracture toughness is obtained and listed as damage tolerance in Table 2. For comparison, the steady-state toughness calculated from the work of rupture of a single constrained ductile phase is also listed in the table.

It is noted that a very large discrepancy exists between the fracture toughnesses calculated from the two aforementioned methods. The discrepancy is believed to be due to the fact that the fracture toughness

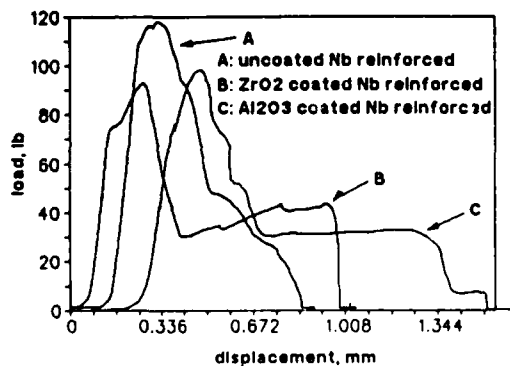


Fig. 12. Typical load-displacement curves of bend tests on chevron notched laminates reinforced with 20 vol.% of coated and uncoated niobium foils, hot pressed at 1400°C.

measured from the peak load of the bend test on the chevron notched specimens is not a steady-state fracture toughness, but merely an indicator of the damage tolerance of the composites. The previous study has shown [8] that a primary crack has already propagated through the entire MoSi<sub>2</sub> matrix at a load level of about 20% of the peak load in the bend test. Beyond this level, the load is mainly carried by the niobium reinforcement alone. Therefore, to measure the actual toughness using the bending test of chevron notched specimens, a very large size specimen has to be used. An alternative approach would be to reduce the size of the ductile phase, which would in turn lead to a decrease in the length of the bridging zone, making the ductile phase more effective in preventing the crack opening. Thus, the size of the crack will be much smaller than that of the specimen dimensions. Under these conditions, the damage tolerance measured from the bend test on chevron notched specimens may become a valid measurement of fracture toughness. In contrast, the fracture toughness calculated from the work of rupture is a steady-state fracture toughness. Therefore, only with an appropriate combination of sizes of test specimen and ductile reinforcement can the two testing methods exhibit a similar result. Calculation of the critical size of the ductile reinforcement for such a situation is currently under development.

Figure 12 also reveals another salient feature for ductile phase toughening, that is that the mechanical behaviors of ZrO<sub>2</sub>- and Al<sub>2</sub>O<sub>3</sub>-coated systems are similar, and both show an increase in the carried load in the last part of the displacement curves which is caused by extensive delamination at the interface; this means that the niobium can deform under a much less constrained condition and much more niobium participates in deformation. Because of this feature, the total energy consumed to break a specimen (area under the curve) for the coated composites is larger than for the uncoated composites. To reflect this feature, the work of fracture, defined as the total energy normalized with respect to the generated crack area during the bend test [29], is calculated and included in Table 2. Comparing the values measured from these tests shows that the damage tolerance and the peak stress have the same trends as the interfacial fracture energy changes, whereas the steady-state fracture toughness and the work of fracture follow the opposite trend. These results indicate that whether or not strong interfacial bonding is conducive to improving the toughness depends on the criterion used to describe the toughness of the composite. If the damage tolerance measured from chevron notched specimens is used as an indicator of the toughness, strong bonding would be desirable. However, if the work of fracture and/or steady-state toughness are used as indicative of its

toughness, then a relatively weak bonding would be preferable.

#### 4. Concluding remarks

The present set of experiments shows that niobium interacts with MoSi<sub>2</sub> extensively at high temperatures forming various interfacial compounds. The nature and composition of the compounds are found to depend on the processing temperature, and to depend on the diffusion kinetics of silicon, niobium and molybdenum. The oxide coatings (Al<sub>2</sub>O<sub>3</sub> and ZrO<sub>2</sub>) suppress the interdiffusion of niobium and molybdenum, and limit the diffusion of silicon, leading to the very limited interaction between niobium and MoSi<sub>2</sub>.

It has been demonstrated that the degree of constraint on the ductile phase decreases with decreasing fracture energy of the interface. Fractographic analysis has been utilized to estimate the degree of constraint on the ductile phases and provide an alternative to analyzing the constraints when the stress states are complicated.

Toughness analyses indicate that whether or not a strong interfacial bonding is conducive to increasing toughness depends on the criterion used to describe the toughness of the composites. If the damage tolerance measured from chevron notched specimens is used as an indicator of the toughness, strong bonding would be desirable. However, if the work of fracture measured from chevron notched specimens and/or steady-state toughness measured from the tensile test on a single constrained ductile phase are used as indicative of the composite toughness, then a relatively weak bonding is preferable.

#### Acknowledgments

The authors are grateful to the support of the Defense Advanced Research Projects Agency (DARPA) and Office of Naval Research (ONR) through grant N00014-91-J-4075.

#### References

- 1 E. Fitzer, in R. A. Bradley, D. E. Clark, D. C. Larsen and J. O. Stegler (eds.), *Whisker- and Fiber-Toughened Ceramics*, ASM International, Metals Park, OH, 1988, p. 165.
- 2 C. K. Elliott, G. R. Odette, G. E. Lucas and J. W. Sheckherd, *High Temperature, High Performance Composites*, MRS Proc. Vol. 120, Materials Research Society, Pittsburgh, PA, 1988, p. 95.
- 3 A. V. Virkar and D. L. Jorgenson, *J. Am. Ceram. Soc.*, **60** (1977) 514-519.
- 4 M. I. Mendelson and M. E. Fine, *J. Am. Ceram. Soc.*, **57** (1974) 154-159.
- 5 J. Gurland, *Trans. ASM*, **50** (1958) 1063-1071.
- 6 V. V. Kristie and P. S. Nicholsin, *J. Am. Ceram. Soc.*, **64** (1981) 499-504.
- 7 L. Xiao, Y. S. Kim and R. Abbaschian, *Intermetallic Matrix Composites*, MRS Proc. Vol. 194, Materials Research Society, Pittsburgh PA, 1990, pp. 399-404.
- 8 L. Xiao, Y. S. Kim, R. Abbaschian and R. J. Hecht, *Mater. Sci. Eng., A144* (1991) 277-285.
- 9 A. G. Metcalfe and M. J. Klein, in A. G. Metcalfe (ed.), *Interfaces in Metal Matrix Composites, Composite Materials*, Vol. 1, Academic Press, New York, 1974, pp. 125-168.
- 10 L. Xiao and R. Abbaschian, in M. N. Gungor, E. J. Lavernia and S. G. Fishman (eds.), *Advanced Metal Matrix Composites for Elevated Temperatures*, ASM International, Materials Park, OH, 1991, pp. 33-40.
- 11 E. M. Savitsky, V. V. Baron and M. I. Bychkova, *Trudy Inst. Met. Baikova, Acad. Nauk SSSR*, **12** (1963) 179-188.
- 12 E. M. Savitsky, V. V. Baron, M. I. Bychkova, S. A. Bakuta and E. I. Gladyshevskiy, *Russian Metall.*, **2** (1965) 91.
- 13 T. C. Lu, Y. G. Deng, C. G. Levi and R. Mehrabian, in M. N. Gungor, E. J. Lavernia and S. G. Fishman (eds.), *Advanced Metal Matrix Composites for Elevated Temperatures*, ASM International, Materials Park, OH, 1991, pp. 11-19.
- 14 H. Okamoto, A. B. Gokhale and R. Abbaschian, in T. B. Massalski (ed.), *Binary Alloy Phase Diagrams*, ASM International, Materials Park, OH, 1990, p. 2767 and p. 1632.
- 15 I. Barin, O. Knacke and O. Kubaschewski, *Thermochemical Properties of Inorganic Substances*, Springer, Berlin, 1977.
- 16 E. Fitzer and F. K. Schmidt, *High Temp. High Pressures*, **3** (1971) 445-460.
- 17 F. Roux and A. Vignes, *Rev. Phys. Appl.*, **5** (1970) 393.
- 18 J. D. Cotton, Y. S. Kim and M. J. Kaufman, *Mater. Sci. Eng., A144* (1991) 287-291.
- 19 J. P. A. Lofvander, J. Y. Yang, C. G. Levi and R. Mehrabian, in E. J. Lavernia and S. G. Fishman (eds.), *Advanced Metal Matrix Composites for Elevated Temperatures*, ASM International, Materials Park, OH, 1991, pp. 1-10.
- 20 L. Xiao and R. Abbaschian, to be published.
- 21 Y. S. Kim, M. R. Johnson, R. Abbaschian and M. J. Kaufman, *High-Temperature Ordered Intermetallic Alloys IV*, MRS Proc., Vol. 213, Materials Research Society, Pittsburgh, PA, 1990, pp. 839-845.
- 22 S. Jayashankar and M. J. Kaufman, *Scripta Metall.*, **26** (1992) 1245-1250.
- 23 L. Xiao and R. Abbaschian, submitted to *Metall. Trans.*
- 24 L. S. Sigl, P. A. Mataga, B. J. Dalgleish, R. M. McMeeking and A. G. Evans, *Acta Metall.*, **36** (1988) 945-953.
- 25 A. G. Evans and R. M. McMeeking, *Acta Metall.*, **34** (1986) 2435-2441.
- 26 M. F. Ashby, F. J. Blunt and M. Bannister, *Acta Metall.*, **37** (1989) 1847-1857.
- 27 J. R. Rice, *J. Appl. Mech.*, **35** (1968) 379-386.
- 28 D. G. Munz, J. L. Shannon, Jr., and R. T. Busey, *Int. J. Fracture*, **16** (1980) R137-141.
- 29 H. G. Tattersall and G. Tappin, *J. Mater. Sci.*, **1** (1966) 296-301.

## Reactive Synthesis of NbAl<sub>3</sub> Matrix Composites

L. LU, Y.S. KIM, A.B. GOKHALE, AND R. ABBASCHIAN  
 Department of Materials Science and Engineering  
 University of Florida, Gainesville, FL 32611

### ABSTRACT

NbAl<sub>3</sub> matrix composites were synthesized "in-situ" via reactive hot compaction (RHC) of elemental powders. It was found that the simultaneous application of pressure during synthesis was effective in attaining a near-theoretical density matrix at relatively low temperatures and pressures. Using this technique, two types of composites were produced: (1) matrices containing a uniform dispersion of second phase particles (either Nb<sub>3</sub>Al or Nb<sub>2</sub>Al with an Nb core or Nb<sub>2</sub>Al) and (2) matrices reinforced with coated or uncoated ductile Nb filaments. It was found that a limited amount of toughening is obtained using the first approach, while composites containing coated Nb filaments exhibited a significant increase in the ambient temperature fracture toughness. In this paper, various aspects of RHC processing of NbAl<sub>3</sub> matrix composites, the effect of initial stoichiometry and powder size on the microstructure, as well as the mechanical behavior of the composites will be discussed.

### INTRODUCTION

Transition metal aluminides have lately been the focus of increased research activity due to their potential for development as high temperature structural materials. In particular, NbAl<sub>3</sub> possesses a desirable combination of relatively high melting point (1605°C) and low density (4.55 g/cm<sup>3</sup>) [1]. However as with many other ordered intermetallics, NbAl<sub>3</sub> (DO<sub>22</sub>) exhibits low toughness and ductility at room temperature. For example, Raison and Vignes [2] found that NbAl<sub>3</sub> is brittle up to 827°C under compression, while Shechtman and Jacobson concluded based on a post-compression dislocation structure study that the material has a high APB energy with no discernible separation of <110> superdislocations [3]. More recently Shneibel, Becker and Horton [4] obtained room temperature mechanical property data for NbAl<sub>3</sub> samples prepared by hot pressing of pre-alloyed powder. They reported a fracture toughness of 2.5 ± 0.5 MPa·√m, as measured by a micro-indentation technique. This indicates that NbAl<sub>3</sub> is an extremely brittle material, with very limited inherent damage tolerance.

The poor mechanical properties of NbAl<sub>3</sub> impose a severe limitation on its use in practical applications. While some attempts have been made to improve its mechanical properties by micro or macro alloying [5], the development of this intermetallic remains largely in the experimental stage. We have focussed on the alternative approach of compositing to improve the ambient temperature fracture toughness of NbAl<sub>3</sub>. In the present work, the composites were processed via reactive hot compaction (hereafter RHC) because previous work on hot-pressing of pre-alloyed NbAl<sub>3</sub> powder indicated that it is difficult to reach full density even at significant fractions (0.89 and 0.95) of the absolute melting point [4]. On the other hand, Paine et al. [6] reported that high density samples could be obtained by combining reactive sintering with hot-pressing. Another reason for using RHC was that it offered a unique route for producing the composites "in-situ." Two types of composites were produced: (1) with matrices containing a uniform dispersion of second phase particles (hereafter Type I) and (2) with matrices containing Nb filament reinforcements which were either uncoated or coated with an alumina diffusion barrier formed "in-situ," i.e. during synthesis of the matrix (hereafter Type II).

In this paper, the basic processing steps for RHC of NbAl<sub>3</sub>, reaction sequences, and the effect of initial stoichiometry and particle size on microstructure will be described. It will be shown that Type I composites exhibit a limited improvement in the fracture toughness, while the Type II composites were significantly tougher than the unreinforced matrix. Fracture surface analysis revealed that, in Type I composites, the toughening was related to crack blunting and/or shielding.

while in Type II composites, an effective load transfer following partial interfacial decohesion caused an increase in the toughness.

## EXPERIMENTAL METHODS

For Type I composites, pure elemental powders of Nb and Al, and for Type II composites, the elemental powders together with reinforcement filaments, were mixed in a cylindrical blender for 1 hour. The average size of the Nb powder (obtained from two sources: Source A and Source B) was  $< 45 \mu\text{m}$ , while Al powders of two average sizes (11 and  $6.2 \mu\text{m}$ , source: Source A) were used. The mixtures were cold compacted into a disk shape (38 mm dia., 8 mm thick) under a pressure of 10 ksi, followed by hot pressing in a BN coated graphite die. The hot pressing was carried out at  $1350^\circ\text{C}$  with a total cycle time of  $\sim 145$  minutes. A typical hot pressing cycle, shown schematically in Figure 1, consisted of an initial heat-up period during which the sample was heated from ambient temperature to  $1350^\circ\text{C}$  at a rate of  $70^\circ\text{C}/\text{min}$ . under a pre-load of  $\sim 1$  ksi. After attainment of the final processing temperature ( $1350^\circ\text{C}$ ), the pressure was increased to 7 ksi; these pressure-temperature conditions were maintained for 60 minutes, following which the sample was cooled under pressure at a rate of  $\sim 20^\circ\text{C}/\text{min}$ .

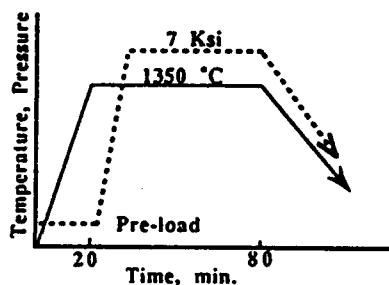


Figure 1 RHC processing cycle (schematic).

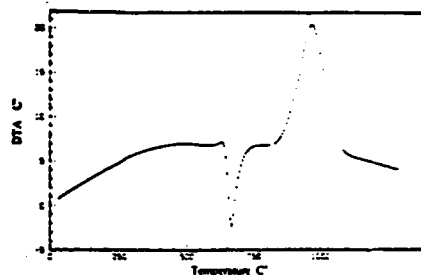


Figure 2 Differential thermal analysis showing the reaction sequence during  $\text{NbAl}_3$  synthesis.

Reaction sequence for the matrix was determined using DTA. The composite microstructures were characterized by quantitative measurements of the volume fractions and mean spacing of second phase particles, electron microprobe compositional analysis, and scanning electron microscopy of fracture surfaces. The quantitative measurements of microstructural features were carried out using standard point counting and linear intercept methods, and the compositional analyses were performed with an estimated accuracy of  $\pm 1$  at.% using a JEOL JXA-733 microprobe and pure Nb and Al as standards. The fracture toughness of the composites was measured either semiquantitatively via the microhardness indentation technique or quantitatively via three point bend testing of chevron notched samples. For the latter, the tests were performed on small specimens ( $5 \times 3 \times 24$  mm), with a  $90^\circ$  root angle Chevron notch. Fracture toughness values ( $K_{IC}$ 's) were calculated on the basis of the stress intensity factor formula developed by Wu [7], using the measured load-displacement curves. All tests were performed on an MTS-810 machine at a crosshead speed of  $10^{-4}$  mm/s.

## RESULTS AND DISCUSSION

### Reactive Synthesis

It is well known that many intermetallics with high heats of formation ( $\Delta H_f$ ) can be synthesized via a solid-state reaction between the constituent elemental powders. Previous work [8] on  $\text{NbAl}_3$  ( $\Delta H_f = -119$  kJ/mol) indicated that the synthesis is self-propagating in character if a localized high heat pulse is applied to the powder mass. Under these conditions, it was found that a sustained

(self-propagating) synthesis reaction initiated at approximately 1000°C. Although a broad discussion of the characteristics of self propagating synthesis (SPS) is beyond the scope of this paper, it may be noted that SPS reactions require a low heat transfer coefficient of the powder mass, leading to a high localization of the heat of formation at the reaction interface.

Although this method of synthesis is simple in principle, it has several disadvantages [9]: the reaction is difficult to control, and generally yields a porous structure. In addition, the high temperatures generated at the product/reactant interface can lead to a loss of the low melting component by vaporization.

By contrast, if the Nb + Al powder mass is heated relatively slowly (as during RHC of NbAl<sub>3</sub>), the synthesis reaction is preceded by the melting of Al in the mixture. This is seen clearly by differential thermal analysis (DTA), Figure 2, of a sample corresponding to the stoichiometry of NbAl<sub>3</sub>. The data were obtained at a heating rate of 30°C/min, and show a variation of the sample temperature versus the temperature differential between the sample and a pure alumina reference. It can be seen that there is an endothermic peak associated with Al melting, followed by an exothermic peak at around 980°C, associated with the synthesis reaction. It should be noted that the reaction is relatively slow and lasts approximately 3 minutes, in sharp contrast to the high reaction rates (on the order of meters/s) commonly observed in self propagating synthesis [9].

It is thus clear that when the synthesis reaction is initiated, the released heat of formation is dissipated due to rapid heat transfer in liquid Al. Consequently, the synthesis proceeds not by the rapid propagation of a single "wave," but relatively slowly at a large number of sites in the powder mass. In addition, if external pressure is applied prior to the formation of a rigid network, the resulting sinter body is low in porosity. This is a key aspect of RHC. As shown schematically in Figure 1, a pre-load was maintained on the sample, which resulted in a continuous densification during Al melting as well as during NbAl<sub>3</sub> formation. The pressure was further increased to 7 ksi just past the synthesis reaction in order to additionally densify the sample, while ensuring that no free liquid Al would be "squeezed out" at the elevated pressure. The pressure on the sample was maintained for 60 minutes at 1350°C to enhance the microstructural homogeneity and densification. The microstructure of a sample processed under these conditions is shown in Figure 3. It can be seen from this optical micrograph (polarized light illumination) that the sample is fully dense (< 2 vol.% porosity) and with a uniform grain size.

**Effect of Stoichiometry** It was found that a dispersion of second- (or multi-) phase particles could be produced in reactively synthesized samples, as shown in Figure 4. It can be seen in this low magnification micrograph (secondary electron image) that the particles are dispersed relatively uniformly in the matrix.\*

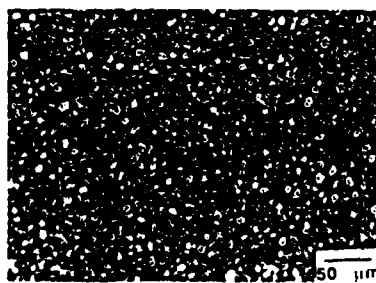


Figure 3 Microstructure of NbAl<sub>3</sub> produced by RHC.

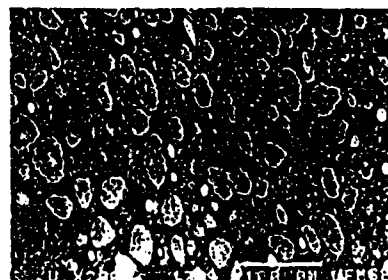


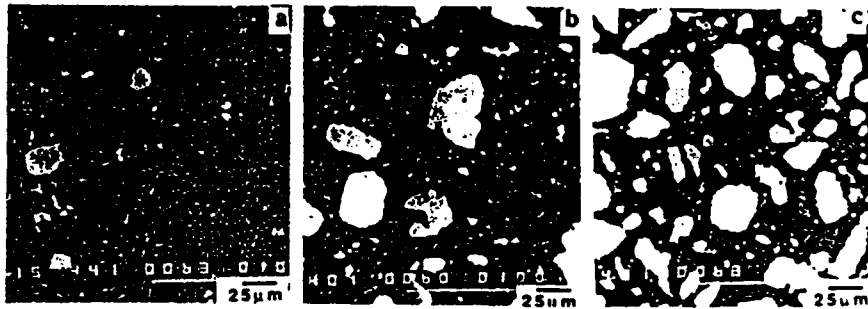
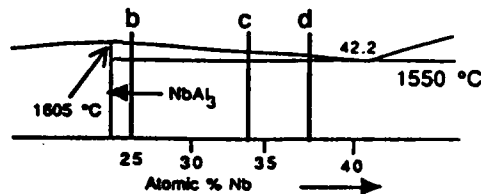
Figure 4 NbAl<sub>3</sub> matrix containing a dispersion of second phase particles.

\* This sample also contained chopped EP alumina fibers. However, their presence is of no consequence for the purposes of present discussion.

Also, some of the particles contain a central "core," as indicated by arrows on the micrograph. The presence (or absence) of the central core is related to the powder particle size, as discussed below.

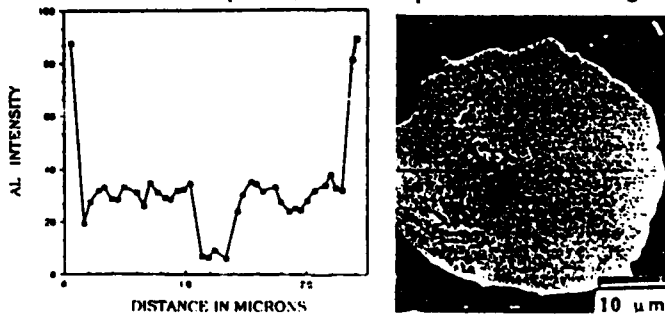
The volume fraction of the second phase dispersion could be controlled by controlling the starting stoichiometry of the powder mixture, as illustrated by Figures 5(a) to 5(d). Figure 5(a) shows the relevant portion of the Al-Nb equilibrium phase diagram with three initial compositions indicated by lines labelled b, c, and d. The corresponding microstructures exhibited an increase in the volume fraction of Nb<sub>2</sub>Al (from 6.9 to 27.7%) with increasing Nb content, as shown in Figures 5(b)-5(d), respectively. The measured volume fractions were less than those calculated on the basis of the equilibrium lever rule, with the amount of deviation increasing with increasing Nb content. It appears likely that the difference arises due to the presence of an Nb-rich core in some of the particles, which also provides the basis for the observed increase in the volume fraction deviation with increasing Nb content. Compositional analysis of the samples indicated that the matrix was close to the stoichiometry of NbAl<sub>3</sub> (74 at.% Al), while the average composition of particles without the core was 62 at.% Nb. Note that the latter composition agrees well with the low temperature equilibrium homogeneity limit of Nb<sub>2</sub>Al on the Al-rich side.

Figure 5 (a) Portion of Nb-Al diagram indicating the initial compositions of microstructure in (b), (c), and (d). (b)-(d) RHC processed NbAl<sub>3</sub> matrix composites containing dispersion of second phase particles.



**Effect of Particle Size** As noted earlier, some of dispersed particles in the matrix contained a central core. Compositional analysis of these particles indicated the core to be Nb-rich, as shown in Figures 6(a) and 6(b). Figure 6(a) is a compositional linescan across a particle and Figure 6(b) is the corresponding particle microstructure. It can be seen that there is a good correspondence between the compositional profile and the morphology of the particle: the aluminum content remains relatively constant in the bulk of the particle, shows a sharp decrease in the core region,

Figure 6 (a) Compositional linescan along a multiphase particle in NbAl<sub>3</sub> matrix. (b) Corresponding microstructural morphology showing a central (Nb) core.



and increases toward the periphery. This indicates a transition from the matrix to the particle core in the following order:  $NbAl_3 \rightarrow Nb_2Al$  (or  $Nb_3Al$ )  $\rightarrow$  (Nb). It was further observed that particles with the core were encountered more frequently in samples synthesized using the Source A Nb powder than with those synthesized using the Source B powder, while the average size of the Al powders had no discernible effect on the microstructure. A comparison of the two powders is shown in Figures 7(a) and 7(b), respectively. From the micrographs, it is clear that the Source A powder has a narrower size distribution and a larger mean size than the Source B powder. Although no attempt was made to further characterize the size distributions of these powders, it may be assumed that they are log-normally distributed, based on literature [10]. Schematic plots of the two size distributions are shown in Figure 8: a cut-off line representing a 10  $\mu m$  size is also shown on the plot, based on the observation that particles smaller than  $\sim 10 \mu m$  are completely consumed during the reaction. It can be seen from Figure 8 that the fraction of particles greater than 10  $\mu m$  is larger for the Source A size distribution compared to the Source B distribution. Consequently, the fraction of particles which are incompletely reacted would be greater for the Source A powder. It must be noted however that the 10  $\mu m$  cut-off is not absolute: several other factors such as the local heat and mass transfer and the surface to volume ratio of the particles will also affect the extent of the reaction.

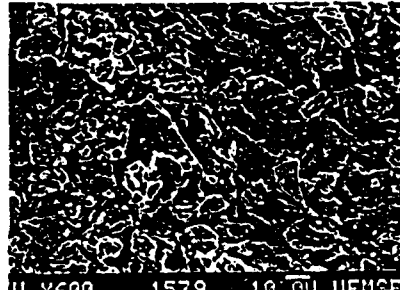
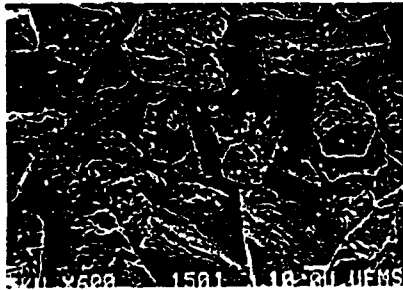


Figure 7 (a) Microstructure of Nb powder from Source A

(b) Microstructure of Nb powder from Source B.

Based on the foregoing analysis, the RHC of  $NbAl_3$  is summarized in Figure 9. The figure shows schematically the synthesis sequence and the effect of powder particle size. The sequence not only illustrates the synthesis and densification of  $NbAl_3$ , but also a key aspect of the use of RHC to form "in-situ" particle dispersed (Type I) composites: because of a random distribution of sites at which the second- (or multi-) phase particles are formed, uniformity of the dispersion is "built-in" into the process.

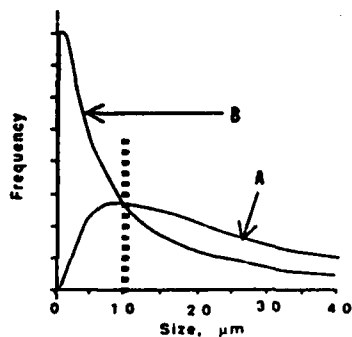


Figure 8 Size distributions of Source A and Source B powders (schematic).

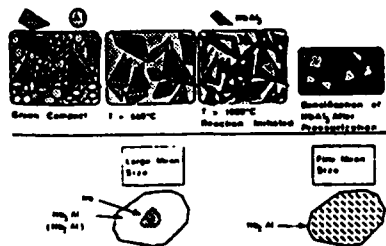


Figure 9 Synthesis sequence for RHC of  $NbAl_3$  (schematic).

### Fracture Toughness of Type I Composites

The fracture toughness was measured by two methods: (1) microhardness indentation and (2) three-point bend testing of chevron notched samples. In the microhardness indentation method, crack lengths produced by a 1000 g load for 10 indents were averaged and converted to  $K_{Ic}$  ( $\text{MPa}\cdot\sqrt{\text{m}}$ ) using the semi-theoretical relationship developed by Niihara et al. [11].

The average crack length was approximately related to the mean interparticle spacing, as shown in Figure 10. It can be seen that the average crack length decreases with decreasing mean interparticle spacing; furthermore, the average crack length should approach that of the monolithic matrix asymptotically at infinite mean interparticle spacing (i.e. zero volume fraction of second phase), as indicated by the dotted curve. One exception to the trend appears to be the sample labelled 4; the reason for this deviation is not clear, but may be related to the very large interparticle spacing (380  $\mu\text{m}$ ) in the sample. Based on this analysis, the  $K_{Ic}$  of the matrix was found to be 2.5, which is close to the value determined by three point bend testing of a chevron notched sample (1.6  $\text{MPa}\cdot\sqrt{\text{m}}$ ). The  $K_{Ic}$  value for the sample with the smallest average crack length was 3.5  $\text{MPa}\cdot\sqrt{\text{m}}$ , indicating a limited toughening by the second phase dispersion.

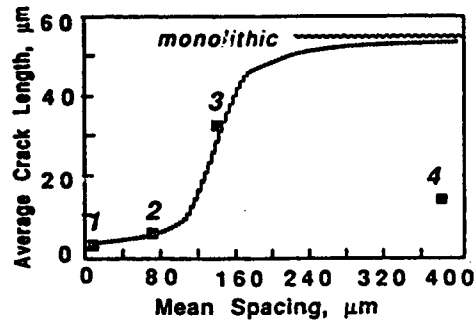


Figure 10 Dependence of average crack length on mean interparticle spacing in particle dispersion toughened  $\text{NbAl}_3$  matrix composites.

Analysis of the crack/particle interactions indicated that the mechanisms predominantly responsible for the increased toughness were crack blunting or shielding, rather than crack bridging, indicating an unfavorably strong matrix/particle bond. However, in a limited number of cases, crack bridging and deflection were also observed at the core of some of the particles. The three types of mechanisms are illustrated in Figures 11(a)-11(c), respectively. Some regions around the

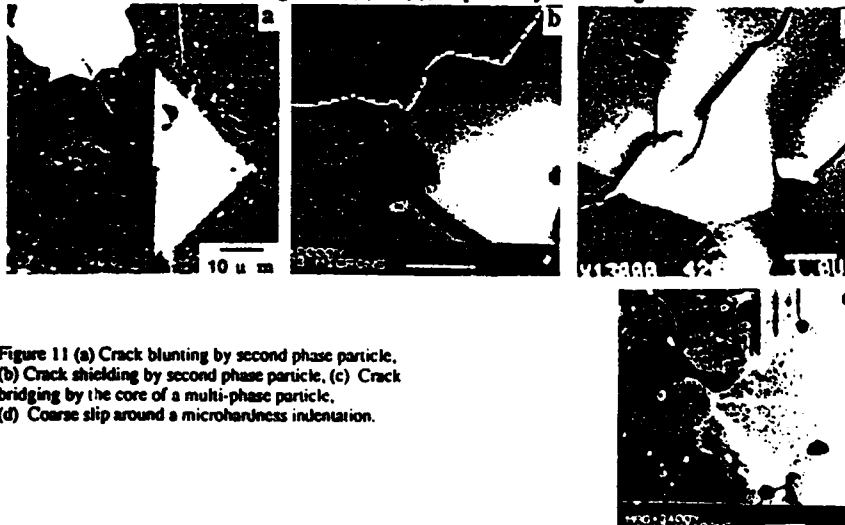


Figure 11 (a) Crack blunting by second phase particle, (b) Crack shielding by second phase particle, (c) Crack bridging by the core of a multi-phase particle, (d) Coarse slip around a microhardness indentation.

microhardness indents exhibited features resembling coarse slip, as shown in Figure 11(d). While this is contradictory to the brittle nature of the matrix, it is possible that some plastic deformation may have taken place under the high and complex state of stress generated by the indentation.

### Synthesis of Type II Composites

It was shown in the preceding sections that NbAl<sub>3</sub> matrix composites containing a dispersion of second phase particles could be reactively synthesized with good microstructural control. Although these particles imparted a limited amount of toughening, the fracture toughness of the composites was not adequate.<sup>†</sup> Consequently, ductile Nb filament reinforced composites were produced in order to improve the ambient temperature fracture toughness. For this purpose, a method was developed to form a diffusion barrier coating on the Nb filaments "in-situ" via an unique coupling of filament pre-treatment with RHC of the matrix.<sup>‡</sup>

Chopped Nb filaments (0.25 mm dia. X ~4 mm) with and without a pretreatment were blended with the elemental powders and processed as per the procedure described for Type I composites. The details of the pretreatment, coating formation mechanisms, the microstructural and compositional characteristics of the coating, etc. are outside the scope of this paper, and will be given in a future publication.

The microstructures of two Type II composites (with uncoated and "in-situ" coated Nb filaments) in the as-processed condition are shown in Figures 12(a) and 12(b), respectively. It can be seen from the optical micrographs (polarized light illumination) that in the case of uncoated filaments (12(a)), there is an extensive matrix/filament interaction leading to the formation of an intermetallic layer and porosity at the interface, as well as filament degradation due to Al diffusion in the bulk. By contrast, these interactions are significantly reduced upon formation of a diffusion barrier coating (12(b)). The microstructural appearance of the coating is shown at a higher magnification in Figure 13. Note that the coating is dense, and relatively uniform in grain size. Long-term annealing (100 hours at 1200° C) indicated that the coating was extremely stable and provided an excellent protection to the Nb filaments.

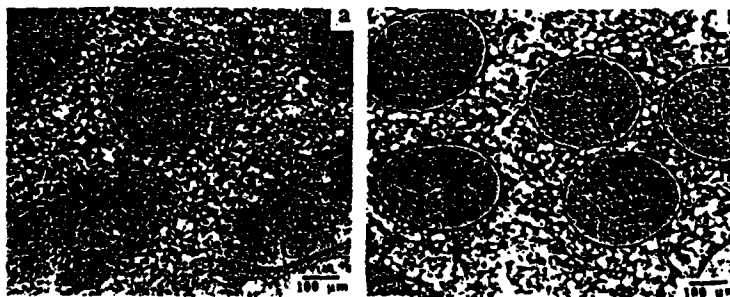


Figure 12 Microstructure of Nb filament reinforced NbAl<sub>3</sub> matrix composites. (a) Uncoated filaments, (b) Coated Nb filaments.

### Fracture Toughness of Type II Composites

Preliminary fracture toughness measurements of composites (chevron-notched samples) containing "is-situ" coated Nb filaments indicated a significant improvement over matrix. This is illustrated in Figure 14 with the load-displacement curves for the monolithic matrix and a composite containing 20 vol.% of the reinforcement. It is clear that the composite is significantly stronger and tougher

<sup>†</sup> The main benefit of these particles may lie in their ability to strengthen the matrix at high temperatures.

<sup>‡</sup> Patent application pending

than the matrix. Also, the curve for the composite beyond the maximum load is "stepwise," which suggests that the failure mechanism is sequential, incorporating filament necking and fracture. The calculated  $K_{IC}$  value for the composite ( $9.6 \text{ MPa}\cdot\sqrt{\text{m}}$ ) indicated an  $\sim 50\%$  increase in the fracture toughness compared to the monolithic matrix.

The general microstructural appearance of a fracture surface at the chevron notch is shown in Figure 15(a) and at a higher magnification in Figure 15(b). It can be seen that there is a clear

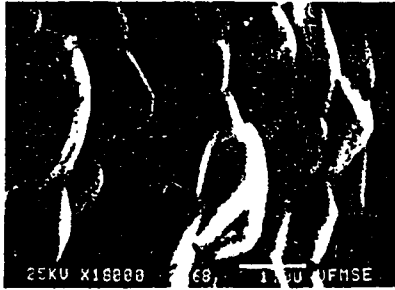


Figure 13 Microstructural appearance of an "in-situ" coating on the surface of an Nb filament

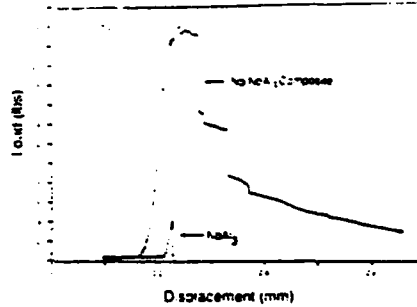


Figure 14 Three-point bend test load-displacement curves for chevron notched specimens of monolithic matrix and 20 vol.% Nb filament reinforced composite.

evidence of filament pull-out and necking during fracture. There is also evidence of partial decohesion at the filament/coating/matrix interfaces, as shown in Figure 15(c) (arrow). Thus, the

Figure 15 (a) General microstructural appearance of chevron notch fracture surface, (b) Higher magnification fractograph of (a) showing filament pull-out, (c) Illustration of partial interfacial decohesion at the filament/coating/matrix interfaces (arrow).



increase in toughness appears to be related to a combination of mechanisms including (1) crack bridging by the filaments with partial decohesion at the interface in the wake of the crack and (2) effective matrix-to-filament load transfer leading to filament deformation and necking. Note that for the filament necking to take place, *both* partial interfacial decohesion and effective load transfer are required. Therefore, it may be inferred that the filament/coating/matrix interfaces have optimum characteristics for facilitating the operation of a variety of toughening/strengthening mechanisms.

#### SUMMARY AND CONCLUSIONS

(1) Near-theoretical density NbAl<sub>3</sub> was obtained by reactive hot compaction (RHC) of elemental powders at 1350° C under a pressure of 7 ksi. (2) It was shown that by controlling the initial stoichiometry of the powder mixture prior to RHC, NbAl<sub>3</sub> matrix composites containing a dispersion of second- (or multi-) phase (either Nb<sub>3</sub>Al or Nb<sub>2</sub>Al with an Nb core or Nb<sub>2</sub>Al) could be formed "in-situ." A limited improvement in the fracture toughness was obtained via this route, indicating a strong matrix/particle bond. (3) NbAl<sub>3</sub> matrix composites reinforced with coated or uncoated Nb filaments were processed via RHC. It was shown that filaments without a diffusion barrier coating degraded to an significant extent during processing, while filaments with an "in-situ" formed protective diffusion barrier coating minimized matrix/filament interactions. A significant improvement in the fracture toughness of NbAl<sub>3</sub> matrix composites was observed upon reinforcing with coated ductile Nb filaments. (4) The "in-situ" coating appears to provide both: an excellent and stable diffusion barrier and optimum properties for the operation of various toughening/strengthening mechanisms.

#### ACKNOWLEDGEMENTS

The authors gratefully acknowledge the support of DARPA through the DARPA-AMMP program on Composites to the University of Florida under grant # MDA972-88-J-1006. The authors also acknowledge TWCA and John Haygarth for supplying the Nb powder.

#### REFERENCES

1. C.E. Lundin and A.S. Yamamoto, *Trans. AIME*, **236**, 863 (1966).
2. G. Raission and A. Vignes, *Rev. Appl. Phys.*, **2**, 535 (1970).
3. D. Shechtman and L.A. Jacobson, *Met. Trans.*, **6A**, 1325 (1975).
4. J.H. Schneibel, P.F. Becker, and J.A. Horton, *J. Mater. Res.*, **3**, 1272 (1988).
5. F.R. Frasier, Master's Thesis, University of Washington, Seattle (1989).
6. R.M. Paine, A.J. Stonehouse, W.W. Beaver, Wright Air Development Center Tech. Rep. # 5929- Part II, (1959).
7. S.X. Wu, Chevron-Notched Specimens, ASTM STP-855, edited by J.H. Underwood, S.W. Freiman, and F.I. Baratta, (1984).
8. A.B. Gokhale and A. Amini, (Unpublished work).
9. W.L. Frankhouser, K.W. Brendley, M.C. Kieszek, and S.T. Sullivan, Gasless Combustion Synthesis of Refractory Compounds, Noyes Publications, Park Ridge, NJ (1985).
10. G. Herdan, Small Particle Statistics, American Elsevier Publishing Company, New York, (1953).
11. K. Niihara, R. Morena, and D.P. H. Hasselman, *J. Mat. Sci. Lett.*, **1**, 13 (1982).

# *In situ* formation of an alumina interface coating in reactively synthesized NbAl<sub>3</sub>-Nb composites

Lixion Lu, A. B. Gokhale and Reza Abbaschian

Department of Materials Science and Engineering, University of Florida, Gainesville, FL 32611-2046 (U.S.A.)

## Abstract

Recent results on the formation of an alumina (Al<sub>2</sub>O<sub>3</sub>) layer at the matrix-reinforcement interfaces in reactively synthesized NbAl<sub>3</sub>-Nb composites are presented. The interfacial Al<sub>2</sub>O<sub>3</sub> layer was formed *in situ* via a unique coupling of the surface pre-oxidation of niobium filament reinforcements and reactive synthesis of the matrix from a mixture of the elemental constituents. Details of the processing methodology are presented together with the structural, morphological and compositional characterization of the composites. The *in situ* Al<sub>2</sub>O<sub>3</sub> coating was found to be stable during long-term annealing and acted as an effective barrier to elemental interdiffusion. Composites with the *in situ* interfacial coating were found to be significantly tougher than the monolithic matrix; the various toughening mechanisms are discussed with special emphasis on the role of the multilayered multiphase interfacial morphology.

## 1. Introduction

Transition metal aluminides are considered to be potential candidate materials for high temperature structural components in aerospace applications [1]. NbAl<sub>3</sub> in particular possesses a desirable combination of low density (4.62 g cm<sup>-3</sup>), relatively high melting temperature (1605 °C) and adequate ambient temperature elastic modulus and compressive strength (above 120 GPa and 520 MPa respectively). However, as with many other ordered intermetallics, NbAl<sub>3</sub> exhibits a low ambient temperature fracture toughness and consequently a very limited damage tolerance [2].

Artificially compositing such brittle intermetallics with ductile refractory reinforcements shows promise for overcoming this significant limitation. However, for these artificial composites the reinforcements are, in general, embedded in the matrix in a thermodynamically non-equilibrium state. Consequently, during high temperature processing of the composites, matrix-reinforcement interactions are commonly encountered. In addition, the extent of such interactions is likely to be enhanced upon exposing the composites to high service temperatures. The interactions, which may result in the formation of other brittle intermetallics, significant interdiffusion of the

elemental constituents or formation of local stress raisers due to altered interface geometry, are in a majority of the instances undesirable. For example, the diffusion of an elemental species into a ductile reinforcement can lead to one or more of the following: a loss of strength, a lowering of the fracture stress, or a change in the failure mechanism from ductile to brittle. Additional damage also can result if the reaction products lead to an unfavorable interface strength or if the reaction layers experience premature fracture [3].

It is clear that stable matrix-reinforcement interfaces are critical to the integrity of a composite. As noted earlier, inherent thermodynamic stabilization is indeed rare in artificial composites. Consequently, a kinetic stability is generally sought in the form of diffusion barrier coatings at the interfaces. Among several coating materials, alumina (Al<sub>2</sub>O<sub>3</sub>) is known to be one of the best for its microstructural stability, chemical compatibility (especially with aluminide intermetallics) and low diffusivity at high temperatures.

In this paper, a new technique is described by which an alumina coating is formed *in situ* during the synthesis and consolidation of NbAl<sub>3</sub> matrix composites. The approach is based on reactive hot compaction (RHC), which combines reactive synthesis of the matrix with hot pressing. RHC is

well suited to the fabrication of intermetallics as well as intermetallic matrix composites in general and for transition metal aluminides in particular, because of the formation of a low melting point (typically aluminum-rich) transient liquid during the process. The presence of such a liquid not only accelerates the diffusional mixing but also aids in a rapid consolidation of the powder mass [4]. In the present work, a new concept was tested, namely to expand the scope of the formation reaction not only to include the synthesis of the intermetallic matrix but also to form simultaneously an interface coating *in situ* via coupling of a reinforcement pre-treatment with RHC.

## 2. Experimental methods

Fabrication of the composites was based on a unique coupling of the reactive synthesis of the matrix and an oxidation pre-treatment of the reinforcement, as reflected in the fabrication sequences described below.

### 2.1. Reinforcement pre-treatment

Chopped niobium filaments 250  $\mu\text{m}$  in diameter and 5 mm long were used as the reinforcement. Prior to the oxidation pre-treatment, the filaments were cleaned ultrasonically in acetone followed by surface etching in a 1:2 mixture of HF-HNO<sub>3</sub> solution and a final distilled water rinse. The cleaned filaments were placed in a quartz tube and oxidized at 500 °C in a stream of pure oxygen flowing under a pressure slightly in excess of one atmosphere for various lengths of time ranging from 3 to 15 min. During oxidation, the quartz tube was rotated to ensure a uniform exposure of the filament surface.

### 2.2. Reactive hot compaction

The pre-treated niobium filaments were mixed in a cylindrical blender with niobium and aluminum elemental powders, pre-mixed to yield a near-NbAl<sub>3</sub> stoichiometry. The average size of the niobium and aluminum powders was less than 45  $\mu\text{m}$  and 20  $\mu\text{m}$  respectively. The mixtures were cold compacted into a disk shape (38 mm in diameter and 8 mm thick) under a pressure of 10 klbf in<sup>-2</sup>, followed by hot pressing under vacuum in a BN-lined graphite die. A previously optimized hot-pressing schedule was followed as shown in Fig. 1.

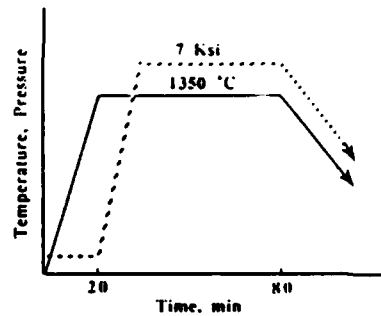


Fig. 1. RHC processing cycle (schematic).

## 2.3. Characterization and testing

The characterization of microstructures and interfaces of the composites was carried out using optical and scanning electron microscopy, electron probe microanalysis, transmission electron microscopy of the interfaces, and phase identification via X-ray diffraction (XRD) analysis.

The composites were tested for thermal stability via inert atmosphere annealing at 1200 °C for 100 h. The fracture toughness of the composites was measured by three-point bending tests on chevron-notched specimens (3.3 mm  $\times$  5 mm  $\times$  greater than 25 mm) with a test fixture span of 20 mm. The dimensions of the tested samples were strictly in accordance with *ASTM Standard 392-87* [5], with a 90° root angle chevron notch cut using a diamond wheel (blade 0.15 mm thick) saw fitted with a special in-house built fixture. All samples were tested on an MTS-810 at a cross-head speed of 10<sup>-4</sup> mm s<sup>-1</sup>; the toughness  $K_{Ic}$  values were calculated on the basis of a modified stress intensity factor formula developed by Wu [6], using the measured peak load on load-displacement curves.

## 3. Results and discussion

### 3.1. Reactive hot compaction

Previous work [7] on the RHC processing of NbAl<sub>3</sub> indicated that sinter bodies close to full density (less than 2 vol.% porosity) could be synthesized using the reactive hot-pressing schedule shown in Fig. 1. Because the detailed analysis of NbAl<sub>3</sub> RHC has been presented in an earlier publication [7], only a summary of the salient features of the reaction sequences are given here: the first dominant reaction during heat-up is that of aluminum melting, resulting in a

rapid spreading of liquid aluminum throughout the powder mass. This is followed by the matrix synthesis reaction (initiated at approximately 980 °C), accompanied by a sharp temperature rise due to release of the heat of formation ( $-119 \text{ kJ mol}^{-1}$ ) of  $\text{NbAl}_3$ . Subsequent densification via pressurization then yields a sample of near-theoretical density, as shown in Fig. 2. In addition, it was found that, by controlling the initial stoichiometry of the Nb-Al powder mixture and selecting an appropriate niobium powder size, a uniform dispersion of  $\text{Nb}_2\text{Al}$  particles in an  $\text{NbAl}_3$  matrix can be obtained. Such two-phase *in situ* composites are expected to possess better high temperature mechanical properties (owing to the higher melting temperature of  $\text{Nb}_2\text{Al}$ ), without sacrificing the ambient mechanical properties. In fact, a slight increase in ambient fracture toughness has been observed previously [7].

The scope of RHC can be expanded to include the fabrication of niobium-filament-toughened  $\text{NbAl}_3$  matrix composites with a diffusion barrier coating at the matrix-reinforcement interfaces. As discussed below, the synthesis reaction can be extended not only for producing the  $\text{NbAl}_3$  matrix but also the simultaneous *in situ* formation of an  $\text{Al}_2\text{O}_3$  layer at the Nb-NbAl<sub>3</sub> interfaces. Conceptually, the strategy for forming the  $\text{Al}_2\text{O}_3$  layer *in situ* was based on initially providing a layer of niobium oxide on the surface of niobium filament reinforcements via a pre-oxidation treatment. Subsequent coupling with the reactive synthesis and consolidation of the aluminide matrix was utilized for the reactive conversion of the niobium oxide into an  $\text{Al}_2\text{O}_3$  interfacial layer.

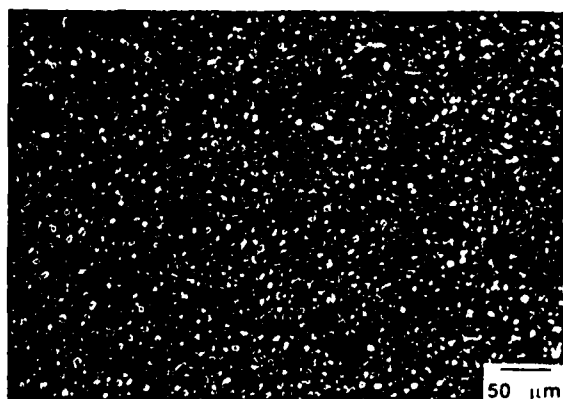


Fig. 2.  $\text{NbAl}_3$  fabricated by the RHC process (polarized light illumination)

Thermodynamic data indicated that the niobium oxide(s) could be reduced by aluminum to produce  $\text{Al}_2\text{O}_3$  during subsequent processing. This is illustrated by a plot of the Gibbs energy of formation of  $\text{Al}_2\text{O}_3$  and the three possible niobium oxides ( $\text{NbO}$ ,  $\text{NbO}_2$  and  $\text{Nb}_2\text{O}_5$ ) as a function of temperature (Fig. 3), indicating that  $\text{Al}_2\text{O}_3$  is thermodynamically more stable than each of the three niobium oxides at all temperatures.

### 3.2. Pre-oxidation and its coupling with reactive hot compaction

The chopped niobium filaments (250  $\mu\text{m}$  in diameter) were pre-oxidized at various temperatures and lengths of time. It was found that at temperatures above about 550 °C, a spontaneous uncontrollable self-propagating oxidation reaction occurred. Evidently, the high oxidation rate and the high heats of formation of the niobium oxides (ranging from  $-406$  to  $-1990 \text{ kJ mol}^{-1}$ ) result in a rate of temperature rise which greatly exceeds the rate of heat removal from the specimen under the experimental conditions employed. Consequently, setting the upper limit of the treatment temperature at 500 °C, the thickening kinetics of the oxide layer were determined as described below. In addition, diffusion calculations indicated that, at 500 °C, the oxygen penetration depth in niobium was limited to about 4  $\mu\text{m}$  if the treatment times were kept under 10 min, thus minimizing the potential embrittlement of the niobium filaments.

The thickening kinetics of the oxide layer at 500 °C are shown in Fig. 4 with a plot of the measured oxide layer thickness as a function of the square root of oxidation time. The linearity of

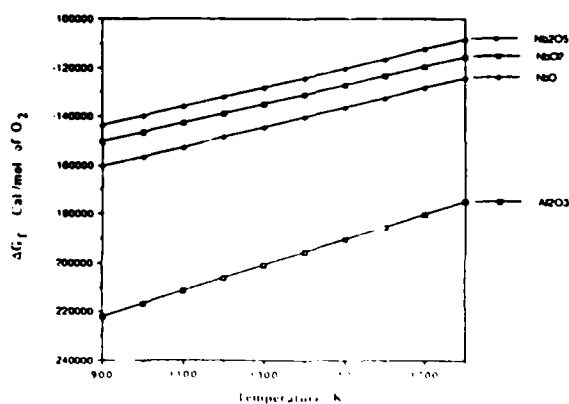


Fig. 3. The Gibbs free-energy data for niobium oxides and  $\text{Al}_2\text{O}_3$ .

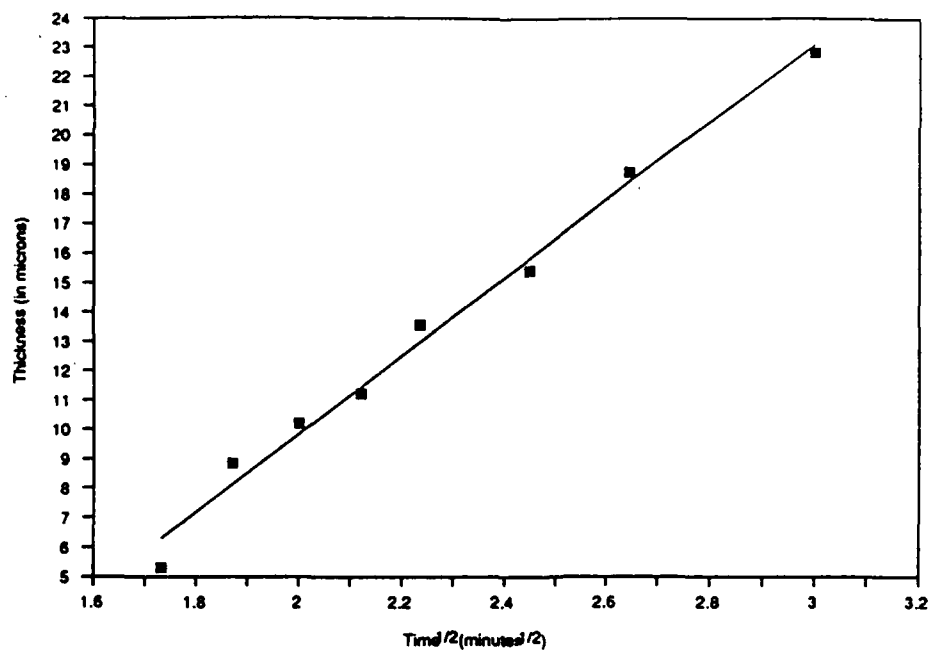


Fig. 4. Thickening of niobium oxide layer at 773 K under an oxygen pressure of 14.7 lbf in<sup>-2</sup>.

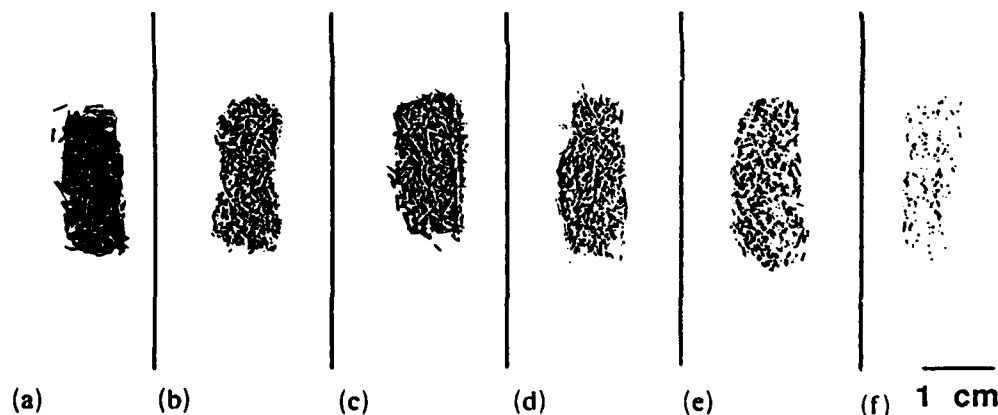


Fig. 5. Appearance of oxidized niobium filaments treated for various times: (a) 3 min; (b) 4 min; (c) 5 min; (d) 6 min; (e) 7 min; (f) 9 min.

the data indicates a parabolic oxidation rate during the short-term oxidation treatment and that the rate is most probably controlled by oxygen diffusion through the oxide layer.

The oxidized niobium filaments exhibited a continuous color change from blue through gray to white with increasing oxidation time, as shown in Fig. 5 (which shows the color change as gray shades), while XRD analysis of the oxidized filaments (Fig. 6) indicated that the major oxide formed on the niobium surface is Nb<sub>2</sub>O<sub>5</sub>. Neither

NbO nor NbO<sub>2</sub> were detected, in agreement with data in the literature [10], while according to the relative peak intensities the amount of Nb<sub>2</sub>O<sub>5</sub> increased with increasing treatment time. Consequently, it may be concluded that the oxide layer thickening is solely a result of additional Nb<sub>2</sub>O<sub>5</sub> formation and is not due to the formation of other oxides.

The morphology of the oxide scale was examined by scanning electron microscopy (SEM) of epoxy-mounted and metallographically prepared

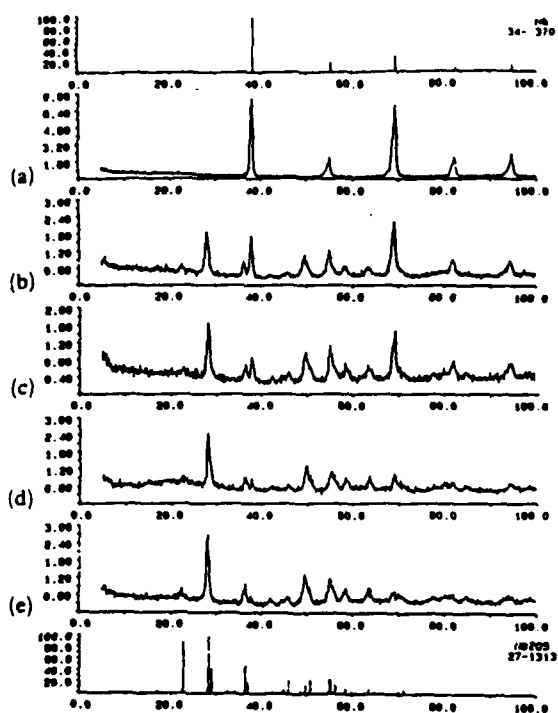


Fig. 6. XRD patterns corresponding to the oxidized filaments shown in Figs. 5(a)–5(e). The top and the bottom patterns are the patterns given in refs. 8 and 9 for niobium and  $\text{Nb}_2\text{O}_5$ , respectively.

oxidized filaments. Micrographs of niobium filaments oxidized for 3 min, 4 min, 5 min, 6 min, 7 min and 9 min are shown in Figs. 7(a), 7(b), 7(c), 7(d), 7(e) and 7(f) respectively. The common feature of the  $\text{Nb}_2\text{O}_5$  layer is a porous structure, as shown in the higher magnification micrograph in Fig. 8; the amount of porosity was found to vary from 30 to 50%, depending on the thickness of the oxide layer. In addition, significant radial cracking developed when the thickness of the oxide layer exceeded  $20\ \mu\text{m}$ ; this is believed to be due to a drastic volume expansion caused by density change from  $8.4\ \text{g cm}^{-3}$  for niobium to  $4.7\ \text{g cm}^{-3}$  for  $\text{Nb}_2\text{O}_5$ . Continued thickening beyond 7 min resulted in a non-uniform oxide layer because of spalling, as shown in Fig. 7(f). Table 1 gives a summary of oxide layer thickness, color of the oxide film, and its stability on cooling with respect to cracking and spalling as functions of the oxidation time. On the basis of these observations, the upper time limit for the oxidation treatment was restricted to 7 min.

The pre-oxidized niobium filaments were mixed with niobium and aluminum element powders in the desired stoichiometry and reactively hot pressed using the schedule

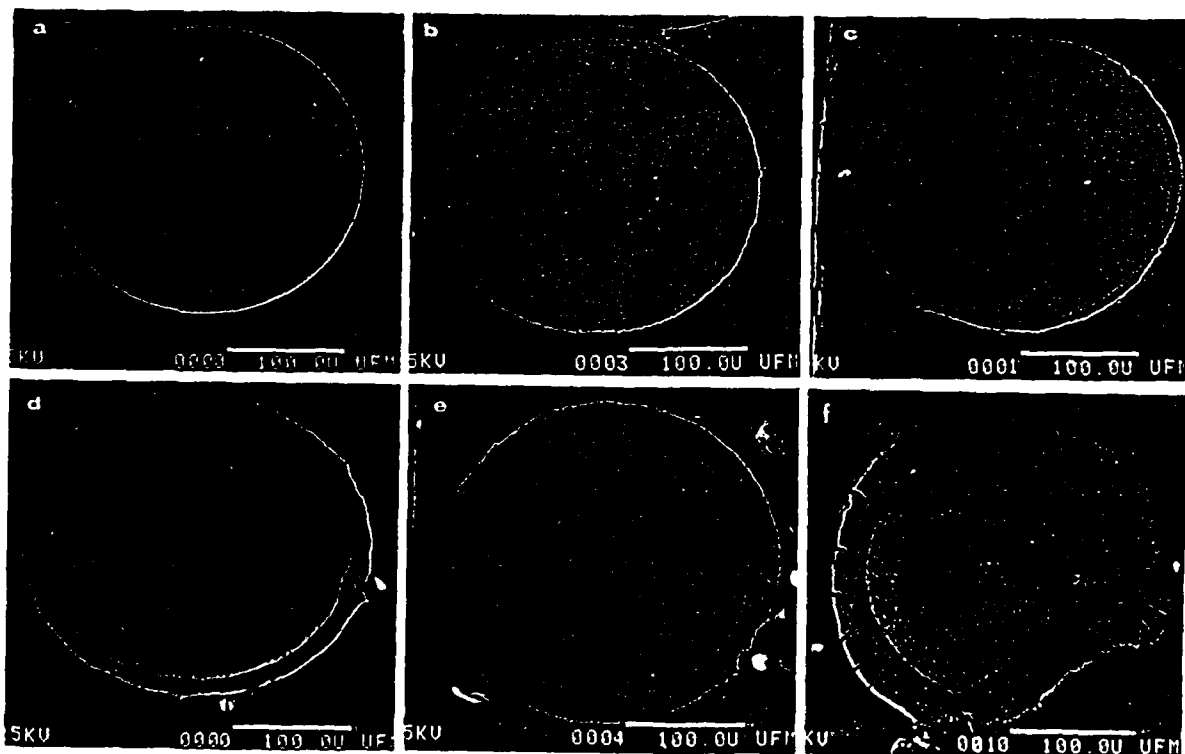


Fig. 7. SEM micrographs of oxidized niobium filaments corresponding to the niobium filaments shown in Fig. 5

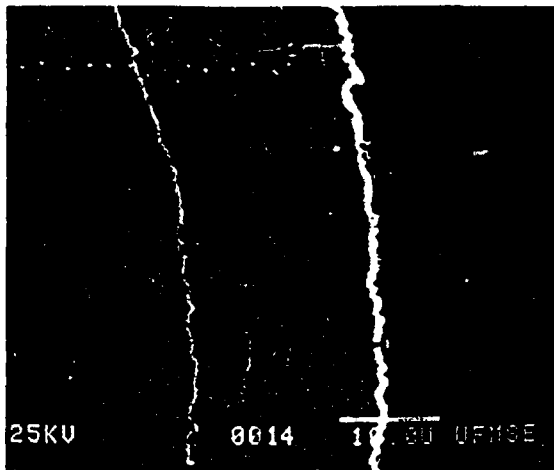


Fig. 8. Microstructure of the  $Nb_2O_5$  scale on a typical oxidized niobium filament.

TABLE I

Summary of niobium oxidation time series at 500 °C under  $14.7 \text{ lbf in}^{-2}$  oxygen pressure

| Oxidation time (min) | Average oxide thickness ( $\mu\text{m}$ ) | Surface color | Layer stability |
|----------------------|---|---------------|-----------------|
| 3.0                  | 5.30                                      | Dark blue     | Stable          |
| 3.5                  | 8.85                                      | Light blue    | Stable          |
| 4.0                  | 10.20                                     | Dark gray     | Stable          |
| 4.5                  | 11.20                                     | Dark gray     | Stable          |
| 5.0                  | 13.55                                     | Light gray    | Stable          |
| 6.0                  | 15.38                                     | Light gray    | Cracks          |
| 7.0                  | 18.0                                      | Light gray    | Cracks          |
| 9.0                  | 22.83                                     | White         | Spalling        |

described earlier. Differential thermal analysis and microstructural analysis of samples at various stages in the reaction sequence [11] indicate that the interfacial  $Al_2O_3$  formation is triggered by the temperature rise which accompanies the matrix synthesis reaction. The interfacial microstructural morphology presented below revealed that the  $Al_2O_3$  layer is surrounded by a layer of  $Nb_2Al(\sigma)$  on the matrix side. This also suggests that the bulk of  $Al_2O_3$  formation occurs via a solid state reaction with the matrix (*i.e.* in the post-matrix-synthesis stage), leading to an aluminum-poor region immediately adjacent to the interface. It should be noted that, although a similar local compositional change would be encountered during  $Al_2O_3$  formation via reaction with liquid aluminum, rapid mass transport in the liquid would tend to level the compositional gradients.

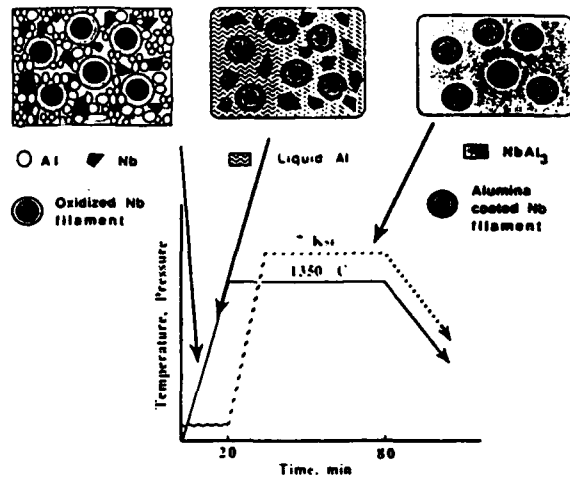


Fig. 9. Synthesis sequence for RHC of an Nb-NbAl<sub>3</sub> composite (schematic).

The various reactions, their sequence and the related sequence of microstructural development of an RHC processed composite are shown schematically in Fig. 9 together with their location in relation to the processing cycle used.

It was found that the thickness of the subsequently formed  $Al_2O_3$  layer was linearly related to the original thickness of the  $Nb_2O_5$  layer, as illustrated in Fig. 10. The plot indicates a significant reduction in the thickness after reactive hot pressing, even though  $Al_2O_3$  has a lower density than  $Nb_2O_5$  ( $3.97 \text{ g cm}^{-3}$  for  $Al_2O_3$  compared with  $4.47 \text{ g cm}^{-3}$  for  $Nb_2O_5$ ). Linear least-squares regression analysis of the experimental data ( $R^2 = 0.98$ ) gave the following relation:

$$t_{Nb_2O_5} = 5.07 + 2.53t_{Al_2O_3}$$

One of the reasons for the observed thickness reduction is believed to be due to the 30–50% porosity in the initial  $Nb_2O_5$  layer. In addition, it is likely that the higher temperature encountered during RHC (compared with that for the pre-oxidation treatment) may decrease the amount of  $Nb_2O_5$  because of the increased oxygen solubility in niobium.

### 3.3. Microstructure of the composites

The microstructures of RHC-processed NbAl<sub>3</sub>-Nb composites reinforced with bare (uncoated) and  $Al_2O_3$ -coated niobium filaments are shown in Figs. 11(a) and 11(b) respectively. It can be seen that, in the absence of an interfacial coating, there is an extensive matrix-filament interaction in the form of intermetallic formation

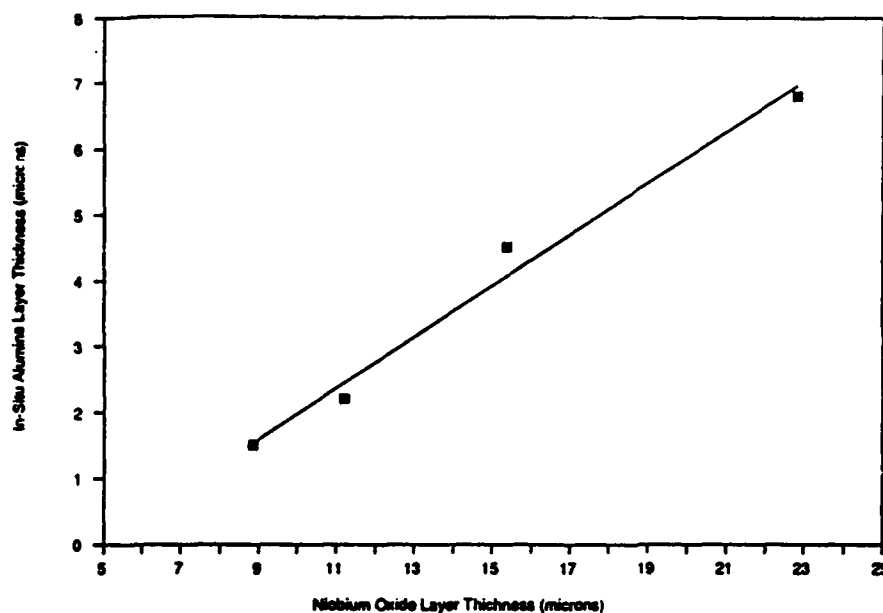


Fig. 10. Thickness relation between the initial  $\text{Nb}_2\text{O}_5$  scale and the alumina layer formed *in situ*.

as well as the penetration of aluminum (with characteristics similar to grain boundary embrittlement) into the niobium filaments. By contrast, these interactions were significantly reduced upon formation of the  $\text{Al}_2\text{O}_3$  layer at the interface (Fig. 11(b)). These uncoated and coated composites were further annealed at  $1200^\circ\text{C}$  for 100 h. The microstructure of the two types of niobium filaments after annealing are shown in Figs. 12(a) and 12(b) respectively. It is clear that the interfacial reaction zone has thickened for the uncoated reinforcements. In addition, it was found that the microhardness of the reinforcement increased sharply towards the periphery for the uncoated filaments, which is clearly an undesirable situation. Furthermore, the interfacial layer continued to thicken with further annealing, leading to an unstable composite microstructure. By contrast, the microhardness across the coated filament was approximately constant. This is corroborated independently by compositional line scans across the coated reinforcement-matrix interfaces in the pre-annealed and post-annealed ( $1200^\circ\text{C}$  for 100 h) conditions (Figs. 13(a) and 13(b) respectively). It can be seen that after the annealing treatment there is only a limited amount of aluminum diffusion in the filaments coated *in situ*.

The above line scans and the interfacial microstructural morphology (Fig. 14) also reveal that a

multilayer structure is formed at the interfacial region, with a sequence of  $\text{NbAl}_3 \rightarrow \text{Nb}_2\text{Al} \rightarrow \text{Al}_2\text{O}_3 \rightarrow \text{Nb}$ , upon traversing from the matrix to the reinforcement side. Also, it is noted that the aluminum profile in the  $\text{Al}_2\text{O}_3$  layer decays towards the niobium side of the  $\text{Nb}-\text{Al}_2\text{O}_3$  interface in both samples, suggesting that the aluminum diffusion could be one of the rate-controlling steps in the  $\text{Al}_2\text{O}_3$  formation process. Furthermore, it should be noted that there is a slight increase in the niobium content of the  $\text{Al}_2\text{O}_3$  scale toward the niobium filament side, indicating that the  $\text{Al}_2\text{O}_3$  formation sequence must also be controlled by a niobium rejection and transport mechanism.

Transmission electron microscopy (TEM) analysis of the interfacial regions [12] also supported this morphological sequence, as shown by the bright field micrograph in Fig. 15(a). The analysis indicated that the  $\text{Al}_2\text{O}_3$  was present in the stable  $\alpha$  modification, while niobium precipitates were detected in the  $\text{Al}_2\text{O}_3$  layer toward the niobium filament side of the interface (Fig. 15(b)), supporting the compositional analysis. The presence of niobium particles predominantly near the niobium side and their near-absence toward the matrix side reveal an interesting aspect of the  $\text{Al}_2\text{O}_3$  formation reaction: it appears that the niobium released during  $\text{Nb}_2\text{O}_5$  reduction by aluminum according to the reaction  $3\text{Nb}_2\text{O}_5 +$

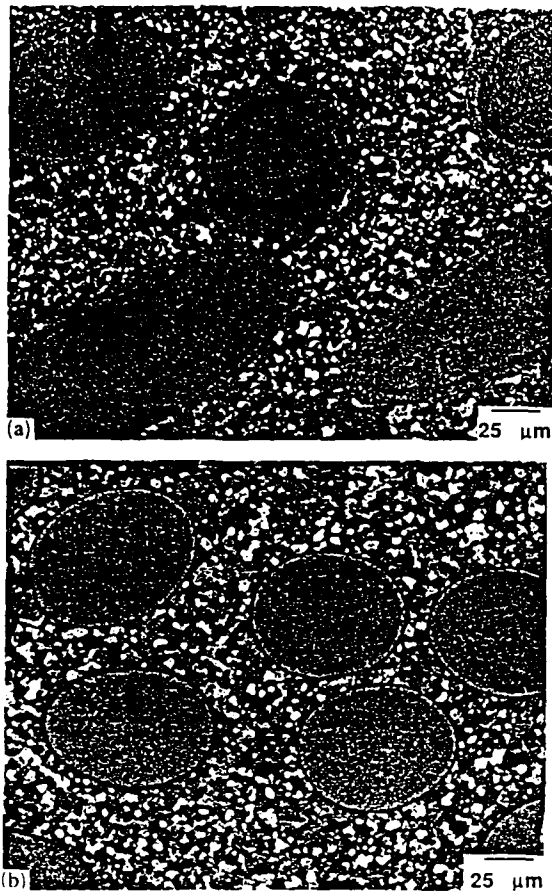


Fig. 11. Microstructures of niobium-filament-reinforced  $\text{NbAl}_3$  composites (as processed): (a) uncoated filaments; (b) filaments coated *in situ*.

$10\text{Al} = 5\text{Al}_2\text{O}_3 + 6\text{Nb}$  may be accommodated by the unreacted  $\text{Nb}_2\text{O}_5$  ahead of the  $\text{Al}_2\text{O}_3$ - $\text{Nb}_2\text{O}_5$  interface. Subsequently, the continued transformation of  $\text{Nb}_2\text{O}_5$  to  $\text{Al}_2\text{O}_3$  may lead to the observed precipitation of niobium. The interface morphology is summarized schematically in Fig. 15(c).

It was critical for the success of the *in situ* alumina coating technique that the niobium reinforcements themselves do not degrade because of the pre-oxidation treatment, since it is well known that interstitial elements such as oxygen can significantly embrittle niobium. The Vickers microhardness of the pre-oxidized niobium filaments embedded in the matrix was measured as a function of the pre-oxidation time. It was found that the Vickers microhardness ranged from a minimum of 20HV (for 4 min of oxidation treatment) to a maximum of 300 HV (for 9 min of

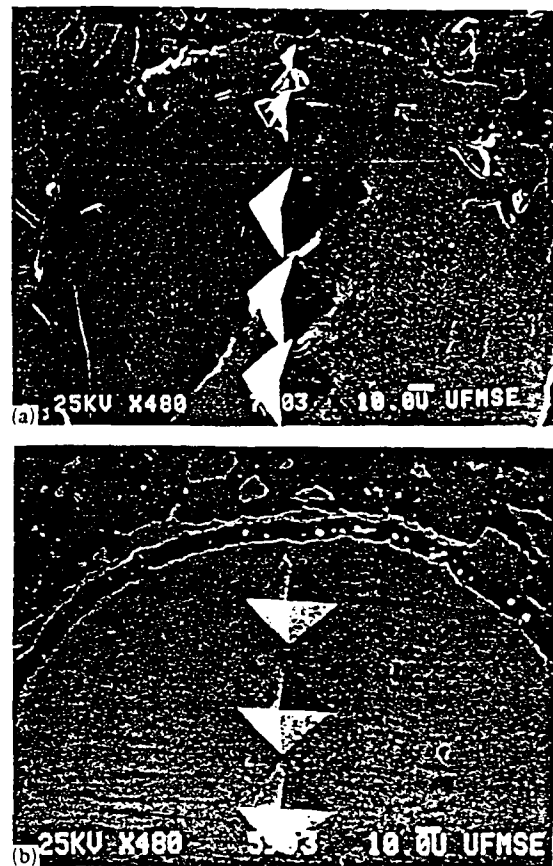
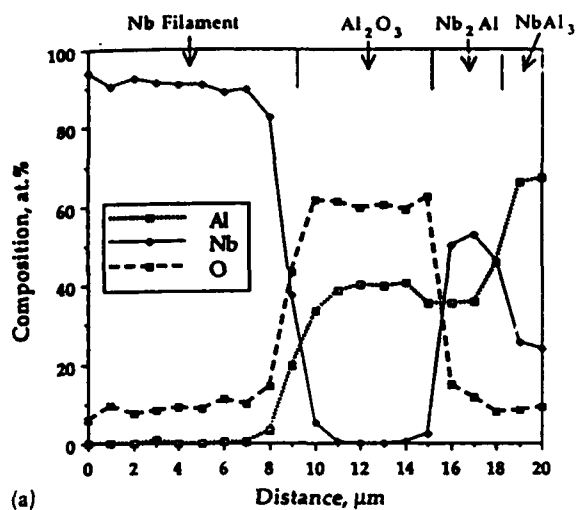


Fig. 12. Microstructures of niobium filaments embedded in an  $\text{NbAl}_3$  matrix after long-term annealing: (a) uncoated filament; (b) filament coated *in situ*.

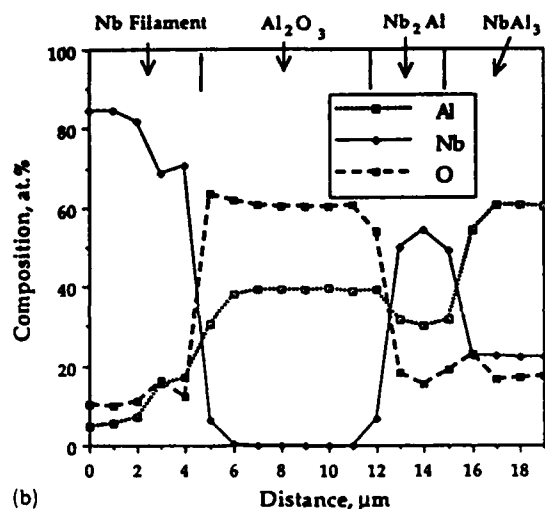
oxidation treatment). On comparison of these values with the data of other investigators [13] (60 HV for pure niobium to a maximum of 325 HV for niobium containing 0.35 wt.% O), it is clear that the maximum oxygen content in the pre-oxidized niobium filaments may not exceed 0.35 wt.%. This is important, since Stoop and Shaniyan [13] found that below 0.35 wt.%, the ductility of niobium was not degraded and all other mechanical properties were slightly improved at both ambient and elevated temperature owing to the dynamic-strain-aging effects [14].

#### 3.4 Fracture toughness

The fracture toughness of the matrix and niobium filament-reinforced composites was measured via three-point bending tests on chevron-notched specimens. The tests indicated a significant increase in  $K_{IC}$  upon reinforcing with the niobium filaments coated with  $\text{Al}_2\text{O}_3$  *in situ*.



(a)



(b)

Fig. 13. Compositional profiles across the  $Al_2O_3$  layer formed *in situ*: (a) as processed; (b) annealed.

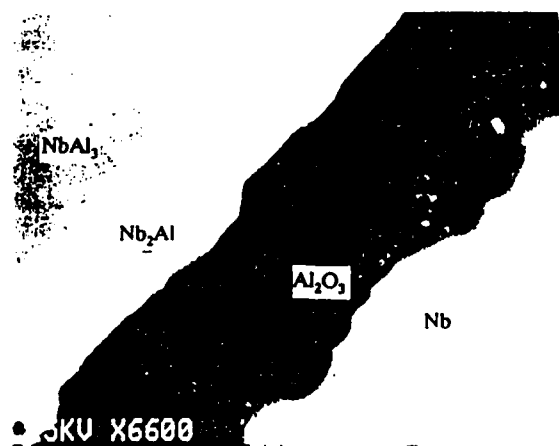


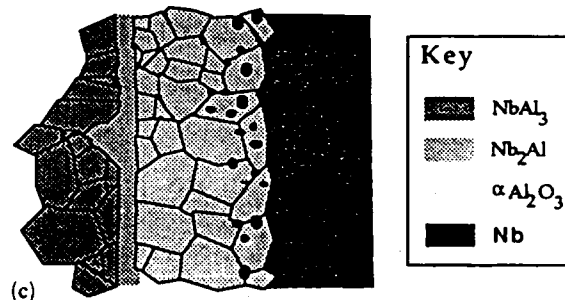
Fig. 14. Microstructure of the interface showing a multilayer structure.



(a)



(b)



(c)

Fig. 15. The  $Al_2O_3$  interfacial region formed *in situ*: (a) bright field TEM image, showing a dense fine-grained  $Al_2O_3$  layer; (b) high magnification TEM micrograph, showing an  $Al_2O_3$  layer containing a fine dispersion of niobium particles; (c) schematic illustration of the interface structure.

as illustrated by the load-displacement curves for the unreinforced matrix and a composite containing 20 vol.% Nb filaments (Fig. 16). The unreinforced matrix showed typical catastrophic brittle failure after the peak load, implying an insignificant damage tolerance. By contrast, the composite shows an initial linear elastic region, followed by a non-linear load increase with some fine perturbations caused most probably by microcrack generation in the matrix up to the maximum

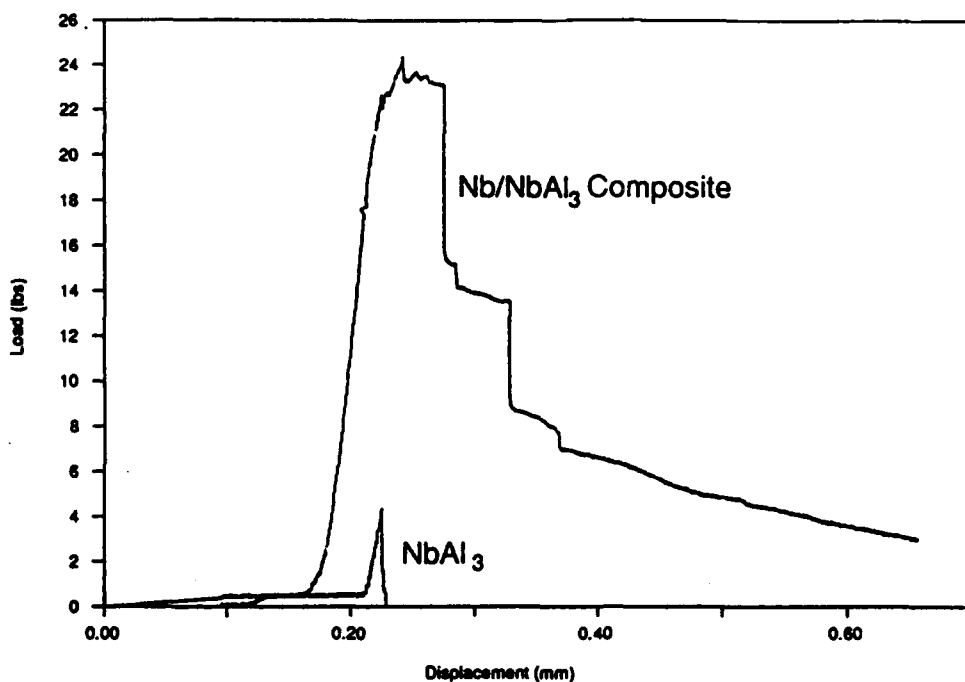


Fig. 16. Load-displacement curves of three-point bending tests with chevron-notched toughened composite specimens consisting of a monolithic matrix and 20 vol.% Nb ( $\text{Al}_2\text{O}_3$  coated).

load, followed by a continuous and stepwise load decrease. It should be noted that both the higher fracture toughness and the higher damage tolerance of the composite arise because of an effective load transfer to the reinforcing phase.

Observation of the fracture surface of the tested samples provides an insight into the characteristics of the load-displacement curves. Figure 17(a) shows the general appearance of the fracture surface at a low magnification of an  $\text{NbAl}_3$  composite reinforced with niobium filaments coated with  $\text{Al}_2\text{O}_3$  *in situ*. The figure clearly demonstrates a significant degree of bridging by the niobium reinforcements. Furthermore, the fracture surface topography suggests that crack deflection occurred when the cracks intersected the niobium filaments. The niobium filament reinforcements failed typically in a highly ductile manner as shown in Fig. 17(b). Several observations may be illustrated from this micrograph; the filament fracture is a "knife edge", indicating extremely ductile behavior, while there is clear evidence of partial circumferential decohesion at the interface. A closer look at the interfaces on the fracture surfaces indicated that the decohesion occurs first on that side of the filament first encountered by the crack front and

subsequently on the other side, contributing to the knife-edge nature of the niobium filament fracture.

From physical considerations, it is apparent that a certain amount of ductility of the reinforcement is needed for any significant improvement in the toughness of brittle matrix composites. It has also been recognized that ductility of the reinforcing phase alone is not sufficient for achieving a significant improvement in the fracture toughness; equally as important is the matrix-reinforcement interfacial strength. For example, if the interface is very strong, a high degree of geometrical constraint can lead to a triaxial state of stress, resulting in a brittle failure of the ductile reinforcement [15]. Consequently, there would not be a significant increase in the composite toughness under these circumstances. On the contrary, for a very low reinforcement-matrix interface strength, the reinforcement would readily debond and there would be no crack surface bridging action, again resulting in a limited improvement in the toughness.

On the contrary, a significant improvement in the fracture toughness would be expected if a partial interfacial debonding (decohesion) can remove the geometrical constraints and allow the

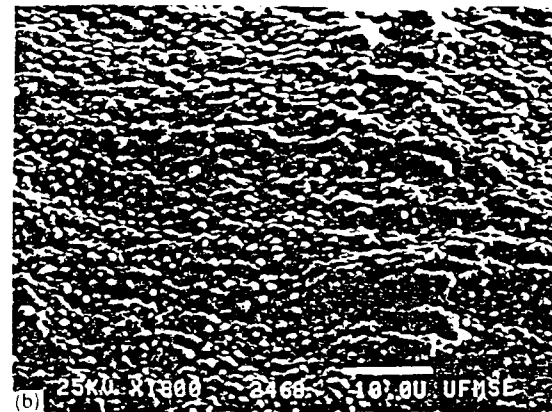
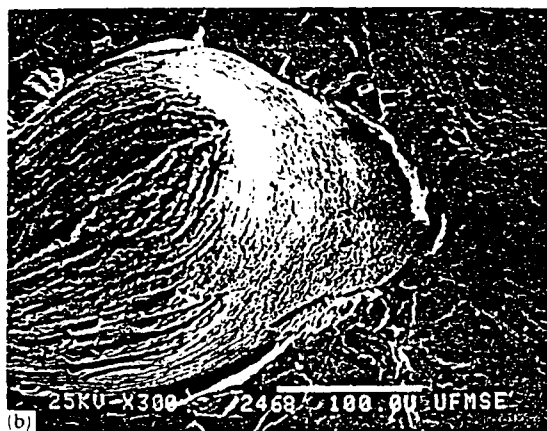
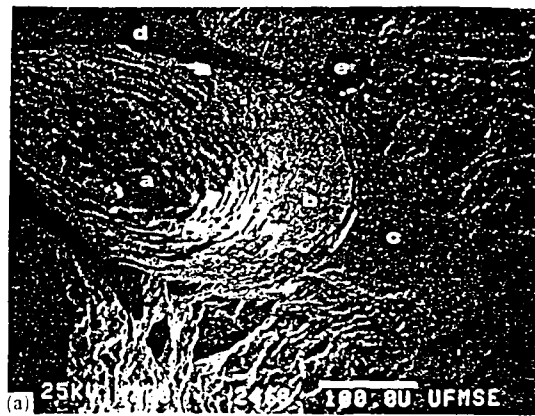


Fig. 17. Fractographs of Nb-NbAl<sub>3</sub> composite coated *in situ*: (a) general fracture surface; (b) fractured niobium filament showing knife-edge failure and partial interfacial bonding.

reinforcement to neck, while the remaining interface area in contact with the matrix (because of a combination of the interface bonding strength and mechanical interlock) allows an effective load transfer to the reinforcement.

The niobium filament-matrix interface in the present instance clearly shows evidence of partial decohesion along the fracture surface with associated filament necking and ductile fracture. This suggests that the interface of the composite fabricated by this processing technique possesses optimal interface properties. Since the interfacial regions exhibited a multiphase multilayered morphology, it was important to determine the exact location (within the layers) of interfacial decohesion. A closer look at the interface via SEM and energy dispersive spectroscopy (EDS) analysis of the fracture surface revealed that the interface between the Nb-Al<sub>2</sub>O<sub>3</sub> layer and the Al<sub>2</sub>O<sub>3</sub> formed *in situ* had the weakest bond. This

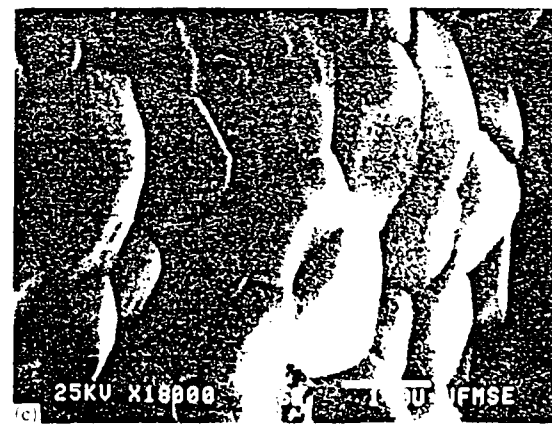
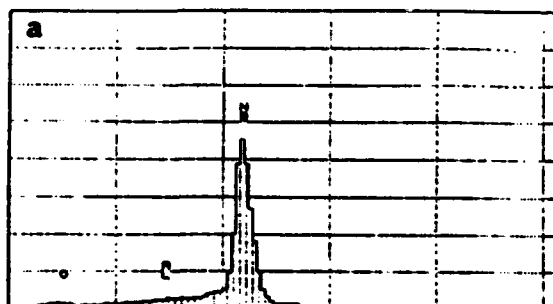


Fig. 18. Surface geometry of the debonded interface: (A) general view; (B) surface geometry of the niobium filament corresponding to the area labeled b in (A); (C) surface geometry of the Al<sub>2</sub>O<sub>3</sub> layer formed *in situ* corresponding to the area labeled c in (A) showing typical intergranular fracture surface.

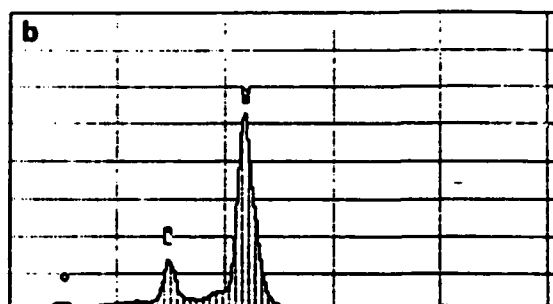
is illustrated in Fig. 18 with a set of micrographs. Fig. 18(A) is the general view of the debonded interface, Fig. 18(B) a magnified view of the area labeled b in Fig. 18(A), and Fig. 18(C) a magni-

Series II University of Florida / JEOL FRI 15-JUN-90 09:21  
Current @ 800keV = 0



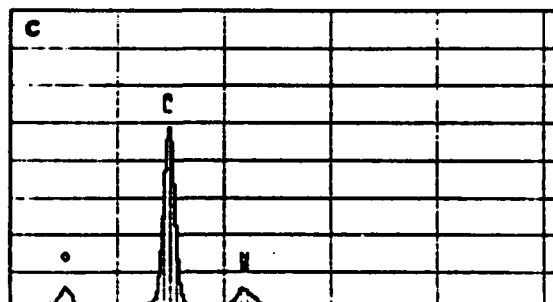
C 009  
70 1824chans 26NDT RT+ 0sec  
VPS = 0192 S 120  
@ 800keV

Series II University of Florida / JEOL FRI 15-JUN-90 09:30  
Current @ 800keV = 0



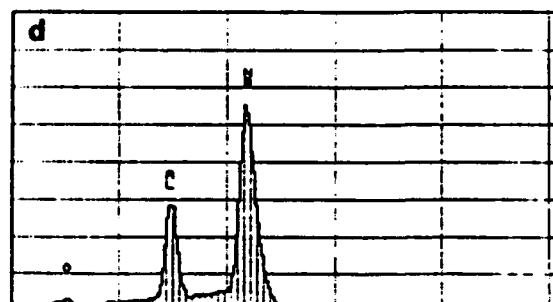
C 009  
70 2040chans 31NDT RT+ 0sec  
VPS = 4896 S 120  
@ 800keV

Series II University of Florida / JEOL FRI 15-JUN-90 09:30  
Current @ 800keV = 0



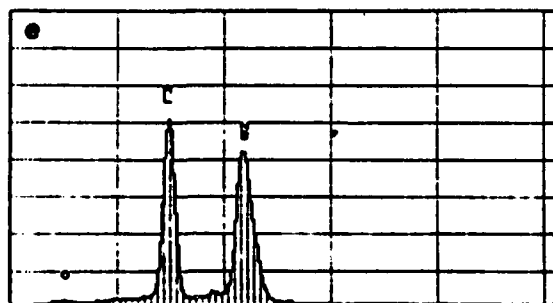
C 009  
70 2040chans 26NDT RT+ 0sec  
VPS = 4896 S 120  
@ 800keV

Series II University of Florida / JEOL FRI 15-JUN-90 09:02  
Current @ 800keV = 0



C 009  
70 2040chans 23NDT RT+ 0sec  
VPS = 4896 S 120  
@ 800keV

Series II University of Florida / JEOL FRI 15-JUN-90 09:13  
Current @ 800keV = 0



C 009  
70 2040chans 23NDT RT+ 0sec  
VPS = 4896 S 120  
@ 800keV

Fig. 19. EDS spectra of the areas shown in Fig. 18(A).

fied view of the area labeled c in Fig. 18(A). A series of EDS spectra is given in Fig. 19 (labeled a-e corresponding to a-e in Fig. 18(A)): a is the filament knife-edge, b is the niobium filament surface, c is the  $\text{Al}_2\text{O}_3$  coating layer formed *in situ*, d is partially debonded matrix surface and e is the  $\text{NbAl}_3$  matrix. The EDS analysis was carried out by directly focusing the electron beam on

these individual areas. It is clear that the spectra for a and b correspond to the niobium filament with a surface morphology shown in Fig. 18(B), while the spectrum for c corresponds to the  $\text{Al}_2\text{O}_3$  coating layer formed *in situ* with the morphology shown in Fig. 18(C); the spectra for d and e correspond to  $\text{Nb}_2\text{Al}$  and  $\text{NbAl}_3$  (matrix) respectively. These observations clearly indicate

that the partial interfacial decohesion is initiated at the  $\text{Al}_2\text{O}_3$ - $\text{Nb}_2\text{Al}$  interface. In addition, during necking of the niobium filaments, decohesion at the  $\text{Nb}$ - $\text{Al}_2\text{O}_3$  interface was observed. However, the  $\text{Nb}_2\text{Al}$ - $\text{NbAl}_3$  interface did not exhibit any decohesion, implying a strong interfacial bond, as supported independently by our previous work on  $\text{Nb}_2\text{Al}$ - $\text{NbAl}_3$  composites [7].

#### 4. Summary and conclusions

With the unique coupling of RHC process with pre-oxidation treatment of the niobium filament reinforcements,  $\text{Nb}$ - $\text{NbAl}_3$  composites were obtained with an  $\text{Al}_2\text{O}_3$  layer formed *in situ* at reinforcement-matrix interfaces during the synthesis and consolidation of the composites. Post-annealing microstructural analysis indicated that the  $\text{Al}_2\text{O}_3$  layer formed *in situ* acts as an effective diffusion barrier, while the uncoated niobium filaments degraded to a significant extent. The fracture roughness of the composites showed a significant improvement over that of the unreinforced matrix. Fracture surface analysis suggested that a partial debonding (decohesion) occurs at the  $\text{Al}_2\text{O}_3$ -matrix interface during crack propagation. Thus the *in situ* coating appears to provide both an excellent and stable diffusion barrier and optimum properties for the operation of various toughening and strengthening mechanisms.

#### Acknowledgments

The authors gratefully acknowledge the support of Defense Advanced Research Projects Agency to the University of Florida under Grant MDA972-88-J1-6. The authors also acknowledge Dr. David Baker and Dr. M. J. Kaufman for the TEM analysis.

#### References

- 1 R. L. Fleischer, *J. Mater. Sci.*, 22 (1988) 2281-2288.
- 2 J. H. Schneibel, P. F. Becher and J. A. Horton, *J. Mater. Res.*, 3 (6) (1988).
- 3 S. Ochiai and K. Osamura, in H. Ishida (ed.), *Interfaces in Polymer, Ceramic and Metal Matrix Composites*, Elsevier, Amsterdam, 1988, pp. 413-423.
- 4 A. Bose, B. Moore, R. M. German and N. S. Stoloff, *J. Met.*, 14-17(9) (1988).
- 5 *ASTM Stand.* 392-87, 1988.
- 6 S.-X. Wu, in J. H. Underwood, S. W. Freiman and F. I. Baratta (eds.), *Chevron-notched Specimens: Testing and Stress Analysis*, *ASTM Spec. Tech. Publ.* 855, 1984, pp. 176-192 (ASTM, Philadelphia, PA).
- 7 L. Lu, Y. S. Kim, A. B. Gokhale and R. Abbaschian, *Proc. Conf. on Intermetallic Matrix Composites, Materials Research Society Spring Meeting, San Francisco, CA, April 16-21, 1990*, Materials Research Society, Pittsburgh, PA, 1990, pp. 79-87.
- 8 *Powder Diffraction File*, Joint Committee on Powder Diffraction Standards, International Center for Diffraction Data, Swarthmore, PA, 1989, Card 34-370.
- 9 *Powder Diffraction File*, Joint Committee on Powder Diffraction Standards, International Center for Diffraction Data, Swarthmore, PA, 1989, Card 27-1313.
- 10 E. A. Gulbransen and K. F. Andrew, *J. Electrochem. Soc.*, 105 (1) (1959) 4-9.
- 11 L. Lu, A. B. Gokhale and R. Abbaschian, *Masters Thesis*, 1991.
- 12 L. Lu, A. B. Gokhale, M. J. Kaufman and R. Abbaschian, *Extended Abstracts, in Conf. on Powder Metallurgy: Key To Advanced Technology, Vancouver, British Columbia, July 30-August 1, 1990*, Metals Park, OH, 1990.
- 13 J. Stoop and P. Shaninian, *Proc. Conf.*, Metallurgical Society of AIME, Warrendale, PA, 1960, Part II, Conf. Symp. 34, pp. 407-432.
- 14 J. F. Ffrietto, G. M. Sinclair and C. A. Wert, *Proc. Conf. on Columbium*, Metallurgical Society of AIME, Warrendale, PA, 1960, pp. 503-521.
- 15 C. K. Elliott, G. R. Odette, G. E. Lucas and J. W. Sheehard, in F. D. Lemkey, S. G. Fishman, A. G. Evans and J. R. Strife (eds.), *High Temperature/High Performance Composites, Materials Research Society Symp. Proc.*, Vol. 120, Materials Research Society, Pittsburgh, PA, 1988, pp. 95-101.

**BOOK II**

**Section 2**

**Mechanical Alloying**

**of**

**MoSi<sub>2</sub>**

**Principal Investigator: M.J. Kaufman**

# MoSi<sub>2</sub> Matrix Composites

**Principal Investigator:**

**M.J. Kaufman**

## **Objectives**

A novel processing method utilizing the combination of mechanical alloying, carbothermal reductions, and carbon additions was developed in the preceding year to synthesize silica-free MoSi<sub>2</sub> and MoSi<sub>2</sub>/SiC composites [1-3]. The studies during the past year have been directed toward meeting the following objectives:

- (1) Optimization of the processing sequence for various compositions corresponding to increasing volume fractions of silicon carbide in MoSi<sub>2</sub> and determination of the maximum SiC loading possible.
- (2) Characterizing the phase evolution sequences for the various compositions as a function of alloying time and consolidation temperature; in particular for differences associated with increasing carbon content.
- (3) Extension of the processing rationale to potential alloy silicide systems such as (Mo,W)Si<sub>2</sub>.
- (4) Mechanical Property Characterization.

## **Research Summary**

- (1) Process Optimization:

Using the processing strategy outlined in [2], MoSi<sub>2</sub>/SiC composites with varying SiC contents have been processed. Thus far, silica-free composites with silicon carbide loadings of up to 60 v/o, and with a minimal amount of the Nowotny (third) phase have been successfully fabricated. Furthermore, near theoretical densification has been achieved in these composites, with the open porosity being limited to 1% or less. The SiC reinforcement size in all the above composites is typically of the order of 1 μm.

In view of the tendency of the silicide to dissociate at elevated temperatures and under low total pressures, considerable modifications were made to the processing method, as outlined in references [8] and [9].

(2) Characterization of the phase evolution sequences:

A combination of DTA/TGA and x-ray diffraction techniques have been utilized to study the phase evolution sequences during mechanical alloying and during consolidation. Significant differences have been noted in the microstructural evolution sequence with changes in the nominal powder composition. For instance, while intermetallic formation during mechanical alloying is predominant for the lower carbon content alloys, the high carbon alloys evolve by initially forming carbides (such as molybdenum and silicon carbide) during mechanical alloying. These in turn lead to significant differences in the phase evolution sequence during powder consolidation. These findings will be elaborated in [5].

(3) Extension of the processing rationale to other silicide systems:

The extension of the processing scheme to process alloy silicide/silicon carbide composites has also been attempted. Thus far, we have looked at forming *in-situ* composites for the (Mo,W)Si<sub>2</sub>/SiC system, with W substituting for Mo in the disilicide. Further improvements in the high temperature strength are anticipated in this system due to the synergistic effects of solid solution strengthening and dispersion strengthening. Thus far, silica-free (Mo,W)Si<sub>2</sub>/SiC composites with 20 v/o SiC, containing 25 and 50 mole percent of WSi<sub>2</sub> in the matrix have been synthesized successfully. The mechanical alloying approach makes it possible to vary alloying levels (in the matrix) and the SiC content (in the composite) independently. Details of the processing of these composites are found in [7]. The higher density of WSi<sub>2</sub> necessitates such property improvements to be considered on a density-compensated basis.

(4) Mechanical property Characterization:

Finally, efforts are underway to evaluate the elevated temperature properties of the silica-free MoSi<sub>2</sub>/SiC composites and compare them with composites processed by conventional blend and consolidate techniques. It is anticipated that the absence of the grain boundary silica and the presence of micron sized SiC will lead to improved elevated temperature strengthening due to increased resistance to grain boundary sliding and potential dispersion strengthening effects [6].

### Publications

- (1) S. Jayashankar and M.J. Kaufman, "*In-situ* Reinforced MoSi<sub>2</sub> Composites by Mechanical Alloying", *Scripta Metallurgica et Materialia*, 1992, vol. 26, pp. 1245-50.
- (2) S. Jayashankar and M.J. Kaufman, "Tailored MoSi<sub>2</sub>/SiC Composites by Mechanical Alloying", *Journal of Materials Research*, 1993, vol. 8, no. 6, pp. 1428-41.

- (3) A. Costa e Silva, S. Jayashankar, P. Krishnan and M.J. Kaufman, "Novel Processing of Intermetallic Composites by *in-situ* Displacement Reactions", in Processing and Fabrication of Advanced Materials for High Temperature Application - II, TMS, 1993.
- (4) S. Jayashankar and M.J. Kaufman, "Processing Related Effects Pertaining to  $\text{MoSi}_2/\text{SiC}$  Composites", to be submitted to Journal of the American Ceramic Society.
- (5) S. Riddle, S. Jayashankar and M.J. Kaufman, "Microstructural Evolution in Compositionally Tailored  $\text{MoSi}_2/\text{SiC}$  Composites", to be presented at the Silicides Symposium, MRS Fall Meeting, 1993.
- (6) S. Jayashankar, S. Riddle and M.J. Kaufman, "Effect of Siliceous Intergranular Phase on the Elevated Temperature Properties of  $\text{MoSi}_2/\text{SiC}$  Composites", to be presented at the Silicides Symposium, MRS Fall Meeting, 1993.
- (7) S. Jayashankar and M.J. Kaufman, "Fabrication and Properties of *in-situ* Alloy Silicide/ $\text{SiC}$  Composites", under preparation.

#### Patents

- (1) "Composite Silicide/Silicon Carbide Mechanical Alloy", Serial #08/069,730, Application pending.
- (2) "Refractory Metal Reinforced  $\text{MoSi}_2/\text{SiC}$  Composites with Matched Coefficients of Expansion", Serial #08/069,706, Application pending.

## *IN-SITU* REINFORCED MoSi<sub>2</sub> COMPOSITES BY MECHANICAL ALLOYING

S. Jayashankar and M.J. Kaufman  
Department of Materials Science and Engineering  
University of Florida, Gainesville, FL 32611

(Received December 31, 1991)  
(Revised February 18, 1992)

### Introduction

Intermetallics have been the focus of recent interest in the development of high temperature structural materials. MoSi<sub>2</sub> is one of the promising candidate materials for such applications due to its excellent oxidation resistance, low density, and high electrical and thermal conductivity. However, it is plagued by low room temperature fracture toughness and elevated temperature strength, in addition to intermediate temperature peaking behavior [1]. While powder processing appears to be the preferred route to the fabrication of MoSi<sub>2</sub> [2-8], it results in the incorporation of substantial amounts of an amorphous silica phase [1] upon consolidation. The presence of these amorphous silica particles is thought to be detrimental to the mechanical properties, as they can serve as potential crack nucleation sites that ultimately degrade the room temperature strength and toughness. The elevated temperature properties are also degraded by the silica due to its softening characteristics at temperatures above 1473K. It has also been shown [9] that the presence of both silica and free silicon degrades the protective diffusion barrier coatings on ductile fiber reinforced MoSi<sub>2</sub> composites.

A survey of the available literature indicates that little effort has gone into understanding and controlling the silica phase. Maxwell [6] studied the effect of varying amounts of carbon additions to the starting MoSi<sub>2</sub> powder and reported improved flexural creep properties and decreased high temperature plasticity as a result of these additions. More recently, Maloy et al. [10] have also reported on the beneficial effects of carbon additions on the elevated temperature fracture toughness of MoSi<sub>2</sub>. The beneficial effects of the carbon additions were attributed to the deoxidation of the silicon and molybdenum oxides while hot-pressing.

The present study aims at improving the MoSi<sub>2</sub> matrix by the selective elimination of the silica phase via its conversion into silicon carbide, which has excellent high temperature stability. This study takes advantage of the carbothermal reduction reaction for converting silica to silicon carbide [6,11-13] in order to control the microstructure of MoSi<sub>2</sub>.

### Experimental

Elemental powders of commercial purity molybdenum (purity 99.9%, 2-4 μm) and silicon (purity 98%, <44 μm) were obtained from Cerac and blended in stoichiometric proportions corresponding to MoSi<sub>2</sub>. About 4 wt. % of carbon was also added to the mixture. The mixture was subjected to mechanical attrition in a high energy Szegvari attrition mill for 60 h using 3 mm diameter hardened steel balls with a ball to powder weight ratio of approximately 5:1. To minimize contamination from oxygen, a continuous flow of gettered high purity argon was maintained in the attritor. A second batch of mechanically attrited MoSi<sub>2</sub> (MA MoSi<sub>2</sub>) with no carbon additions was prepared for purposes of comparison. Consolidation of the mechanically attrited powder was carried out by vacuum hot pressing in inductively heated graphite dies at a pressure of 35 MPa for 1 h. The consolidation temperatures were 1873K and 1723K respectively for the MA MoSi<sub>2</sub> powders with and without carbon additions. The progress of the mechanical attrition and consolidation processes was followed by x-ray diffractometry (XRD). A Philips ADP 3720 diffractometer operated at 40 kV and 20 mA with Cu Kα radiation and digital data acquisition over 2θ angles of 5°-100° was used in this study.

Z phase) and either Mo<sub>5</sub>Si<sub>3</sub> or CMo<sub>5</sub>Si<sub>3</sub> (high Z phase). It is also apparent that the Mo<sub>5</sub>Si<sub>3</sub> and/or CMo<sub>5</sub>Si<sub>3</sub> regions tend to adjoin the dark regions thereby suggesting that the origin of these phases is probably due to local deviations from stoichiometry resulting from either SiO<sub>2</sub> or SiC formation.

TEM analysis of the C-modified material revealed a homogeneous microstructure with uniformly distributed second phases such as those marked A and B in Fig 4. The average grain size of the MoSi<sub>2</sub> was between 3 and 5 μm, much larger than that of the material without carbon additions, presumably because of the higher consolidation temperatures. EDS microanalysis (with Be window) of region A showed the presence of silicon alone, indicating that these regions correspond to the dark (low Z) regions such as those shown in Fig. 3. Selected area diffraction patterns (SADPs) were obtained along the major zone axes from these and other silicon rich regions (Fig. 4) and were consistently indexed to a cubic β-SiC structure with a lattice parameter ( $a = 0.4359$  nm) essentially identical to that determined by x-ray diffraction (described below). The SiC was present in the form of 1 μm-sized particles located predominantly along grain boundaries and at triple point regions. Furthermore, the SiC particles were easily distinguishable based on the internal twinning observed. Based on the juxtaposition of the SiC particles, it appears that the silica that had spheroidized at the grain boundary and triple point regions had subsequently transformed to SiC. In addition to β-SiC, both Mo<sub>5</sub>Si<sub>3</sub> and CMo<sub>5</sub>Si<sub>3</sub> were observed (region B), consistent with the findings by Cotton et al. [2], who pointed out the possible role of carbon in the evolution of second phases. Since silica formation displaces the matrix composition away from MoSi<sub>2</sub> towards Mo<sub>5</sub>Si<sub>3</sub>, it results in the formation of these higher molybdenum phases. The grain boundaries also appeared to be free of any silica (Fig. 5) although a small amount was occasionally observed within the grains.

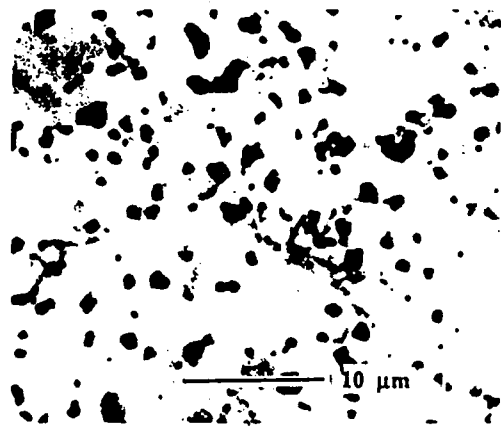


Figure 3. Backscattered electron image of the hot-pressed carbon-modified MA MoSi<sub>2</sub>.

XRD of the carbon-modified material (Fig. 6) also confirmed the results of the TEM analysis. The results of the peak positions, intensities, indices, and  $d$  spacings of the various reflections are summarized in Table 1. All the reflections could be ascribed to tetragonal MoSi<sub>2</sub> and cubic β-silicon carbide. No reflections corresponding to Mo<sub>5</sub>Si<sub>3</sub> or CMo<sub>5</sub>Si<sub>3</sub> were seen, which is not surprising since they were present in insufficient volume fractions.

A brief look at the Mo-Si-C-O system reveals the presence of a number of phases, MoSi<sub>2</sub>, Mo<sub>5</sub>Si<sub>3</sub>, CMo<sub>5</sub>Si<sub>3</sub>, MoO<sub>3</sub>, Mo<sub>2</sub>C, SiO, SiO<sub>2</sub>, SiC, CO, CO<sub>2</sub>, etc. Based on the free energy data of these compounds,

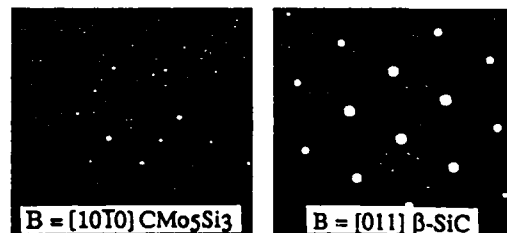


Figure 4. BFTEM of the C-modified MA MoSi<sub>2</sub> and SADPs of β-SiC and CMo<sub>5</sub>Si<sub>3</sub>.

The transformation characteristics of the powders were also monitored by differential thermal analysis (DTA) and thermogravimetric analysis (TGA). DTA/TGA was performed on a Netzsch STA-409 system with heating rates of 10 K per minute under flowing argon (1cm<sup>3</sup>/sec).

Optical, scanning and transmission electron microscopy were performed on the consolidated samples. Thin foil TEM specimens were prepared from bulk samples following standard procedures of dimpling and ion-milling using Ar<sup>+</sup> ions at 4.5 kV. Final thinning was done at 2.5 kV at an angle of 13° for 30 minutes. Microstructural characterization was carried out in a JEOL 200CX analytical transmission electron microscope operated at 200 keV. Elemental identification of the phases was achieved with the aid of an energy dispersive spectrometer attachment and appropriate data analysis facilities.

### Results and Discussion

The results of the XRD analysis of the mechanically attrited powders indicated that these submicron-sized powders consisted of molybdenum and tetragonal MoSi<sub>2</sub>, with apparent traces of the hexagonal MoSi<sub>2</sub> phase.

The microstructures of the hot pressed MoSi<sub>2</sub> specimens without carbon additions are shown in Fig. 1. A uniform distribution of second phase particles with volume fractions in the range 0.15-0.20 were present in the MoSi<sub>2</sub> matrix. TEM/EDS analysis of these samples (Fig. 2) revealed the presence of submicron-sized grains of MoSi<sub>2</sub> and second phase particles which were amorphous and silicon-rich, indicating the presence of the glassy silica phase. In addition, there were considerable amounts of very fine (10 nm) dispersoids typically within the MoSi<sub>2</sub> grains and occasional grains of the Mo<sub>5</sub>Si<sub>3</sub> phase.

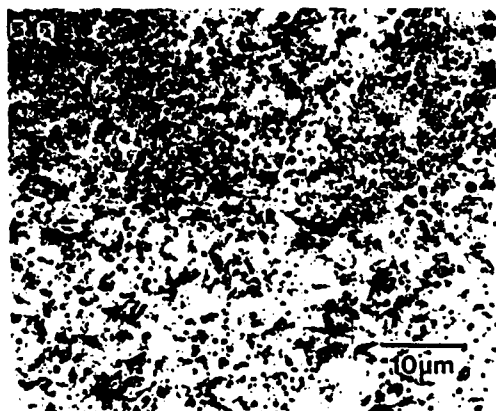


Figure 1. Scanning electron micrograph (SEM) showing the microstructure of hot-pressed MA MoSi<sub>2</sub>.

Fig. 3 shows a backscattered electron image of the specimen derived from the carbon-modified MA MoSi<sub>2</sub> powder. A dramatic improvement in the overall homogeneity and cleanliness of the microstructure is apparent when compared with the MA MoSi<sub>2</sub> compacts without carbon. Using EDS, the dark areas in the Fig. 3 were confirmed to be silicon rich, while the grey and bright areas were observed to contain molybdenum and silicon in approximate ratios 1:2 and 5:3 respectively, thus indicating the presence of either SiO<sub>2</sub> or SiC (low Z phase), MoSi<sub>2</sub> (intermediate



Figure 2. Bright field transmission electron micrograph (BFTEM) and SADP of silica particles in hot-pressed MA MoSi<sub>2</sub>.

TABLE I  
Summary of X-ray Diffraction Results

| Peak No. | 2θ     | Intensity (cps) | I/I <sub>max</sub> | d (nm) | hkl*               |
|----------|--------|-----------------|--------------------|--------|--------------------|
| 1        | 22.872 | 1340            | 27.26              | 3.8850 | 002 (M)            |
| 2        | 30.325 | 1391            | 28.31              | 2.9451 | 101 (M)            |
| 3        | 35.922 | 408             | 8.30               | 2.4979 | 111 (S)            |
| 4        | 39.951 | 1832            | 37.28              | 2.2549 | 110 (M)            |
| 5        | 41.675 | 46              | 0.94               | 2.1655 | 200 (S)            |
| 6        | 44.893 | 4914            | 100.00             | 2.0175 | 103 (M)            |
| 7        | 46.445 | 942             | 19.18              | 1.9536 | 112 (M)            |
| 8        | 57.648 | 625             | 12.72              | 1.5977 | 200 (M)            |
| 9        | 60.268 | 193             | 3.93               | 1.5344 | 220 (S)            |
| 10       | 62.755 | 381             | 11.82              | 1.4794 | 202 (M)            |
| 11       | 66.391 | 762             | 15.50              | 1.4070 | 105 (M)            |
| 12       | 68.485 | 14              | 0.28               | 1.3689 | ?                  |
| 13       | 72.288 | 467             | 9.49               | 1.3060 | 006 (M)<br>311 (S) |
| 14       | 75.693 | 1482            | 30.16              | 1.2555 | 213 (M)            |
| 15       | 75.911 | 900             | 18.31              | 1.2533 | 222 (S)            |
| 16       | 76.833 | 172             | 3.49               | 1.2397 | 204 (M)            |
| 17       | 85.743 | 1082            | 22.03              | 1.1322 | 220 (M)            |
| 18       | 86.051 | 666             | 13.55              | 1.1317 | doublet            |
| 19       | 90.108 | 108             | 2.20               | 1.0883 | 222 (M)            |
| 20       | 93.431 | 462             | 9.41               | 1.0582 | 400 (S)            |
| 21       | 93.808 | 246             | 5.02               | 1.0575 | 301 (M)            |
| 22       | 98.961 | 841             | 17.11              | 1.0133 | 310 (M)            |
| 23       | 99.353 | 449             | 9.15               | 1.0128 | 331 (S)            |

\* M = MoSi<sub>2</sub> S = SiC

The overall reaction is thus



It is also thermodynamically possible for the carbon monoxide to react with the silicon dioxide to form silicon monoxide.



Analysis of the energetics of reaction (1) suggests that it is feasible above 1700K under atmospheric pressures. The effect of the lower partial pressures (due to the vacuum in the hot press) and the reducing environment of the carbon dies would be to lower this reaction onset temperature, as has been shown by Ishizaki [14]. Calculations of the magnitude of the lowering in the onset temperature are currently being performed.

Thermogravimetric analysis under flowing argon (at heating rates of 10K/min) of the MA MoSi<sub>2</sub> powders with and without carbon additions (Fig. 7) indicated that there were significantly greater weight losses in the case of the C-modified material at temperatures above 1423K. In separate experiments conducted under flowing argon at similar heating rates, the overall weight loss of a carbon-modified sample heated to 1773K was about

12.5 percent. Based on the reaction mechanisms discussed previously, the weight losses in the C-modified material can be ascribed to the formation of gaseous products such as CO and CO<sub>2</sub> during the reaction, as well as a partial loss of gaseous SiO and MoO<sub>3</sub>. The above mentioned weight-loss data must be interpreted with caution bearing in mind that the actual sample consolidation was carried out under vacuum whereas the TGA experiments were done in flowing argon.

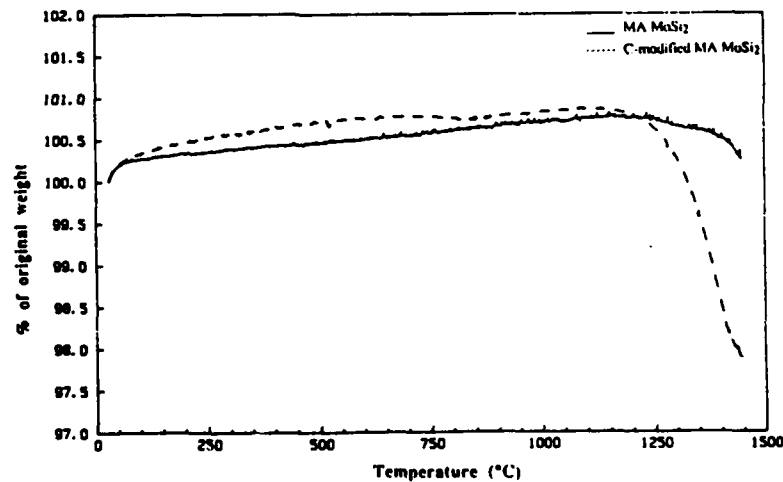
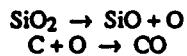


Fig. 7. TGA data showing weight losses as a function of temperature for MA MoSi<sub>2</sub> and C-modified MoSi<sub>2</sub>.

it is clear that the most stable phases at 1700K (where most of the reactions occur) are MoSi<sub>2</sub>, CMo<sub>5</sub>Si<sub>3</sub>, Mo<sub>5</sub>Si<sub>3</sub>, and SiC. The possibility of Mo<sub>2</sub>C is discounted based on its higher free energy (lower stability) compared to the other phases. This is confirmed by the absence of the Mo<sub>2</sub>C phase in the samples analysed. Comparison of the observed microstructures with thermodynamically calculated predominance regimes will be dealt with in a separate publication.

The carbothermal reduction of silica is best depicted as occurring in the following sequence:



followed by the reaction of silicon monoxide to form silicon carbide, i.e.,

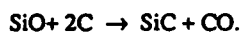


Figure 5. BFTEM of the C-modified MA MoSi<sub>2</sub> showing the absence of grain boundary SiO<sub>2</sub>.

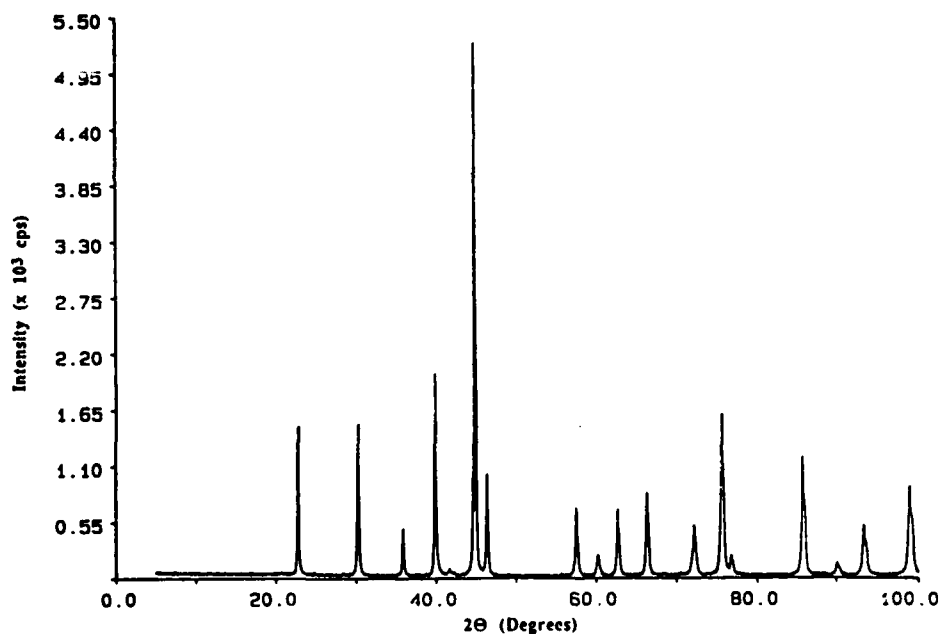


Figure 6. Variation of intensity as a function of 2θ for the hot-pressed, carbon-modified MA MoSi<sub>2</sub>

Consolidation experiments were also performed on carbon-modified commercial powder (-325 mesh) under identical processing conditions as the C-modified MA MoSi<sub>2</sub>. The resultant microstructures lacked homogeneity in the silicon carbide distribution when compared to those derived from MA MoSi<sub>2</sub> powder, suggesting that the increased specific surface area of carbon and its uniform distribution that are brought about by the mechanical attrition process leads to an enhanced rate of the carbothermal reduction reaction and a more efficient conversion to SiC. Presently, it is unclear as to whether the silicon carbide formation mechanism involves a vapor-liquid-solid reaction or vapor phase species reacting initially at small nuclei, and further studies are underway to elucidate this information.

The above results might also be used to explain the defect-free microstructures observed in SiC reinforced MoSi<sub>2</sub> where the addition of SiC was observed to lead to a reduction of the SiO<sub>2</sub> phase. It is suspected that the commercial SiC used in those studies contained substantial amounts of free carbon which is responsible for the microstructural enhancement of the resulting SiC/MoSi<sub>2</sub> composites, due to the ensuing carbothermal reduction reactions.

#### Summary

MoSi<sub>2</sub> containing a uniform distribution of *in-situ* formed silicon carbide has been successfully synthesized from mechanically attrited powders. The glassy silica phase that is characteristic of all powder processed MoSi<sub>2</sub> has been effectively eliminated and converted into the high temperature stable silicon carbide phase. Plausible reaction mechanisms have been discussed, and an explanation for the gettering effect seen in SiC reinforced MoSi<sub>2</sub> has been proposed.

#### Acknowledgement

This work was supported through a Grant (#MDA972-88-J-1006) under the Defense Advanced Research Projects Agency composites program. The contract monitors were Drs. S. Fishman and W. Barker and their support is greatly appreciated. Finally, the technical assistance of Mr. Randy Smith in preparing the TEM samples is gratefully acknowledged.

#### References

1. J.B. Berkowitz-Matuck, P.E. Blackburn, and E.J. Felten, *Trans. TMS-AIME*, vol. 233, pp. 1093-99, 1965.
2. J.D. Cotton, Y.S. Kim and M.J. Kaufman, *Mater. Sci. Eng.*, A144, pp. 287-291, 1991.
3. F.D. Gac and J.J. Petrovic, *J. Am. Ceram. Soc.*, vol. 68, no. 8, pp. C200-201, 1985.
4. Y.S. Kim, M.R. Johnson, R. Abbaschian and M.J. Kaufman, *Mat. Res. Soc. Symp. Proc.*, vol. 213, pp. 839-845, 1991.
5. J-M. Yang and S.M. Jeng, *J. Mater. Res.*, vol. 6, no. 3, pp. 505-513, 1991.
6. W.A. Maxwell, NACA RM E52B06, 1952.
7. W.A. Maxwell, NACA RM E9G01, 1949.
8. R.A. Long, NACA RM E50F22, 1950.
9. L. Xiao and R. Abbaschian, private communication, 1991.
10. S. Maloy, A.H. Heuer, J.J. Lewandowski, and J.J. Petrovic, *J. Am. Cer. Soc.*, vol. 74, no. 10, pp. 2704-706, 1991.
11. R. Hamminger, *J. Am. Cer. Soc.*, vol. 72, no. 9, pp. 1741-44, 1989.
12. G. Chia-Tsing Wei, *J. Am. Cer. Soc.*, vol. 66, no. 7, pp. C111-113.
13. W. van Rijswijk and D.J. Shanefield, *J. Am. Cer. Soc.*, vol. 73, no. 1, pp. 148-149.
14. K. Ishizaki, *Acta Metall. et Mater.*, vol. 38, no. 11, pp. 2059-2066, 1990.

# Tailored MoSi<sub>2</sub>/SiC composites by mechanical alloying

S. Jayashankar and M. J. Kaufman

Department of Materials Science and Engineering, The University of Florida,  
Gainesville, Florida 32611-2066

(Received 25 August 1992; accepted 3 February 1993)

MoSi<sub>2</sub>-based composites have been synthesized through the mechanical alloying (MA) of elemental molybdenum and silicon powders with and without carbon additions. The interplay between the phase formation sequence in the powders and the microstructural evolution in the consolidated samples is described. It is shown that the glassy SiO<sub>2</sub> phase characteristic of conventional powder processed MoSi<sub>2</sub> can be effectively eliminated by combining mechanical alloying, carbon additions, and an *in situ* carbothermal reduction reaction. Using this approach, composites consisting of uniformly distributed micron-size SiC in an MoSi<sub>2</sub> matrix can be formed. The effect of important processing variables such as the extent of carbon additions, extraneous iron pickup during MA, partial pressures of oxygen, consolidation temperatures, and consolidation atmospheres is discussed based on the evidence obtained from DTA, TGA, TEM, and XRD.

## I. INTRODUCTION

The intermetallic MoSi<sub>2</sub> has long been considered a potential material for high-temperature structural applications due to its high melting point, excellent oxidation and corrosion resistance, low density, and good electrical and thermal conductivity. Similar to many other high-temperature intermetallics, the use of MoSi<sub>2</sub> is limited as a structural material due to its low ambient temperature fracture toughness and poor elevated temperature strength.

A number of approaches for the processing of this intermetallic are unsuitable due to its high melting point and owing to the fact that it exists as a line compound. Furthermore, the relatively high dissociation pressures of MoSi<sub>2</sub> at elevated temperatures result in uncontrolled second phase formation due to silicon volatilization.<sup>1,2</sup> In view of these characteristics, powder processing appears to be the preferred fabrication route due to the lower processing temperatures that it affords; unfortunately, it also results in the incorporation of silica (originally formed as a surface layer on the powder particles<sup>3</sup>) into the consolidated samples. The presence of grain boundary silica either as a continuous film or as discrete particles is expected to be detrimental, since the particles may serve as crack nucleation sites at lower temperatures, while enhancing deformation via grain boundary sliding at temperatures above 1200 °C where the silica softens appreciably. In fact, recent studies have shown that low silica polycrystalline MoSi<sub>2</sub> demonstrates negligible "plasticity" below 1400 °C.<sup>4</sup> Silica formation also alters the matrix stoichiometry and results in the formation of Mo<sub>5</sub>Si<sub>3</sub>. Such stoichiometric deviations degrade the intermediate temperature oxidation resistance<sup>5</sup> of the

silicide. Finally, silica has also been reported to cause the degradation of the diffusion barrier coatings at the fiber-matrix interface in ductile fiber-reinforced MoSi<sub>2</sub>.<sup>6</sup>

In attempting to control the oxygen content of MoSi<sub>2</sub> by varying the starting powder size and by intentional carbon additions (deoxidant), Maxwell<sup>7</sup> found that a fine-grained material with carbon additions had better creep properties and lower high-temperature plasticity than a similar grain-size material without carbon. More recently, Maloy *et al.*<sup>8</sup> also reported improved elevated temperature fracture toughness with varying levels of carbon additions. However, substantial (~40%) weight losses were reported on consolidating these samples, resulting in uncontrolled formation of Mo-rich second phases. Hardwick and co-workers<sup>9</sup> attempted to process oxygen-free MoSi<sub>2</sub> by conducting all the powder handling and consolidation steps under vacuum or inert gas atmospheres. However, these approaches<sup>9,10</sup> are impractical from the standpoint of processing bulk structural parts, due to the difficulties involved in the scale-up of the evacuation systems, as well as the excessive costs that would be associated with such processes.

It is therefore clear that further enhancements in the properties of MoSi<sub>2</sub> and MoSi<sub>2</sub>-based composites are possible only with the elimination of silica (and oxygen) in the matrix along with close control of the overall stoichiometry, through the use of simple and economical processing schemes that do not necessitate elaborate care during powder handling. Thus, the major focus of the present study was to achieve the above-mentioned objectives through a combination of mechanical alloying and carbothermal reductions for the silica-free synthesis

of MoSi<sub>2</sub>. While mechanical alloying (MA) would result in the formation of a microstructurally uniform and compositionally homogeneous alloy of the desired stoichiometry, the carbothermal reduction process<sup>11,12</sup> would utilize the reducing effect of carbon to convert silica to silicon carbide. Furthermore, mechanical alloying would enable the homogeneous dispersion of carbon in the matrix to facilitate these reactions.

## II. BACKGROUND

### A. Phase equilibria

Optimizing the processing conditions and understanding the microstructural evolution requires a knowledge of the phase equilibria and crystal chemistry of the binary Mo–Si and the ternary Mo–Si–C systems; these are summarized in Table I. It should be pointed out that many of the earlier thermodynamic and structural determinations of these systems were in error due to oxygen and carbon contamination of the samples, as well as due to the high melting points of the compounds.

Ternary isotherms of the Mo–Si–C system, as shown in Fig. 1(a), were constructed by Nowotny and co-workers<sup>16</sup> at 1600 °C and by Brewer and Krikorian<sup>20</sup>

at around 1727 °C. Subsequently, van Loo and co-workers<sup>21</sup> constructed a 1200 °C isotherm [see Fig. 1(b)] after examining arc-melted alloys and diffusion couples. The only ternary phase in the Mo–Si–C system is the “Nowotny phase” which has the approximate formula, C<sub><1</sub>Mo<sub><5</sub>Si<sub>3</sub>, and a relatively wide homogeneity range.<sup>16,17,20,21</sup> Minor additions of carbon to Mo<sub>5</sub>Si<sub>3</sub> destabilize its tetragonal structure and result in the formation of a carbon stabilized hexagonal Nowotny phase. These Nowotny phases have the general formula, T<sub>3</sub>T<sub><2</sub>M<sub>3</sub>X<sub><1</sub>, where T denotes a transition metal, M represents Ge or Si, and X denotes a nonmetal such as C, O, B, or N.<sup>17</sup> The presence of carbon-centered tetrahedra is characteristic of the Nowotny phases and accounts for their stability. While the isotherms of Nowotny *et al.* and Brewer and Krikorian are in good agreement with each other in their prediction of the existence of a three-phase field between MoSi<sub>2</sub>, C<sub><1</sub>Mo<sub><5</sub>Si<sub>3</sub>, and SiC, the results of Van Loo indicate the coexistence of Mo<sub>5</sub>Si<sub>3</sub>, SiC, and C<sub><1</sub>Mo<sub><5</sub>Si<sub>3</sub> at 1200 °C. Recently, it has been postulated by Costa e Silva and Kaufman<sup>22</sup> that the van Loo and Brewer diagrams are consistent with each other only if a class II, four-phase reaction (MoSi<sub>2</sub> + Nowotny → SiC + Mo<sub>5</sub>Si<sub>3</sub>) exists between the temperatures at which these isotherms were constructed, i.e., 1200 °C and 1727 °C.

TABLE I. Summary of the binary and ternary phases of the Mo–Si–C system.

| System  | Formula  | Temp. (°C)                           | Crystal system | Structure                           | Lattice parameters (nm)                                     | Ref. | Comments  |
|---------|--|--------------------------------------|----------------|-------------------------------------|---|------|---|
| Mo–Si   | Mo <sub>3</sub> Si                                     | 2025                                 | Cubic          | <i>Pm</i> $\bar{3}$ <i>n</i>        | <i>a</i> = 0.4890   | 14   | Forms by the peritectic reaction, L + $\alpha$ $\rightleftharpoons$ Mo <sub>3</sub> Si  |
|         | Mo <sub>5</sub> Si <sub>3</sub>                        | 2100                                 | Tetragonal     | <i>I4/mcm</i>                       | <i>a</i> = 0.9648<br><i>c</i> = 0.4910                      | 14   | Incorrectly identified as Mo <sub>5</sub> Si <sub>2</sub> until Aronson. <sup>18</sup> Solubility range ~ 3 at. %.  |
|         | $\alpha$ -MoSi <sub>2</sub>                            | 1900                                 | Tetragonal     | <i>I4/mmm</i>                       | <i>a</i> = 0.3202<br><i>c</i> = 0.7843                      | 14   | $\alpha$ - $\beta$ transformation is polymorphic. However, Ref. 13 considers $\beta$ decomposition to $\alpha$ and Mo <sub>5</sub> Si <sub>3</sub> through a eutectoid reaction. $\beta$ may be stabilized by impurities, e.g., Ti. |
|         | $\beta$ -MoSi <sub>2</sub>                             | 2020                                 | Hexagonal      | <i>P6</i> <sub>2</sub> <i>22</i>    | <i>a</i> = 0.4642<br><i>c</i> = 0.6529                      | 14   |   |
| Si–C    | $\alpha$ -SiC  | ~2800                                | Hexagonal      | <i>P6</i> <sub>3</sub> <i>mc</i>    | <i>a</i> = 0.3081<br><i>c</i> = 1.511                       | 15   | Numerous other polytypes exist.   |
| Mo–C    | $\beta$ -SiC   | ~2800                                | Cubic          | <i>F4</i> $\bar{3}$ <i>m</i>        | <i>a</i> = 0.4358   | 15   |   |
|         | $\beta$ -Mo <sub>2</sub> C                             | 2650                                 | Hexagonal      | <i>P6</i> <sub>3</sub> / <i>mmc</i> | <i>a</i> = 0.2932<br><i>c</i> = 1.097                       | 16   | Forms by the peritectic reaction, L + MoC $\rightleftharpoons$ Mo <sub>2</sub> C  |
|         | MoC  | 2520                                 | Hexagonal      | <i>P6</i> <sub>3</sub> / <i>mmc</i> | <i>a</i> = 0.3006<br><i>c</i> = 0.4753                      | 15   | Other metastable forms which are slightly carbon rich such as $\alpha$ - and $\eta$ -carbides exist at high temperatures and transform at lower temperature by eutectoid reaction to $\beta$ -Mo <sub>2</sub> C + C.                |
| Mo–Si–C | C <sub>&lt;1</sub> Mo <sub>&lt;5</sub> Si <sub>3</sub> | 2000–2060<br>(composition dependent) | Hexagonal      | <i>P6</i> <sub>3</sub> / <i>mcm</i> | <i>a</i> = 0.7286<br><i>b</i> = 0.7287<br><i>c</i> = 0.5002 | 17   | <i>c/a</i> changes slightly with carbon content. First structure determination made by Schachner <i>et al.</i> <sup>19</sup> but incorrectly identified as Mo <sub>5</sub> Si <sub>3</sub> .  |

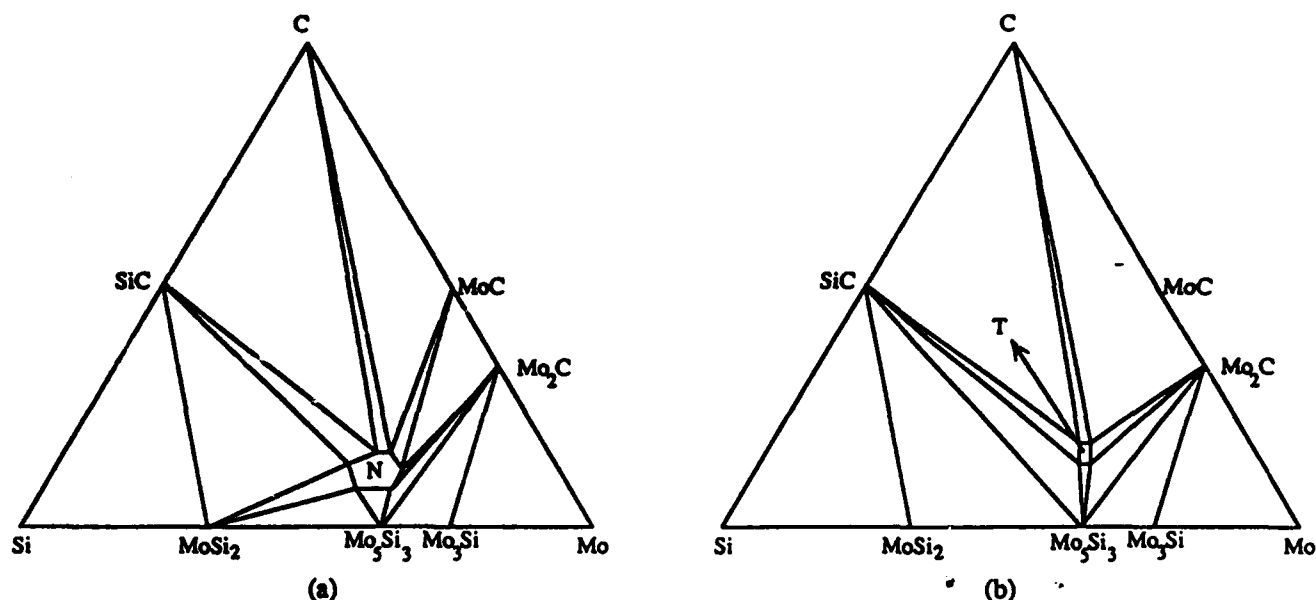


FIG. 1. Schematic of the ternary isotherms of the Mo-Si-C system as proposed by (a) Nowotny *et al.*<sup>16</sup> at 1600 °C and (b) van Loo *et al.* at 1200 °C.<sup>21</sup> N in (a) and T in (b) denote the C<sub>1</sub>Mo<sub>3</sub>Si<sub>3</sub> phase.

## B. Processing rationale

Based on the 1600 °C isotherm of Nowotny and the 1727 °C isotherm of Brewer, it is clear that ternary powder alloys within the composition limits established by the MoSi<sub>2</sub> + C<sub>1</sub>Mo<sub>3</sub>Si<sub>3</sub> + SiC three-phase field should form a *thermally stable*, three-phase microstructure when consolidated at these temperatures, provided that the powders are sufficiently homogeneous to minimize the diffusion length scales so as to establish equilibrium within the short time frames of the consolidation process. Here, it is assumed that the nature of the isotherms is unaltered by the presence of small amounts of oxygen present as surface SiO<sub>2</sub> on the powders. While part of the carbon would take part in the deoxidation/carbothermal reduction reactions, the unreacted residual carbon would exist in equilibrium, as dictated by the isotherm.

For the formation of MoSi<sub>2</sub>/SiC composites with a minimal amount of the Nowotny phase, it is necessary to start with nominal compositions slightly to the Mo-rich side of the MoSi<sub>2</sub>-SiC tie line; this ensures that the compositional variations (carbon and silicon losses) due to the carbothermal reduction reactions do not shift the overall composition to the adjacent Si + MoSi<sub>2</sub> + SiC field, where the Si phase would experience incipient melting above ~1400 °C and thus result in the degradation of the high temperature mechanical properties. Bearing this in mind, it is possible to vary the amount of the reinforcing SiC phase in the MoSi<sub>2</sub> matrix by simply choosing compositions at various points along the tie line. Note that the formation of the thermodynamically expected microstructures may also be limited by various

kinetic constraints. Similarly, processing related effects such as porosity should also be appropriately controlled in view of the gaseous by-products formed as a result of the carbothermal reduction reaction.

It is worth noting that the deoxidation of commercial MoSi<sub>2</sub> by carbon additions without a commensurate increase in the silicon content<sup>7,8</sup> would result in compositional shifts along an imaginary line between MoSi<sub>2</sub> and C and a corresponding increase in the amount of the Nowotny phase, according to the diagrams by Nowotny and Brewer [Fig. 1(a)].

In the present study, two powder compositions were chosen for mechanical alloying (MA). One corresponded to stoichiometric binary MoSi<sub>2</sub> as a baseline for comparison, and the other was a ternary alloy in the MoSi<sub>2</sub> + C<sub>1</sub>Mo<sub>3</sub>Si<sub>3</sub> + SiC three-phase field, according to the Nowotny diagram [Fig. 1(a)].

## III. EXPERIMENTAL PROCEDURE

The compositions investigated by mechanical alloying in this study were Si-28Mo-14C and Si-33.33Mo (stoichiometric binary MoSi<sub>2</sub>) (all compositions in atomic percent). Mechanical alloying was performed in a water-cooled Szegvari attrition mill (planetary type) using hardened steel balls as the milling media and a ball to charge ratio of 5:1. Elemental powders of commercial purity molybdenum (purity 99.9%, 2-4 μm) and silicon (purity 98%, <44 μm) obtained from Cerac and high-purity carbon powder (99.5% pure, -300 mesh, amorphous) obtained from Johnson Matthey were the starting materials. To minimize oxygen contamination during processing, high-purity titanium-

gettered argon (oxygen content less than 4 ppm) under a slightly positive pressure was maintained in the attritor. The progress of MA was monitored by withdrawing small amounts of powder samples from the same attrition batch after 0, 0.5, 7, 17, 29, 40, and 42 h of milling. The powders were characterized for structure and morphology by SEM and XRD. In addition, powders obtained after 17 and 40 h of milling were analyzed by TEM. For the TEM analysis, powders were ultrasonically dispersed in acetone, and a small droplet was spread on a holey carbon film. The fine size ( $<1 \mu\text{m}$ ) of the powders ensured their electron transparency.

Consolidation of the MA binary and ternary powders was carried out by hot pressing under a vacuum of  $10^{-2}$  Torr or less in an inductively heated graphite die at both 1450 °C and 1600 °C at a pressure of 35 MPa for 1 h. To prevent cracking of the sample, the pressure was released prior to cooling. Samples for microstructural characterization were diamond-saw cut, ground, and polished to a  $1 \mu\text{m}$  diamond finish. Thin foil TEM samples were prepared from the bulk samples following standard procedures of dimpling and argon ion-milling at 4.5 kV. Microstructural analysis of the consolidated samples as well as the MA powders was performed using a JEOL JSM 6400 SEM equipped with a Tracor Northern EDS unit with light element detection capabilities and JEOL 200CX and JEOL 4000FX TEM's, the latter equipped with a Princeton Gamma Tech EDS unit with a light element detector.

The transformation characteristics of the MA powders were monitored by differential thermal analysis (DTA) and thermogravimetric analysis (TGA). DTA/TGA was performed under flowing gettered argon (1 cc/min, oxygen content less than 4 ppm) on a Netzsch STA-409 system with heating/cooling rates of 10 °C/min. Errors due to the differing specific heats of the sample and the reference were eliminated by using commercial MoSi<sub>2</sub> powder that had been previously calcined under gettered argon at 500 °C as the reference. For more detailed investigations, powders were heated at 10 °C/min under gettered argon above each DTA exotherm, held at that temperature for less than a minute, and rapidly cooled for subsequent analysis. Structural analysis of the powders and the consolidated samples was carried out using a Philips ADP 3720 diffractometer operated at 40 kV and 20 mA with Cu K<sub>α</sub> radiation and digital data acquisition over  $2\theta$  ranges of 5°–100°.

## IV. RESULTS AND DISCUSSION

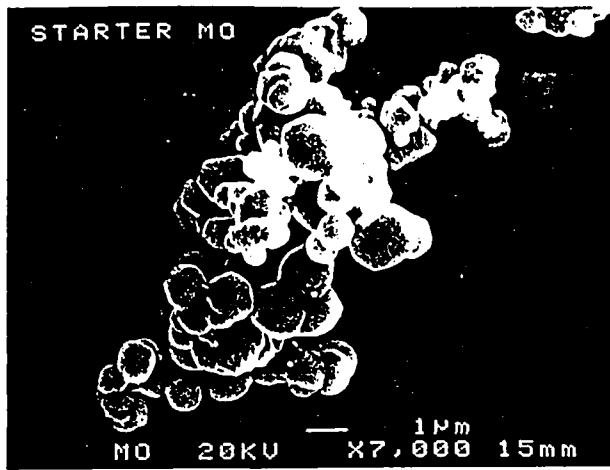
### A. Powder microstructure

The development of the powder morphology with increasing milling times is shown in Fig. 2. After 0.5 h of milling [Fig. 2(c)], large particles with a diameter of

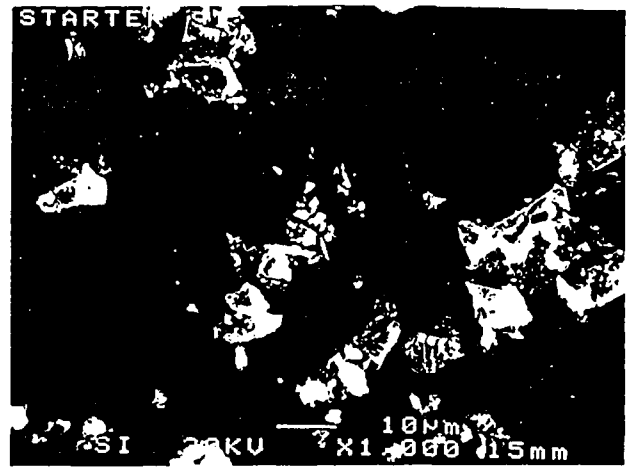
5–6  $\mu\text{m}$  are predominant. Refinement of the powder continues through 7 h of milling [Fig. 2(d)], beyond which the reduction in powder size is gradual. The powder size stabilizes around 1  $\mu\text{m}$  after 29 h [Fig. 2(e)] and remains constant thereafter [Fig. 2(f)].

Structural evolution studies of the powders as a function of milling time (Fig. 3) indicated the formation of traces of  $\beta$ -MoSi<sub>2</sub> (hexagonal form) after short milling times [0.5 h, see Fig. 3(a)]. Further milling [7 h, Fig. 3(b)] results in a slight increase in the amount of  $\beta$ -MoSi<sub>2</sub> along with the gradual appearance of  $\alpha$ -MoSi<sub>2</sub> (tetragonal form). Further increases in the amount of  $\alpha$ -MoSi<sub>2</sub> continue through 17 h of milling [Fig. 3(c)], at which time elemental molybdenum and silicon are still present. Milling beyond 17 h through 29 h [Fig. 3(d)] results in the almost complete disappearance of the silicon peaks, along with a considerable broadening of the  $\alpha$ -MoSi<sub>2</sub> peaks; this is presumably due to the decrease in the crystallite size of  $\alpha$ -MoSi<sub>2</sub> rather than the effect of lattice strain since MoSi<sub>2</sub> is brittle at the milling temperatures. This was confirmed by TEM observations. Beyond 29 h, milling has little effect on the structure of the powders, a fact which was also corroborated by the SEM observations, which showed particle size stabilization after 29 h.

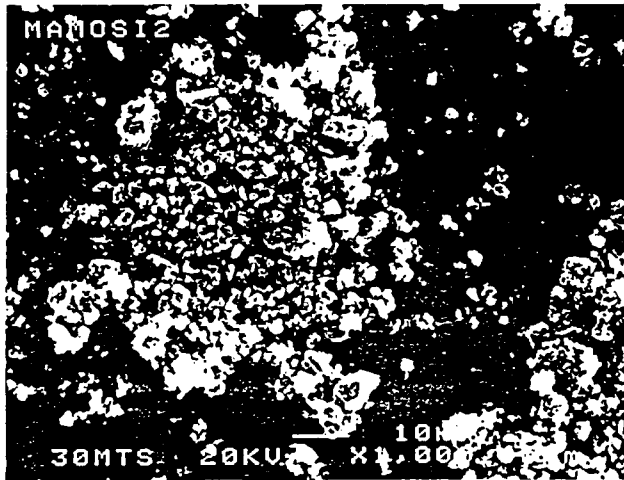
Powders were characterized for their microstructure by TEM. A dark-field TEM micrograph of a MA MoSi<sub>2</sub> powder particle milled for 40 h is shown in Fig. 4(a). Close examination reveals a fine distribution of crystallites, the sizes of which are between 4 and 7 nm. In addition, the surfaces of the powder particles appear to be covered with a layer of amorphous oxide, the projected thickness of which varies from 5 to 15 nm. The selected area diffraction pattern (SADP) [Fig. 4(b)] from this powder indexes to the interplanar spacings of Mo and  $\alpha$ -MoSi<sub>2</sub>. X-ray diffractograms [Figs. 5(a) and 5(b)] from these powders not only confirm the presence of the predominant phases (Mo and  $\alpha$ -MoSi<sub>2</sub>) determined in the SADP's, but also reveal traces of the metastable  $\beta$ -MoSi<sub>2</sub>, which reportedly occurs only above 1900 °C under equilibrium conditions. The formation of the  $\beta$ -MoSi<sub>2</sub> at lower temperatures is not surprising and has been reported during the annealing of amorphous Mo-Si multilayers prepared by sputtering,<sup>23,24</sup> as well as in ion-implanted MoSi<sub>2</sub> films.<sup>25</sup> The presence of Mo and MoSi<sub>2</sub> in the as-milled powders suggests that silicon is dissolved in the MoSi<sub>2</sub> and Mo crystallites; this is also a metastable effect caused by mechanical alloying, since the terminal solubilities of Si in Mo and MoSi<sub>2</sub> are negligible at room temperature although both Mo and MoSi<sub>2</sub> are known to exist over a certain homogeneity range above ~1500 °C.<sup>13,14</sup> The possibility of amorphization of part of the silicon was considered, but was eliminated in view of the experimental evidence against it.<sup>26</sup> The fine



(a)



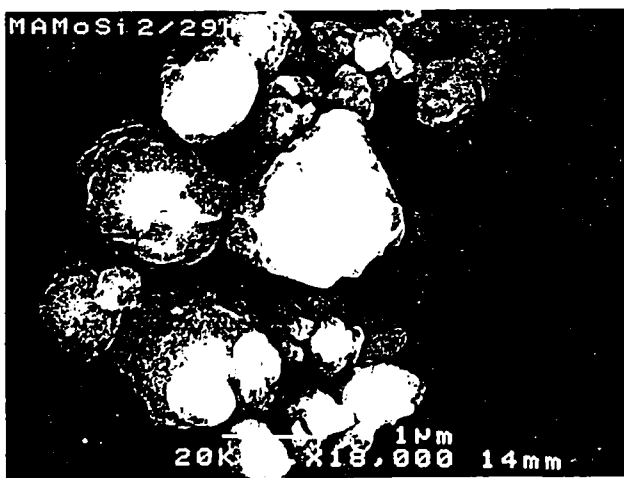
(b)



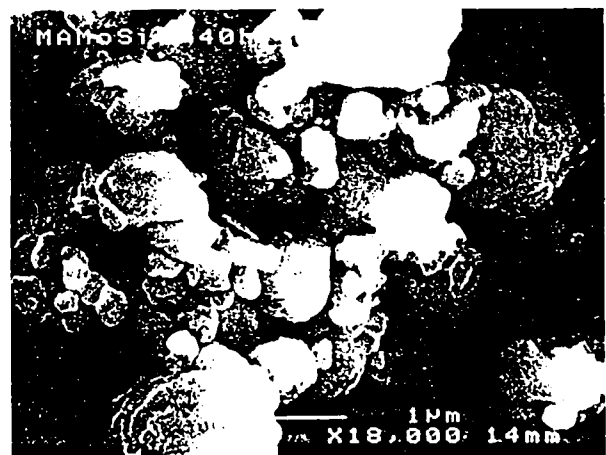
(c)



(d)



(e)



(f)

FIG. 2. Morphological evolution of the MA MoSi<sub>2</sub> powders as a function of milling time. Elemental Mo ( $d_p = 15 \mu\text{m}$ ) powder is prior to milling, (b) after 0.5 h of milling, (c) after 7 h of milling, (d) after 29 h of milling, (e) after 29 h of milling, and (f) after 40 h of milling.

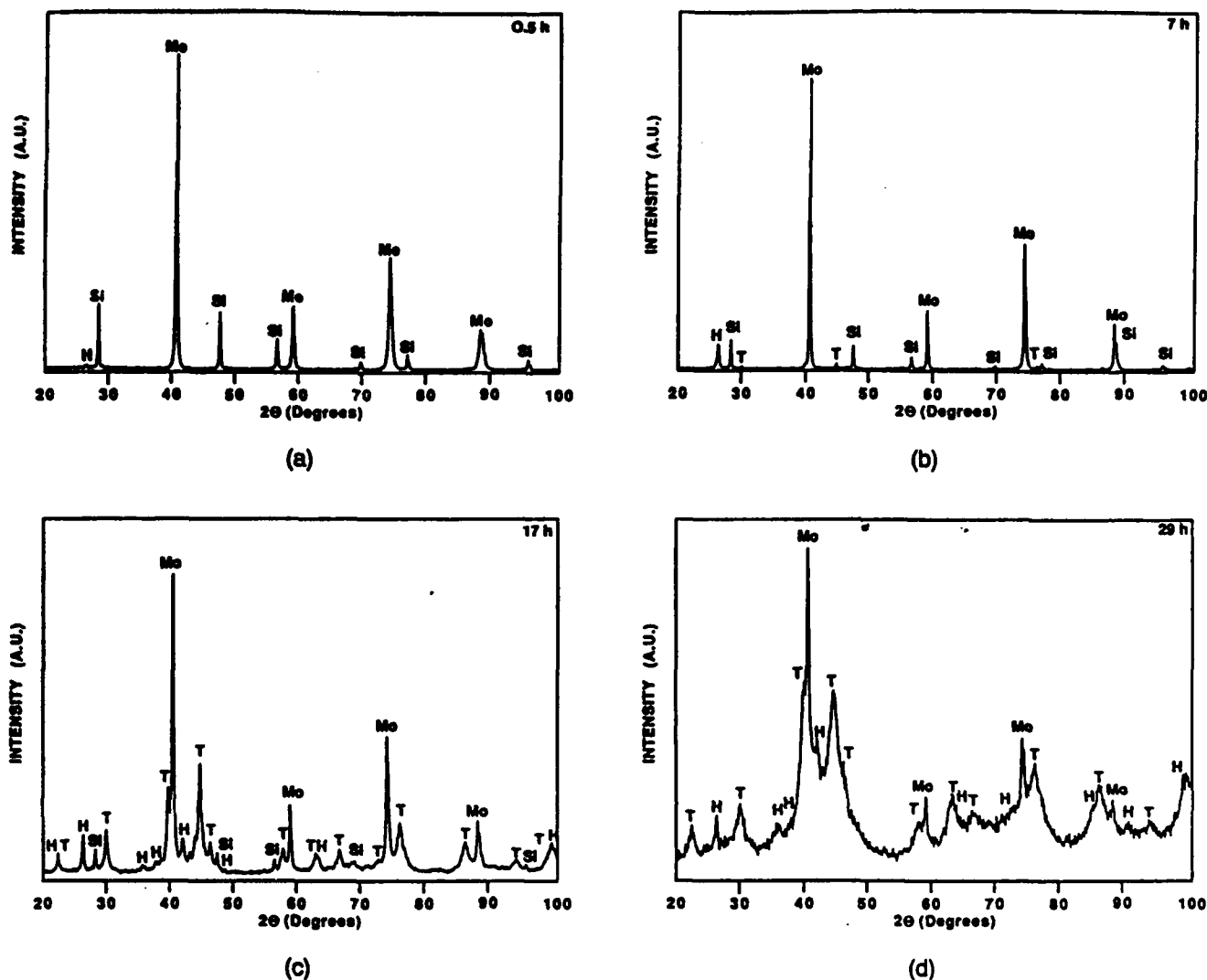


FIG. 3. Structural evolution of the ternary MA MoSi<sub>2</sub> powder as a function of milling time. XRD patterns of the powders milled for the indicated times: (a) 0.5 h (b) 7 h (c) 17 h and (d) 29 h (Mo is molybdenum, Si is silicon, T is tetragonal  $\alpha$ -MoSi<sub>2</sub>, and H is hexagonal  $\beta$ -MoSi<sub>2</sub>).

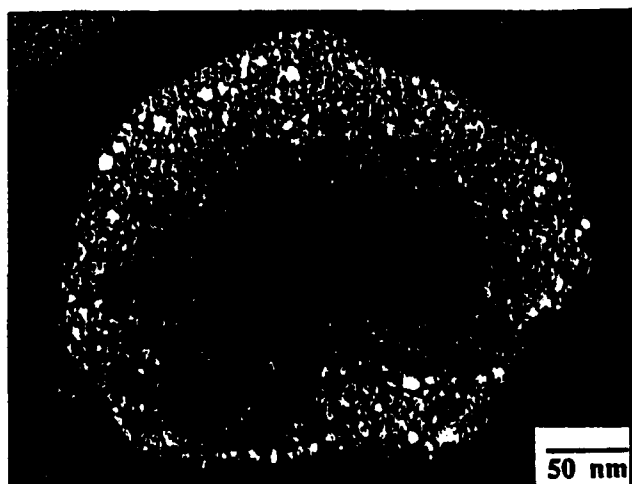
scale of the powder microstructures and the intermetallic compound formation during mechanical alloying suggest a homogeneous distribution of alloying elements. EDS analysis of the powders also revealed the presence of trace amounts of iron impurities that were probably picked up from the hardened steel balls used for milling.

In order to ascertain the effects of carbon additions on the final structure of the MA powders, XRD patterns from the binary [Fig. 5(a)] and ternary samples [Fig. 5(b)] after 40 h of milling were compared. It can be seen on the basis of the relative intensities of the molybdenum and  $\alpha$ -MoSi<sub>2</sub> peaks that the formation of  $\alpha$ -MoSi<sub>2</sub> is suppressed by the carbon additions.

### B. Phase evolution

The phase evolution of the binary and ternary MA MoSi<sub>2</sub> powders as a function of temperature was studied

by DTA. A typical heating trace of the binary MA MoSi<sub>2</sub> powder is shown in Fig. 6, where weak exotherms corresponding to 580 °C, 780 °C, and 1020 °C are apparent. The transformations corresponding to these exotherms were studied by XRD analysis of powders heated to temperatures above the end of each exotherm under identical heating conditions (10 °C/min under flowing argon), and the results are shown in Fig. 7. Comparison of the room temperature and the 690 °C XRD patterns [Fig. 5(a) and Fig. 7(a), respectively] showed that the mild 580 °C exotherm is associated with the formation of more  $\alpha$ -MoSi<sub>2</sub>, as is evidenced by the change in the relative intensities of the  $\alpha$ -MoSi<sub>2</sub> and Mo peaks. Likewise, comparison of the 690 °C and 950 °C XRD patterns shows that the 780 °C exotherm corresponds to the simultaneous growth of  $\alpha$ -MoSi<sub>2</sub> and Mo<sub>5</sub>Si<sub>3</sub> (tetragonal). The 1020 °C exotherm appears to be as-



(a)

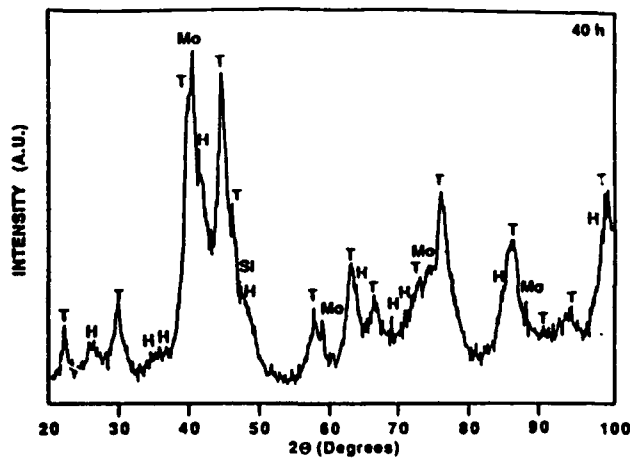


(b)

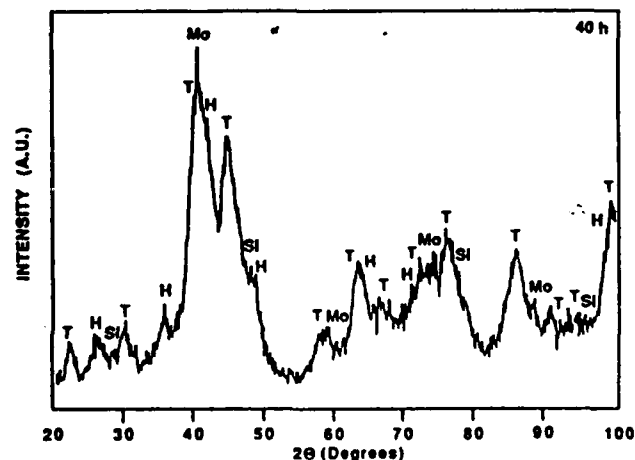
FIG. 4. (a) Dark-field TEM of the unannealed, as-mechanically-alloyed powder after 40 h milling, showing the distribution of fine crystallites of Mo,  $\alpha$ - and  $\beta$ -MoSi<sub>2</sub> in the micron-sized MA powder. Also note the presence of an amorphous layer surrounding the powder particle. (b) Selected area diffraction pattern from the above powder particle.

sociated with the growth of  $\alpha$ -MoSi<sub>2</sub> at the expense of  $\beta$ -MoSi<sub>2</sub> and tetragonal Mo<sub>5</sub>Si<sub>3</sub>. Further heating to higher temperatures [1300 °C, Fig. 7(d)] resulted in a decrease in the amount of Mo<sub>5</sub>Si<sub>3</sub> due to its transformation to  $\alpha$ -MoSi<sub>2</sub>, although minor amounts of the Mo<sub>5</sub>Si<sub>3</sub> were still apparent.

Figure 8 shows the DTA trace of the ternary MoSi<sub>2</sub>. Exothermic reactions with peaks at 540 °C, 875 °C, and 1030 °C were observed. The transformation sequences of these powders were monitored in the same manner as the binary MA MoSi<sub>2</sub> powders, and the results of the XRD analysis are shown in Fig. 9. Comparison of the room temperature [Fig. 5(b)] and 750 °C patterns



(a)



(b)

FIG. 5. XRD of the (a) MA binary stoichiometric MoSi<sub>2</sub> and (b) MA ternary MoSi<sub>2</sub> (Si-28Mo-14C) after 40 h of milling. Note the relative intensities of the molybdenum and  $\alpha$ -MoSi<sub>2</sub> peaks (Mo is molybdenum, Si is silicon, T is tetragonal  $\alpha$ -MoSi<sub>2</sub>, and H is hexagonal  $\beta$ -MoSi<sub>2</sub>).

[Fig. 9(a)] indicates that the mild 540 °C peak corresponds to the partial transformation of molybdenum to  $\beta$ -MoSi<sub>2</sub>, while the analysis of the 750 °C and 935 °C patterns [Figs. 9(a) and 9(b), respectively] suggests that the 875 °C exotherm corresponds to the formation of the carbon-stabilized C<sub><1</sub>Mo<sub>5</sub>Si<sub>3</sub> (Nowotny) phase at the expense of molybdenum. The possibility of this higher molybdenum silicide forming as an oxidation product rather than as a phase transformation product was also considered, but was discounted on the basis of the TGA data (discussed in detail in a later section), which did not show any inflections (due to weight loss or gains that are normally associated with oxidation reactions) at the corresponding exothermic temperature (875 °C, Fig. 16). Furthermore, the 1030 °C exotherm corresponds to the

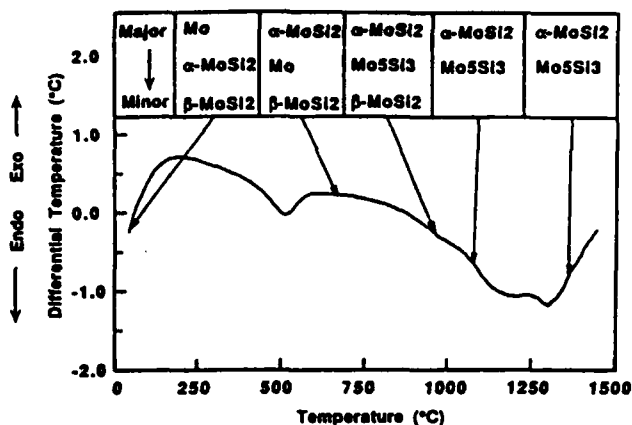
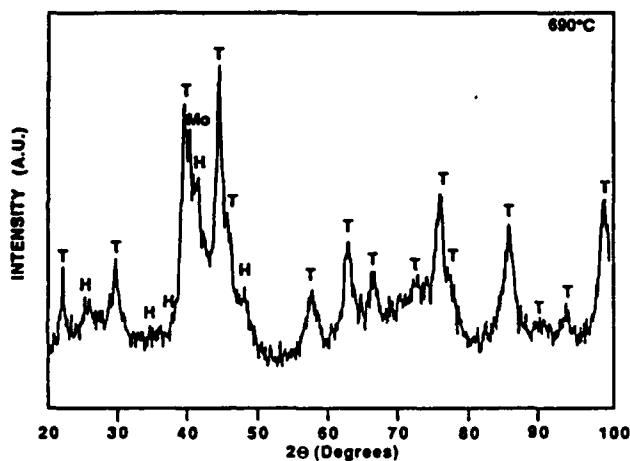
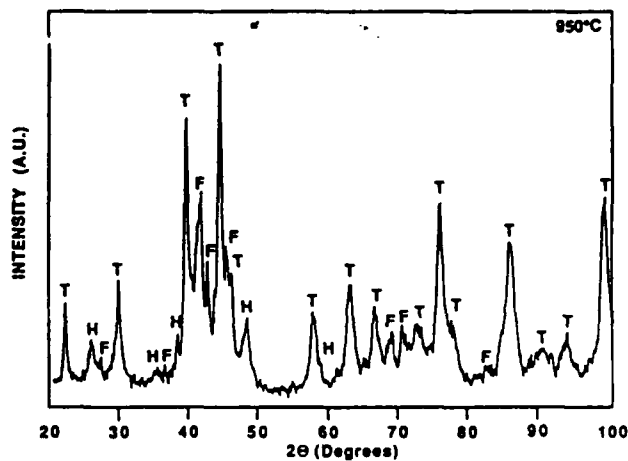


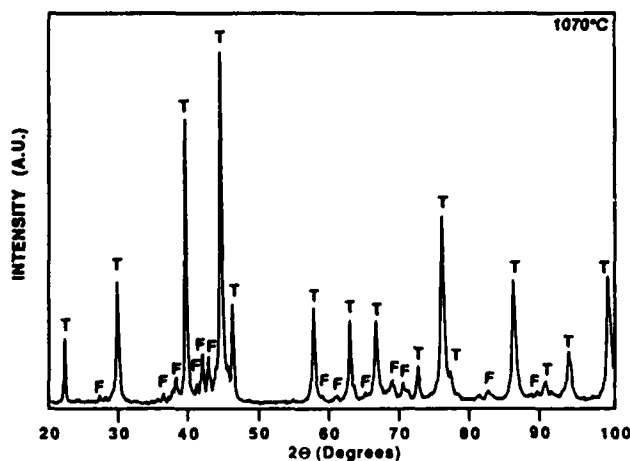
FIG. 6. DTA of binary stoichiometric MoSi<sub>2</sub> under flowing Ar at a heating rate of 10 °C/min, along with the corresponding phases observed by XRD.



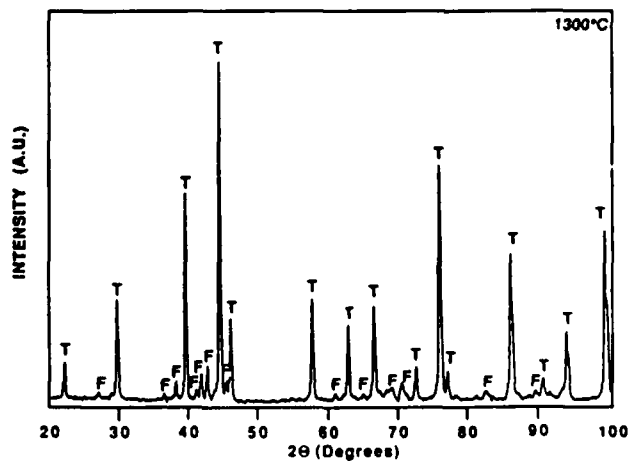
(a)



(b)



(c)



(d)

FIG. 7. XRD of the MA binary stoichiometric MoSi<sub>2</sub> powders heated at 10 °C/min under flowing argon to the temperatures indicated: (a) 690 °C (b) 950 °C (c) 1070 °C and (d) 1400 °C (Mo is molybdenum, Si is silicon T is α-MoSi<sub>2</sub>, H is β-MoSi<sub>2</sub>, and F is the tetragonal Mo<sub>5</sub>Si<sub>3</sub> phase).

transformation of the Nowotny phase and β-MoSi<sub>2</sub> to the more stable α-MoSi<sub>2</sub>, as evidenced by a comparison of the 935 °C and 1070 °C XRD patterns [Figs. 9(b) and 9(c), respectively]. Heating to higher temperatures [1400 °C, Fig. 9(d)] results in a decrease in the amount of the Nowotny phase and an increase in α-MoSi<sub>2</sub>. The DTA cooling curves of the binary and the ternary powders were flat in nature, thereby indicating stable structures.

The low-temperature formation of the carbon-stabilized Nowotny phase instead of the thermodynamically preferred α-MoSi<sub>2</sub> phase is probably related to its greater ease of nucleation and growth. The stability of the β-MoSi<sub>2</sub> up to 1030 °C is also not surprising. Hexagonal β-MoSi<sub>2</sub>, formed by isothermal annealing of sputtered Mo-Si multilayers, has been reported to be stable up to 800 °C. The higher tem-

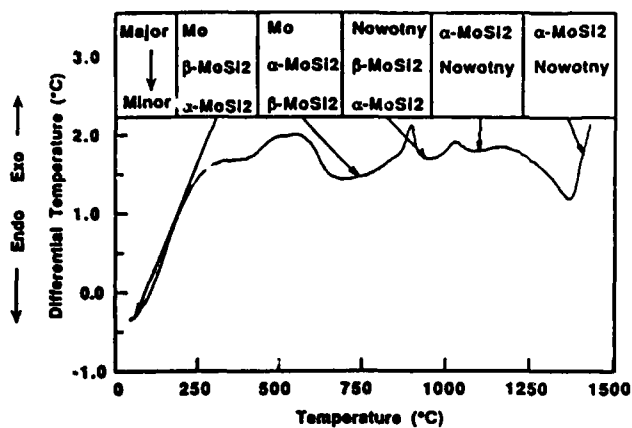
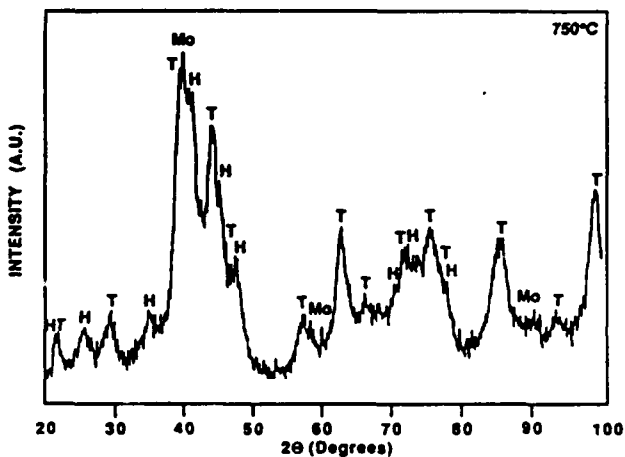
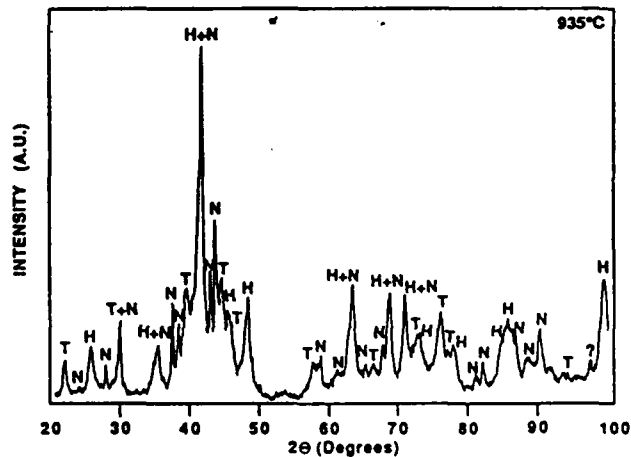


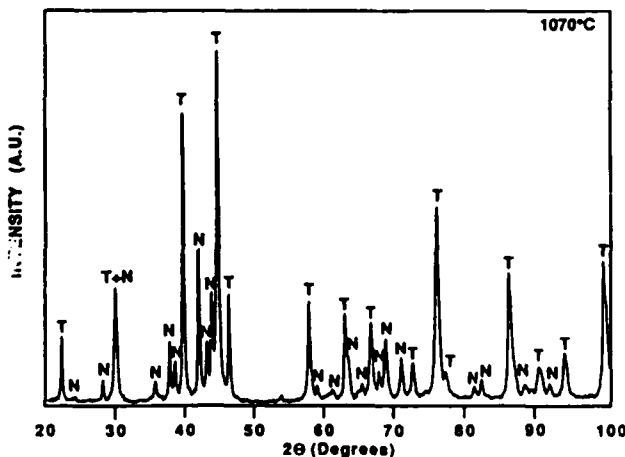
FIG. 8. DTA of ternary MoSi<sub>2</sub> under flowing argon at a heating rate of 10 °C/min, along with the corresponding phases identified by XRD. ("Nowotny" refers to the Nowotny phase, C<sub><1</sub>Mo<5Si<sub>3</sub>.)



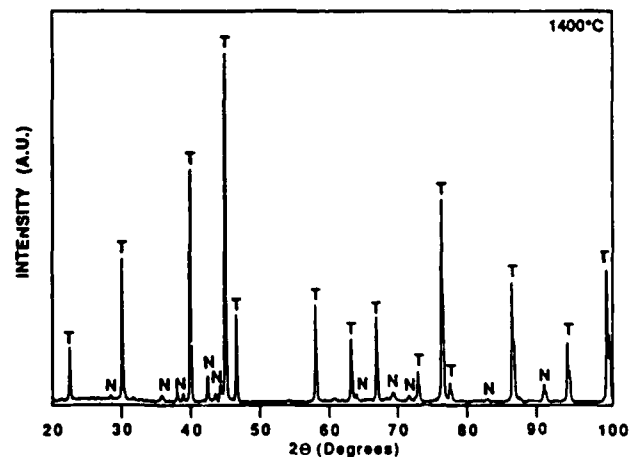
(a)



(b)



(c)



(d)

FIG. 9. XRD of the MA ternary MoSi<sub>2</sub> powders (Si-28Mo-14C) heated at 10 °C/min under flowing argon to the temperatures indicated: (a) 750 °C, (b) 935 °C, (c) 1070 °C, and (d) 1400 °C (Mo is molybdenum, Si is silicon, T is α-MoSi<sub>2</sub>, H is β-MoSi<sub>2</sub>, and N is the hexagonal Nowotny phase).

perature stability of the β phase in this study is probably related to the presence of iron and oxygen impurities rather than the relatively high heating rates of the powders; this is consistent with the experimental evidence obtained from the isothermal annealing of the MA binary and ternary powders (820 °C for a period of 1 h), which demonstrated the stability of the β-MoSi<sub>2</sub> phase.

### C. Consolidated microstructures

Figure 10 shows the microstructures of a hot-pressed specimen derived from the MA nominally stoichiometric MoSi<sub>2</sub> powders. Considerable amounts of second-phase particles with volume fractions of about 0.15 are present in the MoSi<sub>2</sub> matrix. TEM/EDS analysis of these samples (Fig. 11) revealed the presence of submicron-sized grains of MoSi<sub>2</sub> and second-phase particles which were amorphous and silicon-rich, indicating the presence of

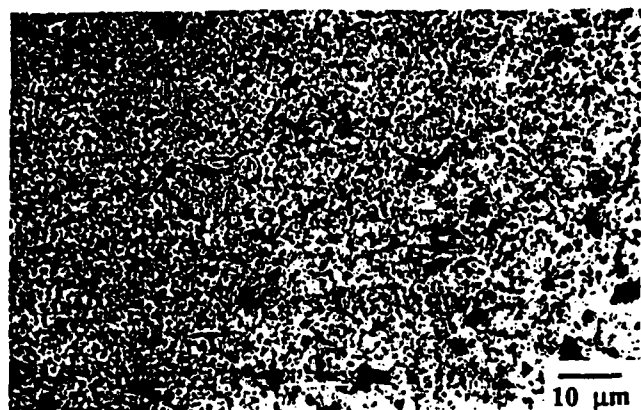


FIG. 10. Scanning Electron Micrograph (SEM) showing the microstructure of the hot-pressed binary MA MoSi<sub>2</sub>.

a glassy silica phase. The silica was present at the grain boundaries and triple points. In addition, very fine

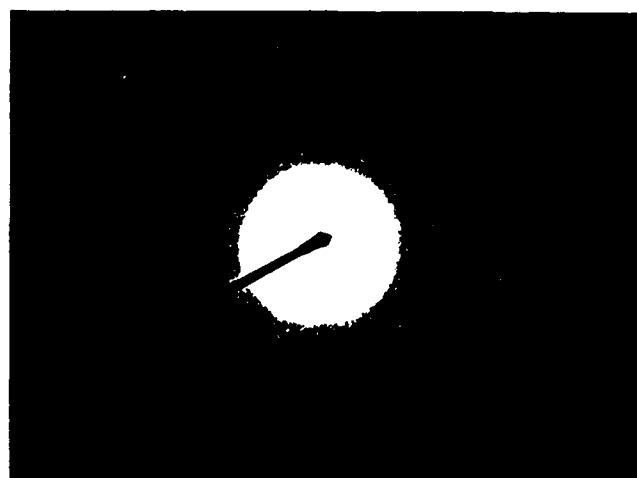


FIG. 11. Bright-Field Transmission Electron Micrograph (BFTEM) and SADP of silica particles in hot-pressed binary MA MoSi<sub>2</sub>. S denotes a typical silica particle.

(10 nm) dispersoids were found within the MoSi<sub>2</sub> grains, along with occasional grains of Mo<sub>5</sub>Si<sub>3</sub>.

Figure 12 shows a backscattered electron image of a hot-pressed specimen derived from the carbon-modified MA MoSi<sub>2</sub> powder. Considerable improvement in the overall homogeneity and cleanliness of the microstructure is apparent in comparison with the samples derived from the binary MA MoSi<sub>2</sub> powder. Based on the atomic number (Z) contrast, it is apparent that the material has three phases.

Following qualitative analysis by EDS, the compositions of each of these phases, as well as the overall matrix composition, were determined by electron microprobe analysis. In addition, quantitative estimation of the volume fraction of these phases was obtained using standard point count techniques. These results are summarized in Table II. The data indicate the presence of SiC (low Z phase), MoSi<sub>2</sub> (intermediate Z phase), and an iron-containing Nowotny phase C<sub><1</sub>(Mo, Fe)<sub><5</sub>Si<sub>3</sub> (high Z phase) in the microstructure, and thus seem to support the isotherms proposed by Nowotny *et al.* and Brewer and Krikorian<sup>16,20</sup> [see Fig. 1(a)] rather than that of van Loo *et al.*<sup>21</sup> [see Fig. 1(b)]. Furthermore, the volume fractions of these phases are in reasonable agreement with the location of the nominal compositions in the MoSi<sub>2</sub> + SiC + C<sub><1</sub>Mo<sub><5</sub>Si<sub>3</sub> three-phase field in the Nowotny diagram. As mentioned earlier, the source of the iron is believed to be the hardened steel milling media. Interestingly, no iron was detected in the MoSi<sub>2</sub>, despite the fact that it has a limited amount of solubility for iron.<sup>27</sup> The preferential location of iron in the Nowotny phase is probably related to the greater affinity of iron toward the carbon-centered octahedra of this phase. The relatively small size differences between the atomic radii of Mo and Fe, together with the low

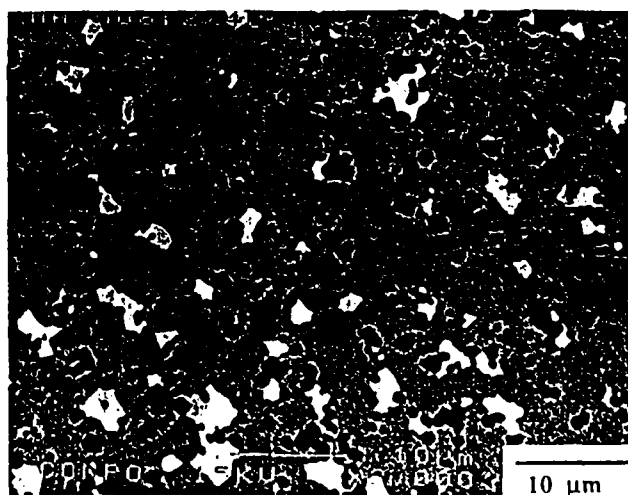


FIG. 12. Backscattered electron image of the hot-pressed ternary MA MoSi<sub>2</sub> (Si-28Mo-14C)

TABLE II. Microstructural characteristics of the consolidated samples derived from the ternary MA MoSi<sub>2</sub> powders.

| Phase             | Composition (at. %) |       |       |      | Volume fraction (%) |
|-------------------|---------------------|-------|-------|------|---------------------|
|                   | Si                  | Mo    | C     | Fe   |                     |
| MoSi <sub>2</sub> | 64.55               | 35.45 | 0.0   | 0.0  | 79.15               |
| SiC               | 0.0                 | 48.29 | 50.20 | 0.0  | 11.83               |
| Nowotny           | 54.91               | 35.26 | 5.22  | 4.59 | 9.028               |
| Overall           | 58.16               | 31.7  | 9.765 | 0.37 |                     |
| Initial           | 58.00               | 28.00 | 14.00 |      |                     |

levels of the iron impurity, make iron substitution on the molybdenum sites easy, since the resulting lattice strains would be small. It is also apparent that the Nowotny phase tends to adjoin the SiC grains, thereby suggesting that its origin is probably due to local deviations from stoichiometry resulting from either SiO<sub>2</sub> or SiC formation.

TEM analysis of the carbon-modified material revealed a homogeneous microstructure with uniformly distributed second phases such as those marked A and B in Fig. 13(a). The average grain size of the MoSi<sub>2</sub> was between 3 and 5  $\mu\text{m}$ , which is much larger than that of the material without carbon. The larger grain size is a temperature-related effect as ternary powder samples consolidated at 1450 °C exhibited submicron grain sizes. EDS microanalysis, with an ultrathin polymeric window, of region A showed the presence of silicon and carbon alone, indicating that these regions correspond to the dark (low Z) regions, such as those shown in Fig. 12. SADP's were obtained along the major zone axes from these and other silicon-rich regions [Fig. 13(b)] and were consistently indexed to the cubic  $\beta$ -SiC structure (with  $a = 0.4359 \text{ nm}$ ). The  $\beta$ -SiC was present in the form of 1  $\mu\text{m}$ -sized particles located predominantly along grain boundaries and at triple-point regions. Furthermore, the SiC particles were easily distinguishable based on the internal twinning observed (Fig. 14). Although the microstructural origin of these SiC particles is presently not well understood, it is probable that their formation would involve the following reactions: (A) the carbothermal reduction of silica to SiC, and (B) the cooperative displacements of Si and C from MoSi<sub>2</sub> and C<sub><1</sub>Mo<sub>3</sub>Si<sub>3</sub> to form SiC. While the reaction mechanisms for (A) have been discussed previously<sup>11</sup>, the results of the phase evolution studies on the ternary powders do not indicate the formation of SiC within the limits of detection of the XRD. However, the fact that these studies were conducted on loosely packed powders, at atmospheric pressures under flowing argon, as opposed to the consolidation conditions that involve densely packed powders under highly reducing atmospheres, might have precluded effective conversion of silica to SiC. On the other hand, direct reaction between

cooperatively displaced Si and C is also feasible above 1435 °C, based on the DTA data of Singh.<sup>28</sup> In addition to  $\beta$ -SiC, grains of the iron-containing Nowotny phase (region B) were also easily distinguishable, based on their lower ion-milling rates. Most importantly, the grain boundaries also appeared to be free of silica (Fig. 15), although a small amount was occasionally observed within the grains. Contrary to Maxwell's hypothesis that molybdenum carbides would be present in the matrix as a reduction product of MoO<sub>3</sub><sup>7</sup> and in accordance with the 1600 °C isotherms of Nowotny, none of the molybdenum carbides such as MoC and Mo<sub>2</sub>C were detected.

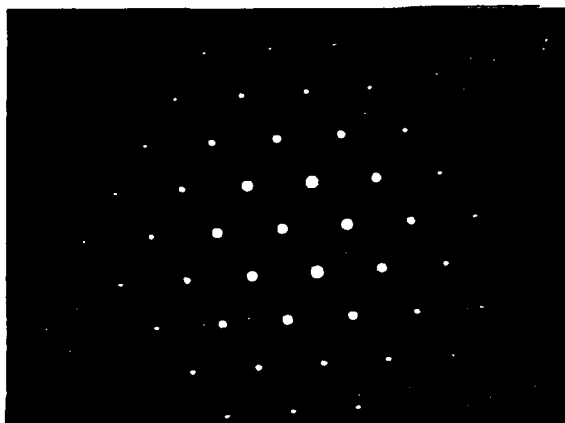
#### D. Thermogravimetric analysis

The results of the thermogravimetric analysis (heating and cooling rates of 10 K/min) of the MA binary (solid line) and ternary powders (dotted lines) are shown in Fig. 16. The top and bottom curves in each set represent the weight changes of the powders during heating and cooling, respectively. While both the samples experienced weight losses above 1200 °C, those exhibited by the C-modified ternary MA MoSi<sub>2</sub> powders were much higher than those of the binary MA MoSi<sub>2</sub> at all temperatures. Examination of the XRD patterns of the binary MA MoSi<sub>2</sub> at temperatures above 1200 °C [Fig. 7(d)] revealed minor amounts of tetragonal Mo<sub>5</sub>Si<sub>3</sub>, indicating a silicon depleted powder. With the knowledge that the oxygen content of micron-sized MoSi<sub>2</sub> powders is about 1.5 at.%,<sup>7</sup> it is quite possible that the weight losses above 1200 °C are caused by the dissociation of SiO<sub>2</sub> (under very low partial pressures of oxygen) to the volatile SiO. On the other hand, the higher weight losses in the C-modified MA MoSi<sub>2</sub> powders can be ascribed to the presence of carbon. However, the mechanism in this case is the reduction of SiO<sub>2</sub> by carbon to volatile oxides such as CO, CO<sub>2</sub>, and SiO.

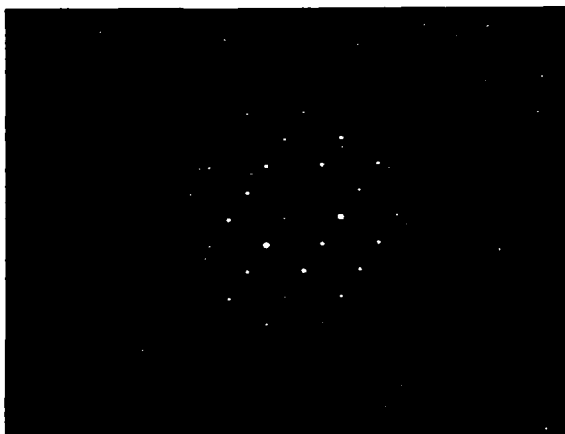
The above data are consistent with the weight losses experienced during the actual hot consolidation of the ternary MA MoSi<sub>2</sub> samples. Vacuum hot pressing of the C-modified samples at temperatures of 1550 °C and



(a)



(b)



(c)

FIG. 13. (a) BFTEM of the ternary MA MoSi<sub>2</sub>. (b) SADP of β-SiC along  $B = [011]$  (region A). (c) SADP of the Nowotny phase along  $B = [10\bar{1}0]$  (region B).

below resulted in weight losses near ~4%, while higher consolidation temperatures (1700 °C) resulted in a near doubling of the weight loss (~8%). However, it should



FIG. 14. BFTEM of a β-SiC particle formed *in situ* in the ternary MA MoSi<sub>2</sub>.



FIG. 15. BFTEM of the ternary MA MoSi<sub>2</sub> showing the absence of grain boundary silica.

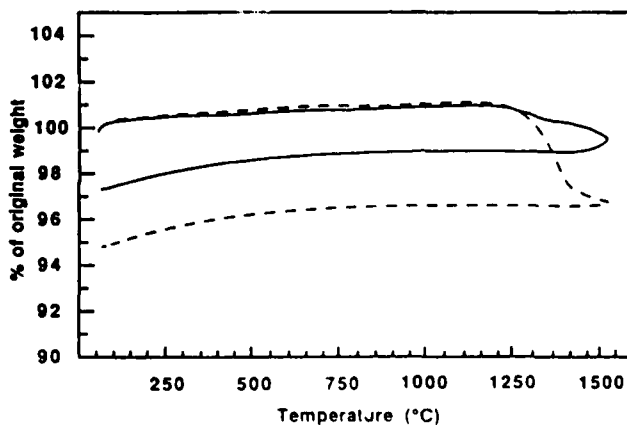


FIG. 16. TGA of the binary stoichiometric MA MoSi<sub>2</sub> (—) and ternary MA MoSi<sub>2</sub> (Si-28Mo-14C) (---) under flowing argon at a heating and cooling rate of 10 °C/min. The top curve in each set represents heating while the bottom curve represents cooling.

be recognized that the weight losses at temperatures above 1700 °C are caused by the volatilization of silicon from MoSi<sub>2</sub> due to the relatively high vapor pressures of silicon over MoSi<sub>2</sub>,<sup>1,2</sup> rather than by the carbothermal reduction of the SiO<sub>2</sub>. This implies that while relatively minor weight losses (up to 5%) due to carbothermal reduction of silica are unavoidable, careful control of the consolidation temperature and vacuum levels can be used to prevent substantial weight losses (~40%), such as those reported in previous studies.<sup>8</sup>

### E. Significance of the *In situ* reactions

The ability to form silica-free MoSi<sub>2</sub> and MoSi<sub>2</sub>-based composites containing micron-sized SiC reinforcements opens up some exciting possibilities. Uniformly dispersed SiC in a modified MoSi<sub>2</sub> matrix should lead to considerable elevated temperature strengthening in addition to improved fracture properties, due to the enhanced resistance to grain boundary sliding brought about by the SiC particles dispersed along silica-free grain boundaries. It is also conceivable that the synthesis of MoSi<sub>2</sub>/WSi<sub>2</sub> alloys with carbon additions by means of mechanical alloying would result in improved strengthening due to the synergistic effects of solid solution and dispersion strengthening with *in situ* formed SiC or WC.

Utilization of this strategy holds promise in refractory metal (Nb, Mo, W) toughening also. In these systems, the major problems encountered are the degradation of the diffusion barrier coatings due to reactions with silica, and the severe residual stresses caused by the mismatch in the coefficients of thermal expansion (CTE) between the matrix and the reinforcement phases. Through the use of the ternary MA MoSi<sub>2</sub> powders, it should be possible to form the desired volume fraction of SiC reinforcements *in situ* so as to tailor the effective CTE of the matrix to match that of the reinforcement. For example, the CTE of a refractory metal such as molybdenum or tungsten is intermediate between that of MoSi<sub>2</sub> and SiC. As has been shown by Maloney and Hecht,<sup>29</sup> controlled additions of micron-sized SiC lower the effective CTE of the MoSi<sub>2</sub>-SiC composite in accordance with the rule of mixtures and enable the use of refractory metals that have better strength retention at elevated temperatures (such as Mo and W), but are otherwise limited in their use due to their low CTE's. Such an *in situ* modified matrix would also have the added advantage of being free of silica and silicon, compared to composites processed using commercial powders; this should prevent the coating degradation and enhance the useful life of these composites.

## V. SUMMARY AND CONCLUSIONS

A processing strategy utilizing carbothermal reduction reactions, mechanical alloying, and carbon additions

has been developed for the synthesis of silica-free MoSi<sub>2</sub> and MoSi<sub>2</sub>/SiC composites. Using this approach, MoSi<sub>2</sub> and MoSi<sub>2</sub>/SiC composites have been fabricated starting from pure elemental molybdenum and silicon powders with and without carbon additions. The structural and morphological evolution of the powders has been studied as a function of milling time. It has been shown that complete attrition is achieved after 29 h of alloying. The resultant powders are micron-sized and contain 4 to 7 nm crystallites of molybdenum,  $\alpha$ -MoSi<sub>2</sub>, and traces of  $\beta$ -MoSi<sub>2</sub>. The addition of carbon to the starting elemental powder mixture suppresses the formation of  $\alpha$ -MoSi<sub>2</sub> in the fully milled powders. Minor amounts of iron impurities were also found in the powders due to the contamination from the milling media.

The phase evolution studies of the binary and ternary MoSi<sub>2</sub> powders indicated that  $\beta$ -MoSi<sub>2</sub> is stable to 1020 °C at heating rates of 10 °C/min, in contrast to previous studies on the isothermal annealing of Mo-Si multilayers which demonstrated stabilities to only 800 °C. While minor amounts of tetragonal Mo<sub>5</sub>Si<sub>3</sub> were evolved as an intermediate transformation product in the binary MA MoSi<sub>2</sub> powders, the evolution of the ternary MoSi<sub>2</sub> powders showed the formation kinetics of the Nowotny phase C<sub><1</sub>Mo<sub>5</sub>Si<sub>3</sub> to dominate that of tetragonal  $\alpha$ -MoSi<sub>2</sub> at lower temperatures. However, temperatures above 1000 °C resulted in the progressive decrease in the amount of these higher molybdenum phases.

Complete consolidation of the MA powders was achieved at 1450 °C. Amorphous silica that is found in all conventional powder-processed matrices was essentially eliminated through *in situ* carbothermal reactions brought about by the additions of carbon through mechanical alloying. It is shown that composites consisting of uniformly distributed micron-sized SiC particles with varying volume fractions can be formed using this approach. Significant grain size differences exist between the microstructures processed from the binary powders and those of the ternary powders, probably due to the higher consolidation temperatures used in the latter. The formation of the iron and molybdenum containing Nowotny phase of the approximate composition C<sub><0.5</sub>Mo<sub><4.4</sub>Fe<sub><0.4</sub>Si<sub>3</sub> is also reported. The co-existence of the Nowotny phase with MoSi<sub>2</sub> and SiC is in agreement with the isotherm proposed by Nowotny *et al.*, rather than that proposed by van Loo and co-workers.

The possibilities of utilizing MA powders to overcome the CTE mismatch and coating degradation problems in ductile phase composites are discussed. The use of these *compositionally tailored* powders would alter the matrix CTE so as to match that of the ductile reinforcements, thus minimizing the problems of matrix cracking. The absence of silica should also improve the stability of the diffusion barrier coatings of these composites.

## ACKNOWLEDGMENTS

Sincere appreciation is expressed to A. Costa e Silva for stimulating discussions and to Mr. G. Scheffele for his assistance with the thermal analysis. This work was supported through a Grant (No. MDA972-88-J-1006) from the Defense Advanced Research Projects Agency.

## REFERENCES

1. T. G. Chart, *Metal Science* 8, 344 (1974).
2. A. W. Searcy and A. G. Tharp, *J. Phys. Chem.* 64, 1539 (1960).
3. J. B. Berkowitz-Mattuck, P. E. Blackburn, and E. J. Felten, *Trans. Metall. Soc. AIME* 233, 1093 (1965).
4. R. M. Aikin, Jr., *Scripta Metall.* 26, 1025-1030 (1992).
5. P. J. Meschter, *Metall. Trans.* 23A, 1763-1772 (1992).
6. L. Xiao and R. Abbaschian, *Mater. Sci. Eng. A155*, 135 (1992).
7. W. A. Maxwell, NACA RM E52B06, 1952.
8. S. Maloy, A. H. Heuer, J. J. Lewandowski, and J. J. Petrovic, *J. Am. Ceram. Soc.* 74, 2704 (1991).
9. D. A. Hardwick, P. L. Martin, and R. J. Moores, *Scripta Metall.* 27, 391 (1992).
10. R. B. Schwarz, S. R. Srinivasan, J. J. Petrovic, and C. J. Maggiore, *Mater. Sci. Eng. A155*, 75 (1992).
11. G. C. Wei, *J. Am. Ceram. Soc.* 66, C-111 (1983).
12. K. Ishizaki, *Acta Metall. Mater.* 38, 2059 (1990).
13. *Atomic Energy Review*, special issue No. 7, edited by L. Brewer (International Atomic Energy Agency, Vienna, Austria, 1980).
14. A. B. Gokhale and G. J. Abbaschian, *J. Phase Equilibria* 12, 493 (1991).
15. P. Villars and L. D. Calvert, *Pearson's Handbook of Crystallographic Data for Intermetallic Phases* (ASM, Metals Park, OH, 1985), Vols. 1 and 2.
16. H. Nowotny, E. Parthe, R. Kieffer, and F. Benesovsky, *Monatsh. Chemie* 85, 255 (1954).
17. E. Parthe, W. Jeitschko, and V. Sadagopan, *Acta Crystallogr.* 19, 1031 (1965).
18. B. Aronson, *Acta Chem. Scand.* 9, 1107 (1955).
19. H. Schachner, E. Cerwenka, and H. Nowotny, *Monatsh. Chemie* 85, 245 (1954).
20. L. Brewer and O. Krikorian, *J. Electrochem. Soc.* 103, 38 (1956).
21. F. J. J. van Loo, F. M. Smet, and G. D. Rieck, *High Temp. High Press.* 14, 25 (1982).
22. A. Costa e Silva and M. J. Kaufman, submitted to *Metall. Trans.*, 1993.
23. O. B. Loopstra, W. G. Sloof, Th. H. de Keijser, E. J. Mittemeijer, S. Radelaar, A. E. T. Kuiper, and R. A. M. Wolters, *J. Appl. Phys.* 63, 4960 (1988).
24. C. M. Doland and R. J. Nemanich, *J. Mater. Res.* 5, 2854 (1990).
25. F. M. d'Heurle, C. S. Petersson, and M. Y. Tsai, *J. Appl. Phys.* 51, 5976 (1980).
26. C. C. Koch, personal communication, 1992.
27. G. V. Raynor and V. G. Rivlin, *Int. Metals Rev.* 30, 68 (1985).
28. M. Singh, presented at the 94th Annual Meeting of the American Ceramic Society, Minneapolis, MN, 1992.
29. M. J. Maloney and R. J. Hecht, *Mater. Sci. Eng. A155*, 19 (1992).

NOVEL PROCESSING OF INTERMETALLIC MATRIX COMPOSITES USING IN SITU  
DISPLACEMENT REACTIONS

A. Costa e Silva, S. Jayashankar, P. Krishnan and M. J. Kaufman

Department of Materials Science and Engineering, University of Florida, Gainesville, FL

*Abstract*

The utilization of in-situ displacement reactions is being investigated as a means of producing in-situ dispersoids and tailored interfaces in intermetallic matrix composites. The systems under investigation include  $\text{MoSi}_2$  and  $\text{NiAl}$  matrices containing ceramic (e.g.,  $\text{SiC}$  and  $\text{Al}_2\text{O}_3$ ) and/or refractory metal (e.g.,  $\text{Mo}$  and  $\text{W}$ ) reinforcements. Processing schemes include conventional compositing routes, *mechanical alloying and diffusion couples* for more fundamental studies. The elimination of silica and the production of  $\text{SiC}$  dispersoids in  $\text{MoSi}_2$  by mechanical alloying  $\text{Mo}$ ,  $\text{Si}$  and  $\text{C}$  powders prior to consolidation will be described. In addition, it will be shown that it is possible to form refractory metal carbides at the interfaces between  $\text{NiAl}$  and molybdenum and tungsten by alloying the  $\text{NiAl}$  with small additions of carbon.

## Introduction

The progress in understanding the close relationships between properties and processing of materials over the past few decades has led to considerable advances in processing of materials from enlightened empiricism to more scientific based process design. Perhaps some of the most significant advances towards the tailoring of properties via processing has occurred in the field of composite materials. The ability to define, a priori, the initial phases and constituents present in composites is unique to these materials. This selection will, in principle, define a set of properties derived from those of the initial phases and constituents; this has been the basic concept behind the introduction of composites. The final micro and macrostructures, however, are governed by the same principles controlling the processing of other classes of materials and become especially important when high temperature processing or application is considered. The objective of this paper is to present a systematic analysis of the factors relevant to the processing of intermetallic matrix composites, comparing them, where applicable, to the experience and knowledge available with more conventional, non-composite materials. Of particular interest is the application of these aspects to the subset of processing operations leading to *in-situ* displacement reactions. Two examples which utilize these concepts will then be given.

### The Case for Intermetallic Matrix Composites

Intermetallic materials have promising properties for high temperature structural applications. The environmental resistances of the aluminides and silicides, their high melting points and low densities when compared to metals make these materials potential candidates for next generation high temperature structural materials. Significant obstacles to their application include their low ambient temperature toughnesses and poor high temperature strengths.

Different approaches for improving the room temperature toughness and high temperature strength of intermetallic materials have been attempted. Alloying (both macro and micro) (1) and compositing are probably the most frequently considered approaches. A truly successful approach should be able to influence the deformation mechanisms operating both below and above the ductile to brittle transition temperature. The understanding of these mechanisms is somewhat limited at present (2) as is the understanding of the effects of other elements (e.g., impurities) which might be present. To a certain extent, even the phenomenological description of the mechanical behavior of some of the promising silicides (and the aluminides to a lesser extent) and the effect of third elements on this behavior is not well established (3,4).

The simplest view of a composite system is based only on the mechanical behavior of the matrix and the reinforcement phases. This has been the initial driving force for the large number of attempts to develop metal matrix composites (MMCs) and intermetallic matrix composites (IMCs). Although the "rule-of-mixtures" approach suggests that the overall composite behavior should be related to the properties of the individual phases present, such behavior is frequently not observed. For instance, the importance of coefficient of thermal expansion (CTE) mismatch, long established in other areas of materials processing (e.g., 5), is dramatically amplified when comparatively larger volume fractions of the phases are present as in composites. On the other hand, the paramount importance of interface mechanical behavior (6,7) in defining overall composite properties finds little parallel in the previous experience of processing other classes of materials. Also, thermodynamic compatibility and stability of the phases cannot be overlooked, especially when high temperature processing and application are considered. Therefore, although the first justification for the use of compositing as a technique for improving the mechanical behavior of intermetallic materials might have been the fact that only relatively straightforward phenomenological information was required, experience (i.e., the large number of unsuccessful attempts) has shown that, in order to fully utilize the possibilities afforded by this approach, other types of fundamental information (often not readily available) is required.

## Matrix/Reinforcement Considerations in the Processing of IMC's

The requisite information for designing a successful IMC is encompassed in the following:

- Mechanical behavior of matrix and proposed reinforcements.
- Thermodynamic compatibility between matrix and reinforcement.
- Matrix-reinforcement interface properties.
- Thermophysical and mechanical compatibility of phases present.

All the properties in these groups are processing sensitive and to a large extent will play a role in defining viable processing schemes. On the other hand, processing may be designed to deliberately affect some of these properties. Evidently, the properties are interrelated and cannot, in most cases, be adjusted individually. In the next sections, these aspects are discussed in greater detail.

### Mechanical Behavior of Matrix and Reinforcements

The silicides and aluminides of interest for the applications in question are, by necessity, high melting compounds. In many cases, these high melting temperatures preclude the viability of melting and casting to produce IMC's due to the effects of these high temperatures on the degradation of the reinforcing materials, especially in the case of ductile phase reinforcements (refractory metals), and to the lack of adequate crucible materials.

In addition, the effects of third elements (impurities) on the mechanical properties of the intermetallics are largely unknown. It is known that very small amounts of elements such as carbon and oxygen can have significant effects on the properties of metallic materials both as solutes and due to the formation of second phases. Although this in itself is an extensive field of research in conventional metals and alloys it seems that its importance in the field of intermetallic materials may have been largely overlooked until recently. In fact, some stages of metals processing are now completely dedicated to residual element control, and astounding improvements in both properties and reproducibility have been made recently.

### Thermodynamic Compatibility between Matrix and Reinforcement

The ability to combine essentially any set of initial phases or constituents in a material is unique to composites. Multiphase metal or ceramic systems are evidently limited to the stable and metastable phases present in the selected system. If the initial phases or constituents are not in equilibrium, however, kinetic considerations will dictate the time stability of the system. Well known examples include dispersion strengthened alloys and, in particular, precipitation strengthened alloys which rely on the control of mismatch strains and interfacial energies to maintain metastable phase distributions over long time periods.

The XD process developed by Martin-Marietta (8) uses precipitation reactions to generate the reinforcements; in this respect, the phase relations are closer to those observed in a multiphase metal or ceramic system. A large number of the IMC systems studied thus far, however, are comprised of thermodynamically incompatible constituents (due to their potentially desirable mechanical properties); in these systems the matrix-reinforcement reactions are controlled via intermediate "barrier" layers. Alternatively, intermediate "compliant" layers may have to be introduced in otherwise stable systems in order to tailor interface properties and to avoid degradation due to CTE mismatch effects, see item 3.3 below. The way these interface layers are produced may vary considerably, however.

In most studies, the reinforcements are coated prior to incorporation into the matrix material (9,10,11). The coating methods investigated include sol-gel, sputter deposition and physical and chemical vapor deposition (PVD and CVD). Unfortunately these methods tend to be expensive, time consuming and somewhat unreliable due to non-uniformity (cracks and discontinuities) that are either present after the coating process or develop during drying (sol-gel), handling or consolidation.

A slightly different approach is to use displacement reactions where the interfacial layer is formed or modified *in-situ* during the further processing (consolidation or heat treatment) of the composite. Likewise, it is possible to produce desirable dispersoid phases and even eliminate undesirable phases as part of this approach.

In a generic sense, *in-situ* reaction schemes can be described by:



where the elements A and B may be present in the matrix or the reinforcement either as solutes or in phases expected to be decomposed during the *in-situ* reaction. Figure 1 illustrates some of the topologically possible variations of these *in-situ* reaction schemes.

The similarities to techniques successfully employed in the processing of other materials are not only striking but inspiring. Some relevant examples include the nitriding of high aluminum steels to precipitate a dispersion of AlN, vacuum carbon deoxidation of nickel- or iron-based alloys (although that is normally conducted in the liquid state) and the coating of alumina inclusions with sulfides in bearing steels (discussed further in section 3.4 below).

For the case of a silicide ( $M_I Si$ ) reinforced by a metal  $M_{II}$ , it is evident that some knowledge of the thermodynamic behavior of several systems such as  $M_I - M_{II}$ , A-M-Si, B-M-Si and, eventually, quaternaries such as A-B-M-Si is necessary to screen the possible reaction schemes.

The availability of thermodynamic data on some of the systems envisaged for application in IMC's is limited. Besides the usual techniques for acquisition of thermodynamic data, some semi-quantitative techniques can be used to derive useful phase relations in these systems (12). In addition, diffusion couples may be used to derive empirical phase relations (e.g., 13). One must be aware that kinetics play an important role in defining the phases present in a diffusion couple, i.e., the phases present at a certain position in a diffusion couple may represent a metastable equilibrium. More importantly, the preference for a given diffusion path on a ternary diagram does not constitute proof of the non-equilibrium of other possible diffusion paths (e.g., 14). Traditional techniques such as arc melting and heat treatment are also useful. Estimation of bounds for thermodynamic functions based on known phase relationships can also be employed (12,15,16). Lastly, assessment of thermodynamic data and application of solution models (sometimes of relatively high complexity) may also be used to predict phase relations in the complex systems in question.

#### Matrix-Reinforcement Interface Properties.

One of the most extraordinary characteristics of composites is the importance of the interfacial properties on the overall mechanical behavior. The ability to tailor composite toughness and strength via interface control is a powerful tool only recently adequately appreciated (7). The aptitude to conciliate in an interface the thermochemical requirements discussed in the previous section with the desired mechanical characteristics is not always simple. The adequate characterization of interface behavior is still in its infancy at least for IMC's, and most discussions are still done in a qualitative way. The general concepts associated with increased toughness caused by partial debonding are well established but a priori specification of the desired properties for an interfacial phase is still not feasible.

#### Thermophysical and Mechanical Compatibility of Phases Present.

The possibility of tessellated stresses in composites of materials having different CTE's is well established. The effect of interfacial phases can be of enhancing or reducing these stresses. On the other hand, these stresses play an important role on the overall mechanical behavior of the interface and of the composite (7). The introduction of second phases to modify the resulting tessellated stresses has been shown to be an effective technique in some instances (e.g., 17). From the processing viewpoint, the usual approach in IMC fabrication has been the mechanical dispersion of a second phase into the matrix material by, for example, mixing powders. Obtaining a uniform dispersion is a key factor in achieving a regular stress distribution. Typical ceramic processing techniques of co-dispersion of the matrix and second phases followed by

drying or wicking have been applied with different degrees of success. Defining the proper medium, surfactants and adequate conditions are the main difficulties reported by many investigators. In situ displacement reactions are a viable alternative for the production of second phases with uniform distribution. Precipitation of coating phases to reduce or even eliminate tessellated stresses is a well-established processing route in metals processing. When alumina inclusions are coated by sulfides in bearing steels, not only can tessellated stresses be controlled but also more adequate inclusion morphologies can be achieved, thereby minimizing stress concentrations (18). Since most sulfide precipitation occurs at temperatures below the steel liquidus, the process is similar to the *in-situ* displacement reactions proposed presently.

### Examples of Process Design for Composites

In the following, we will present two examples of the use of *in-situ* reactions in the development of IMCs. The first example involves the reaction of carbon with molybdenum and silicon powders to both eliminate the amorphous, and probably detrimental, silica phase and to form SiC as a displacement reaction product. The second example concerns the formation of interfacial carbides in refractory-metal reinforced NiAl. The latter approach involves making small additions of carbon to the NiAl matrix and allowing it to react with the refractory metal of interest.

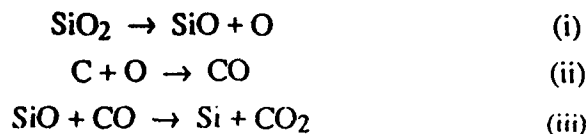
### Application of *in-situ* displacement reactions to the processing of MoSi<sub>2</sub>

**Background** A number of approaches for the processing of MoSi<sub>2</sub> are unsuitable due to its high melting temperature and owing to the fact that it is a line compound. In addition, the relatively high dissociation pressures of MoSi<sub>2</sub> at elevated temperatures could lead to silicon volatilization (19,20), resulting in the uncontrolled formation of second phases. Consequently, powder processing appears to be the preferred route to the fabrication of this material due to the intrinsically lower processing temperatures that it affords. However, this processing route results in the incorporation of substantial amounts of silica (SiO<sub>2</sub> originally present as a surface oxide on the powder surfaces) (21,22) into the consolidated samples. The silica phase softens at temperatures above 1200°C and may be responsible for the poor elevated temperature properties of MoSi<sub>2</sub>. Silica particles in the matrix may also affect the ambient fracture toughness, serving as weak links where cracks nucleate easily. Finally, silica formation in an initially stoichiometric matrix also makes it molybdenum rich, leading to Mo<sub>5</sub>Si<sub>3</sub> formation.

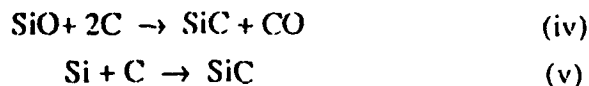
It therefore becomes clear that improvements in the properties of MoSi<sub>2</sub> and MoSi<sub>2</sub> based composites for structural applications are possible only with the elimination of silica (and oxygen) in the matrix along with close control of the overall stoichiometry. The present study utilizes an *in-situ* carbothermal reduction reaction for the elimination of the silica and its conversion to silicon carbide. Carbon, the essential ingredient in this *in-situ* reaction, was incorporated into a mixture of elemental molybdenum and silicon powders by mechanical alloying. This mixture had a stoichiometric ratio corresponding to MoSi<sub>2</sub>. Mechanical alloying was selected due to its ability to produce a homogeneous dispersion of carbon in the matrix; this facilitates the *in-situ* carbothermal reduction reactions during the subsequent hot-consolidation of the mechanically alloyed powders. A detailed description of the processing parameters and the transformation sequences that occur during the attrition and consolidation processes is presented elsewhere (22).

***In-situ* Reactions** The importance of gas phase reactions in the Si-C-O system is well established. The kinetics of the reduction of solid silica in refractories as well as the production of SiC by the carbothermal reduction of silica indicate that the gaseous species CO and SiO play a critical role in these processes. Simplified calculations in the Mo-Si-O system indicate that in the presence of either one of the silicides in question, all the molybdenum oxides become unstable at much higher oxygen potentials than silica and SiO. Whether SiO or silica is the stable oxide at a given temperature depends on the total system pressure. These calculations justify the use of the Si-C-O system for preliminary analyses of the processes occurring.

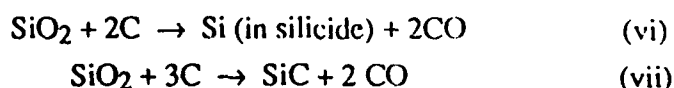
The reduction of SiO<sub>2</sub> to SiC by carbon occurs through a multistep reaction that involves the initial reduction of SiO<sub>2</sub> to Si or SiO, followed by the reaction to form SiC (23,24). The reaction sequence can be depicted as follows:



followed by the reaction of silicon monoxide or silicon to form silicon carbide, i.e.,



The overall reaction is thus:



It is interesting to note that the reduction of silica (reaction (vi)) is sensitive to total pressure. As in any carbon reduction process, the effect of the positive standard entropy of reaction is to make carbon monoxide the most stable phase as the temperature is increased. This is reflected in the standard free energy change of reaction (vii).

Reaction (vii) is thermodynamically viable above 1700K under atmospheric pressures. Changes in the total pressure of the system would shift the equilibrium towards either SiC formation or SiO<sub>2</sub> retention. Ishizaki (24) has shown that a lowering of the oxygen partial pressures and/or a reducing environment (conditions that typically exist during vacuum hot pressing using graphite dies) favor SiC formation at lower temperatures. Reaction (vii) also shows that two out of every three reacting carbon atoms are converted to CO. Therefore, the consolidation sequences during powder processing should be chosen so as to allow the product gases of the deoxidation reaction to escape in order to achieve full densification without any residual gas porosity.

**Results** The effectiveness of the *in-situ* reactions in modifying the microstructure is demonstrated by comparing the microstructures of MoSi<sub>2</sub> matrices processed with and without carbon additions. As shown in Figure 2, the microstructures of hot pressed specimens derived from the (nominally stoichiometric) MA binary MoSi<sub>2</sub> powders without carbon additions (i.e., without *in-situ* displacement reactions) consists of submicron grains of MoSi<sub>2</sub> and second phase particles with volume fractions in the range of 0.15-0.20. TEM/EDS analysis of these second phase particles revealed them to be amorphous and silicon-rich, indicating the presence of a glassy silica phase. This glassy phase was present at the grain boundaries and triple points. In addition, unidentified fine (10 nm) dispersoids were found within the MoSi<sub>2</sub> grains along with occasional grains of Mo<sub>5</sub>Si<sub>3</sub>.

The microstructure of the carbon-modified samples is shown in Figure 3a. A significant improvement in homogeneity and cleanliness (absence of silica) is apparent in comparison to the samples derived from the binary MA MoSi<sub>2</sub> powder without carbon. TEM analysis of this carbon-modified material revealed a homogeneous microstructure with uniformly distributed second phases such as those marked A in Figure 3a. The average grain size (3-5 μm) of the carbon-modified MoSi<sub>2</sub> was much larger than that of the material without carbon additions (<1 μm), possibly due to the higher consolidation temperatures used in the former. Both silicon and carbon were detected via EDS

microanalysis (thin window) of region A in Figure 3a indicating that these regions correspond to grains of SiC. Selected area diffraction patterns (SADPs) obtained along the major zone axes from these and similar silicon rich regions (Figure 3b) consistently indexed to a cubic  $\beta$ -SiC structure (with  $a = 0.4359$  nm), thereby confirming the occurrence of the *in-situ* reactions outlined earlier. These micron-sized SiC particles were located predominantly along grain boundaries and triple point regions. In addition, grains of a molybdenum-rich phase containing minor amounts of iron (region B) were also detected: EDS analysis indicated that this phase has the approximate formula  $C_{<1}(Mo,Fe)_{<5}Si_3$ .

#### Application of *in-situ* displacement reactions to the processing of NiAl

**Background** Recently, Bowman et al. (25) showed that for fiber-reinforced NiAl, tungsten fibers provided considerable strengthening but negligible toughening whereas alumina fibers resulted in considerable toughening and negligible strengthening. They related these differences to the low interfacial bond strength in the alumina/NiAl case and high bond strength in the tungsten case. Furthermore, they noted that the tungsten-reinforced NiAl was more susceptible to thermal fatigue due to the large mismatch in CTE between the two materials.

***In-situ* reactions** In this case, we have studied interface modification in both tungsten and molybdenum-reinforced NiAl via the *in-situ* reaction schemes described above. The initial attempts were focused on the possibility of alloying the NiAl matrix with a ternary addition selected to react with the refractory metals of interest, i.e., to form a reaction product at the NiAl/refractory metal interface. Ideally, this coating would have an intermediate CTE between those of NiAl and the refractory metal to reduce the materials susceptibility to cracking during thermal cycling. In addition, this coating would reduce the interfacial strength and lead to a tougher composite.

Carbon was selected as a candidate element due to the stabilities of both tungsten and molybdenum carbides. Preliminary thermodynamic calculations suggest that a low activity of carbon in the NiAl is necessary for these reactions to be favored (26). Thus, rods of NiAl alloyed with 1 wt. pct. (3.5 at. pct.) carbon were prepared by non-consumable arc melting, sectioned, polished and then combined with slices of tungsten and molybdenum to form diffusion couples via a hot pressing operation. The diffusion bonded samples were heat treated at 1300°C for 2 h under purified argon and then sectioned, polished and examined in a JEOL 733 electron microprobe. In order to produce partial reaction while avoiding the development of a strong interfacial bond so that subsequent x-ray diffraction studies might be performed on the reaction products, similar reaction studies were performed by placing the polished sections in contact and heat treating them at 1300°C for 3h without the application of an external load. After this treatment, the samples were separated and XRD patterns from the molybdenum and tungsten surfaces were obtained using a Philips APD 3720 diffractometer.

As can be seen in Figure 4 the reaction zone in both the samples is characterized by the presence of a thin layer at the interface between the NiAl(+C) alloy and the refractory metals. Compositional data obtained at several points along the reaction layers and also close to the layers on the refractory metal side (Table II) indicate that the layer in the molybdenum couple probably corresponds to Mo<sub>2</sub>C, whereas the NiAl(+C)/tungsten sample contained two reaction layers. The reaction layer adjacent to the tungsten corresponds to W<sub>2</sub>C and is continuous along the length of the interface. The second reaction layer corresponds to WC and is present only at a few places along the interface between the W<sub>2</sub>C and the NiAl. The compositional analysis in both refractory metals close to the reaction layer does not show the presence of any dissolved carbon. This implies that essentially all the carbon that diffuses into the refractory metals reacts to form the carbide, which is consistent with the low solubility of carbon in these refractory metals. XRD patterns obtained from the molybdenum and tungsten surfaces are consistent with the Mo<sub>2</sub>C and W<sub>2</sub>C identifications (see Figure 5) whereas, not surprisingly, no evidence of the WC phase was observed due to its low volume fraction and discontinuous nature.

## Summary

It is clear from the present study that, as in other classes of materials (e.g., alloys), in-situ reactions can be used as a means of removing undesirable phases (e.g., SiO<sub>2</sub>), or forming desirable phases (e.g., dispersoid phases or interfacial layers) in intermetallic matrix composites. Clearly, processing will play an important role in defining the resulting microstructures and, ultimately, the properties of these IMC's. While only two examples have been presented, it is clear that are a large range of possible schemes could be conceived using this approach. Furthermore, this approach is rather general in nature and should be applicable to both metal and ceramic matrix composites as well. It is emphasized that in order to achieve the maximum profit from in-situ displacement reactions of this type, an understanding of both the thermodynamics and kinetics of the reactions is essential.

## Acknowledgments

The authors would like to acknowledge the financial support of the Defense Advanced Research Projects Agency (Grant #MDA972-88-J-1006) and the Office of Naval Research (Grant # N00014-91-J-4132). One of the authors (ACS) would like to acknowledge the support of a CAPES-ME-Brazil Fellowship.

## References

1. J.D. Cotton, R.D. Noebe and M.J. Kaufman, to be published.
2. M. Yamaguchi and Y. Umakoshi, Progress in Materials Science, 34 (1990), 1-148.
3. J. Schlichting, High Temp.- High Pres., 10 (1978), 241
4. A. Basu, A. Gosh, Advanced Metal Matrix Composites for Elevated Temperature, Conf. Proc., eds. M.N. Gungor et al. (Metals Park, OH, 1991), 1.
5. D. Brooksbank and K. W. Andrews, J.I.S.I., 206 (1968), 595.
6. M.F. Ashby, F.J. Blunt and M. Bannister, Acta Met., 37 (7) (1989), 1847.
7. A.G. Evans, F.W. Zok and J. Davis, Comp.Sci. Tech., 42 (1991), 3.
8. R.M. Aikin, Jr., Ceram.Eng.Sci.Proc., 12 (1991), 1643-1655.
9. E. Fitzner and W. Remmele, ICCM-V, Fifth Intl.Conf.Comp.Mat., ed. W.C.Harrigan, Jr., et al., (Warrendale, PA, TMS-AIME, 1985), 515-530
10. L.Xiao, Y.S. Kim and R. Abbaschian, MRS Soc.Symp.Proc., ed. D.L. Anton, et al. (Pittsburgh, MRS, 194, 1990), 399-404.
11. T.C. Lu, et al., Acta Metall. Mater., 39 (8) (1991), 1853.
12. A. Costa e Silva and M.Kaufman, to be published.
13. J.M. Yang, et al., MRS Soc.Symp.Proc., ed. D.L. Anton, et al. (Pittsburgh, MRS, 194, 1990), 385-392.
14. F.J.J. van Loo and G.D. Rieck, Acta Met., 21 (1973), 73-84.
15. L. Brewer and O. Krikorian, J. Electrochem. Soc., 103 (1) (1956), 38-51.
16. J.H. Norman, G.H. Reynolds and L. Brewer, MRS Soc.Symp.Proc., ed. D.L. Anton, et al., (Pittsburgh, MRS, 194, 1990), 369-377
17. M. Maloney and R.J. Hecht, Mater. Sci. & Eng., A155 (1992), 19-31.
18. D.Brooksbank and K.W. Andrews, J.I.S.I., 210 (1972), 246-255.
19. T.G. Chart, Metal Science, 8 (1974), 344-348
20. A.W. Searcy and A.G. Tharp, J. Phys. Chem., 64 (1960), 1539-1542.
21. J.B. Berkowitz-Mattuck, P.E.Blackburn, and E.J.Felten, Trans. TMS-AIME, 233 (1965), 1093-1099.
22. S. Jayashankar and M.J. Kaufman, submitted to J. Mater. Res., 1992.

23. G.C. Wei, *J. Am. Cer. Soc.*, 66 (1983), C-111-C-113
24. K. Ishizaki, *Acta Metall. Mater.*, 38 (1990), 2059-2066.
25. R.R. Bowman and R.D. Noebe, *HITEMP Review 1990, Proc. of 3rd. Annual HITEMP Review*, (Cleveland, Ohio, October, 1990), 40-1.
26. P. Krishnan and M.J. Kaufman, to be published.

TABLE I - EXAMPLES OF POSSIBLE PROCESSING STRATEGIES BASED ON THE SCHEMES OF FIGURE 1

| ROUTE    | MATRIX   | REINFORCEMENT | IN-SITU REACTIONS                         | FINAL STRUCTURE         |
|----------|--|---------------|---|-------------------------|
| M3→C1    | MoSi <sub>2</sub> , SiO <sub>2</sub> , Mo <sub>5</sub> Si <sub>3</sub> , C | -             | SiO <sub>2</sub> +C → CO+Si               | MoSi <sub>2</sub>       |
| M3→C1+C2 | MoSi <sub>2</sub> , SiO <sub>2</sub> , Mo <sub>5</sub> Si <sub>3</sub> , C | -             | SiO <sub>2</sub> +C → Co+Si<br>Si+C → SiC | MoSi <sub>2</sub> +SiC  |
| M2→C3    | NiAl+C   | W             | W+C → W <sub>2</sub> C                    | NiAl/W <sub>2</sub> C/W |

TABLE II COMPOSITIONAL DATA IN DIFFUSION COUPLE SAMPLES.

| Area | Ni<br>at. pct. | Al<br>at. pct. | C<br>at. pct. | W<br>at. pct. | Mo<br>at. pct. |
|------|----------------|----------------|---------------|---------------|----------------|
| A    | 2.0            | 0.8            | 34.1          | 0             | 63.6           |
| B    | 1.7            | 0.3            | 0             | 0             | 98.5           |
| C    | 4.7            | 0.5            | 26.9          | 67.9          | 0              |
| D    | 4.3            | 1.9            | 51.9          | 43.4          | 0              |
| E    | 0.5            | 0.2            | 0             | 99.3          | 0              |

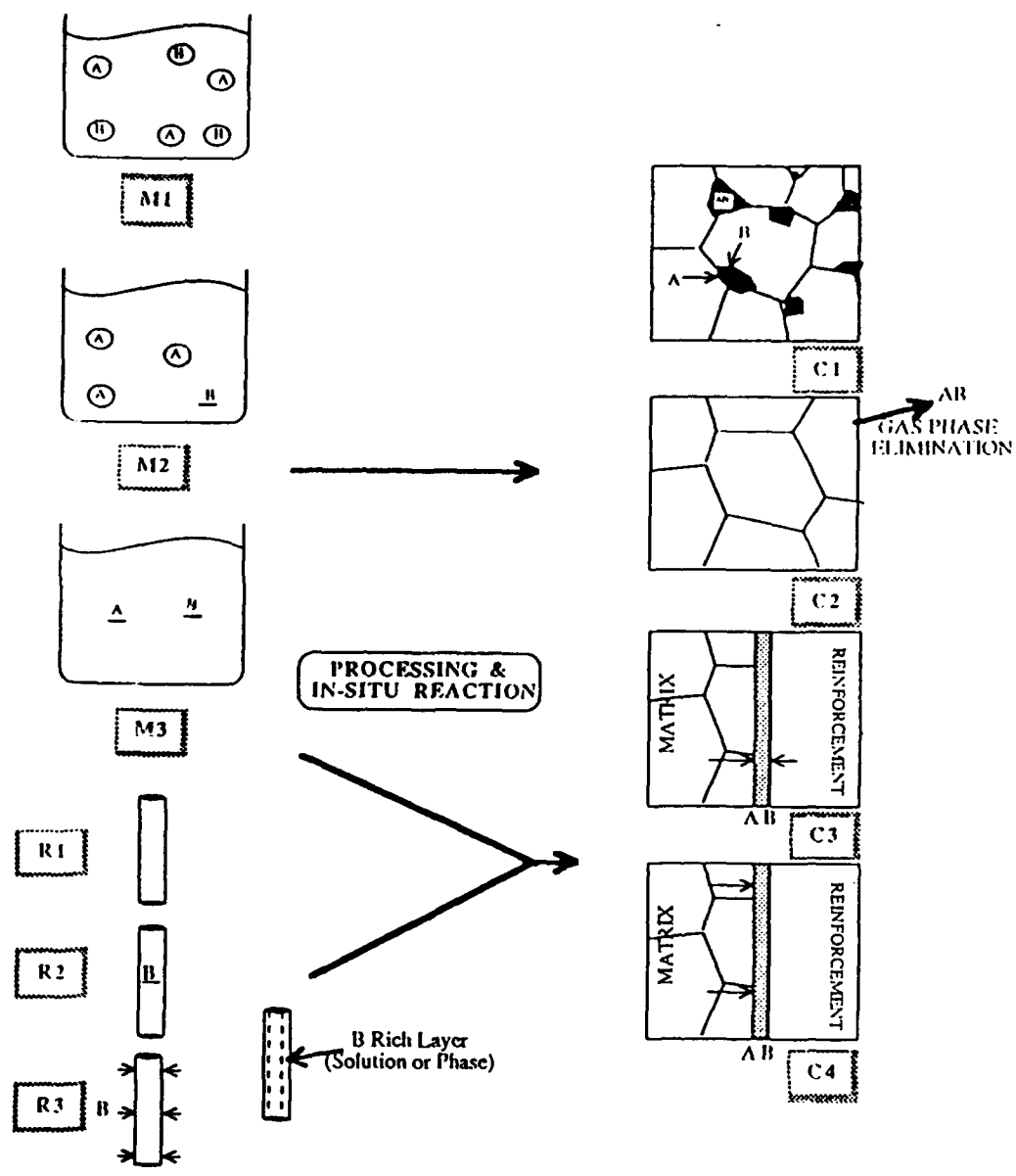


Figure 1 Some possible topological variations of in-situ reactions in composites processing. Actual composites may profit from combinations of features exemplified in the right column. See Table I for some examples of proposed processing strategies.  
A, B : Elements in solution. (A), (B) : Phase containing the particular element.

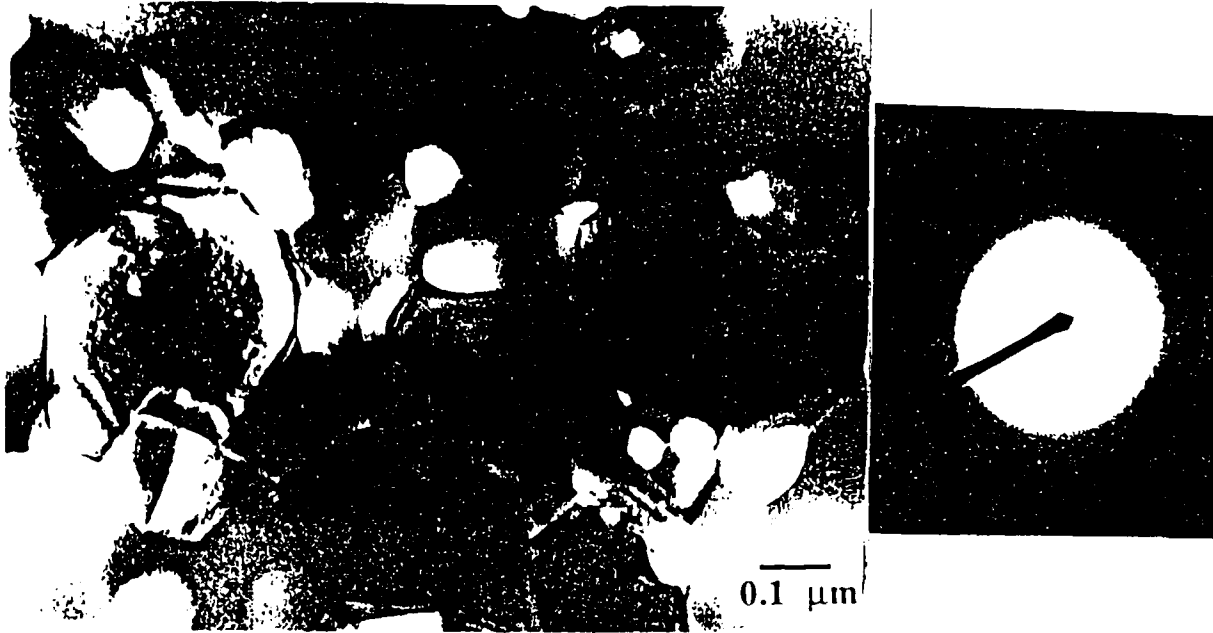


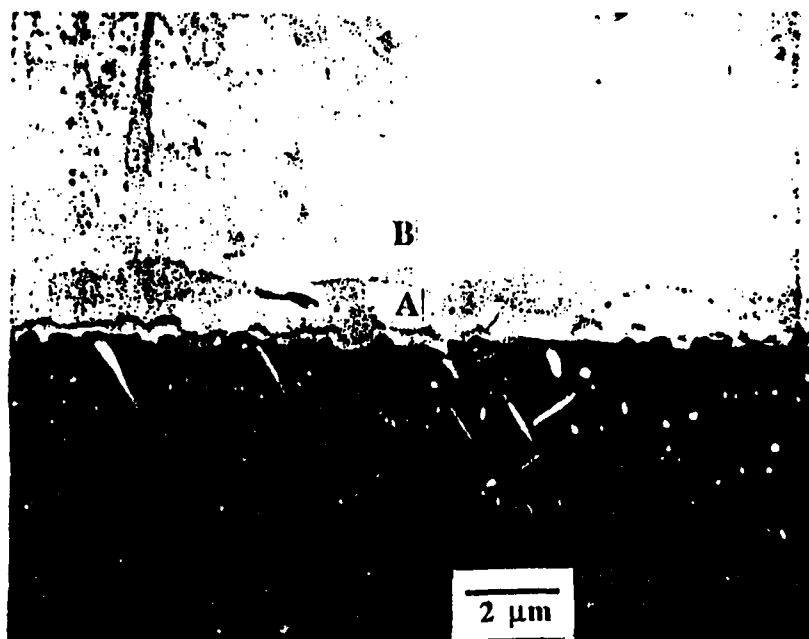
Fig. 2a Bright Field Transmission Electron Micrograph of the typical microstructure of MoSi<sub>2</sub> derived from binary MA MoSi<sub>2</sub> powder, showing the presence of silica along the grain boundaries and triple points.

Fig. 2b Selected area diffraction pattern from a silica-containing region showing the presence of the amorphous phase.

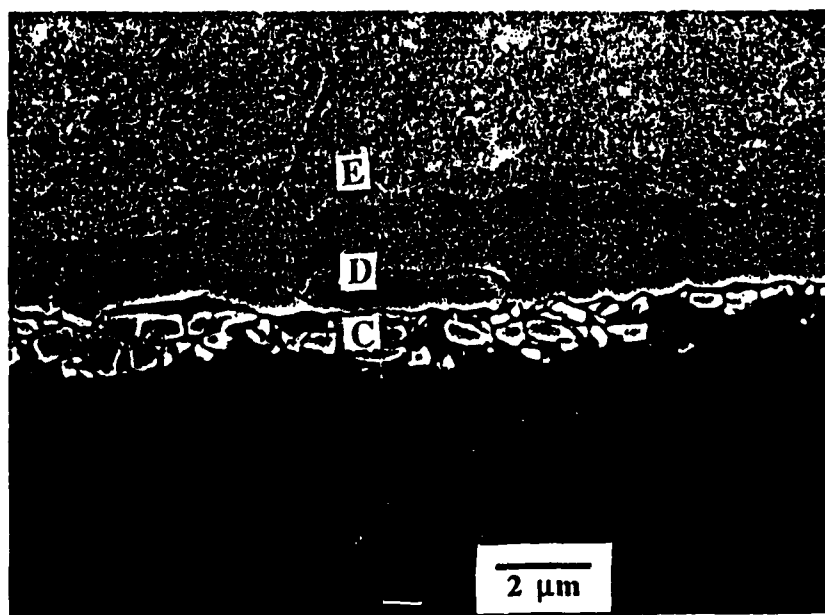


Fig. 3a Bright Field Transmission Electron Micrograph of the typical microstructure of the carbon-modified MoSi<sub>2</sub> processed utilizing the *in-situ* displacement reactions. Region A is a typical *in-situ* formed β-SiC particle. Note the absence of silica particles such as those found in Fig. 2a.

Fig. 3b Selected area diffraction pattern of a β-SiC particle along B = [011]



(a)



(b)

Fig. 4 Secondary electron images of the interface between NiAl(+C) alloy and the refractory metals, showing the *in-situ* formed carbide layers. (a) NiAl(+C)/Mo couple (b) NiAl(+C)/W couple. (region A is Mo<sub>2</sub>C, region B is Mo, region C is WC, region D is W<sub>2</sub>C, and region E is W)

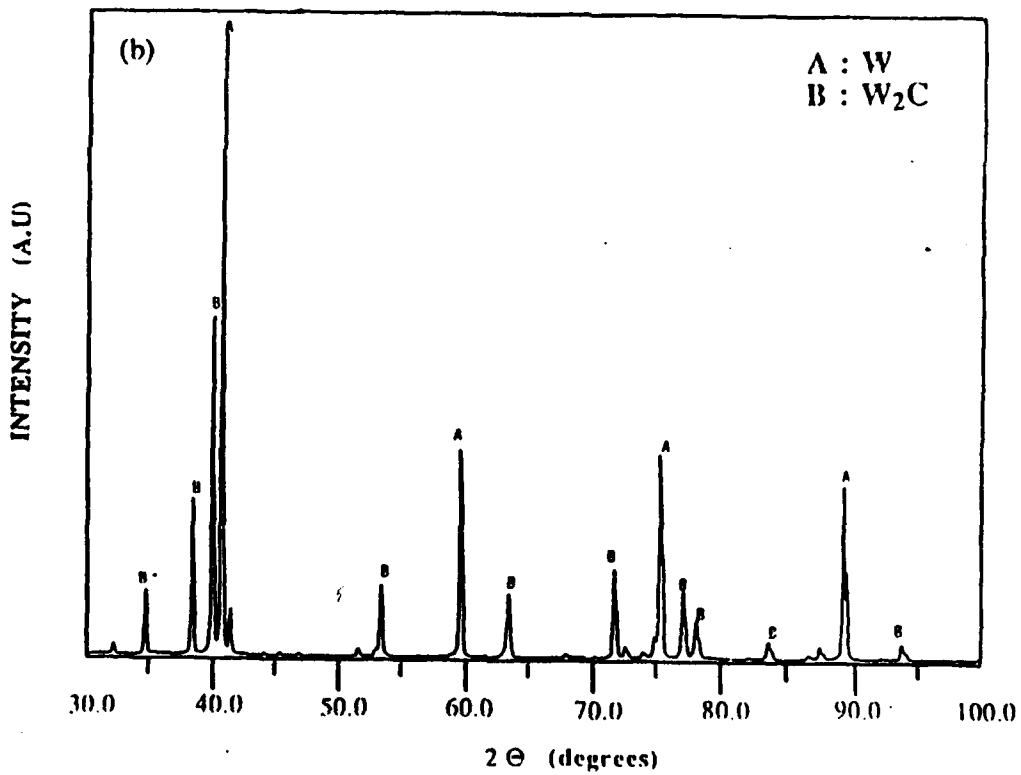
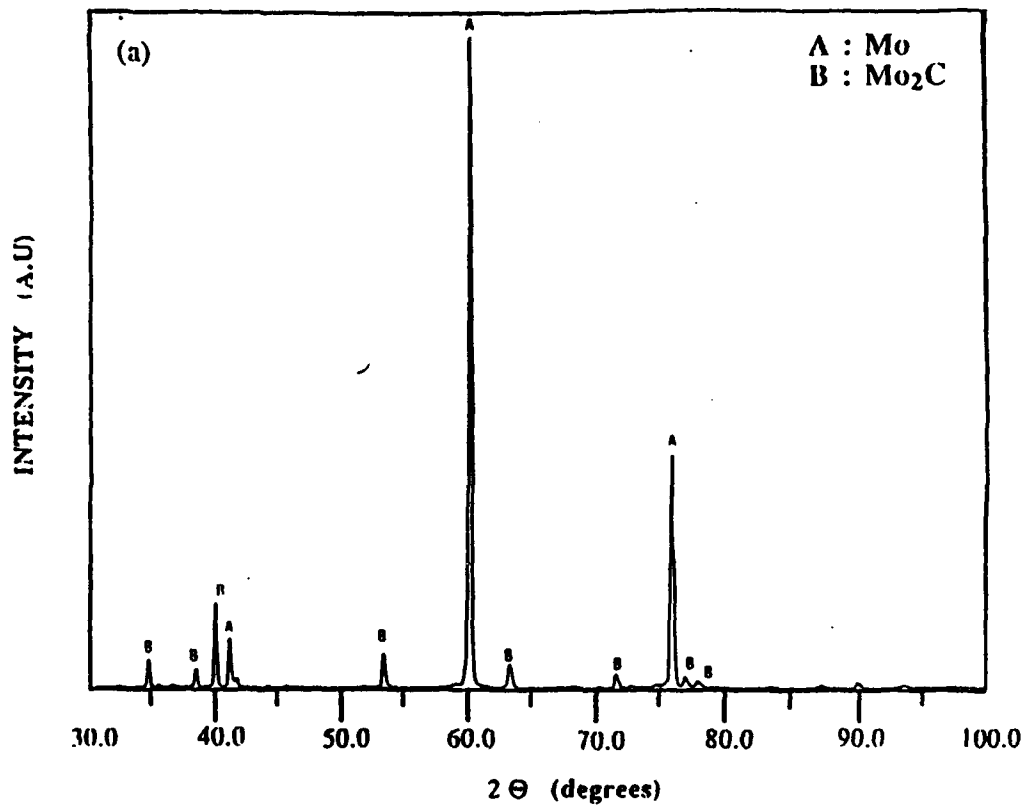


Fig.5. X-ray diffractograms of the refractory metal surfaces in contact with the NiAl (+ C) alloy for 3 h at 1300°C, showing the formation of the carbides. (a) NiAl (+C)/Mo couple (b) NiAl (+C)/W couple.